FCRD-SWF-2013-000073
INL/EXT-12-27936
Revision 1

Separations and Waste Forms Research and Development

FY 2012 Accomplishments Report

February 2013

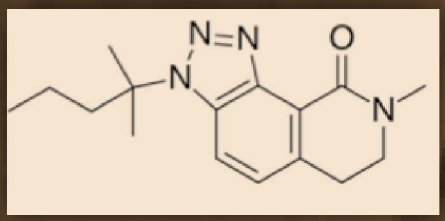

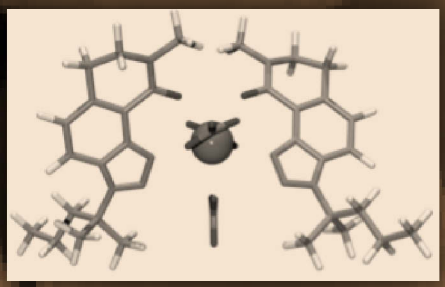

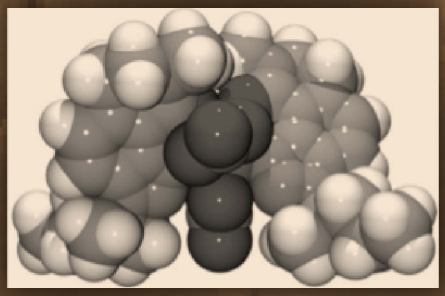

Cover Graphics: [background] SEM analysis of $Cs_{0.90}Ba_{0.05}Al_{0.95}Fe_{0.05}Si_2O_6$; [Insets] Preorganized mixed-donor extractant, L, (top) and views of the predicted geometry for an $[AnL_2(NO_3)_3]^0$ complex obtained from molecular mechanics calculations.

FCRD-SWF-2013-000073
INL/EXT-12-27936
Revision 1

Separations and Waste Forms Research and Development

FY 2012 Accomplishments Report

February 2013

Idaho National Laboratory
Idaho Falls, Idaho 83415

http://www.inl.gov

Prepared for the
U.S. Department of Energy
Office of Nuclear Energy
Under DOE Idaho Operations Office
Contract DE-AC07-05ID14517

This page intentionally left blank.

Separations and Waste Forms Research and Development

FY 2012 Accomplishments Report

FCRD-SWF-2013-000073
INL/EXT-12-27936
Revision 1

February 2013

Compiled and Edited by:

Jason Schulthess (jason.schulthess@inl.gov)
Douglas Hamelin (douglas.hamelin@inl.gov)
INL Systems Engineering

Approved by:

Terry Todd	Date
Separations and Waste Forms National Technical Director	

This page intentionally left blank.

EXECUTIVE SUMMARY

The Separations and Waste Form Campaign (SWFC) under the U.S. Department of Energy (DOE) Fuel Cycle Research and Development Program (FCRD) is responsible for developing advanced separation and waste form technologies to support the various fuel cycle options defined in the *DOE Nuclear Energy Research and Development Roadmap, Report to Congress, April 2010*. The fiscal year (FY) 2012 accomplishments report highlights the results of the research and development (R&D) efforts performed within SWFC in FY 2012. Each section contains a high-level overview of the activities, results, technical point of contact and applicable references.

This report briefly outlines campaign management and integration activities, but the intent of the report is to highlight the many technical accomplishments made during FY 2012. The campaign continued to maintain a balanced effort between scientific investigations to underpin advanced separations and waste forms technologies and engineering advancement to maintain relevance and focus on implementable technologies. There was an increased focus on development of new tools and methods to develop a better fundamental understanding of separation processes and waste form behavior and this effort is closely tied to modeling and simulation activities.

The SWFC campaign management and integration activities included international coordination activities (France, China, Russia, Japan, and the International Atomic Energy Agency [IAEA]), integration of the SWFC activities with other FCRD campaigns, (Advanced Fuels, Used Fuel Disposition, Systems Options, and Material Protection, Accountancy and Control Technologies), and integration with DOE Office of Environmental Management. A major accomplishment for FY 2012 was an external Relevancy Review that the FCRD program held to review the Separations and Waste Form Campaign. The Campaign also provided support in planning and executing of a joint DOE Office of Nuclear Energy (NE)-Office of Environmental Management (EM)-National Nuclear Security Administration Separations Workshop, aimed at developing a Roadmap for Separations Technology across the DOE mission areas.

Technical accomplishments are reported under the following R&D categories:

- Advanced Aqueous Technologies
- Electrochemical Separation Technologies
- Sigma Team for Minor Actinide Separations
- Off-Gas Sigma Team
- Fundamental Science and Methods Development
- Advanced Separation Process Alternatives
- Modeling and Simulation
- Advanced Waste Forms
- Waste Form Performance over Geologic Timescales
- Waste Form Production
- Fuel Resources.

Advanced Aqueous Technologies

Work performed within Advanced Aqueous Technologies was primarily the development of capabilities to support generic aqueous separation technologies (i.e., areas of development that will be needed and important for any aqueous technology). These included spectrophotometric monitoring of key process parameters (e.g., U, Pu, Np, nitrate, acid concentration) in near-real time. Additionally, the same techniques were applied to detecting and monitoring solvent degradation products and measuring metal concentrations in molten salt environments. A state-of-the-art micro-capillary sampling system was developed and designed for taking process samples, transporting them to an instrument and performing the analysis. A solvent degradation test loop, to allow hydrolysis and radiolysis (or both) of process solvents to be tested was used to test the

solvent degradation behavior of the TRUEX process. The test loop, which is one of only two in the world, gives the SWFC the ability to test the solvent degradation of any process solvent planned for future testing or implementation. Finally, additional testing of the Modified Direct Denitration process for conversion of uranium and actinide nitrates to oxides was performed.

Electrochemical Separation Technologies

Work performed under this area includes fission product and TRU drawdown from spent salt, process monitoring of metals in molten salt using volumetric and spectrophotometric techniques, , and salt-metal separations for U/TRU product. An additional project focused on limited recycle using molybdate melts was selected as part of an FY 2011 call for white papers and work was completed in FY 2012. These are areas that fall outside of the Joint Fuel Cycle Studies project and are focused on long term improvements for the electrochemical processing technology.

Sigma Team for Minor Actinide Separations

This multi-lab, multidisciplinary Sigma Team is taking a number of approaches at trying to develop a simplified, economic and robust separation scheme for Am from Cm and lanthanides or Am and Cm from lanthanides. This is without a doubt one of the most difficult chemical separations in the nuclear industry and represents tens of millions of dollars of R&D spent each year worldwide. Significant progress has been made in the Sigma team in its first four years, setting the foundation for possible future separation technologies. The team has demonstrated outstanding collaboration and teamwork, while maintaining individual research projects.

Off-Gas Sigma Team

This team has only been in existence for three years and has already made important discoveries relative to the capture and immobilization of iodine and krypton. The team has demonstrated key fundamentals for iodine capture on silver mordenite (the reference case) including the effects of silver aging and the fundamental sorption mechanics. Novel new sorbents such as silica aerogels, chalcogenide glass aerogels, and metal organic frameworks (MOFs) have also been demonstrated at a laboratory scale.

Fundamental Science and Methods Development

This activity is focused on developing the tools and methods to better understand the fundamental properties and driving forces behind the separation processes and waste form behavior. This work is closely tied to the applied R&D effort to support process development as well as subscale and first principle models. This work includes studies on the thermodynamics and kinetics of SX processes, study of non-ideality in separation processes, fundamental radiation chemistry and the effects of radiation on separation chemistry (e.g., speciation of multivalent cations), generation of data and models for the first principle modeling of metal-water interactions, and understanding decay impacts on waste form stability.

Advanced Separation Process Alternatives

This area looks for game changing concepts that could radically change fuel processing in the long-term future. A peer review process was used in FY 2011 to select projects from laboratory-generated white papers. Projects currently funded are the rational design of extractants by understanding their covalency, and two projects focused on electrochemical methods, one in aqueous media and one in room temperature ionic liquids. Three additional projects for concepts that would apply to limited recycle concepts were continued from FY 2011. The three projects are: Supercritical CO_2 Separations, Combination of Hard and Soft Donor Ligands for Actinide Co-extraction from UREX Raffinate, and Functionalized Ultra-Porous Ceramic Nanofiber Membranes.

Modeling and Simulation

Development of the next generation separations processes, waste processes, and waste forms requires the closely coupled use of testing, modeling, and theory. Modeling and simulation efforts are currently focused on several high priority areas including plant scale modeling, waste form performance, and computational fluid dynamic (CFD) modeling within separation equipment. The Separations and Safeguards

Performance Model (SSPM), developed in Matlab Simulink, has been used as a base to integrate modeling capabilities for reprocessing plants. A time dependent AMUSE model has been integrated into the SSPM allowing for a more realistic plant model for safeguards analysis. Relative to waste form performance, a set of energy barriers have been provided for silica hydrolysis reactions developed from the first principles calculations that can be used for modeling borosilicate glass dissolution. Additionally, glass dissolution rates were experimentally measured for a SON68 glass analog. CFD modeling efforts for solution flow within centrifugal contactors continued with development of a novel hybrid multiphase CFD solver. This tool enables three-phase, liquid-liquid-air simulations in which a sharp interface is maintained between each liquid and air, but dispersed phase modeling is used for the liquid-liquid interactions.

Advanced Waste Forms

The objective of the advanced waste management activity is to develop the next generation waste forms and processes with higher performance suitable for advanced separations. By higher performance, these technologies are aimed at order of magnitude improvement in chemical durability for troublesome radionuclides, significant reduction in waste management costs, and/or significant reduction in waste volumes. Six projects were selected in FY 2010 by a peer review process from laboratory generated white papers and were first funded in FY 2011 (with continued funding for the first five in FY 2012): (1) glass ceramics for mixed fission products waste with 50% higher waste loading relative to borosilicate glass using essentially the same process, (2) zirconium purification and recycle to reduce the waste requiring deep geologic disposal by ~25% and reuse nuclear grade zirconium, (3) epsilon metal (a Ru, Pd, Rh, Tc, Mo metal phase formed in irradiated nuclear fuel) for Tc, UDS, and noble metals with 100% waste loading and ~2 orders of magnitude higher durability than waste glass, (4) titanate ceramics for Tc with four orders of magnitude increase in durability, and (5) titanate ceramics for mixed fission product waste for 50% higher waste loading and up to 4 orders of magnitude higher durability. Development on these six technologies began in FY 2011 and already significant progress has been made, in particular, on the glass ceramics, titanate ceramics, and epsilon metal.

Waste Form Performance over Geologic Timescales

The primary objective of a waste form is to prevent the release of the immobilized radionuclides from release to the biosphere during storage, transportation, and disposal. As the half-lives of radionuclides being immobilized are as long as millions of years, the waste form should be stable for at least that long in the environment. This activity is focused on developing the tools and science necessary to predict the performance of waste forms for geologic timescales with sufficient confidence to be effective in convincing the public, regulators, and stakeholders of the safety of nuclear waste disposal. Two example waste forms are used for the development – borosilicate glass and iron based alloys. These two waste forms are both likely candidates for long-lived radionuclide immobilization and serve to give a range of processes that need to be understood for the prediction of repository performance. A reference alloy waste form was developed and characterized in FY 2011. Innovative characterization techniques were developed for glass corrosion studies, and a long-term isotope exchange study was initiated to determine how different non-radioactive isotopes of the same elements, one from the glass and one from the solution, interacted to form glass alteration products.

Waste Form Production

Advanced waste form production efforts seek to apply advanced processing methods developed over the last two decades to enable the effective processing of advanced waste forms with improved performance. Two technologies were initially selected for development based on their ability to improve process efficiency and allow for the fabrication of the advanced waste forms being developed by the campaign – Cold Crucible Induction Melter (CCIM) and Spark Plasma Sintering (SPS). A successful, first-of-a-kind, CCIM test was performed in FY 2012 that

demonstrated the ability to fabricate glass ceramics waste forms. Specifically, this test showed: (1) liquid feeding of a simulated HLW raffinate, (2) the melting of the high-loaded glass ceramics composition, (3) repeated stopping and starting of glass ceramic pours, and (4) ability to form glass ceramics for a number of canister cooling profiles. Research on SPS has been initiated under the activities of the advanced waste forms section of this report.

Fuel Resources

The primary objective of the Fuel Resources effort is to develop advanced absorbent materials for the extraction of uranium from seawater. This resource accounts for greater than four billion tonnes of uranium, but at parts per billion concentration levels. To accomplish an economic recovery of this uranium resource, the developed adsorbent must have high extraction capacity, high selectivity for uranium, and must be durable in the marine environment. The approach to developing adsorbents with these characteristics focused on five primary areas; development and improvement of the reference amidoxime ligand adsorbent using irradiation grafting techniques on polymer-based materials, understanding the fundamental chemistry and thermodynamics of uranium extraction from a seawater matrix, computational modeling of alternative ligands that would increase capacity, selectivity, and durability, investigation of advanced materials technologies (nano-synthesis or nano-manufacturing) for preparing new adsorbents, and development of a cost/energy balance model that could be used to evaluate process improvements and focus the R&D to the higher return areas. In FY 2011 and 2012, this area has seen significant progress in increasing the adsorbent material capacity, the development of the cost/energy model, investigation of alternative extraction ligands, and has begun the testing of the most promising adsorbent materials at marine testing facilities. The Marine Sciences Laboratory at PNNL is leading the adsorbent materials testing effort with additional support from the Wood Hole Oceanographic Institute and The Rosenstiel School of Marine and Atmospheric Sciences at the University of Miami. The adsorbent development team received an R&D 100 Award (the prestigious Award that recognizes the top 100 technology innovations of the year) for the development of the higher surface area/high capacities adsorbents in collaboration with Hills, Inc.

CONTENTS

FIGURES

TABLES

This page intentionally left blank.

ACRONYMS

ACC	annular centrifugal contactors
AES	Auger Electron Spectroscopy
AFCI	Advanced Fuel Cycle Initiative
AHTGR	Advanced High-Temperature Gas-Cooled Reactor
AIM	atoms-in-molecules
AIROX	Atomics International Reduction-Oxidation
ALSEP	americium/lanthium separations
ANL	Argonne National Laboratory
ANSTO	Australian Nuclear Science and Technology Organization
APS	Advanced Photon Source
APT	atom probe tomography
ATR	attenuated total reflectance
BET	Brunauer, Emmet, and Teller (theoretical surface area model)
BWR	boiling water reactor
CA	chronoabsorptometry
CCIM	cold crucible induction melter
CEA	Commissariat à l'énergie atomique
CFD	computational fluid dynamics
CFR	Code of Federal Regulations
CRIEPI	Central Research Institute of the Electric Power Industry
CSULB	California State University – Long Beach
CTE	critical technology elements
CV	cyclic voltammetry
D&D	decontamination and decommissioning
DEOX	declad and oxidize
DF	decontamination factor
DFT	density functional theory
DOE	U.S. Department of Energy
-EM	Office of Environmental Management
-NE	Office of Nuclear Energy
-SC	Office of Science
DPV	differential pulse voltammetry
EDAX	energy dispersive analysis x-ray

EDL	Engineering Development Laboratory
EDS	energy dispersive spectroscopy
EIS	electrochemical impedance spectroscopy
EMSL	Environmental Molecular Sciences Laboratory
EPA	Environmental Protection Agency
EPMA	electron probe microanalyzer
ERT	electrical resistance tomography
ESI-MS	Electrospray Ionization-Mass Spectroscopy
EXAFS	extended X-ray absorption fine structure
EXT	External (INL document type designator)
FCO	Fuel Cycle Options
FCRD	Fuel Cycle Research and development
FCTWG	Fuel Cycle Technology Working Group
FFT	fast Fourier transforms
FP	fission product
FTIR	Fourier transform infrared
FY	fiscal year
GCM	Glass Composite Material
GDE	Guide (INL document designator)
GIXRD	grazing incidence X-ray diffraction
GUI	graphical user interface
HFDA	Hot Fuels Dissolution Apparatus
HFEF	Hot Fuel Examination Facility
HIM	helium ion microscopy
HIP	Hot Isostatic Pressing
HLW	high-level waste
HOMO	highest occupied molecular orbital
HPLC	high pressure liquid chromatography
HSAB	hard and soft acids and bases
HWR	heavy water reactor
IAD	ion-assist deposition
ICP-AES	Inductively Coupled Plasma-Atomic Emission Spectroscopy
ICP-MS	Inductively Coupled Plasma-Mass Spectrometer
ICP-OES	Inductively Coupled Plasma-Optical Emission Spectrometry

ICPP	Idaho Chemical Processing Plant
IDIQ	Indefinite Delivery, Indefinite Quantity
IEDF	Idaho Engineering Development Facility
IL	ionic liquid
INL	Idaho National Laboratory
INTEC	Idaho Nuclear Technology and Engineering Center (formerly ICPP)
JAEA	Japan Atomic Energy Agency
KAERI	Korean Atomic Energy Research Institute
kGy	kilogray
LANL	Los Alamos National Laboratory
LBNL	Lawrence Berkeley National Laboratory
LCC	liquid cadmium cathode
LET	linear energy transfer
LTD	Limited (INL document type designator)
LUMO	lowest unoccupied molecular orbital
LWR	light water reactor
MA	minor actinide
MDD	modified direct denitration
MEI	maximally exposed individual
MEXT	Ministry of Education, Culture, Sports, Science and Technology (Japan)
mM	millimoles
MOC	modified open cycle
MOIT	Ministry of Industry and Trade (Czech Republic)
MOU	Memorandum of Understanding
MOX	mixed oxide
MPa	megapascal
MS	microwave sintering
MTZ	mass transfer zone
NBO	natural bond orbital
NDA	non-destructive analysis
NEUP	Nuclear Energy University Programs
NMR	nuclear magnetic resonance
NNSA	National Nuclear Safety Administration
NRC	Nuclear Regulatory Commission

NTD	National Technical Director
OECD	Organisation for Economic Co-operation and Development
OIM	orientation imaging microscopy
ORNL	Oak Ridge National Laboratory
P&T	packaging and transportation
PCT	product consistency test
PDF	Pair Distribution Function
PEST	parameter estimation
PI	principal investigator
PLS	partial least squares
PNNL	Pacific Northwest National Laboratory
PRI	passivating reactive interphase
PSAL	Process Science Analytical Laboratory
PSI	pounds per square inch
PUREX	plutonium-uranium extraction
PVD	physical vapor deposition
PWR	Pressurized Water Reactor
R&D	research and development
RAW	reference alloy waste form
RBS	Rutherford backscattering spectrometry
RGR	Reactive Gas Recycling
RIAR	Research Institute of Atomic Reactors (Russia)
RoHUP	remotely operated hot uniaxial press
RSD	relative standard deviation
RTD	resistance temperature detector
SANS	small angle neutron scattering
SCFH	standard cubic feet per hour
SEC	spectroelectrochemistry
SEM	scanning electron microscopy
SIMS	secondary ion mass spectroscopy
SNF	spent nuclear fuel
SNL	Sandia National Laboratory
SPS	spark plasma sintering
SRNL	Savannah River National Laboratory

STMAS	Sigma Team for Minor Actinide Separation
SULI	Science Undergraduate Laboratory Internships
SWFC	Separations and Waste Forms Campaign
SX	solvent extraction
TALSPEAK	trivalent actinide-lanthanide separations by phosphorus reagent extraction from aqueous complexes
TEM	transmission electron microscope
TGA	thermogravimetric analysis
TMP	technology maturation plan
TRISO	tri-structural-isotropic
TRL	technology readiness level
TRU	transuranic
TRUEX	transuranic extraction
UDS	undissolved solids
UFD	Used Fuel Disposition
UHV	ultra-high vacuum
UNF	used nuclear fuel
UREX	uranium extraction
UV-Vis	ultra violet-visible
UV-vis-NIR	ultra violet-visible-near-infrared
VFP	Visiting Faculty Program
VHT	vapor hydration test
VOF	volume of fluid
VPO	vapor pressure osmometry
WBS	work breakdown structure
WDA	wavelength dispersive analysis
WDS	wavelength-dispersive x-ray spectroscopy
XANES	X-ray absorption near edge spectroscopy
XAS	x-ray absorption spectroscopy
XPS	X-ray photoelectron spectroscopy
XRD	X-ray diffraction

Chemical Compounds

AG	silver-functionalized aerogel
AgZ	silver-zeolite
AHA	acetohydroxamic acid
BSG	borosilicate glass
CMPO	octyl (phenyl)-N,N-diisobutylcarbonoylmethyl-phosphine oxide
CS/LN/TM	cesium, strontium, lanthanide, and transition metal
DAAP	diamyl(amyl)phosphonate
DIBAA	N,N-diisobutylacetamide
DIBFA	N,N-diisobutylformamide
DMA	N,N-dimethylacetamide
DMAH	N,N-dimethylacetamidium
DPAH	dithiophosphinic acid
DTPA	diethylenetriaminepentaacetic acid
EDTA	ethylenediaminetetraacetic acid
EMIM	1-ethyl-3-methylimidazolium
FS-13	trifluorophenyl sulfone
HDBP	dibutylphosphoric acid
HDEHP	di-2-ethylhexylphosphoric acid
HEH[EHP]	2-ethylhexyl phosphonic acid mono-2-ethylhexyl ester
MOR	mordenite
SiC	silicone carbide
T2EHDGA	N,N,N',N'-tetra-2-ethylhexyldiglycolamide
TBP	tributyl phosphate
TODGA	N,N,N'N'- tetraoctyl diglycolamide
UOX	uranium oxide

CHAPTER 1
INTRODUCTION

CHAPTER 1: INTRODUCTION

T. Todd, terry.todd@inl.gov

The Separations and Waste Forms Campaign (SWFC) is one of the major research and development (R&D) areas under the U.S. Department of Energy (DOE) Fuel Cycle Research and Development (FCRD) program. The SWFC has the responsibility to develop advanced separations and waste forms technologies using a science-based, engineering-driven approach.

Accomplishments made during fiscal year (FY) 2012 are highlighted in this report, which focuses on completed work and results. Process details leading up to the results are not included; however, the technical contact is provided for each research effort. The order of accomplishments in this report is consistent with the SWFC work breakdown structure (WBS).

Campaign Objective

T. Todd, terry.todd@inl.gov

The objective of the SWFC is to develop advanced fuel cycle separation and waste management technologies that improve current fuel cycle performance and enable a sustainable fuel cycle, with minimal processing, waste generation, and potential for material diversion.

Campaign Structure

T. Todd, terry.todd@inl.gov

The campaign is organized in a flat structure to facilitate cross campaign integration. Figure 1 shows the campaign WBS for FY 2012. Federal Project Directors are responsible for oversight and approval of all work activities in the SWFC. The National Technical Director (NTD) and Deputy NTD are responsible for work prioritization, integration, and management. Control account managers are responsible for the day-to-day oversight of the work packages and the integration of work packages within the control account, as well as monthly progress and budget status reporting.

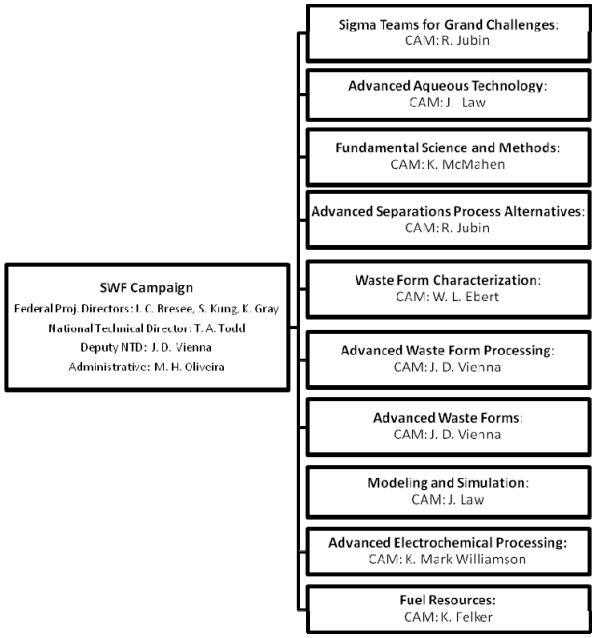

Figure 1. Separations and waste forms campaign WBS

Campaign Relevance Review

T. Todd, terry.todd@inl.gov

In June 2012, independent experts in the area of separations and waste forms evaluated several aspects of the campaign to assess their relevance in responding to overall DOE guidance [Harmon 2012]. The results of this review are summarized below:

- Reviewers concluded that SWFC has an excellent program in place, and high quality results are being achieved. Numerous publications (400-500) and accomplishments show excellent productivity and results-oriented work.

- Reviewers were impressed by the caliber and breadth of technical managers and researchers that are involved. The campaign has engaged the top people in the country in all areas of work. Reviewers know them and respect them.
- Reviewers recognized the difficulty in managing this program given the rapidly changing environment and continued uncertainties ahead for both the DOE Office of Nuclear Energy (NE) and contractors. The management team has learned to cope with change while still maintaining commitment and enthusiasm among the program participants. In short, the program is in good hands.
- The campaign has made excellent use of industry, national laboratories, and universities. The program has been proactive in engaging the universities via the Nuclear Energy University Program (NEUP) and through direct contracts from the SWFC.
- Reviewers suggested that university programs can be further integrated into the SWFC with benefits to both activities.

In addition, the relevancy of different aspects of the program was judged as shown in Table 1:

Table 1. Relevancy assessment of program R&D activities.

R&D Activity	Relevancy Assessment	
	Chairman	Panel Member
Fundamental Science and Methods Development / Modeling & Simulation	Moderate to High	Moderate to High
Sigma Team for Minor Actinide Separations	Moderate to High	Moderate to High
Sigma Team for Off-gas Capture and Immobilization	High	Moderate
Advanced Aqueous Separations	Moderate to High	Moderate to High
Advanced Waste Forms / Waste Form Processing	High	High
Waste Form Performance Over Geologic Timescale	High	High
Domestic Electrochemical Processing	Moderate	Moderate
Transformational Separation Approaches	Moderate	Moderate
Fuel Resources (U Extraction from Seawater)	Moderate	Moderate to High

This page intentionally left blank.

CHAPTER 2
COLLABORATIONS

CHAPTER 2: COLLABORATIONS

T. Todd, terry.todd@inl.gov

The SWFC has a number of collaborations that contribute to the success of the FCRD program. Key international collaborations include France, Japan, China, and Russia. Collaborations among other campaigns within the FCRD program provide a critical interface to ensure that the results of the SWFC are well integrated and consistent across the FCRD program. Key collaborations also exist with other DOE offices, such as the Office of Environmental Management (EM) and the National Nuclear Security Administration (NNSA). Finally, important collaborations have been established with the Nuclear Energy University Programs (NEUP) and the universities performing research in support of the SWFC. The results of the university NEUP projects are not reported in this document, but in several instances are very closely integrated with the program work being performed.

CEA-DOE Collaboration

T. Todd, terry.todd@inl.gov

The United States and France share a long history of nuclear energy R&D collaboration, particularly in the area of separations and waste management. In particular, the DOE and the Commissariat à l'Énergie Atomique (CEA) have had a very successful nuclear technology interchange for several decades. A Nuclear Energy Cooperative Action Plan was drafted in 2012, and a joint planning meeting was held in October 2012 at Argonne National Laboratory (ANL). The Action Plan is organized into four working Groups:

- Working Group 1: Next Generation Reactors
- Working Group 2: Separations and Waste Forms
- Working Group 3: Advanced Fuels and Materials
- Working Group 4: Modeling and Simulation.

Breakout sessions at the October meeting at ANL led to the identification of a number of actions for further elaboration of future collaborative activities. The general areas jointly identified for future collaboration are: glass corrosion, solvent degradation, off-gas capture, and on-line process monitoring. Further consideration will be given to collaborating on studies to elucidate minor actinide (MA) selectivity. Additional actions, to be included later in the year, will (1) benchmark separation approaches with the objective of providing constructive feedback to each country's approaches and (2) evaluate possible future flowsheet tests with actual used fuel in the Atalante facility at Marcoule.

JAEA-DOE Collaboration

J. J. Laidler, laidler@cmt.anl.gov
and R. T. Jubin, jubinrt@ornl.gov

Collaboration with Japan on separations technology is carried out by the Fuel Cycle Technology Working Group (FCTWG), chartered under the *United States – Japan Joint Nuclear Energy Action Plan*. Japanese technical participation in the activities of the working group comes primarily from the Japan Atomic Energy Agency (JAEA), with occasional involvement of the Central Research Institute of the Electric Power Industry (CRIEPI). The responsible Japanese ministry is the Ministry of Education, Culture, Sports, Science and Technology (MEXT).

Japanese scientists visited ANL and the Idaho National Laboratory (INL) in January 2012. Topics of the visit included advanced aqueous and pyrochemical technologies, as well as treatment of TMI-2 damaged fuel. Tours of ANL and INL research facilities were provided to the Japanese visitors.

A *United States – Japan Joint Nuclear Energy Action Plan* planning and review meeting was held in Washington D.C. in June 2012. Limited progress has been made in moving forward on

proposals, largely due to FY 2013 budget uncertainties in the areas of proposed collaboration.

Rosatom-DOE Collaboration

T. Todd, terry.todd@inl.gov

The *United States – Russia Civil Nuclear Energy Cooperation Action Plan* provides a framework, with agreed upon areas of joint civil nuclear energy R&D cooperation, for possible future collaborative activities. The *United States – Russia Civil Nuclear Energy Action Plan* is comprised of four technical elements:

1. Reactor Demonstration Projects
2. R&D for Innovative Nuclear Energy Technology Options
3. Global Civil Nuclear Energy Framework Development
4. Modeling and Simulation.

The Action Plan identifies specific technical activity areas of mutual interest within each of these technical elements.

The long-term objectives of the Action Plan are to leverage U.S. and Russian scientific and engineering resources and facilities to advance the growth of clean, safe, secure, and affordable nuclear energy through the development of innovative nuclear energy technologies, systems, and services. Both parties understand that the initial collaborative activities will be limited to those that do not require entry into force of the *Agreement between the Government of the United States of America and the Government of the Russian Federation for Cooperation in the Field of Peaceful Uses of Nuclear Energy* (the "123 Agreement").

The third Civil Nuclear Energy Sub-Working Group meeting was held in Obninsk, Russia, in April 2012 and covered technical elements 1, 2 and 4. At this meeting, a second workshop on Separation and Waste Form Technologies was held on Thursday and Friday, April 19-20, 2012. Six formal presentations were made: (1) *Fundamentals of Partitioning of Curium and Rare Elements in Chloride Melt*, by A. Osipenko; (2) *Summary of Recent Studies Related to Molten Salt Electrolytes in the Uranium Electrorefiner*, by G. Fredrickson; (3) *Complete Testing of SNF Reprocessing Technology for Experimental Demonstration Center in the Hot Cells of KRI*, by Yu. Fedorov; (4) *Summary of U.S. Voloxidation Tests with LWR Fuel*, by T. Todd; (5) *Study of Boroaluminosilicate Glass Behavior over Geologic Time Scales*, by J. Ryan; and (6) *Glass Composition and Vitrification Technology Development for Liquid HLW of Experimental Demonstration Center at MCC*, by A. Aloy.

In addition, areas of common interest in separations and waste form R&D were discussed. Each country has their own path forward for managing used or spent nuclear fuel (SNF) and radioactive waste streams, but there are many approaches that are common to both strategies. A review of the national interests and priorities was completed to identify where R&D would significantly advance the availability of needed technical options and which of those options would benefit from a cooperative R&D program. These areas of common interest will form the basis for future collaboration. Specific collaborative R&D activities will be identified and initiated following approval of the *DOE – R. F. Rosatom Research and Development Agreement*. Specific accomplishments from this collaboration and plans for future years are provided later in this report.

Russian scientists (primarily from the Research Institute of Atomic Reactors [RIAR]) visited ANL and INL in December 2012. A number of technical presentations were given by both Russian and U.S, researchers, and tours were provided of ANL and INL research facilities. This meeting represents the third workshop on Separations and Waste Form Technologies.

Czech Republic-DOE Collaboration

T. Todd, terry.todd@inl.gov

The U.S. Department of Commerce, DOE, and the Czech Ministry of Industry and Trade (MOIT) signed a *Joint Declaration on Civil Nuclear Commercial Cooperation* on December 6, 2010. The Joint Declaration states that both parties will "foster the importance of scientific R&D to make nuclear solutions to future energy supply

challenges safe, effective, economical and friendly for the environment." Several areas of mutual interest have been identified to date:

1. Nuclear reactor safety (light-water reactor [LWR] extension, materials aging and degradation, Probabilistic Safety Assessments, risk-informed decision making, etc.)
2. The transfer of salt coolant from the United States to the Czech Republic to support Czech research in molten salt reactor technologies and U.S. research applicable to fluoride salt-cooled high-temperature reactors
3. Fluoride volatility chemistry as applied to the treatment of used fuel
4. Research collaborations between U.S. and Czech universities and faculty/student exchanges.

The first Czech Republic – DOE workshop was held January 24-26, 2012, in Prague to advance the dialogue on items 2, 3, and 4 and to determine specific projects that could be pursued by both countries. Topics of interest in the SWF area include the following:

1. The U.S. and Czech Republic nuclear programs have a common interest in advanced radioactive iodine retention and stabilization. The U.S. program is investigating iodine capture from fuel recycle systems, including ultimate waste forms, while the Czech program has an interest in fluoride volatility technology from which radioiodine may be released during operations. Bilateral collaboration is proposed on ways to improve radioiodine collection and its conversion to a stable form for safe disposal.
2. The U.S. and Czech Republic nuclear energy R&D programs are both working on improved alloys for fluorine resistance. The United States is conducting research regarding fluoride volatility nuclear recycle and the possible use of molten fluoride salts as coolants for high-temperature reactors. While the Czech Republic shares an interest with the U.S. in fluoride volatility, it is also involved in molten fluoride salt-based power reactors. Cooperative research on fluoride-resistant alloys based on both molten salts and fluoride volatility methods should be mutually beneficial.
3. The United States and Czech Republic share a technical interest in advanced halide waste forms for radioactive nuclear wastes. The Czech molten salt reactor R&D program and its associated fluoride volatility and electrochemical refining may produce several different fluoride waste streams, while the United States has chloride wastes associated with electrochemical processing of metal fast reactor and fluoride wastes from the experimental study of sulfur and nitrogen fluorides as fluorinating agents for used fuel. Collaboration on developing and testing of halide waste forms could benefit both countries.

EM Collaboration

J. D. Vienna, john.vienna@pnnl.gov

There has been a long-standing interaction between DOE-NE and DOE-EM, particularly in the areas of separations and waste forms. Many laboratory researchers work jointly for NE and EM, and many of the program objectives are similar. This close collaboration was formalized in 2011 by a Memorandum of Understanding (MOU) entitled, *Memorandum of Understanding between The Department of Energy Office of Environmental Management and The Department of Energy Office of Nuclear Energy for Used Nuclear Fuel and Radioactive Waste Management and Processing Research and Development*. This MOU, signed by the Assistant Secretaries [P. Lyons and I. Triay] in March 2011, describes a general policy of collaborative research and highlights several example collaborative research tasks.

Two joint NE-EM-NNSA nuclear separations technologies workshops were held to identify common needs and requirements in separations as well as opportunities for program partnerships between the three offices. The first such workshop was held in 2011 and the second was held in 2012.

The outcome of these workshops will be a joint roadmap that describes the individual and collaborative research areas that will be pursued as part of this joint effort. The roadmap is scheduled to be completed in 2013.

A joint EM-NE-International glass corrosion study that started in 2010 was continued through 2012 with an integrated technical test plan being issued in December 2011 (see Figure 2). Details of the testing and modeling progress are given in Chapter 10.

Figure 2. Integrated test plan, issued December 2011.

A new collaborative task on the development and demonstration of cold-crucible induction melter (CCIM) technology for treatment of U.S. waste streams was initiated. As part of this collaboration, both EM and NE funded a part of a test sequence looking at higher crystal waste glasses and glass ceramics. The two test segments focused on glass ceramics for high-level waste (HLW) raffinate from commercial fuel reprocessing to support NE and Hanford high iron waste to support EM. This initial demonstration was highly successful, as discussed in Chapter 9.

SC Collaboration

J. D. Vienna, john.vienna@pnnl.gov

The DOE Office of Science (SC) supports a number of research projects related to separations and waste forms. The Environmental Molecular Sciences Laboratory (EMSL, a DOE-SC user facility at Pacific Northwest National Laboratory [PNNL]) has awarded a Scientific Research Theme in the area of waste glass corrosion as a result of a competitive bid process. This Scientific Research Theme makes equipment, computer, and scientist time available for glass corrosion research as part of the joint NE-EM-International glass corrosion study. The specialized equipment and research experts have already started to make significant progress in understanding the glass corrosion process and our ability to predict performance over geologic time scales.

Fuels/Separations/Waste Forms – Industry Task Force

J. Law, jack.law@inl.gov

The Joint Fuels/Separations/Waste Forms – Industry Task Force was convened to identify and analyze two reference or example recycle fuel cycles at a level of detail sufficient to determine the fuel utilization, waste generation, required R&D, issues, roadblocks, and unknowns involved with implementation. The Task Force team was composed of subject matter experts in separations, fuel fabrication, reactor technology, and waste treatment/disposal.

The team identified the reference full recycle (FR) fuel cycle system as an initial uranium recovery by extraction (UREX)-based aqueous recycle of light water reactor (LWR) fuel. This FR system provides a uranium-transuranic (U-TRU) separations product for manufacture of metal fast reactor fuel that is irradiated in a sodium-cooled fast reactor. The fuel exiting the fast reactor is cooled for one year, and then recycled through a secondary electrochemical separations process, which provides a U-TRU product for return to the metal fuel facility. The FR fuel cycle comes to a near equilibrium fuel composition and reactor power with the initial recycle plus nine primary and secondary recycling steps.

The reference limited recycle (LR) fuel cycle system was identified as fluoride volatility based recycle of LWR fuel, which provides a U-Pu-Np separations product for manufacture of LWR mixed oxide (MOX) fuel for use in an LWR reactor. The recycled fuel would be sent to geologic disposal after one recycle sequence.

The Fuel Cycle Integration and Tradeoffs (FIT) model was used to provide fuel and waste management mass balance information for each recycle system. The FIT model was originally designed to track all elements and isotopes through the recycle processes, but required some modifications and additions to analyze the reference fuel cycles desired for this study. Although FIT is not a perfect model, it provides an excellent understanding of the overall mass balance for the system. FIT models both the mass and composition of inputs and outputs of each segment of the fuel cycle, including every cycle through a multiple recycling setup as that used in the FR fuel cycle. FIT also calculates the reactor power output generated by the recycled fuel. The resulting calculations provide a relatively comprehensive analysis of the performance of the fuel cycles. An especially helpful benefit of the modeling data is the determination of which elemental impurities build up in the fuel as recycling continues and approximately what levels they reach. This impurity data relates directly to the difficulty in fuel fabrication as well as the absorption cross section of the fuel under irradiation. In some cases, impurities may dictate adjustments in separations methodology or processes to remove specific problem elements to facilitate fabricability/licenseability of fuel or its longevity in a reactor.

Comparison of the reference FR fuel cycle to the reference LR fuel cycle is not readily done on a fully impartial basis. It was decided to compare the FR fuel cycle where it has essentially reached equilibrium—found to be continuous aqueous LWR recycle plus 9 secondary electrochemical recycle sequences (in calendar time expected to take about 60 years). This FR fuel cycle was compared with an equivalent 60 years of LR fluoride volatility recycling. Using this basis and the assumptions used in this document, the following comparisons can be made:

1. FR fuel utilization is 138 MWd/kg vs. 46.4 MWd/kg for the LR fuel cycle.
2. Total process waste generation for LR is 48.3 metric tons/yr vs. 22.7 metric tons/yr for the FR fuel cycle (not including radioactive-contaminated operations and maintenance low-level wastes generated during processing, which are outside the scope of this study). This equates to a waste volume of 13.2 versus 6.6 m^3/yr. (The waste generation for the LR process is greater than that for FR due to the assumption that fluorine is not recycled.)
3. Total recovered uranium to be stored for LR is 16.7 metric tons/yr vs. 17.9 metric tons/yr for the FR fuel cycle.
4. If the FR fuel is sent to waste when equilibrium is reached, the FR system will send 47 metric tons of SNF to a geologic repository vs. 410 metric tons of spent fuel from the LR fuel cycle.

Analysis of fuel cycle process and equipment maturity indicates that significant engineering scale demonstrations of both processes and remote equipment will be needed prior to full implementation of either fuel cycle. Demonstrations are needed primarily to prove out processes with actual TRU nuclear material and equipment for operation in the remote, high radiation environments involved with recycle separations and fuel fabrication. Regulatory structure changes in the United States also force the implementation of new technologies that have not previously been required for fuel recycling, primarily in the capture and management of used fuel fission gases. Some of these technologies are still in the early R&D stage.

Nonproliferation regulatory considerations may be a major hurdle with either fuel recycling system. LR requires the use of recovered plutonium at ≥13.3 wt% with recovered U to achieve sufficient reactivity for use in an LWR system. Although the separations product will be contaminated with Np, it will not be highly radioactive until buildup of the Pa occurs from Np decay. FR fuel will be highly radioactive but consistently requires over 30 wt% TRU in the U-TRU fuel form.

The key volatile radionuclide limits to the public from recycle facilities are Environmental Protection Agency (EPA) requirements of 25 mrem/yr (whole body) and 75 mrem/yr (thyroid), in addition to limits on specific radionuclides based on releases per unit of power produced (it is unclear how such limits would be applied). Overall, the regulations make highly effective volatile radionuclide capture and treatment essential to the technical feasibility of fuel recycling.

This study confirms that implementation of any recycle fuel cycle in the United States would be a major undertaking. Integrated multi-discipline planning, development, design, demonstration, regulatory efforts, and construction will be necessary to have a recycle fuel cycle available when needed.

Support to the Used Fuel Disposition Campaign

J. D. Vienna, john.vienna@pnnl.gov

The SWFC works closely with the Used Fuel Disposition (UFD) Campaign in two areas that are crucial to both campaigns. The first area addresses the disposal of HLW. HLW disposal environment and engineered system are being evaluated by UFD, while HLW forms and their performance in the near-field environment are being developed by SWFC. Many researchers are common among the two tasks to enhance the collaboration and ensure there is no unwanted overlap in scope. To this end, the two campaigns jointly issued a report recommending the waste management metrics to be used by the Fuel Cycle Options (FCO) Campaign in their initial screening of fuel cycles: *Proposed Waste Management Metrics for the 2013 Evaluation and Screening of Fuel Cycle Options*, FCRD-UFD-2012-000061.

The second area of combined scope addresses waste inventories and secondary waste management options. For this scope, the two campaigns, along with the FCO, are managing and incorporating the results of Indefinite Delivery, Indefinite Quantity (IDIQ)-Task 9: *Improving the Estimates of Waste from Recycling*. A task has also been initiated to evaluate (1) the benefits of treating secondary wastes prior to disposal under the current U.S. infrastructure and (2) potential changes due to proposed low-level waste disposal regulations being promulgated by the Nuclear Regulatory Commission (NRC). Both of these studies are expected to be completed in FY 2013.

This page intentionally left blank.

CHAPTER 3
ADVANCED AQUEOUS

CHAPTER 3: ADVANCED AQUEOUS

J. Law, jack.law@inl.gov

Transformational Sampling

J. M. Svoboda, john.svoboda@inl.gov

The goal of the transformational sampling project was to identify innovative sampling methods using state-of-the-art techniques that could evolve into the next generation sampling and analysis system for metallic elements present in aqueous processing streams. Sampling and analysis of nuclear fuel recycling plant processes are required to monitor process efficiency while ensuring safeguards and security goals are met. In addition, environmental regulations lead to additional sampling and analysis to meet licensing requirements. The volume of samples taken by conventional means can restrain productivity while samples are analyzed, require process holding tanks that are sized to address analytical issues rather than process issues (creating a larger facility footprint), or in some cases overwhelm analytical laboratory capabilities. These volumes can also provide a significant radiation dose to analytical personnel and equipment. These issues only grow when process flow sheets propose new separations systems and new byproduct material for transmutation purposes. A novel means of streamlining sampling and analysis was evaluated to increase efficiency while meeting all process information requirements.

During FY 2009 and 2010, sampling technologies were evaluated and a microfluidics sampling chip technology was selected and tested. This analysis is detailed in INL/EXT-09-16997, *Enhanced AFCI Sampling, Analysis, and Safeguards Technology Review*, and INL/EXT-10-17919, *Enhanced Sampling and Analysis, Selection of Technology for Testing*. The report detailing the sample chip testing performed during the third and fourth quarter of FY 2010 (including tests by INL, ANL, and Los Alamos National Laboratory [LANL]) is INL/LTD-10-20710, Rev 1, The conceptual design for a fully automated, microcapillary-based system is also presented in that report. During FY 2011 and 2012, a robotic automated sampling system was fabricated and initial proof of principal testing was conducted. The fabricated system is described in INL/LTD-11-23497.

In FY 2012, the mechanical and sampling operation of the completed sampling system was investigated. In addition, the production of a less expensive, mass produced sampling chip was investigated to avoid chip reuse, thus increasing sampling reproducibility/accuracy.

Robotic System Description

The microfluidic-based robotic sampling system (see Figure 3) includes sample chip handling equipment that can load, transport, unload, and deliver a sample chip to an elemental analysis instrument, such as an Ultra Violet-Visible (UV-Vis) spectrophotometer or Inductively Coupled Plasma-Mass Spectrometer (ICP-MS) for automated analysis. It is capable of obtaining samples from two (but expandable up to six) independent solutions using the sample chips. The analysis results can then be compared to quantify the effects of accuracy, repeatability, cross contamination, and reliability of the system and the sample chips.

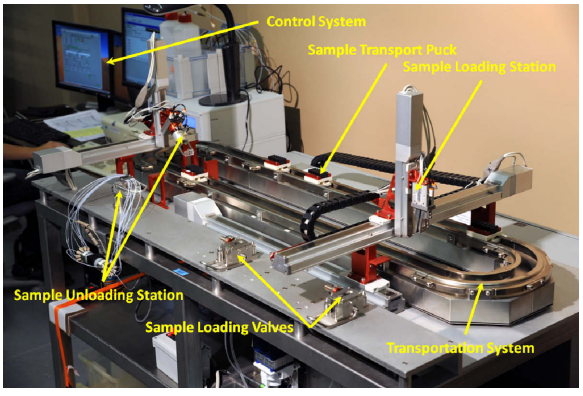

Figure 3. Microfluidic based robotic sampling system.

The system requires a 6×4 ft footprint but is intended to contain all the functionality and capability that would be required in a processing facility occupying several acres of area. It is upward scalable. The system is not designed to be

installed in a contaminated high-radiation area because it is only intended for demonstration purposes. However, it does contain some features demonstrating remote maintenance functionality. Equipment compatibility with high-radiation fields is not part of this effort's scope.

The analytical instrument of choice for sample chip analysis would be an ICP-MS. It is a very sensitive analytical instrument and, in this case, would be desired for elemental analysis in aqueous solutions. Mass spectrometers are high value assets and could not be dedicated full-time to testing the sampling system. In place of the ICP-MS, a UV-Vis was used during FY 2012 testing. INL dedicated an available UV-Vis solely for use with this project.

Sample Chips

Previously, glass sampling chips were manufactured to INL's specifications (see Figure 4). Each 16.25×30.0 mm chip consists of four 2µl channels and four 10µl channels. The 2µl channels are straight and the 10µl channels are serpentine in shape to accommodate a larger sample volume in the same size chip. The sample chips cost about $300.00 each. One FY 2012 goal was to design an inexpensive, one time use, disposable sample chip that costs a few dollars in large quantity, thus eliminating the need for a sample chip cleaning process.

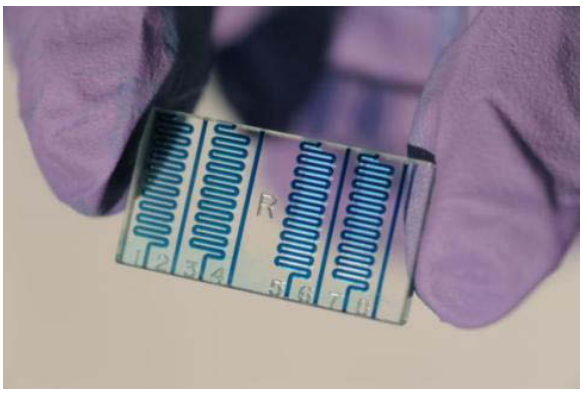

Figure 4. Glass sample chip.

An injected molded sample chip made from thermoplastic was pursued as an inexpensive disposable alternative to the expensive glass sample chip used for the tests described in this document. Grilamid TR™ is a moldable polyamide (nylon) thermoplastic that exhibits excellent transparency, good chemical resistance, resistance to stress cracking, and low moisture absorption. It was selected based on its properties and discussions with injection molding companies concerning moldability. Three types of Grilamid plastic samples were received from the manufacturer for testing before determining which to use for the chip material.

Fluid to solid interface contact angles were measured using three solutions on the three types of Grilamid plastic selected for potential sample chip material. The contact angle measurements were used to verify that the length and diameter of the channel in the sample chip were sufficient for the channel to completely fill via capillary action. A smaller contact angle will provide a greater capillary fill action. TR90 had the smallest contact angle for each solution. Contact angle tests were also performed on surgical grade stainless steel tubes as a substitute for glass or plastic based tubes. It was determined from test data that the stainless steel tubes filled to only ~95% of their total height. This is not enough height and leaves no margin for error when considering all other variables that contribute to capillary fill action height.

In addition, the resistance to chemicals used in separations processes was evaluated. Since acids, bases, and organics are used in nuclear fuel reprocessing, these three chemical classes were chosen for the resistance testing. Also, since some processes are heated, the plastic was exposed to the chemicals at raised temperatures in addition to room temperature. The TR55 LX showed the least amount of chemical resistance, and TR90 LX showed the greatest amount. Acid had the most effect on all three types of the Grilamid. The organic had the least effect on the three types of plastic. The longer the plastic is exposed and the higher the temperature of exposure, the greater the effect. This is especially seen with the acid.

A decision was made to procure a thermoplastic injection molded sample chip based on the original glass sample chip design. FY 2011 scoping quotes indicated a molded chip would cost about $20K in one time engineering costs and roughly $2.00 per chip cost in medium quantity. This inexpensive alternative would have allowed the purchase of thousands of disposable chips as

compared to only 70 glass chips for the same cost. A subcontract was awarded to make chips using TR90; however, the manufacturing company later decided they could not meet the specifications for tube diameter, so the contract was terminated. Therefore, additional glass chips were procured to proceed with the FY 2012 system testing.

A task was initiated to investigate the feasibility of using manufactured capillaries molded into an injected molded housing that meets the existing sample chip specifications. A design was chosen (see Figure 5), and plans are to make a few sample chips during FY 2013 for testing. After the initial tooling costs have been amortized, the estimated cost of these chips is $13-$15 per chip.

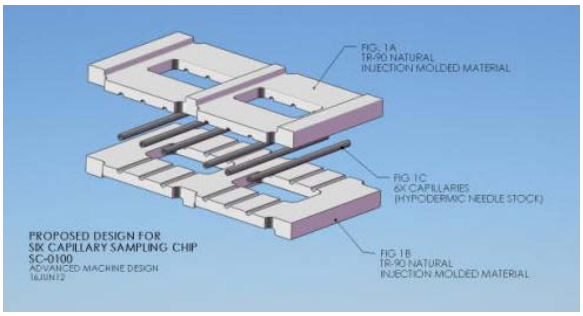

Figure 5. Representation of chip concept SC-0100.

System Testing

The system's mechanical elements were tested through visual inspection of both single chip and multiple chip runs to ensure reproducibility and the optimum safe handling of microfluidic sampling chips. Some leaking occurred at the sample unloading header during testing. This anomaly was mitigated by programming the pick and place robot to release the chip before the sample unloading header closed, ensuring the lines to and from the header were inserted flush with the gasket and cut at 90° angles where they meet with the sample chip, and increasing the air pressure to the clamping mechanism. Other adjustments were made to increase the probability the chip would completely fill and to decrease the potential for contamination of the sample carriers, including decreasing the rate the chip was drawn out of the sample loading header, increasing the time and depth of dipping the chip into the sample loading header, and increasing the flow rate of solution through the sample loading port.

To decrease the potential for cross-contamination during chip unloading directly to the UV-Vis, the time set for the elution of each channel on the chip (i.e., dwell time for the 8-port sample manifold) was increased to 90 seconds/channel for the low concentration solutions and 300 seconds/channel for high concentration solutions. This allowed the UV-Vis to return to the baseline prior to the sample from the next channel arriving. This adjustment may not be required if the samples go directly to an ICP-MS, as shown by previous INL testing, which sent the samples through a mixing tubing coil to mix the sample with the 1% nitric acid (HNO_3) carrier for dilution prior to spraying directly into the ICP-MS chamber.

A comparison of the FY 2012 testing with the UV-Vis and the previous testing conducted with the ICP-MS is shown in Table 2.

Table 2. Comparison of UV-Vis and ICP-MS chip evaluations for accuracy and repeatability.

	INL* ICP-MS		**ANL* ICP-MS**		**LANL* ICP-MS**		**INL Demonstration** UV-Vis**	
	2µL	10µL	2µL	10µL	2µL	10µL	2µL	10µL
% Error	16.5% high	3.5% high	31.5% low	3.7%low	~10%low	~2% low to 1%high	Varied w/UV-Vis calibration	
% RSD	10.3%	5.0%	65.2%	13.9%	15-20%	3.3-5%	13.19 %	2.75%
# channels	12	12	16	15	6	6	20	20

*calculated from FY 2010 work detailed in INL/LTD-11-23497, Rev 1
**based on final run of 5 chips.

General observations/recommendations made during chip testing and analyses are as follows:

- The 10µL channels generally produced data with much smaller relative standard deviations (RSD) than the 2µL channels, as would be expected as even a tiny variation in the smaller channel is a much higher percentage difference overall.
- Chip loading is an issue. Filling with capillary action requires a very small diameter and is contingent upon the solutions sampled and the materials used for the chips. Through modification of dipping depth and time, the system was able to routinely fill the glass chips completely. Even with complete filling, there may be some variation between

channels due to the formation of meniscuses.

- Once a full chip is placed in the sample unloading header, there will always be a small air bubble at each end of the channel that could affect analytical results with instruments like the UV-Vis. This shouldn't be an issue when using the ICP-MS.
- The surfaces around each channel on the holder could be cleaned between runs using a dummy cleaning chip.
- Leaking due to channel blockage reemphasizes the need for clean chips and solutions that are free from particulates.
- Adjustments were made to the lines to mitigate leaking; however, on occasion the lines would need to be readjusted. Implementing a header with permanently attached lines would eliminate leaks associated with changes in tube positioning and sealing.
- Evaporation from the chips is an issue especially with the 2µL channels that can lose 8–11% of their volume in 15 minutes and over 23% in 1 hour. With the 10µL channels, the effect is less due to the five times larger volume to start with; still, after an hour, about 5% of the liquid evaporated from the channel. Therefore, the present design, which enables loading several chips at one time and taking them to one unloading station, is not recommended. If more than one chip needs to be filled and analyzed at the same time, additional unloading stations/ analytical instruments would be needed. The point is to minimize the time between chip loading and chip unloading. One pertinent note is that on previous tests, LANL stored filled chips for 24 hours using a Dolomite storage cartridge with no reported solution volume losses.
- During earlier testing, LANL pumped the solutions through the chips to fill and had some holdup of certain analytes on the glass walls of the chips (i.e., some analytes displayed an affinity toward the chip surface and built up when using the method of flowing a relatively large volume of sample through the chip).
- As noted in a previous report, relying on the capillary action of the microfluidic chip channels may not be the optimum method for filling the chips. Active flow may be better (i.e., filling the channels in a chip holder by flowing fluid through the chip). This would minimize surface contamination issues from "dipping" the chips, ensure that each channel is sufficiently purged with a representative sample, and ensure that the channel is completely filled. It would also potentially allow plastic chips with a slight larger channel diameter to be used.
- The tiny volume of the 2µL samples amplifies any fill volume errors and causes the results to have a high percentage RSD in general. One possibility is to focus on a chip that would fill with pumping that could contain several 10µL samples instead of 2µL samples to increase the accuracy of the results.

Online Monitoring

S. A. Bryan, sam.bryan@pnnl.gov,
and T. G. Levitskaia

The overall objective of this task is to obtain fundamental information needed for online, real-time, process spectroscopic instrumentation to be designed for use in monitoring and controlling fuel reprocessing flow sheets. Previously conducted work included measuring Raman and ultra violet-visible-near-infrared (UV-vis-NIR) spectroscopic responses of U, Pu, and Np in matrix simulants; evaluating sensitivity and detection limits of U, Pu, Np, and NO_3^- in each simulant for available in-house spectroscopy instrumentation; and developing and verifying chemometric models.

The key result from FY 2012 work is the demonstration that mass balance could be obtained by real-time measurement of input and output streams during Plutonium-URanium EXtraction

(PUREX) solvent extraction (SX) system tests. Researchers also independently and simultaneously monitored the real-time spectroscopic and flow monitoring of the fuel simulant extraction system for the feed, solvent (inlet), raffinate, and organic product (outlet) streams, demonstrating mass balance during a 3-hour extraction scheme.

Process Monitoring of HNO_3 in Online Counter-Current Centrifugal Contactor Extraction System

The goal of this study is to demonstrate the utility of optical process monitoring methods, equipped with the optical-multiplexer, for directly and simultaneously measuring the multiple sample locations of aqueous feed inlet, aqueous raffinate outlet, organic solvent inlet, and organic product outlet, employing Raman and vis-NIR spectroscopic methods. This section contains results of Raman and vis-NIR measurements using solutions mimicking PUREX reprocessing streams.

The extraction of HNO_3 by tributyl phosphate (TBP) was chosen for use in flow testing of the cold centrifugal contactor system. The organic solvent system used for this demonstration was TBP/*n*-dodecane with an aqueous feed containing variable concentrations of nitric acid. The concentrations for the aqueous and organic phases simulated the PUREX process conditions. This process was chosen for demonstration purposes because there is ample information to compare the performance of resulting test measurements to those in the literature and historic information.

For HNO_3, the Raman spectra have multiple concentration bands (see Figure 6) suitable for use in quantitative measurement in aqueous solution. These spectra were used to construct a database for use in interpreting the concentrations of new spectra measured during a contactor run with variable concentrations of HNO_3 in solution. The aqueous feed solution used for the contactor run contained 0, 0.47, 0.95, 1.89, 2.84, and 3.79 M HNO_3. The organic solvent used in this demonstration consisted of 30 vol% TBP in *n*-dodecane.

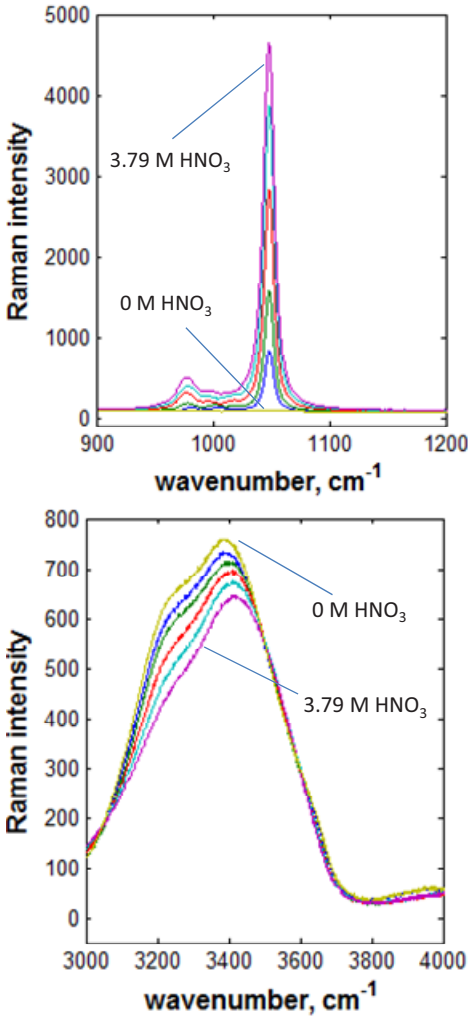

Figure 6. Raman spectra of HNO_3 used in aqueous model. The concentrations of nitric acid range are 0, 0.47, 0.95, 1.89, 2.840, and 3.79 M.

Figure 7 is a schematic representation of the bank of four centrifugal contactors used in the study. The locations of feed, raffinate, organic inlet, and loaded organic product streams are shown. The vis-NIR and Raman monitoring probes are positioned at four locations representing the inlet and outlets for both aqueous and organic streams.

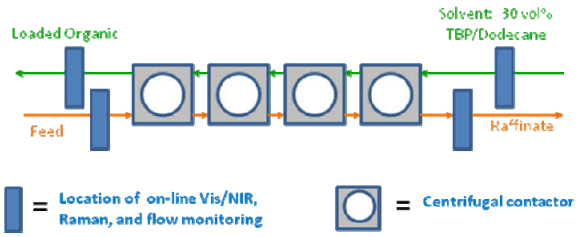

Figure 7. Schematic of centrifugal contactor system. The location of feed, raffinate, organic inlet, and loaded organic product are shown. The vis-NIR and Raman monitoring probes are positioned on the inlet and outlet of each stream.

The centrifugal contactor system test was initially started with an aqueous feed composed of water wash (0 M HNO_3) and an organic phase (TBP/*n*-dodecane). The centrifugal contactor system was allowed to completely fill with the aqueous feed and organic solvent. Spectroscopic monitoring of the feed, raffinate, solvent, and organic product steams were recorded during the entire flow test. The real-time Raman spectroscopic measurements recorded at the feed inlet are shown in Figure 8 (top).

As shown, the water band located at 3000 to 4000 cm^{-1} and the nitrate band located at 1050 cm^{-1} are evident. The nitrate band at 1050 cm^{-1} increased in intensity as a function of increasing nitric acid in the system. The real-time Raman spectroscopic measurements for the raffinate stream are shown in Figure 8 (bottom). The nitrate band intensity also increased with run time for the raffinate stream in response to the increased concentration of nitric acid in this stream. The step changes in nitric acid concentration for both the feed stream and the raffinate streams are evident by the observed incremental increases in the nitrate bands in the Raman spectra in Figure 8.

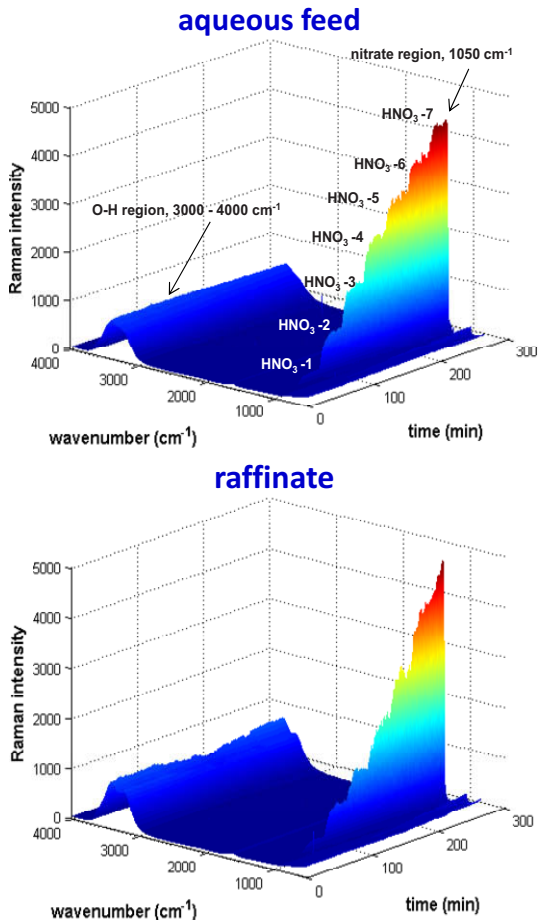

Figure 8. Real-time monitoring of the aqueous feed and raffinate streams containing variable nitric acid in PUREX solvent system. The real-time Raman measurement of the aqueous feed (aqueous inlet) and raffinate (aqueous outlet) solutions are shown.

Chemometric Analysis of Online Measurement

Chemometric analysis was performed on the spectroscopic data from the feed, organic product, raffinate, and solvent streams to measure the concentration of nitric acid in each phase. Figure 9 (top) contains the results of the online measurement of HNO_3 in the aqueous feed. The as-prepared concentrations of the nitric acid (red line) are plotted along with the nitric acid concentrations predicted from the model (blue symbols). As shown, there is a slight variation between measured and predicted values, indicating the lag time between solution feed changes and filling time for the sensor compartment. Overall, the agreement between measured and predicted values is excellent. There is also additional

"smoothing" of the prediction data due to dispersion effects, causing the steps in the concentration profile of the online prediction to be "averaged out" over each incremental change in acid concentration.

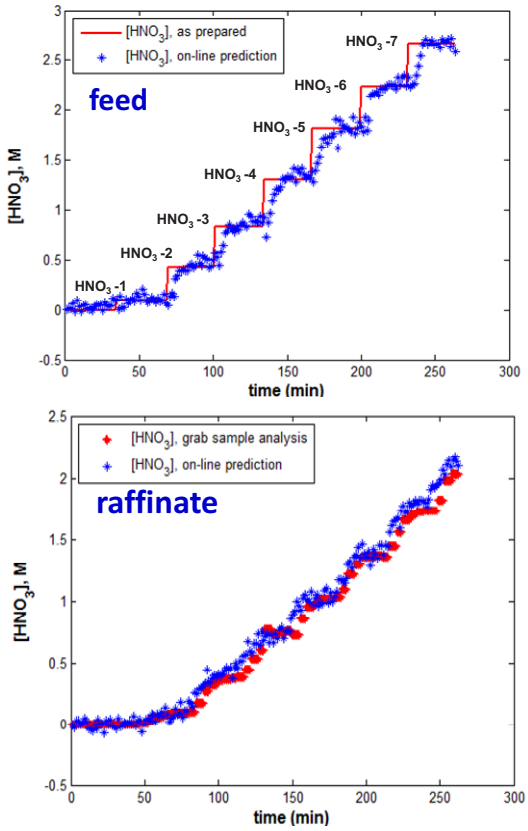

Figure 9. Online measurement of HNO_3 in aqueous feed (top) and raffinate (bottom) during contactor run. Comparison of predicted values in feed and raffinate with as-prepared and "grab sample" analysis, respectively.

The results for the online measurement of HNO_3 in the raffinate stream is shown in Figure 9 (bottom). Raffinate samples were fractioned into separate collection containers at regular intervals for post-contactor analysis. The red symbols represent the concentration of nitric acid determined from acid-base titration of solutions taken from these grab samples during the contactor run. The online model predictions of the nitric acid are also shown in Figure 9 (bottom, blue symbols) as a function of contactor run time, showing excellent agreement with "grab sample" analysis.

The online determination of the nitric acid concentration for feed, raffinate, organic feed and organic product streams during the contactor run are displayed in Figure 10 (top).

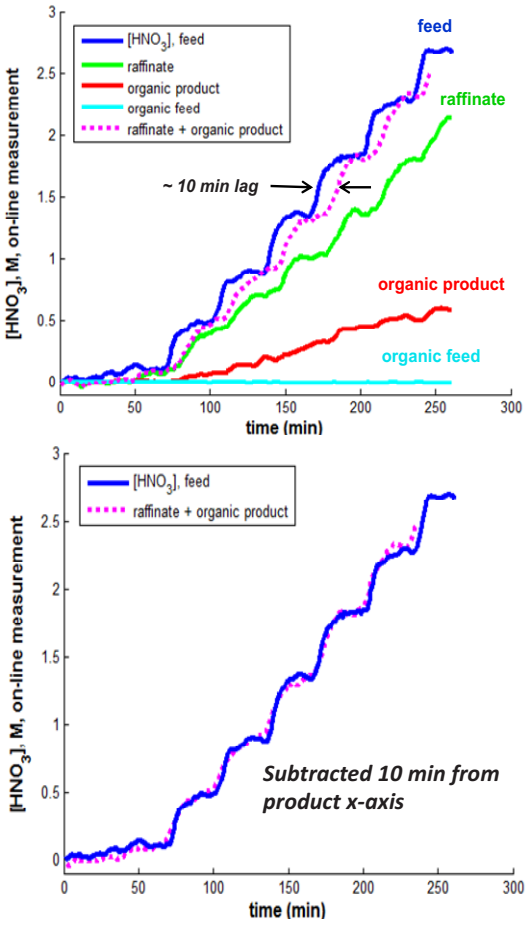

Figure 10. Online HNO_3 measurement from chemometric model, for feed, raffinate, organic feed and product locations during centrifugal contactor run, (top). Ten minutes were subtracted from the product x-axis scale (bottom).

The data for each stream is shown as concentration-versus-time, and for the feed, raffinate, and organic product streams, the nitric acid concentration generally increases as a function of time. This is expected for these streams since the nitric acid feed concentration was designed to increase in concentration in a step-wise fashion during the experiment. Figure 10 (top) also demonstrates that the concentration of HNO_3 in the raffinate stream (green curve) is not equal to the concentration in the aqueous feed (blue curve), owing to the extraction of nitric acid by the TBP/*n*-dodecane solvent. The nitric acid concentration in the organic product (red curve) contains a significant amount of nitric acid and appears from Figure 10 to generally contain the

difference between the original feed and raffinate streams. The nitric acid in the organic feed was also predicted from the spectroscopic data, as shown in Figure 10 (top, light blue curve), to be approximately zero for the entire experiment since the organic feed was prepared fresh to contain no initial nitric acid and was constant during the experiment. For the nitric acid mass balance to be maintained during this experiment, the concentration of acid in the feed (total inlet of nitric acid into the system) must equal the total amount of acid in the sum of the organic product and raffinate (total outlets for nitric acid from the system). The sum of the nitric acid concentrations from the organic product and the raffinate streams is also plotted in Figure 10 (top, shown as the dotted magenta curve). The nitric acid profiles for the "raffinate + organic product" (dotted magenta curve) and "feed" (blue curve) mirror each other fairly closely, but do not overlap due to the time-lag between the feed entering the contactor system and the product stream exiting the system through the raffinate and organic product streams. With a flow rate of approximately 10 mL/min for both organic and aqueous phase in the centrifugal contactor, and a fill volume of approximately 200 mL internal volume, the residence time for a solution within the system is approximately 10 minutes.

Figure 10 (bottom) is a plot of the concentration of HNO_3 measured in the feed (blue curve) compared to the sum of nitric acid in the "raffinate + organic product" streams (magenta dotted line) with 10 minutes subtracted from the x-axis scale. This plot shows excellent agreement between the online measurement of the nitric acid in the feed compared to the nitric acid in the product streams. This also demonstrates that mass balance has been maintained for nitric acid extraction within a PUREX SX system.

Solvent Degradation – PNNL

T. G. Levitskaia, tatiana.levitskaia@pnnl.gov

PNNL is investigating the applicability of online spectroscopic instrumentation for identifying and quantifying radiolytic and hydrolytic degradation products potentially accumulating in extraction organic solvents over time. The long-term goal of this project is to use spectroscopic techniques to monitor for solvent degradation products during aqueous processing of irradiated nuclear fuel and to establish the capabilities to detect degradation products via online monitoring.

The FY 2010–2011 PNNL scope was focused on developing predictive chemometric partial least squares (PLS) regression models for quantifying the main degradation products of the TBP/*n*-dodecane organic solvent contacted with nitric acid and testing them against gamma-irradiated solvent samples generated by INL researchers. The solvent samples received from INL were contacted with aqueous 0.5–4 M HNO_3 solutions and varied in accumulated dose for each sample. These studies identified the spectroscopic signatures of the TBP-based solvent and its main degradation product (i.e., dibutylphosphoric acid [HDBP]) in the extraction phases contacted with nitric acid solutions of the variable concentrations. Developed PLS models successfully predicted HDBP, TBP, and HNO_3 concentrations in the irradiated samples obtained from INL.

The FY 2012 PNNL research continued this effort by including uranyl nitrate $UO_2(NO_3)_2$ into the extraction system. Uranyl nitrate is a major constituent of the dissolved used fuel and significantly changes spectral signatures of HDBP and TBP upon extraction into the organic phase. To account for these changes, a new spectral database was created using organic extraction phases contacted with $UO_2(NO_3)_2/HNO_3$ solutions of variable concentrations to develop the expanded PLS models. Several aqueous solutions containing variable 0.1–1.5 M $UO_2(NO_3)_2$ and 0.5–6 M HNO_3 concentrations were used for the batch contact extraction experiments with 30% TBP/*n*-dodecane organic solvent. Variable amounts of HDBP were added to the post-contact organic solutions. Each solution was subjected to Raman and Fourier transform infrared (FTIR) measurements to create the spectral databases of the organic solutions containing TBP and HDBP at variable molar ratios.

The corresponding Raman and FTIR spectral layouts shown in Figure 11 illustrate spectral differences among 30% TBP/*n*-dodecane contacted with water, HNO_3, and $UO_2(NO_3)_2/HNO_3$ aqueous phases. Comparison of

the organic solutions contacted with water and HNO_3 demonstrates that extraction of HNO_3 results only in subtle Raman spectral changes, specifically in the 620–700 cm^{-1} spectral region due to HNO_3 symmetric stretch, while significant changes to the FTIR spectrum have been observed. Based on this result, it was concluded that FTIR is a technique of choice for monitoring nitric acid in the organic solution. Extraction of $UO_2(NO_3)_2$ into the organic solvent and uranyl complexation with TBP generates the appearance of several new bands and very pronounced differences in both Raman and FTIR spectra. The most significant change in the Raman spectrum is due to the appearance of UO_2^{2+} (859 cm^{-1}) and NO_3^- (1029 cm^{-1}) bands corresponding to the symmetric stretch vibrations. Intensities of both UO_2^{2+} and NO_3^- bands increase as organic phase loading with $UO_2(NO_3)_2$ gradually increases due to the increase of the $UO_2(NO_3)_2$ concentration in the feed.

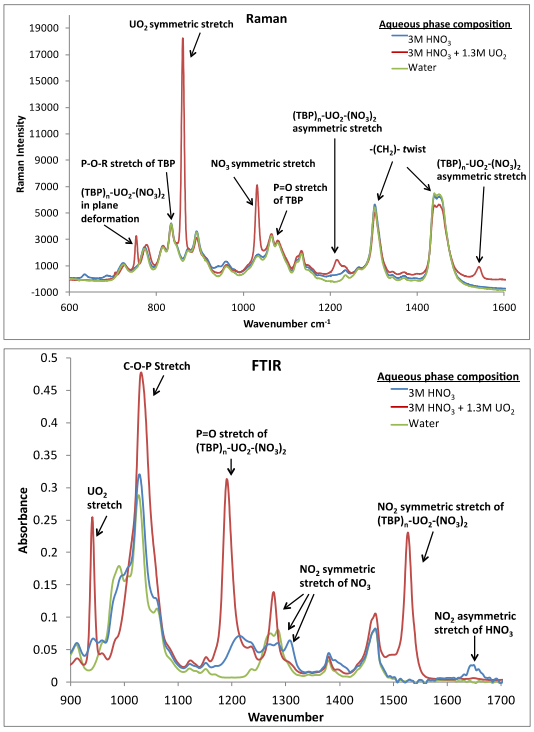

Figure 11. Comparison of Raman and FTIR spectra of organic 30% TBP/n-dodecane solutions contacted with water (green trace), 3 M HNO_3 (blue trace), and 1.3 M $UO_2(NO_3)_2$ in 3 M HNO_3 (red trace).

It was observed that Raman bands due to *n*-dodecane and TBP have not significantly changed upon extraction of $UO_2(NO_3)_2$. The FTIR spectra of the 30% TBP/*n*-dodecane solutions loaded with $UO_2(NO_3)_2$ shows several changes. One noticeable change is significant narrowing accompanied by the slight red shift of the P-O-C stretch at 1020 cm^{-1}. The P=O vibration band is shifted to 1190 due to the complexation of the UO_2^{2+} cation. Also, several bands appeared in the spectrum due to the presence of extracted $UO_2(NO_3)_2$ and HNO_3, including 775 cm^{-1} (O-N-O out-of-plane bend), 913 cm^{-1} (N-OH stretch), 940 cm^{-1} (UO_2^{2+} stretch), 1270 – 1310 cm^{-1} and 1525 cm^{-1} (O-N-O symmetric stretch), and 1672 cm^{-1} (O-N-O asymmetric stretch).

To augment the spectroscopic capabilities to quantitatively measure solution components associated with degradation products, Raman and FTIR spectra were recorded for the mixtures containing variable HDBP and TBP concentrations in n-dodecane solvent loaded with variable $UO_2(NO_3)_2$. The representative spectral layouts are shown in Figure 12.

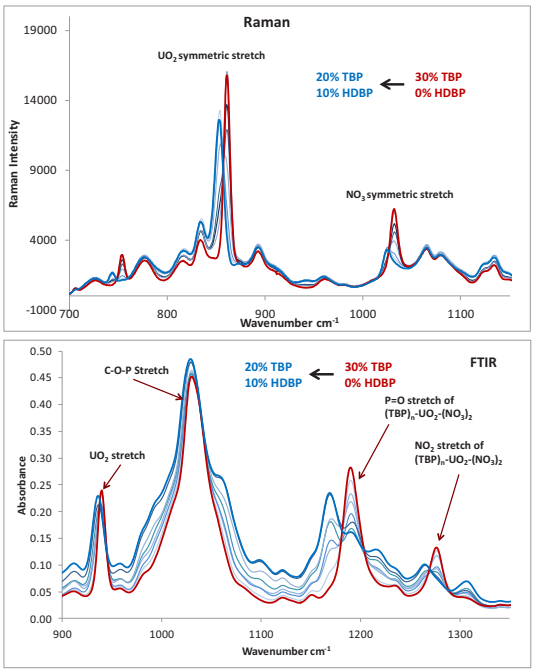

Figure 12. Raman and FTIR spectral layouts of n-dodecane solutions containing variable TBP and HDBP concentrations ranging from 30% TBP – 0 % HDBP (thick red trace) to 20% TBP – 10 % HDBP (thick blue trace) in presence of $UO_2(NO_3)_2$. Organic solutions were obtained by equilibration with aqueous 1 M $UO_2(NO_3)_2$ in 4 M HNO_3 feed.

In these layouts, the thick red and blue traces correspond to the spectra collected using 30%

TBP – 0% HDBP and 20% TBP – 10% HDBP, respectively. In the Raman spectra, addition of HDBP causes a pronounced shift of the UO_2^{2+} symmetric stretch band from 859 to 840 cm^{-1}. The other spectral changes observed for the $(TBP)_n$-UO_2-$(NO_3)_2$ include in-plane deformation band shifting from 750 to 740 cm^{-1} and 1029 cm^{-1} NO_3^- symmetric stretch band slightly shifting to the low-energy at significantly reduced intensity. FTIR spectra have undergone significant changes upon adding HDBP to the $UO_2(NO_3)_2$/TBP/*n*-dodecane solvent system, including broadening of the C-O-P vibration at 1020 cm^{-1} owing to the added hydrogen bonding in the HDBP molecule; shift of the P=O vibration band from 1190 to 1170 cm^{-1}; split of the 1270 cm^{-1} O-N-O symmetric stretch to bands at 1260 and 1310 cm^{-1}; intensity reduction and slight shift of the1525 cm^{-1} O-N-O symmetric stretch; and increase of the 1672 cm^{-1} O-N-O asymmetric stretch in HNO_3.

Together these observations allow researchers to anticipate that PLS spectroscopic modeling using both Raman and FTIR spectral databases would be able to successfully predict solvent components in the presence of extracted $UO_2(NO_3)_2$. The collected spectral data were incorporated into a PSL model to predict the concentration of HDBP degradation product as well as concentrations of TBP and UO_2^{2+} in $UO_2(NO_3)_2$/TBP/HDBP/*n*-dodecane mixtures. The results of these predictions are displayed for HDBP, TBP, and UO_2^{2+} in Figure 13, Figure 14, and Figure 15, respectively.

The HDBP predictions range from 0 to 10% corresponding to the approximate amount of HDBP that could be produced from TBP degradation. Similarly, the TBP ranges from 30 to 20% based on the assumed 0 to 10% conversion. The organic UO_2^{2+} concentration ranged from 0.15 to 0.35 M, the typical extraction range in the PUREX system. Nearly all predicted values reside within a 95% confidence level.

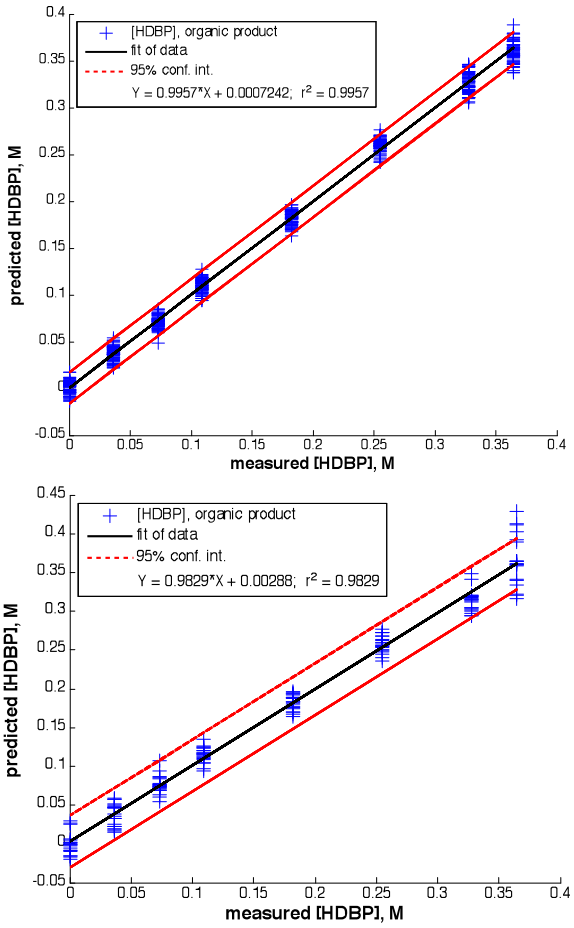

Figure 13. PLS models for prediction of HDBP concentrations in the $UO_2(NO_3)2$/TBP/HDBP/n-dodecane solvent mixtures generated using Raman (top) and FTRI (bottom) spectral databases. Black lines represent the modeling results. Solid red lines indicate 95% confidence interval.

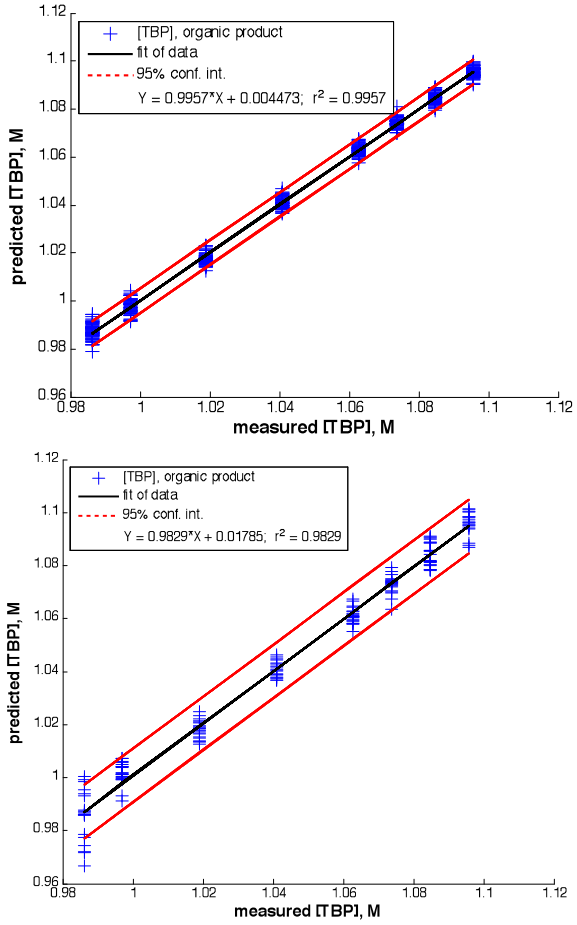

Figure 14. PLS models for prediction of TBP concentrations in the $UO_2(NO_3)2$/TBP/HDBP/n-dodecane solvent mixtures generated using Raman (top) and FTRI (bottom) spectral databases. Black lines represent the modeling results. Solid red lines indicate 95% confidence interval.

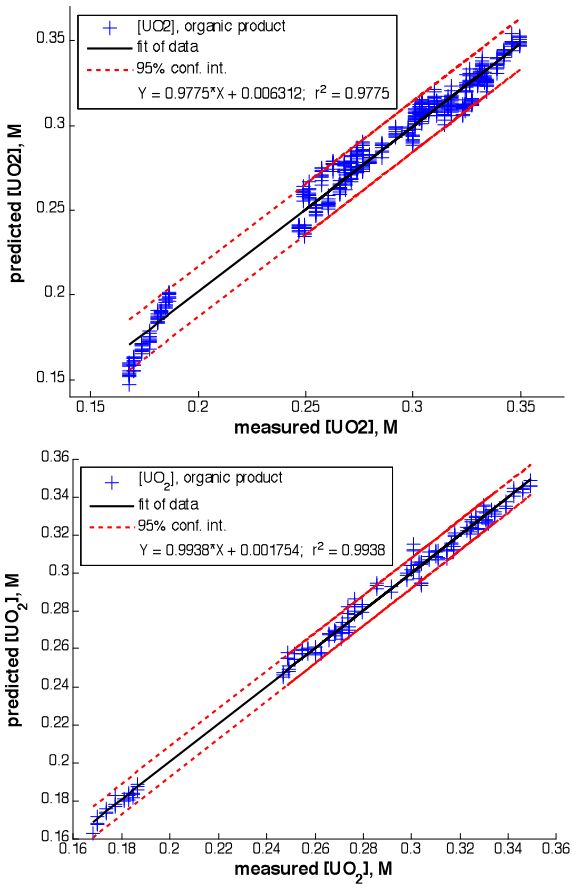

Figure 15. PLS models for prediction of UO_2^{2+} concentrations in the $UO_2(NO_3)_2$/TBP/HDBP/n-dodecane solvent mixtures generated using Raman (top) and FTRI (bottom) spectral databases. Black lines represent the modeling results. Solid red lines indicate 95% confidence interval.

The second FY 2012 task focused on (1) expansion of online spectroscopic capabilities by instrumenting the PNNL centrifugal contactor system with a waveguide FTIR probe and (2) translation of the spectroscopic capabilities for the online monitoring of the degradation products to the flow conditions. The SX test loop consists of four 2-cm counter-current centrifugal contactors in-series fed by the pumps. The inlet and outlet lines of both aqueous and organic phases are instrumented with mass flow/density meters. The system contains 12 resistance temperature detectors (RTD): one on each interstage line, one on each phase inlet and outlet, and two recording the atmospheric temperature around the equipment. The system is equipped with LabVIEW software for continuous data acquisition of the flow rate, density, and

temperature. The pre- and post-contact aqueous and organic lines are instrumented with fiber optics Raman probes in stainless steel sleeves with a quartz window and vis-NIR flow cells. In addition, the post-contact organic line is instrumented with a hollow waveguide FTIR probe with a diamond/zinc selenide composite attenuated total reflectance (ATR) element to monitor organic solvent components in the extraction product phase. In comparison with Raman spectroscopy, the FTIR method offers enhanced detection sensitivity of the organic components, and instrumentation of the flow system with online FTIR probe is of critical importance for the real-time prediction of the organic solvent degradation products. This is one of the first examples of the online in-line application of the FTIR method for testing used fuel solutions.

The centrifugal contactor experiment was conducted to test the performance of the FTIR waveguide probe and translate previously developed PLS models for predicting HDBP and TBP concentrations in *n*-dodecane solutions to the flow conditions.

In this study, organic feed solutions contained variable HDBP/TBP concentrations in *n*-dodecane while keeping the aqueous phase composition constant at 3 M HNO_3. The collected spectroscopic database was used to test the PLS model for predicting HDBP and TBP concentrations in the extraction product phase. The results of the PLS modeling are shown in Figure 16 and Figure 17. The predicted TBP and HDBP concentration values tightly follow the time-dependant analytical concentrations for both analytes and reside within 95% confidence levels with R^2 values of 0.999. An excellent PLS fit of predicted to measured HDBP/TBP concentrations using FTIR spectral database in the presence of nitric acid in the organic product verified the applicability of the waveguide FTIR probe to the online in-line measurements and validated the performance of the PLS model for predicting the organic solvent degradation product under the flow conditions. It should be noted that discrimination of the HDBP degradation product from the TBP major constituent was achieved for the entire 0–10% expected radiolysis conversion range. These experiments demonstrated applicability of the spectroscopic techniques for online monitoring of the organic solvent degradation products under flow conditions.

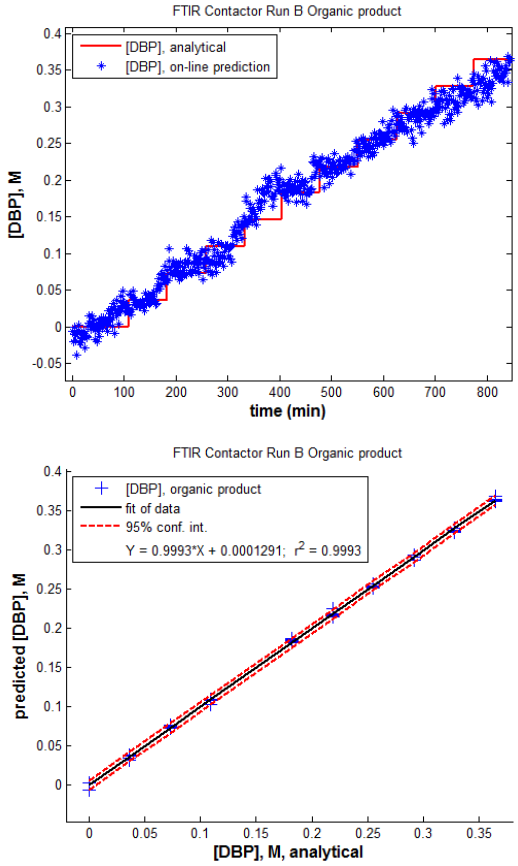

Figure 16. FTIR-based PLS modeling of time-dependent HDBP concentrations in the centrifugal contactor organic product phase. Gotom panels: black lines represent the modeling results; solid red lines indicate 95% confidence interval.

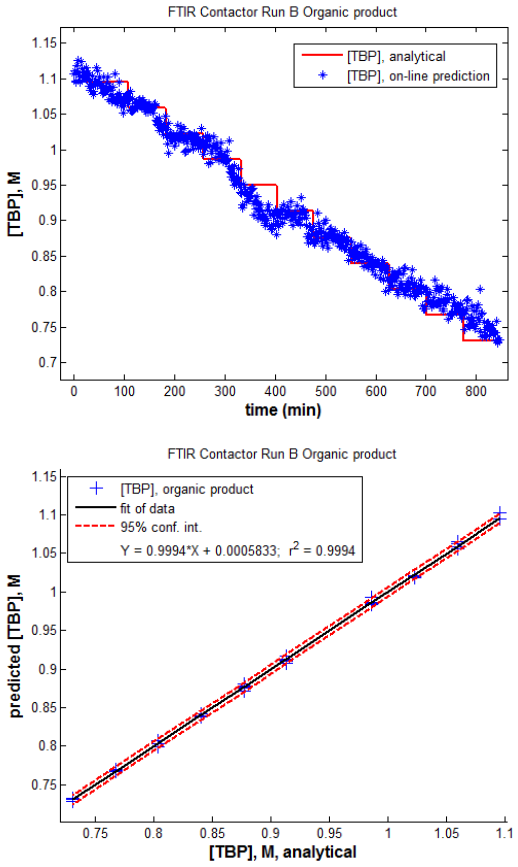

Figure 17. FTIR-based PLS modeling of time-dependent TBP concentrations in the centrifugal contactor organic product phase. Bottom panels: black lines represent the modeling results; solid red lines indicate 95% confidence interval.

In summary, Raman and FTIR spectral databases were created and used to develop the regression PLS chemometric models for the quantitative prediction of HDBP degradation product, TBP, and UO_2^{2+} in the extraction organic product phase. It was demonstrated that both spectroscopic techniques are suitable for the quantification of the solvent components in the presence of $UO_2(NO_3)_2$. Predicting the organic phase degradation products relies on the availability of the FTIR online in-line measurements. To develop this capability, a waveguide FTIR probe was installed in the centrifugal contactor system to monitor an organic product stream. The centrifugal contactor test has accomplished two goals: (1) performance validation of the new online FTIR probe and (2) translation of the predictive models previously developed using the static spectroscopic measurements for determining the HDBP degradation product in the TBP/*n*-dodecane solution to the flow conditions. PLS modeling using the FTIR database was capable of predicting realistic quantities of TBP conversion to the primary degradation product HDBP. This is one of the first examples of the online in-line application of the FTIR method for testing used fuel solutions.

Solvent Degradation – INL

D. Peterman, dean.peterman@inl.gov, and J. Law

The radiolysis/hydrolysis test loop, located at the INL, was used to study the impacts of radiolytic and hydrolytic degradation products on the performance of the TRansUranic EXtraction (TRUEX) process. The successful deployment of any SX ligand proposed for use in fuel cycle separations will depend upon the stability of that ligand in an acidic, radioactive environment. Irradiation of the SX system occurs due to the decay energy of actinides and fission products in the dissolved nuclear fuel solution. The radiation types are predominantly low linear energy transfer (LET) beta/gamma radiation from fission product decay, and high LET alpha radiation from actinide decay. The major reactive species formed by low LET radiolysis of water, alkane diluent, and nitric acid are shown in Equations 1–3, respectively.

$$H_2O \text{ -}\!\!\wwvy\!\!\rightarrow {}^{\bullet}OH + e^- + H^{\bullet} + H_2O_2 + H_3O^+ + H_2 \quad (1)$$

$$CH_3(CH_2)_nCH_3 \text{ -}\!\!\wwvy\!\!\rightarrow e^-_{sol} + CH_3(CH_2)_nCH_3^{\bullet+} + CH_3(CH_2)_nCH_2^{\bullet} + {}^{\bullet}CH_3 + H^{\bullet} + H_2 \quad (2)$$

$$HNO_3 \text{ -}\!\!\wwvy\!\!\rightarrow {}^{\bullet}NO_2 + {}^{\bullet}NO_3 + , HNO_2 \quad (3)$$

Equations 1–3 show that radiolysis of aqueous and organic phases generates a range of oxidizing ($^{\bullet}OH$, $^{\bullet}NO_3$, $^{\bullet}NO_2$) radicals, reducing ($H^{\bullet}$) radicals, the reducing aqueous electron (e^-_{aq}), and reactive molecular species (H_2O_2, HNO_2, H_2).

Due to the relatively low ligand concentrations employed, most decay energy is absorbed by the diluent, and ligand radiolysis is expected to occur by indirect rather than direct mechanisms. For example, the proposed TRUEX solvent contains 0.2 M octyl (phenyl)-N,N-diisobutylcarbonoylmethyl-phosphine oxide (CMPO) as the ligand, while the TBP modifier and dodecane diluent concentrations are about 1.4 M and 3 M, respectively. Consequently, most ligand damage will be due to reaction with

reactive species created by energy deposition in the balance of the organic phase, or in the acidic aqueous phase in contact with that organic phase. Therefore, realistic examination of the impacts of radiolytic degradation upon the efficacy of SX processes used in an advanced nuclear fuel cycle necessitates studying the radiolysis of mixed aqueous and organic systems.

Experiments completed during FY 2012 focused on examining the effect of gamma radiolysis on the stripping section of the TRUEX flowsheet. The TRUEX stripping solution is comprised of a mixture of lactic acid and diethylenetriaminepentaacetic acid (DTPA). Static irradiations of the TRUEX strip solution alone and in contact with TRUEX solvent were performed using the ^{60}Co-γ-irradiation from the Nordion GammaCell 200E (Ottawa, Canada) irradiator. The TRUEX strip solution was also irradiated in contact with TRUEX using the INL test loop and the Nordion GammaCell 200E (Ottawa, Canada) irradiator. The current irradiator sample chamber center-line dose rate is 6.4 kGy/hr. The effective absorbed gamma dose rate of 3.3 kGy/hr delivered to samples in the test loop was based upon decay-corrected Fricke dosimetry, the photo-bleaching of a methyl red solution due to gamma irradiation, and the duration of each irradiation.

The INL radiolysis and hydrolysis test loop has been used to evaluate the effects of hydrolytic and radiolytic degradation on the efficacy of the extraction section of a TRUEX flowsheet used to recover trivalent actinides and lanthanides from acidic solution. The nominal composition of the TRUEX solvent used in this study is 0.2 M CMPO and 1.4 M TBP dissolved in *n*-dodecane. The results demonstrate that solvent hydrolysis does not adversely impact the performance of the process flowsheet. However, hydrolysis does likely account for the small amount of HDBP present in the un-irradiated solvent. Gamma irradiation of a mixture of TRUEX process solvent and nitric acid in the test loop does adversely impact flowsheet performance as measured by the decreasing americium and europium distribution ratios in the extraction section as accumulated dose increases. The radiolytic degradation products, which are in part responsible for the decrease in extraction distribution ratios, inhibit stripping of the irradiated TRUEX solvent with dilute nitric acid. Use of an aqueous complexant (i.e., DTPA) in the aqueous strip solution easily overcomes the decreased stripping performance.

The efficiency of the conversion of absorbed radiation energy (gamma rays) into chemical products is defined here as the *G*-value, in units of $\mu mol \cdot L^{-1} \cdot Gy^{-1}$. A *G*-value can be used to predict the extent of radiolytic degradation of a solvent component for a given absorbed dose. The americium stripping distribution ratios determined for TRUEX solvent and stripping solution irradiated in the test loop increased with increasing absorbed dose. This increase in the magnitude of the stripping distribution may be attributed to either the formation of organic soluble compounds, which inhibit stripping, or to the consumption of the TRUEX stripping reagent due to radiolytic degradation. This information is useful for predicting the over-all performance of a TRUEX flowsheet in a radiation field. To this end, the concentration of lactic acid present in TRUEX solution irradiated in the absence of an organic phase was used to calculate a *G*-value for lactic acid radiolytic degradation. The slope of the linear best-fit to a plot of lactic acid concentration versus absorbed dose corresponds to the *G*-value for the radiolytic decomposition of lactic acid. The determined *G*-value for the destruction of lactic acid is $-G_{LA} = -0.617 \pm 0.033\ \mu mol \cdot L^{-1} \cdot Gy^{-1}$.

While the observed increases in the americium stripping distributions with increasing absorbed dose are statistically significant, the increase from $D_{Am} = <0.001$ at 0 kGy absorbed dose to $D_{Am} = 0.015$ at 1300 kGy absorbed dose is not an insurmountable difficulty. A more troubling observation is the significant decrease in the solvent dispersion number as the strip section of the TRUEX flowsheet is subjected to gamma radiolysis. The dispersion number, N_{Di}, determined for un-irradiated TRUEX solvent and strip solution is $N_{Di} = 1.05 \times 10^{-3}$, which is an acceptable value for typical SX equipment. However, the dispersion number for the irradiated TRUEX solvent and strip solution is 3.94×10^{-4}, which is a poor value for typical SX equipment. Dispersion number determinations for mixtures of irradiated and un-irradiated solutions suggest that

both the aqueous and organic phases play a role in the decrease in the solvent dispersion number.

The INL test loop has been used to evaluate the effects of gamma radiolysis on the efficacy of the strip section of a TRUEX flowsheet for the recovery of trivalent actinides and lanthanides from acidic solution. The nominal composition of the TRUEX strip solution used in this study is 1.5 M lactic acid and 0.05 M DTPA dissolved in water. The nominal composition of the TRUEX solvent used in this study is 0.2 M CMPO and 1.4 M TBP dissolved in *n*-dodecane. Gamma irradiation of a mixture of TRUEX process solvent and strip solution in the test loop does result in a statistically significant increase in the measured americium stripping distribution ratios. However, this increase in D_{Am} for solvent stripping would likely have little impact on the efficacy of the TRUEX process flowsheet. The values of the solvent dispersion number determined for the un-irradiated and irradiated TRUEX strip section indicate that slow phase disengagement may present a challenge to implementing the TRUEX flowsheet.

Continuing work will initially focus on completing the analysis of samples generated during FY 2012. The results of these analyses will be used to calculate *G*-values for the destruction of lactic acid and DTPA due to gamma radiolysis. In addition, attempts will be made to identify differences, if any, in the suite of radiolytic degradation products formed during the irradiation of the extraction and strip sections of the TRUEX flowsheet. The importance of dissolved oxygen in terms of the production of radiolytic degradation products will be investigated by performing irradiations under ambient and inert environments. In addition, experiments will be conducted in an attempt to quantify the concentration of dissolved oxygen present in the test loop under the various irradiation conditions used. The variation in the value of the solvent dispersion number will be measured as a function of absorbed dose to determine how gamma radiolysis may impact the hydrodynamic behavior of the strip section of the TRUEX flowsheet,. If necessary, the solvent dispersion numbers will be determined for the extraction section of the TRUEX flowsheet.

Product Conversion

E. D. Collins, collinsed@ornl.gov

This project was unfunded in FY 2012. However, using carryover funds from FY 2011, an extended modified direct denitration (MDD) uranium conversion run was made to (1) evaluate new rotary kiln internals and (2) measure the heated pipe centerline temperature starting at the feed point and then at one inch increments downstream. The solution converted was uranyl nitrate at a concentration of 300 g of uranium per liter and a uranium/ammonium nitrate mol ratio of 1:2 (stoichiometric for the tetranitrate). The volume fed was 900 mL at rates of 5.0 and 6.1 mL/min. Other conditions were unchanged from standard operating conditions.

The new rotary kiln internals employ two roller rods pinned to retaining disks on the center tube. Pinning the roller rods prevents them from wedging between the stationary center tube and rotating heated pipe and losing their effectiveness. This arrangement still allows the rods to function as intended, which is to crush the agglomerated uranium-ammonium nitrate double salt to ensure full, uniform conversion to oxide (UO_3). The new design worked extremely well.

The steady state temperature profile with the feed section control temperature of 600°C, downstream control temperature of 650°C (two-zone furnace), and a feed rate 5.0 mL/min are shown in Figure 18.

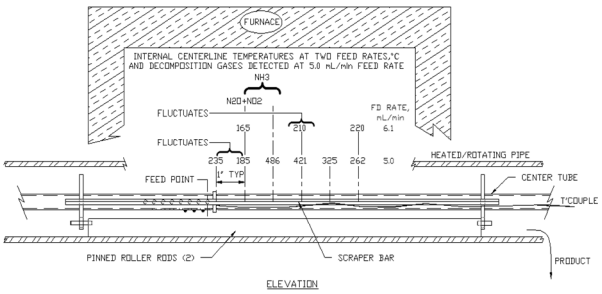

Figure 18. Heated pipe centerline steady state temperature profiles and decomposition gases detected

The centerline temperatures were measured with a thermocouple inserted into the center tube from the product end. The temperature drop-off commencing at ~4 inches from the feed point is probably caused by loss of heat through the gap

between the clamshell furnace and rotating heated pipe. The data indicate that evaporation of free water is complete within ~2 inches of the feed point. Earlier determination of decomposition gases using a Universal Gas Analyzer with the probe inserted into the heated pipe found no significant concentration of decomposition gases downstream at distance greater than 3 inches from the feed point. Thus, evaporation, crystallization, and salt decomposition are essentially complete within ~3 inches downstream of the feed point for the standard operating conditions.

The feed rate was increased from 5.0 to 6.1 mL/min and the centerline temperatures monitored. The higher feed rate caused the internal temperature to precipitously fall below that required to decompose all of the salt. The continuing, rapid temperature drop (much greater than expected from the increased heat load) indicated that undecomposed material was accumulating and insulating the heated pipe. The control temperatures of the two-zone furnace were increased from 600/650°C to 650/690°C and full conversion was restored. Under the standard operating conditions of 6-1/2 degree angle of incline and 3 rpm heated pipe rotation speed, a centerline temperature of ~440°C for the associated residence time is required to ensure full conversion of uranyl nitrate to the trioxide.

A sample of the combined product was calcined at 350°C and brought to the powder analysis glovebox line for characterization. The specific Brunauer, Emmet, and Teller (BET) surface area was measured at 7.6 m^2/g, which is typical of MDD-produced UO_3 powder. The basic conclusion from this work was that the double-salt decomposition (denitration) occurred within a 2-inch distance of the feed solution entry.

This page intentionally left blank.

CHAPTER 4
ELECTROCHEMICAL SEPARATIONS

CHAPTER 4: ELECTROCHEMICAL SEPARATIONS

M. A. Williamson, williamson@cmt.anl.gov

U/TRU Codeposition – Part 1

M. M. Tylka, furczon@anl.gov, J. L. Willit, and M. A. Williamson

A sustainable nuclear fuel cycle requires the recovery and recycle of the TRU elements from LWR and fast reactor fuels. The electrochemical process recovers the TRUs by electrochemically codepositing uranium and TRUs at a cathode. ANL demonstrated U/TRU codeposition at a liquid cadmium cathode (LCC) in the 1980's on the laboratory (gram) scale. Pilot (kilogram) scale U/TRU codeposition was then demonstrated at INL. Several years ago ANL proposed and demonstrated that, under proper conditions, U/TRU codeposition could be achieved at a solid cathode in a manner that preserves the non-proliferation features of the LCC, improves the TRU-lanthanide separation factors and allows for alternative approaches for separation of the residual salt from the U/TRU product thus limiting americium loss from the product.

Experiments performed over the last three years at ANL and INL continue to confirm the theoretical relationship developed at ANL between the composition of the U/TRU deposit and cathode potential, anode-to-cathode area ratio, and the U and TRU concentrations in the molten salt. In FY 2011, researchers began to measure the fundamental parameters related to U/Pu codeposition such as exchange current density and mode of nucleation. FY 2012 R&D activities continued the study of fundamentals of U/TRU codeposition at a solid cathode with a study of several U and Pu concentrations in molten LiCl-KCl. The fundamental electron transfer rates for U and Pu, however, were found to be essentially the same, which means that the composition of the U/TRU codeposit is not affected by differences in interfacial electron transfer rates.

The morphology of uranium electrodeposits varies as a function of current density and is markedly different from the morphology of a U/Pu codeposit as shown above in Figure 19a, b, and c, respectively.

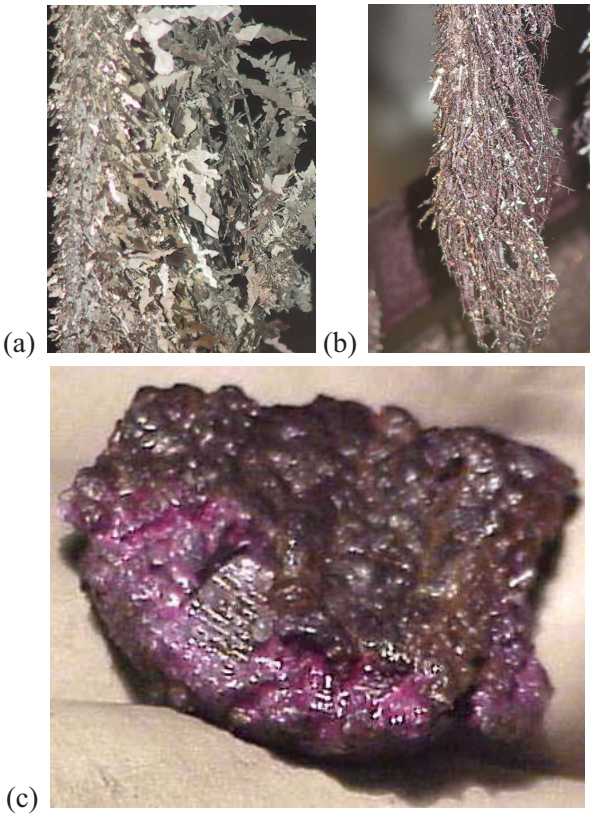

Figure 19. Photographs of (a) uranium deposit at low current density, (b) uranium deposit at high current density and (c) U/Pu codeposit.

Since U and Pu have similar interfacial electron transfer kinetics the difference in morphology is most likely a result of differences in nucleation behavior. In addition to characterizing the electron transfer kinetics, the nucleation of U, Pu, and U/Pu deposits were investigated. The relationship between solution concentrations and the mode of nucleation, the density and diameter of the nucleation sites and the nucleation rate were determined from a careful analysis of chronopotentiometry data (i.e., current vs. time; see Figure 20). The nucleation effect is seen as a hump in the chronocoulometry data. Analysis of the peak current (I_m) and the time at which it occurs (t_m) allows the determination of

the mode of nucleation as well as other fundamental nucleation parameters.

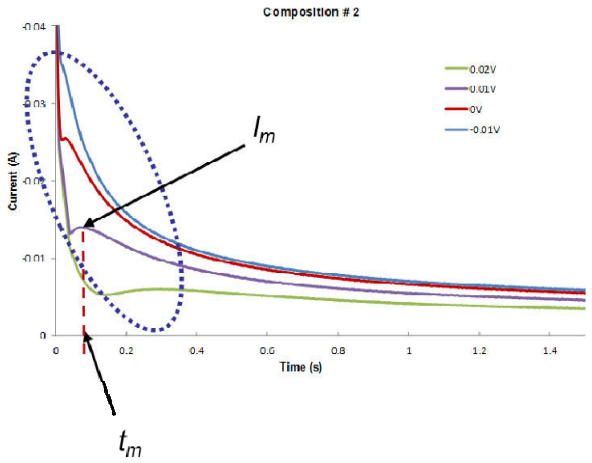

Figure 20. Typical chronopotentiometry data showing nucleation "humps".

Several distinct differences in U and Pu nucleation parameters were identified from fitting the data to a well-established nucleation model. At low U or Pu concentrations, the U and Pu progressive nucleation rates increase with over potential, but the U nucleation rate is faster than the Pu nucleation rate at all over potentials. The size of the Pu nuclei was found to be consistently larger than the U nuclei. With increasing over potentials, the Pu nuclei decreased in size whereas the U nuclei did not change in size. Under instantaneous nucleation conditions, the density of the nuclei (nucleation sites per cm^2) decreases with increasing over potential. It is likely that these differences account for the morphology differences observed between U, Pu and U/Pu electrodeposits. This improved understanding of nucleation will guide experiments in FY 2013 focused on identifying conditions that optimize the morphology of the U/TRU codeposit in terms of cathode adhesion and salt content.

U/TRU Codeposition – Part 2

G. Fredrickson, guy.fredrickson@inl.gov

In FY 2013, voltammetry tests are currently underway in the Hot Fuels Dissolution Apparatus (HFDA), which is located in the Hot Fuel Examination Facility (HFEF) hot cells. These tests are using molten salt systems that are meant to mimic the compositions that develop during the electrorefining stage of pyrochemical reprocessing of LWR oxide fuels. The voltammetry tests are being performed around a series of LCC tests that are drawing down the actinide concentrations in the salt. Typical response plots from anode stripping (Figure 21, top) and open circuit potential (Figure 21, bottom) voltammetry tests collected in FY 2012 are shown below.

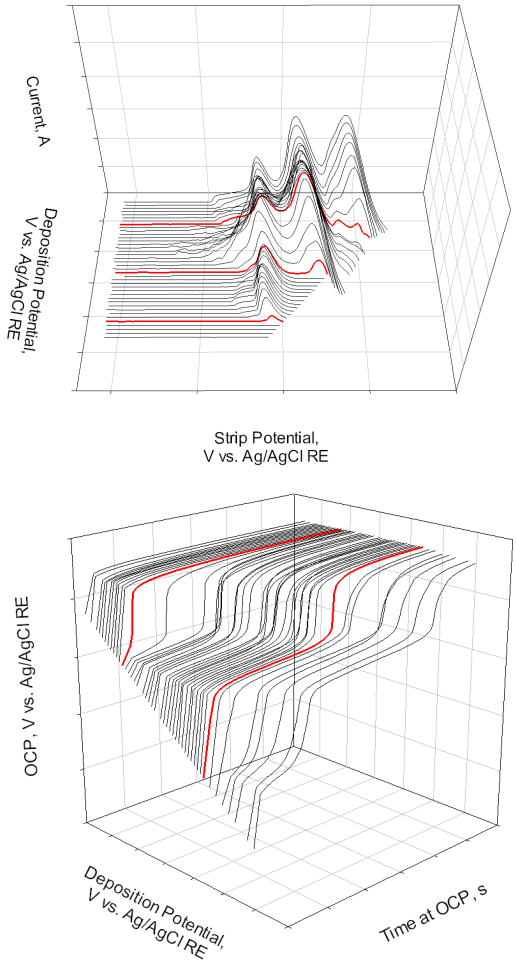

Figure 21. Typical response plots from anode stripping and open circuit potential voltammetry tests.

The anode stripping plot shows peaks for the reduction of uranium, plutonium, and lanthanides; and the open circuit potential plot shows plateaus for uranium, plutonium, and lanthanides. These electrochemical techniques give information about the reduction potential windows for the separation and recovery of actinides from lanthanides as a function of the salt composition.

In FY 2013, in addition to the radiological experiments being performed in HFEF, a series of non-radiological experiments will be performed in argon-shielded gloveboxes in the Engineering Development Laboratory (EDL). These experiments will use surrogates for the actinides, but their primary purpose is to develop new experimental techniques based on our experience with the radiological salt studies to date. It is anticipated that these new experimental techniques will be applied to the measurement of more prototypic salt systems; and will include the use of precision linear actuators to position (vertically and horizontally) the electrodes within the salt and a rotating electrode assembly to study the effect of diffusion layer thickness (i.e., agitation of the salt). Online monitoring tests, for the electrochemical determination of salt compositions, are a perfect complement to codeposition studies.

Cyclic Voltammetry Online Process Monitoring for Electrochemical Systems

M. M. Tylka, furczon@anl.gov, J. L. Willit, and M. A. Williamson

Online monitoring of the actinide concentrations in electrochemical systems is necessary for process control/monitoring as well as for safeguarding the process. For the past several years, ANL has shown that electroanalytical methods such as cyclic voltammetry (CV) can be used to provide high-precision (i.e., relative errors are <1%) online measurements of U and Pu concentrations in a molten salt when standard area addition is combined with proper electrode pretreatment protocols.

Previous studies examined U, Np, and Pu concentrations ranging from 0.5 wt% up to 2 wt%. This fiscal year, U concentrations as high as 10 wt% were examined. The higher concentrations are more typical of actual processing conditions and proved to be more challenging than the lower concentration measurements in three respects. First, the higher concentrations required a more extensive electrode pretreatment protocol as well as a larger electrode diameter to achieve reliable measurements using the standard area addition method. Second, the higher concentration tests indicated that the U^{3+} diffusion coefficient decreases slightly after the concentration exceeds 2 wt%. This result raises the possibility that fission product cations (e.g., Cs^{+}, Ba^{2+}, Sr^{2+}, and lanthanides) may also alter the U and Pu diffusion coefficients requiring solution-specific calibration curves to correlate the voltammetry data with concentration. These calibration curves can be developed either using a range of simulated salt compositions or using ex situ samples of electrorefiner salt with standard additions of U and Pu. Additional study of this effect will take place during FY 2013. Third, voltammetric measurements of multicomponent systems at higher concentrations required a refinement of the data analysis method to prevent interference effects. Specifically, the extended tail of the U^{3+}/U voltammetric peak makes it difficult to accurately determine the baseline for the adjacent Pu^{3+}/Pu voltammetric peak. Fortunately, the difficulty can be resolved by using semi-differentiation, a mathematical manipulation of the voltammetric data.

Applying a semi-differential treatment of the current vs. time data improves the baseline resolution between the U and Pu deposition peaks as well as giving an additional reduction in relative error. Figure 22 shows the voltammetry data at multiple immersion depths after application of the semi-differential treatment of the current vs. time data. After semi-differentiation, baseline determination is straightforward and the resolution between peaks is improved as well. Concentrations were determined with a relative error of less than 1%.

Collectively, these refinements in experimental technique and data analysis continue to demonstrate the viability of using CV for online measurements of U and TRU in the electrorefiner salt over the range of concentrations that will be encountered in processing systems.

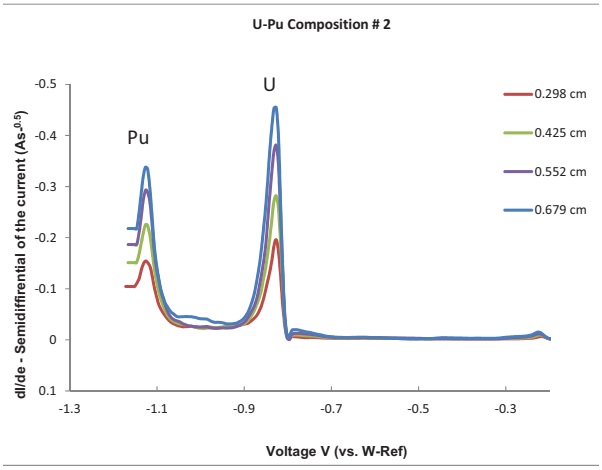

Figure 22. An example of semi-differential voltammetry plots at different electrode heights showing baseline resolution between the two peaks.

Salt/Metal Separations

T. Cruse, cruse@anl.gov, J. L. Willit, and M. A. Williamson

In the electrochemical treatment of used nuclear fuel (UNF), a metallic U/TRU product is collected at the cathode in the electrorefiner. If the cathode is a solid, non-alloying cathode, this U/TRU product is a mixture of metallic U/TRU alloy and electrorefiner salt that both coats the metal (surface) and is entrapped (between dendrites) within the alloy. ANL is developing a lower temperature method for the separation and recovery of the U/TRU product from the salt. Separation of the alloy from the electrorefiner salt is based on the large difference in density and high immiscibility of the two phases in the molten state, and allows recovery of the denser molten U/TRU alloy via bottom-pour casting. Bottom-pour casting is preferable to vacuum distillation of the salt that may also remove some of the more volatile metallic elements, such as americium in the U/TRU alloy, as well as some of the volatile and semi-volatile fission products. The salt-free U/TRU alloy that is recovered can then be recycled into fresh fuel while the recovered salt is recycled to the electrorefiner. Research in FY 2011 demonstrated the viability of this approach for metal/salt separation. FY 2012 R&D has focused improving the automation of the bottom-pour system and evaluating a new crucible design that can be coated with a protective layer for prolonged compatibility with molten metal and salt.

The automated pouring system and electrical resistance probes were modified to prevent shorting between the probes and the crucible wall that occurred during tests conducted last year. A thermocouple probe was also added to allow us to determine when the feed material had completely melted in the crucible. Finally, the pour control logic was modified to incorporate the signal from the thermocouple to ensure the material was molten before pouring.

A new prototype crucible was designed with consideration being given to the use of a coating (e.g., HfN) on crucible components to mitigate salt and metal interaction with the crucible. To allow for coating the walls of the hole, the prototype crucible featured a significantly larger opening for example, the diameter of the pour hole was increased to 5 cm. In conventional bottom-pour crucibles, the liquid is poured by lifting a stopper to open a small hole in the bottom of the crucible and the pour rate is controlled by the size of the hole. With the larger diameter hole and stopper in the new prototype crucible, the liquid pours through a ring-shaped annulus in the bottom of the crucible. The prototype featured steep sides on the pour hole and stopper to allow for sufficient control and adjustment of the pouring rate. The stopper, which never fully leaves the hole in this design, was also extended to facilitate re-seating and pointed to assist in directing the flow of the molten alloy. Due to cost considerations, the prototype was fabricated from alumina and coated with an yttria wash coating for the performance tests.

Tests of the new annular bottom-pour crucible with a U-Mn alloy and salt at 850°C were successful. The steep taper on the hole and plunger provided adequate control of the pouring rate while the plunger also consistently re-seated in the hole to stop the pouring of the liquid metal. The automated pouring system and electrical resistance probes were successfully demonstrated as well. Inclusion of a thermocouple proved to be a good method for determining when then melt temperature was achieved and the automated pouring system could be engaged. These tests demonstrated that an annular bottom-pour

approach can be used to achieve separation of the low melting U/TRU product and the adhering electrorefiner salt. A photograph taken during one of the pouring tests that displays the ring-shaped stream of liquid metal is shown in Figure 23.

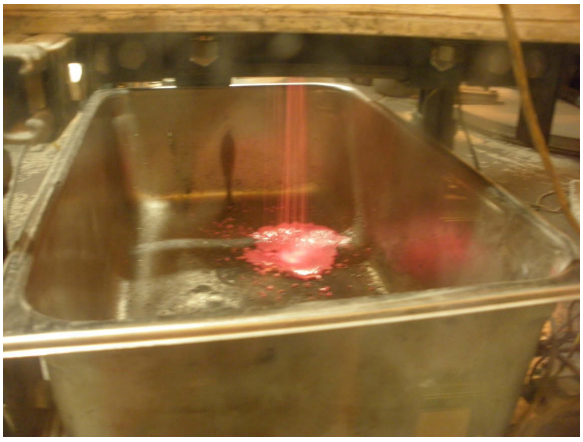

Figure 23. Annulus pouring of U-Mn eutectic alloy at 850°C. Multiple streams are observed in this image as the alloy poured in a ring-shaped curtain.

Optical and Electrochemical Online Monitoring

S. A. Bryan, sam.bryan@pnnl.gov, and
W. R. Heineman (University of Cincinnati)

The overall objective of this task is to obtain the fundamental information needed for online, real-time, process spectroscopic instrumentation to be designed for use in monitoring and controlling fuel reprocessing flow sheets. The goal of this work is to establish quantitative optical detection of U, Pu, and Np in molten salt media to support electrochemical process monitoring under pyroprocessing conditions (LiCl/KCl eutectic, 500° C). Initial experiments are designed to demonstrate this ability using vis-NIR and fluorescence spectroscopy on molten salt/non-aqueous systems. While the goal is to measure actinides in LiCl/KCl molten salt media, initial work was focused on moderate-temperature molten salt systems and using lanthanides as non-radioactive surrogates for the actinides.

The focus of FY 2012 work scope was the advancement into molten salt process monitoring, performing vis-NIR and electrochemical measurements under pyroprocessing (molten salt) conditions. This year, researchers performed both optical and electrochemical research under pyroprocessing (molten salt) conditions. Vis-NIR measurements of a series of lanthanide salts (simulants for actinides Pu, U, and Np) in LiCl/CsCl and LiCl/KCl molten salt media were performed, and Beer's law observance was demonstrated. Quantitative PLS models were demonstrated on multicomponent mixtures of lanthanides within the molten salt media. Electrochemical measurements of Eu, Tm, and Sm in molten salt and ionic liquid (IL) media were performed using various electrochemical and spectroelectrochemical techniques.

The key results from the FY 2012 work were:

- Completed the instrumentation of a commercial furnace for performing vis-NIR spectroscopy of molten salt solutions. This modified equipment allows measurement of vis-NIR spectroscopy of solutions of molten salts up to ~ 800°C.
- Performed vis-NIR spectroscopy of various lanthanide chloride salts ($NdCl_3$, $SmCl_3$, $PrCl_3$, $ErCl_3$, $TmCl_3$, and $HoCl_3$) under pyroprocessing (LiCl/CsCl molten salt) conditions. The adherence to Beer's law was observed over the concentration range studied.
- Demonstrated electrochemistry including CV, spectroelectrochemistry (SEC), chronoabsorptometry (CA), and differential pulse voltammetry (DPV) of lanthanides under molten salt/pyroprocessing conditions using $SmCl_3$, $TmCl_3$, and $EuCl_3$ in molten salt (LiCl/KCl). Determined electrochemical parameters: Eo', n values, and diffusion coefficients for lanthanide metal salts studies.
- Demonstrated quantitative spectroscopic process monitor application using PLS quantitative prediction of lanthanides in molten salt media. Used single and multi-component mixtures of $PrCl_3$, $NdCl_3$, $SmCl_3$, $HoCl_3$, $ErCl_3$, and $TmCl_3$ in LiCl/CsCl.

Figure 24 is a series of photographs of various lanthanide(III) chloride compounds in LiCl/CsCl melts which were used to prepare a spectral

database for use in a spectroscopic process monitoring demonstration.

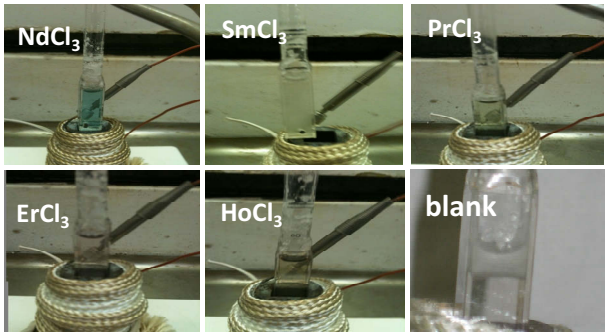

Figure 24. Photographs of various lanthanide chloride compounds in LiCl/CsCl melts. These solutions containing $NdCl_3$, $SmCl_3$, $PrCl_3$, $ErCl_3$, $HoCl_3$, and a blank are suspended just outside the heated zone of the heated cuvette cell holder and were used in Beers-Law Analysis. The "blank" contained LiCl/CsCl and no lanthanide salt.

UV-visible spectroscopy was performed on single- and multi-component mixtures of lanthanide(III) chloride samples to obtain the dependence of their spectral absorbance based on their concentration in solution, and to obtain the value of the molar absorptivities for the various peaks for each lanthanide. A spectral data set comprised of UV-vis spectra of 72 single- and multi-component lanthanide mixtures in LiCl/CsCl molten salt media were obtained; the UV-Vis spectra of six of the mixtures are shown in Figure 25 (top).

Partial least squares (PLS) chemometric analysis was performed on the spectroscopic data set composed of the multi-component mixtures of lanthanides in molten salt, a summary of the results of the modeling is shown in Figure 25 (bottom). The graph in Figure 25 (bottom) is the plot of the predicted versus measured composition of each lanthanide salt, with the best fit line for the data. This result demonstrates the applicability of using PLS predictive techniques for the spectroscopic process monitoring for lanthanides in molten salt media.

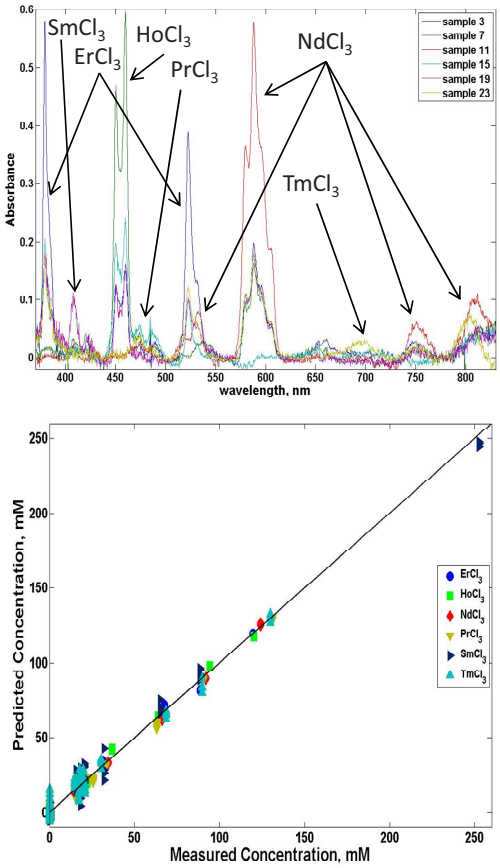

Figure 25. (top) Spectra of six multi-component mixtures (of a total of 72). (bottom) Graph of the PLS prediction of multi-component mixtures containing $ErCl^3$, $HoCl^3$, $NdCl^3$, $PrCl^3$, $SmCl^3$, and $TmCl^3$ in LiCl/CsCl molten salt.

Molybdate Melts

P. Tkac, tkac@anl.gov

Pyrochemical processing of UNF is very attractive for nuclear applications because inorganic salts are more resistant to radiolytic degradation than aqueous or organic solvents, and have a great potential for reducing the cost of processing and waste generation. In this work, use of molybdate melts (MoO_3 and Na_2MoO_4) was studied as an alternative to halide-based molten salts typically used in electrochemical processing. The benefit of using MoO_3 and Na_2MoO_4 binary system is most of the fission products are very soluble in molybdate melt, while UO_2 and PuO_2 do not interact with Na_2MoO_4 under inert atmosphere. The very small solubility of U, Pu dioxides in sodium molybdate is important because re-crystallization from a melt of pure

MoO_3 or melts containing both MoO_3 and Na_2MoO_4 can be used for purification of U and Pu from fission products. The simple separation process is based on physical separation (filtration) of (U, Pu) oxides from the fission product bearing oxide melt, and because there is no change in oxidation state, it does not require use of any electrochemical equipment or chemical reductants/oxidants. Such a process could allow for the recycle of U and Pu from used LWR fuel with limited number of separation steps and significantly reducing the complexity of operations required to process UNF. The concept of the process is illustrated in Figure 26.

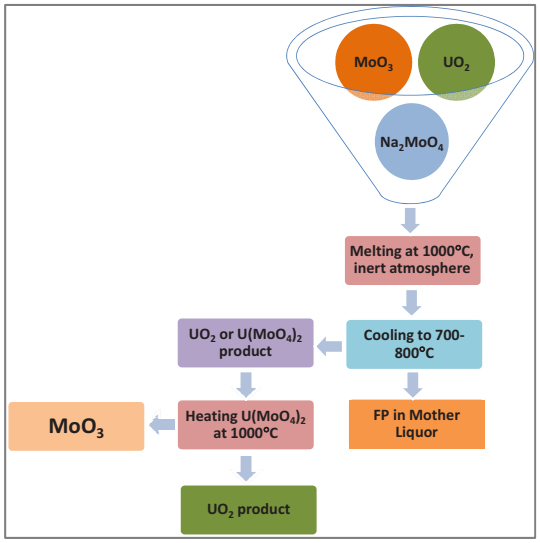

Figure 26. Conceptual process flow diagram for used fuel processing with molybdates.

The used fuel containing fission products is dissolved in the molybdate melt at 1000°C. After fuel dissolution, the temperature of the melt is lowered to 700–800°C to allow precipitation of the $(U,Pu)O_2$. The fission products dissolved in the molybdate melt are separated along with the melt after precipitation of $(U,Pu)O_2$. To simulate processing of UNF, several fission product simulants (Cs, Sr, Zr, Ru, Rh, Pd, La, Ce, Pr, Nd, Sm, Eu, Gd, Tb, Dy, Er, Lu) were added to UO_2 pellets before dissolving uranium oxide in the melt. Various compositions of molybdate salts, heating and cooling temperatures were studied to determine the optimum conditions for best purification of uranium product from selected fission product simulants. Photographs of salts with various initial compositions of MoO_3 and Na_2MoO_4, and 30% UO_2 (by mass) are shown in Figure 27.

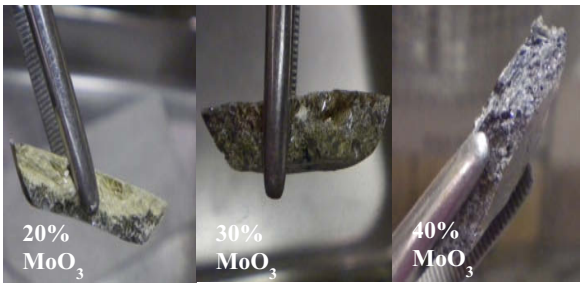

Figure 27. Photographs of several molybdate salts used in process evaluation.

X-ray diffraction (XRD) data for various compositions show that salts with more MoO_3 than UO_2 (by mass) yield uranium molybdate (UMo_2O_8) as the major species, while salts containing less MoO_3 than UO_2 (by mass) lead to the formation of a UO_2 precipitate. If uranium molybdate is washed with excess of sodium molybdate and heated, the UMo_2O_8 decomposes and a UO_2 precipitate is formed. This product is due to the very small solubility of UO_2 in Na_2MoO_4.

Partitioning of fission product simulants between liquid (molybdate melt) and solid (U precipitate) phases at high temperature, separated by Pt filter, was determined after dissolution of the filtered / cooled uranium precipitate using ICP-MS. Partitioning of fission products between melt (liquid phase) and U product (solid phase) is defined by distribution ratio as $D_{FP}=FP_{(melt)}/FP_{(U\ product)}$ and data are presented after one washing step of U precipitate with Na_2MoO_4 in Figure 28. In general, the conditions for best separation of uranium from Ln and transition metals (Figure 28) are 30% MoO_3, 40% Na_2MoO_4 and 30% UO_2 mixture with a heating temperature ~1000°C and fast cooling (~320°C/hr). Increasing the MoO_3 content from 30% to 40–50% leads to a significant decrease in D values for Ru, Rh and, especially, Pd. On the other hand, D values for Zr increases from ~18 to ~31 if the MoO_3 content is increased from 30% to 40%. Data show better partitioning into the liquid phase for lighter lanthanides such as La, Ce, Pr and Nd, while D values for heavier lanthanides are in general below 10 for all salt compositions investigated. The partitioning of lighter lanthanides into the U precipitate seems to

be lower for the compositions in which uranium molybdate is precipitated, while heavier lanthanides partition less into the product if UO_2 is precipitated. The worst separation was observed for Gd with D values of four or less. Very good separation factors were obtained for Cs, Sr, Zr, Ru, Rh and Pd, and separation factors for lanthanides can be improved by performing multiple precipitation steps and optimizing washing steps with molybdate melt.

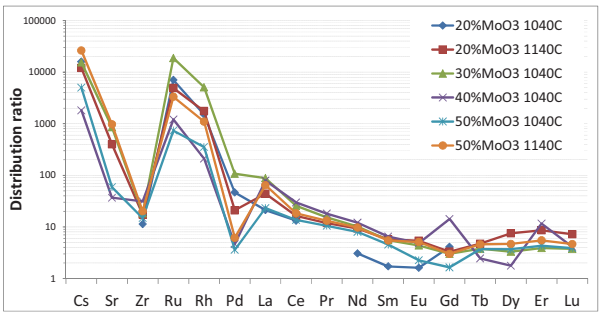

Figure 28. Distribution ratios for fission products between melt and UO_2 for several MoO_3 compositions.

This page intentionally left blank.

CHAPTER 5
SIGMA TEAM FOR MINOR ACTINIDE SEPARATIONS

CHAPTER 5: SIGMA TEAM FOR MINOR ACTINIDE SEPARATIONS

B. A. Moyer, moyerba@ornl.gov

The overarching goal of the Sigma Team for Minor Actinide Separation (STMAS) is to develop more efficient separation methods for americium and other minor actinides (MAs) in order to greatly improve the overall benefit of nuclear fuel recycle. Specific aims of the STMAS are essentially two-fold: to develop the scientific basis for a more robust, more efficient actinide/lanthanide (An/Ln) separation process and to develop the scientific basis for an efficient separation of americium from curium. These two aims are being pursued by integrated hypothesis-driven research mainly within the paradigm of aqueous reprocessing of used oxide nuclear fuel dissolved in nitric acid. Questions being addressed deal with principles of selectivity through various means including aqueous-phase complexation, use of soft-donor extractants, higher oxidation states of americium, and ion exchange. Explicit attention is also paid to the question of robustness of chemical systems under conditions relevant to future technology implementation. Emerging technology concepts are being matured for a potential laboratory-scale demonstration in 2015. This report outlines the goals of the STMAS, significance of achieving these goals, STMAS organization around the above aims and questions, recent highlights, and future direction.

Introduction

The STMAS was formed at the beginning of FY 2009 with the overarching goal to lay the scientific basis for more efficient separation methods for americium and other MAs in order to greatly improve the overall benefit of fuel recycle. Specific aims of the STMAS as elaborated previously[14,15] are essentially two-fold:

- Develop the scientific basis for a more robust, more efficient actinide/lanthanide (An/Ln) separation process
- Develop the scientific basis for an efficient separation of americium from curium

Although the applicable scientific questions remain to be more fully addressed, STMAS has successfully progressed in several directions to the extent that an applied aim can be added to the above aims for future effort:

- Develop emerging technology concepts to readiness for laboratory-scale demonstration

In the timeframe of two more years, this aim may possibly be extended to include performing the target laboratory-scale demonstrations, though the scale and goals of demonstrations remain to be defined.

The above aims are being pursued mainly within the paradigm of aqueous reprocessing of used oxide nuclear fuel dissolved in nitric acid. Given that an array of previously matured separation technologies for MA separations had been brought successfully through demonstrations in the context of the UREX+ suite of processes[6,10,21], the overarching question now before us is not the feasibility of separating MAs, but rather the efficiency and economy with which these separations can be achieved toward a manageable and affordable fuel cycle. The magnitude of this problem will require unprecedented simplification and compaction of separations processes, preferably eliminating and combining steps. It is anticipated that this will entail new chemistry and likely altogether new separation agents.

Significance

The major long-term benefit of this research is expected to be a significant simplification of aqueous-reprocessing schemes that rely on the separation of MAs, leading to overall better economics and increased acceptability of nuclear fuel recycle. As recognized widely by the national and international scientific community[1,4,8,17,23,24,25], the benefits of MA separation in general include reduced long-term radiotoxicity of waste stored in geologic repositories, reducing the timeframe for storage;

reduced heat load and corresponding increased repository capacity; and additional energy utilization of UNF. These benefits directly support program planning and priorities of the DOE FCRD program as described in the Nuclear Energy Roadmap.[26] More specifically, the implementation of the roadmap by FCRD relies heavily on a robust R&D program to address MA separations as one of two grand challenges in the area of separations.[27]

From a technical perspective, the specific requirements for MA separations depend on the nature of the future fuel cycle that will ultimately be implemented, involving such system choices as reactor type, fuel type, and waste disposition. A systems-option study of these myriad choices is in progress within FCRD and will inform R&D planning in the coming year or two.[27] It may also be noted by way of perusal of the series of proceedings of the Organisation for Economic Co-operation and Development (OECD) Partitioning and Transmutation (P&T) Exchange Meetings[19,20] that the general question of MA separation and transmutation is being vigorously pursued internationally from multiple perspectives and has been a lively topic for well over two decades. A recent review summarizes the current situation, pointing to the need for research on numerous aspects of advanced fuel cycles, including MA separations.[23] While specific needs for MA separations are in the process of being more clearly defined, it is taken for present purposes that R&D will play a critical enabling role, primarily within the full-recycle option as opposed to a once-through or modified-open fuel cycle.[27]

The full-recycle option with separation and recycle (i.e., packaging and transportation [P&T]) of MAs can substantially reduce the burden on a geologic repository.[23,28] Benefits include increased repository capacity (performance), decreased long-term radiotoxicity, and reduced risk of low-probability/high consequence scenarios such as geologic events and human intrusion. With no separations whatsoever, as would be the case with the once-through option, the heat load on a geologic repository out to 2000 years is dominated by ^{241}Am ($t_{1/2}$ = 433 y) after the fission products have decayed sufficiently (75 y).[28] Given that heat loading directly determines the storage capacity of a repository, removal of ^{241}Am alone has clear benefit for increasing storage capacity, reducing repository size, or permitting a lower repository operating temperature. Estimates of such benefits have been given for the case of Yucca Mountain[28], which can be used as an illustrative example. Accordingly, a 4.3–5.4 fold increase in waste loading would be expected for 90–99.9% removal of Am, assuming equal removal efficiency of Pu. A maximum 225-fold increase in waste loading would be expected upon removal of 99.9% of the Pu, Am, and Cm, along with the fission products Cs and Sr. Benefits for other types of repositories may also be expected depending on the geology and repository design. Repository benefits of MA separation and transmutation also include decreased overall repository radiotoxicity and decreased radiotoxicity lifetime, goals that also promote public acceptance of nuclear energy.[5] While decreased radiotoxicity of the repository is itself thought to have limited impact on repository performance, substantial reduction of risk is recognized in terms of disruptive events due, for example, to geologic phenomena and human intrusion.[23]

As described in the Introduction, the STMAS has two aims, namely to establish a scientific basis for efficient An/Ln and Am/Cm separations. Given that an effective chemistry already exists for manipulating Np in contemporary solvent-extraction systems employing TBP, the need for Np separations research therefore seems relatively less urgent than the need for Am and Cm separations research. On the other hand, An/Ln or Am/Cm separations have been especially difficult because the chemistry of their common trivalent oxidation states is very similar. Although researchers can point to significant progress, a fully satisfactory solution has not yet been found.[8,9] An efficient An/Ln separation is important because the lanthanides are strong thermal neutron absorbers and thus cannot be recycled in light-water reactor fuel, though fast-reactor fuel is somewhat more tolerant. A separation of Am from Cm has been viewed as a needed process option[10], as Cm presents difficulties in fuel fabrication due to the greater

shielding requirements, though this is not a universally agreed upon opinion.[1]

A clear need to simplify separations in fuel recycle is universally recognized. Although the successful Advanced Fuel Cycle Initiative (AFCI) demonstrations of various Uranium Extraction Plus (UREX+) flowsheets[6,10,21] increased overall confidence in our ability to reprocess used light-water reactor fuel at a commercial scale to meet a variety of potential objectives, the level of complexity and projected cost of deploying multiple process steps was potentially quite high. Whether to separate the MAs in the first place and what types of streams the MAs are best suited to fuel fabrication or waste disposal must be a result of a comprehensive fuel-cycle systems analysis. Since such guidance is being formulated at present, a chemical toolbox approach has been undertaken by STMAS under the philosophy that the chemical understanding in the context of potential separation methods will be available for exploitation as systems goals are more clearly defined. At the most fundamental level, the major product of STMAS effort is intended to be a family of chemical principles and corresponding test data enabling the design of efficient Am and Cm separation processes, one or more of which will be demonstrated at the laboratory scale.

Despite the fundamental nature of the intended research product, some quite specific outcomes can be anticipated from achieving one or both of the STMAS aims. The most straightforward scenario dominant in STMAS strategy follows from within the UREX+ paradigm[7,21] (or coextraction flowsheets) in which MA separation must be performed on a highly acidic raffinate stream from which U, Pu, and Np have already been removed. A major advance by itself would be a one-step An/Ln separation.[8,9,11,13] Two of the most selective solvent-extraction methods were incorporated into the framework of the UREX+ suite in the form of the TRUEX-TALSPEAK (*see Acronym list*) tandem processes or the TRUEX-SANEX tandem processes using Cyanex® 301 as the SANEX extractant.[21] Demonstrations showed a successful separation of Am and Cm from Ln using either technology. On the other hand, both approaches require two separate processes using disparate solvents and chemistries, and Cyanex® 301 is unstable at practical nitric acid concentrations. Both technologies present major challenges in process control, that is, robustness. These challenges involve narrow processing envelopes, complex chemistry, and empirical knowledge bases with limited understanding, reagent stability, and voluminous effluent streams. Control of pH has been especially problematic for TALSPEAK and related systems employing aqueous-phase buffers and complexants, as distribution ratios are not constant over the expected operating range.

Despite these already known challenges, the demonstrations of these technologies confirm the selectivity principles employed, which are outlined further below. Thus, appropriate extractants and aqueous-phase complexants can discriminate between An(III) and Ln(III), and a solution to developing a suitable technology should therefore be within the reach of research that can successfully address the major shortcomings. Given the evident challenge of the task, however, it is also clear that the prior understanding of extraction mechanisms and molecular behavior has been inadequate to generate the needed breakthrough. In the long term, a very attractive though ambitious MA separation meeting both STMAS aims simultaneously would be one in which Am and Cm are separated together and split into separate streams, that is, a co-extraction followed by selective stripping. Potentially such a process could eliminate three separate processes in a UREX+, with a high degree of potential flowsheet simplification. If Pu and Np could also be co-extracted with Am and Cm followed by stripping of all, or certain combinations of, these actinides, the landscape of fuel recycle could be even further simplified.

Approach

Technical Strategy

As shown in Figure 29, dual strategies for Am separation are being pursued by STMAS based on either complexation or the higher oxidation states of Am. Complexation presents particular challenges in that the trivalent 4f and 5f elements have very similar bonding characteristics, dominated by electrostatics. For Am(III)/Cm(III) separations, the ionic radii differ very slightly, and

these fall within the much wider size range of the lanthanides.

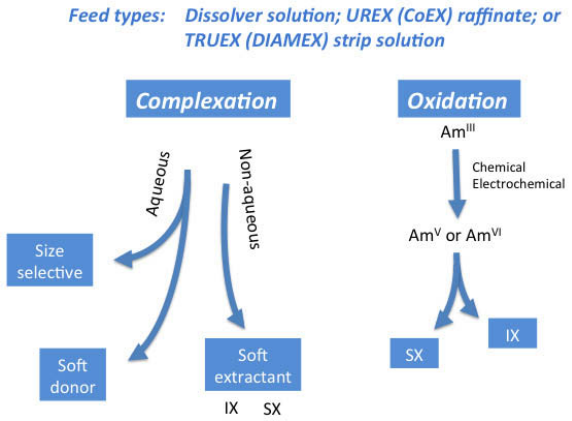

Figure 29. Strategies for achieving selectivity in two-phase separation systems and corresponding questions.

Regarding the second strategy, the higher oxidation states of Am that can be exploited require aggressively high oxidation potentials and are unstable once formed.[22] Both strategies can be used in either phase of a separation system. For example, by use of the extractant di-2-ethylhexylphosphoric acid (HDEHP), which is slightly selective for Ln(III), and addition of the An(III)-selective complexant diethylenetriamine pentaacetic acid (DTPA) to the aqueous phase, the Ln(III) are rendered significantly more extractable than An(III). This principle can be made to operate in an extraction of Ln(III) away from Am(III) (TALSPEAK) or in stripping Am(III) from extracted Ln(III) (reverse TALSPEAK). Alternatively, the actinide-selective complexant can be the extractant, as is the approach in the SANEX processes. One could employ the same ideas in the use of inorganic ion exchangers. For example, an inorganic exchanger with affinity for both An(III) and Ln(III) is used in the presence of an appropriate aqueous-phase complexant that has an affinity for An(III) vs. Ln(III), such that only the Ln(III) are removed from the feed stream. Or the complexant can be added to the eluant after the combined uptake of Am(III) and Ln(III) to selectively desorb the Am(III). Complexation strategies can be sophisticated, taking advantage of subtle effects due to even small differences in ionic radii. Manipulation of the Am oxidation state is in principle a powerful approach for a selective Am separation, either in the context of SX or ion exchange, but the very high oxidation potentials required for oxidation of Am(III) to Am(V) and Am(VI)[22] present a formidable challenge. Indeed, if this were not such a challenge, the two aims of the STMAS likely would have been preempted long ago.

The major questions being pursued within the dual strategy described above naturally sort themselves as follows:

1. Can aqueous complexation provide sufficient discrimination and operational control?
2. Can the higher oxidation states of americium be formed and stabilized for separation?
3. Can soft-donor extractants be made sufficiently robust and effective under desired conditions?
4. Does ion exchange have the selectivity and robustness to operate effectively? (Note: Ion exchange has been used successfully at ORNL to separate Cm from Am in the preparation of Cf-252 but would require engineering development for larger-scale commercial applications.)

In most cases, research inquiry focuses on obtaining the desired An/Ln or Am/Cm selectivity. However, in some cases, selectivity is often not so much in question as such issues as robustness, ability to operate under expected conditions, kinetics, etc. For example, ion-exchange materials have not been strong enough nor stable enough under acidic conditions, and soft-donor extractants like bis(dithiophosphinic) acids have presented stability issues of their own.

In general, pursuing the above strategy requires a team effort often involving more than one laboratory. Administratively, work packages are laboratory-centered. Nine principal investigators (PIs) from six national laboratories and one university were involved in addressing the above questions in FY 2012, as reported in the corresponding annual reports cited in the Sigma Team Publications and Reports section. The participants are listed in Table 3 together with the questions that their projects are primarily concerned with. It should be noted that each PI

leads a team of collaborators, some through subcontract, whose contributions are properly acknowledged in the corresponding annual reports. Questions are crosscutting, as shown in the middle column of Table 3. The composition of the STMAS was selected based on the experience of the PIs in conducting both basic and applied research, having demonstrated success in employing the results of basic research in technology development and in collaborating with engineers in scale-up and implementation. All are chemists specializing in separation science and technology, with backgrounds in SX, resin ion exchange, inorganic ion exchange, crystallization, and dissolution techniques.

Table 3. Participating Institutions and PIs in the Sigma Team for Minor Actinide Separations in FY 2012

Institution	Questions addressed	Lead PI
ANL	#1	Mark P. Jensen
ANL	#1, #4	Artem V. Gelis
INL	#2	Bruce J. Mincher
INL	#3	Dean R. Peterman
LANL	#1, #2,	George S. Goff
ORNL	#1, #2, #3	Benjamin P. Hay
ORNL	#3	Lætitia H. Delmau
PNNL	#1, #2	Gregg J. Lumetta
SRNL	#1, #4	David T. Hobbs
WSU	#1, #3	Kenneth L. Nash

Science-Based Approach

A hypothesis-driven approach is taken, drawing from fundamental principles to address the most significant questions standing as barriers to progress. As one of its first tasks, the STMAS defined what these questions are, as generalized above.[14,15] Some projects have matured sufficiently to begin to address how the basic principle, now largely substantiated, will be impacted the behavior of other system components. Based upon the knowledge base available, individual projects are driven by hypotheses associated with these questions, leading to corresponding experimental thrusts to test the hypotheses. A conceptual cycle of hypothesis and testing is depicted in Figure 30 [Moyer, 2010]. As pertains to the STMAS effort, the input of theory is stressed as playing a key role in each step under the expectation of a significant savings in effort by decreasing empiricism. While the scientific cycle illustrated in Figure 30 is elementary, an important aspect of its use here pertains to what successive cycles look like and what they accomplish. Unlike basic research, it is not desirable in the context of FCRD needs for this cycle to be practically endless. After four years of effort, researchers are probing how the increased understanding at each turn can lead to effective process chemistry. One might suppose the process is not two dimensional but rather a spiral with a direction, driving at each turn toward a solution to the problem of minor-actinide separations.

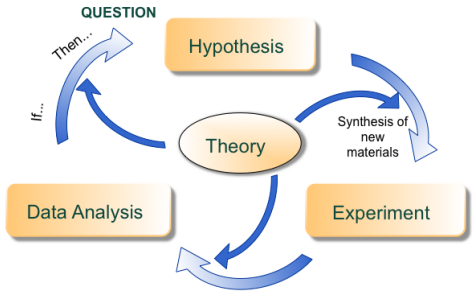

Figure 30. Cycle of hypothesis and testing.

Highlights of Research Progress

The reader is referred to the annual reports of individual PIs of the STMAS for a more complete account of research progress (See Sigma Team Publications section). Below are given summary reports on the Sigma Team's major accomplishments.

Aqueous Complexes for Americium-Curium Separation

M. P. Jensen, mjensen@anl.gov

Although separation of americium from curium could greatly simplify the recycle of UNF, the similar chemistry of these two adjacent actinide elements makes their separation very difficult. Researchers are meeting this challenge head-on by exploring sterically constrained ligands that amplify the very small thermodynamic differences between Am^{3+} and Cm^{3+} arising from the slightly different radii of these two actinide ions. Such sterically strained complexes will allow separation of Am from Cm (and the lanthanides) in a limited number of SX

stages. Our sterically strained ligands are designed to bind the larger Am^{3+} cation in preference to the smaller Cm^{3+} cation. By pairing a sterically strained crown ether ligand, such as BP18C6, that selectively holds Am in the aqueous phase with an extractant that preferentially carries smaller cations (i.e., Cm^{3+}) into the organic phase, researchers have created a SX system with unprecedented size selectivity for the Am/Cm pair and for trivalent lanthanide or actinide cations in general. This system's Cm/Am separation factor is an order of magnitude larger than observed with conventional ligands. The extreme size-based selectivity of this extraction system also is borne out by its selectivity for trivalent lanthanide cations, which also must be separated based on cation size. It separates the smallest lanthanide, Lu^{3+}, from the largest lanthanide, La^{3+}, with an extraordinary single-stage separation factor of more than 10^8. Our experimental studies of the energetic origins of this breakthrough approach to separating Am and Cm are being augmented by computational studies carried out in collaboration with Benjamin Hay (Oak Ridge National Laboratory [ORNL]) and also by our collaborator Prof. Teresa Rodríquez-Blas from the University of Coruña, Spain.

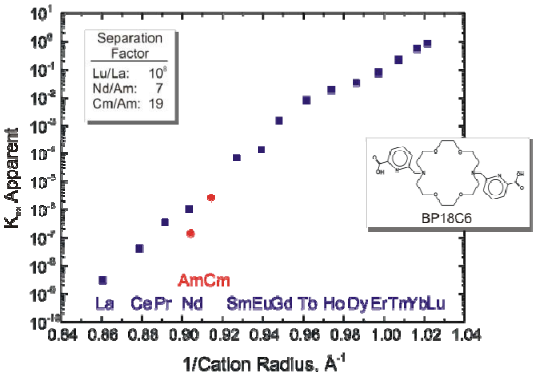

Figure 31. Apparent extraction constants for Ln3+ and An3+ extraction by 0.0010–0.050 M HDEHP/o-xylene from 1 M NaNO3/0.05 M lactic acid/0.001 M bp18c6 at –log [H+] = 3.0, T = 22 °C. Kex Apparent = D[H+]3/[(HDEHP)2]3. (■) Ln3+ ICP-MS, (●) An3+ radiotracer.

Advancing TALSPEAK Systems

K. L. Nash, knash@wsu.edu; G. J. Lumetta and J. C. Braley (PNNL)

During the past several years, studies of the fundamental interactions governing the conventional TALSPEAK process for separating transplutonium actinides from fission product lanthanides (0.2–0.5 M HDEHP in DIPB, 1–2 M lactate/lactic acid buffer at pH 3.5, 0.05–0.10 M DTPA) have demonstrated that the required high concentrations of lactate probably causes (rather than preventing) the moderate pH dependence that is seen in cation extraction of conventional TALSPEAK. Results of small angle neutron scattering (SANS), nuclear magnetic resonance (NMR), electrospray ionization-mass spectroscopy (ESI-MS), fluorescence spectroscopy, and conventional radiotracer distribution experiments have established the identity of the dominant metal extracted complexes ($Ln(DEHP{\cdot}HDEHP)_3$ at low total lanthanide and $Ln_2(Lac)_2(DEHP)_4$ at high lanthanide concentration), and of the extracted lactate species ($HLac(HDEHP)_3$). Metal ion extraction drops with increasing pH because (1) HLac competes with the metal ion for the extractant and (2) specific ion activity effects arising from the high lactate concentrations create inconstant thermodynamic conditions.

Parallel studies of TALSPEAK chemistry operating in extraction chromatography suggested that improvements might arise if HDEHP (see Figure 32) was replaced by a more basic cation exchanging extractant, 2-ethylhexyl phosphonic acid mono-2-ethylhexyl ester (HEH[EHP]; see Figure 33). The lower acidity of HEH[EHP] results in a clean and efficient hydrometallurgical process in which metal ions are the primary species partitioning between the phases rather than lactic acid.

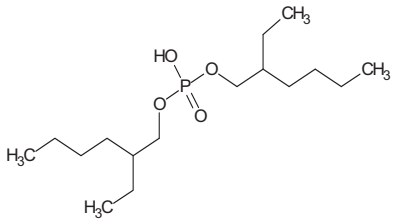

Figure 32. HDEHP

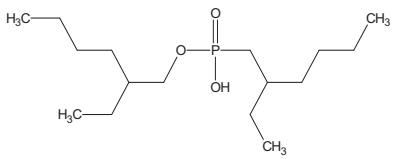

Figure 33. HEH[EHP]

To rebalance the extraction system with the weaker extractant and allow efficient group separation, DTPA was also replaced by the weaker aqueous complexing agent HEDTA. This combination results in significantly reduced extraction of HLac, less partitioning of water into the organic phase, and generally improved rates of mass transfer, in sum, a much more efficient process. Early experiments indicate that the reduced denticity[i] of HEDTA (relative to DTPA) offers additional opportunities for improving system performance by introducing secondary soft donor ligands. In the tradition of hydrometallurgical separations, this adjustment of conditions has been given the acronym TALSQuEAK, to reflect the impact of "Quicker" phase transfer kinetics. This promising development could greatly improve TALSPEAK-like separations. The increased understanding of reactions occurring in such SX systems (see Figure 34) promises potential breakthroughs in efficiency. Initial results have been published [Braley, 2012a,b].

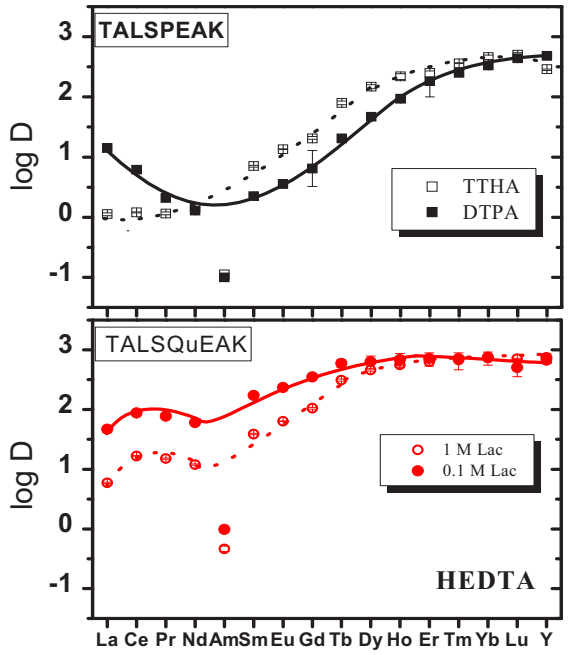

Figure 34. Selectivity of TALSPEAK compared with TALSQuEAK.

[i] Refers to the number of atoms in a single ligand that bind to a central atom in a coordination complex

Combined Process for Actinide/Lanthanide Separation

G. J. Lumetta, gregg.lumetta@pnl.gov, and A. V. Guelis (ANL)

Combining an acidic extractant with a neutral chelating extractant allows a single process to replace two processes in the separation of trivalent MAs from lanthanides. In the past year, researchers have made significant progress in developing improved prototypes for combined solvents and understanding the chemical interactions taking place in extraction and stripping. Several combined solvent systems were investigated in FY 2012 consisting of the neutral extractants CMPO, N,N,N'N'- tetraoctyl diglycolamide (TODGA), or N,N,N',N'-tetra-2-ethylhexyldiglycolamide (T2EHDGA), and the acidic extractants HDEHP or HEH[EHP] (Figure 35).

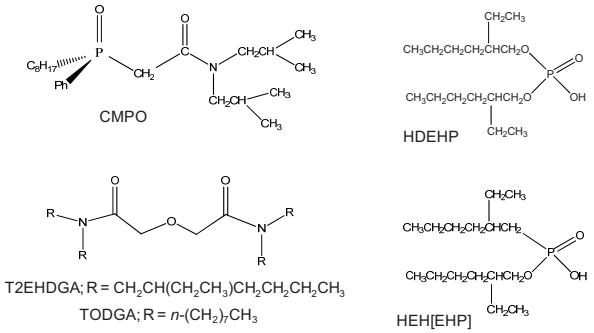

Figure 35. Possible neutral chelating extractants (left) and acidic extractants (right) for use in a single-step process for minor actinide separation.

Replacement of HDEHP with HEH[EHP] leads to potentially more robust MA extraction. The improvements gained by using HEH[EHP] include: (1) improved co-extraction of lanthanides and actinides from nitric acid media, (2) less sensitivity to the pH during the stripping of the MAs, (3) reduced synergistic extraction behavior, which in turn leads to higher Ln/An separation factors, and (4) improved resistance to interfacial crud or third-phase formation. Inclusion of CMPO, TODGA, or T2EHDGA in the solvent formulation allows for the extraction of the MAs and trivalent actinides from strong nitric acid media (Figure 36). Thus, a processing sequence of co-extraction of the actinides and lanthanides, followed by selective striping of the MAs into a

carboxylate-buffered solution of a polyaminocarboxylate ligand (Figure 36), offers a simplified method for separating the MA components of UNF.

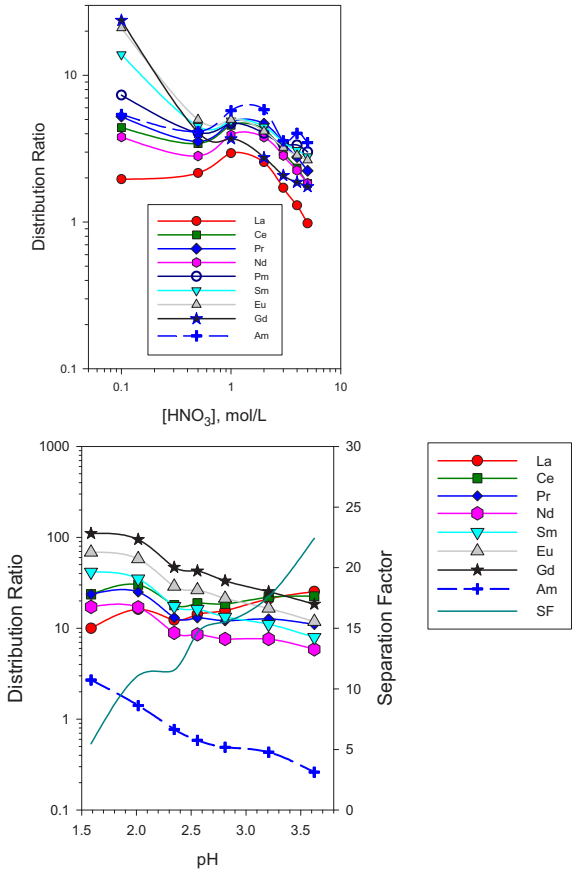

Figure 36. Extraction of Am and the lanthanides from nitric acid with 0.2 M CMPO + 1.0 M HEH[EHP] in n-dodecane (top) and selective stripping of Am with 0.15 M HEDTA in 0.15 M citrate buffer solution (bottom).

Mixed-Donor Extractants

B. P. Hay, haybp@ornl.gov, *A. M. Panagopoulos, and B. A. Moyer*

By combining an amide oxygen donor with heterocylic nitrogen donor, it is possible to obtain a neutral chelating extractant that exhibits selectivity for An(III) over Ln(III). For example, picolinamides formed by attaching ortho –C(=O)NHR groups to pyridine exhibit selectivity for Am(III) over Eu(III) on extraction from nitric acid solution into *t*-butylbenzene.[18] In such a mixed-donor ligand, researchers hypothesize that the hard O-atom donor provides the hard coordination preferred by the hard metal cation, while the soft N-atom donor confers stronger binding of Am(III). By choosing a nitrogen heterocycle with a high dipole moment and preorganizing the ligand architecture to provide a complementary arrangement of binding sites, it should be possible to design a bidentate chelate, L, with a sufficient binding affinity to selectively extract An(III) from nitric acid solution into nonpolar diluents as a neutral $[AnL_2(NO_3)_3]^0$ complex. The dramatic impact of preorganization has already been demonstrated in a closely related system.[11]

Implementing a computer-aided molecular design approach, researchers have identified a candidate architecture attained by fusing 1,2,3-triazole and a cyclic lactam to a central benzene ring (Figure 37).

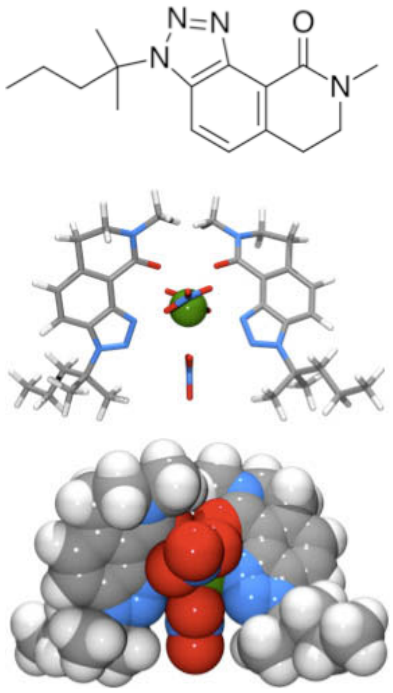

Figure 37. Preorganized mixed-donor extractant, L, (top) and views of the predicted geometry for an $[AnL_2(NO_3)_3]^0$ complex obtained from molecular mechanics calculations (bottom).

Electronic-structure calculations predict this structure to have a very large dipole moment, 7.8 Debye, which on comparison to dipole moments of known neutral extractants, suggests that it will be powerful enough to extract trivalent metals into nonpolar diluents, such as dodecane or kerosene. After the chelate frame is appended with hydrophobic alkyl substituents, molecular-

mechanics calculations confirm that two of these mixed-donor ligands are able to chelate Am(III) in the presence of three inner-sphere nitrates without significant steric hindrance. Synthesis of the designed candidate is now in progress at ORNL.

Investigation of DPAH Stability in Acidic Media

D. R. Peterman, dean.peterman@inl.gov; L. H. Delmau ,and M. E. Freiderich (ORNL)

The degradation of four different dialkyldithiophosphinates having the general formula R_2PS_2H in toluene solution contacted with 1 M HNO_3 was brought to a much deeper level of understanding using direct infusion electrospray ionization mass spectrometry and ^{31}P-NMR spectroscopy. The compound for which R = phenyl (diPh) was found to be stable for in excess of 2 weeks, which contrasted markedly with the behavior of the derivative with R = *o*-trifluoromethylphenyl (Lig1), which degraded completely after about 5 h. The derivative with R = 2,4,4-trimethylpentyl (Cyx) displayed stability for several hours, but then rapidly degraded, suggesting an autocatalytic mechanism. The derivative with R = 3,5-bis(trifluoromethylphenyl) (Lig0) was stable for several days, but then degraded quickly. The degradation pathway for both the R = *o*-trifluoromethylphenyl and R = 2,4,4-trimethylpentyl derivatives involved initial formation of an oxidatively coupled disulfide, which appears to be a precursor to the formation of the corresponding dialkylphosphinic acids (di-oxo derivatives). The disulfide could not be observed for the derivative with R = 3,5-bis(trifluoromethylphenyl)phenyl, but eventually the corresponding dialkylphosphinic acid was seen, suggesting an alternative degradation mechanism for this compound. The overall order of stability of the DPAH ligands with respect degradation by contact with 1.0 M HNO_3 determined in this study is diPh > Lig0 > Cyx > Lig1. Longer exposure to even higher nitric acid concentrations (2 M) can be mitigated by the addition of a radical scavenger. Hydrazine was found to be the most effective. The apparent preference for Eu (Figure 38) is likely due to the high [TOPO]/[DPAH] ratio employed. Preliminary radiolysis experiments to a total absorbed gamma dose of ~100 kGy were performed in order to establish a rough estimate of the radiolytic stability of an An(III)/Ln(III) separations scheme using dithiophosphinic acid (DPAH) extractants and the neutral oxygen-bearing organophosphorus synergist tri-*n*-octylphosphine oxide (TOPO). The distribution ratios of Am(III) and Eu(III) between the irradiated organic phase and an aqueous phase containing 0.1 M HNO_3 + 0.9 M $NaNO_3$ (Figure 39) showed that the studied DPAH extractants exhibit radiolytic stability sufficient to warrant further study.

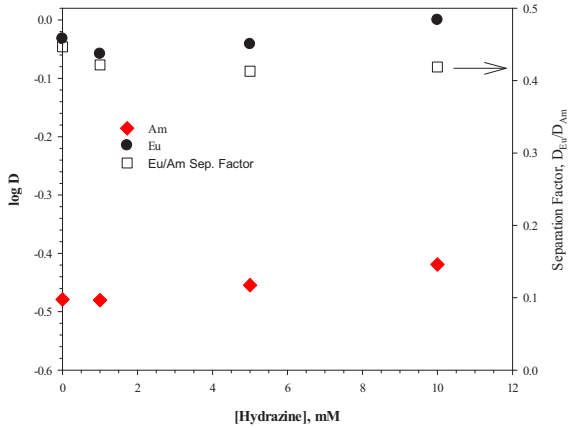

Figure 38. Plot of Am(III) (red diamonds) and Eu(III) (black hexagons) distribution ratios as a function of hydrazine concentration. Organic: 0.01 M Lig 1 + 0.05 M TOPO in nitrobenzene. Aqueous: 0.1 M HNO_3.

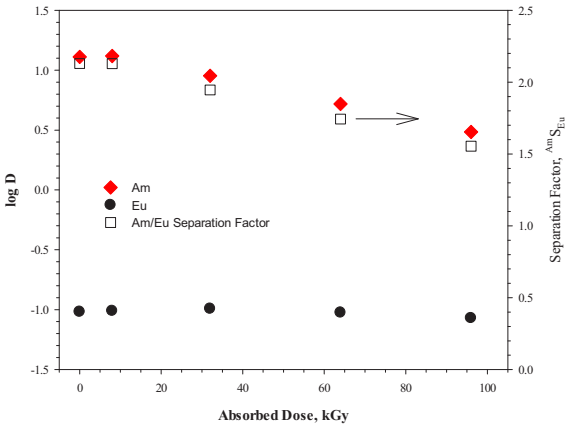

Figure 39. Plot of Am(III) (red diamonds) and Eu(III) (black hexagons) distribution ratios as a function of absorbed dose. Organic: 0.1 M Lig 0 + 0.018 M TOPO in toluene. Aqueous: 0.1 M HNO_3 + 0.9 M $NaNO_3$.

Exploiting the Higher Oxidation States of Americium

B. J. Mincher, bruce.mincher@inl.gov

An unresolved problem in the design of the future fuel cycle is the separation of americium from the lanthanides and curium. One leg of our dual strategy is to oxidize americium to a higher oxidation state, where its chemical behavior is much different than that of the trivalent lanthanides and curium. Researchers have successfully chemically prepared Am(V) and Am(VI) in nitric acid solution using sodium bismuthate as the oxidant, and have characterized their SX behavior with diamyl(amyl) phosphonate (DAAP). That work has demonstrated that high-valent americium can be efficiently separated from the non-oxidizable lanthanides, curium, and many fission products by conventional SX. Among the lanthanides, only cerium is co-extracted, because of its accessible tetravalent oxidation state, and americium is readily selectively stripped using mild reducing agents. The DAAP SX of Am^{VI} and Ce^{IV}, and the selective stripping of americium were demonstrated from nitric acid solution, and from first-cycle raffinate simulant.

Due to the promise shown by this approach, preliminary flowsheet concepts were designed during FY 2012. They use bismuthate oxidation of simulated raffinate adjusted to 6.5 M in nitric acid and 1 M DAAP/dodecane SX followed by dilute peroxide or nitric acid strips. Typical initial D_{Am}, immediately after oxidation is in the range 4–6, corresponding to ~80–86 % extraction. The D_{Ce} remained relatively constant while D_{Am} decreased from ~ 3 at 2 min, to ~1.3 at 10 min following oxidative treatment, which researchers attribute to the slow reduction of Am(VI) in aqueous nitric acid solution. These data indicate that contacts should be performed immediately after filtration to ensure efficient americium partitioning. When the organic:aqueous phase ratio was increased to 10, the initial percent americium extracted was unchanged at 79% (D_{Am} = 0.38). Thus, the efficiency of the extraction appears to be related to the yield of oxidized americium. Similarly, when multiple forward extraction contacts using fresh organic phase are conducted, the D_{Am} decreased with each contact, indicating that much of the remaining americium was not in the hexavalent state.

Attempts to scrub the loaded organic phase with 6.5 M HNO_3 resulted in selective stripping of the americium. This researchers attribute to the fast reduction of Am(VI) in the organic phase and its back-extraction as Am(V). Cerium was not back-extracted under the same conditions. Even when the attempted scrubs contained solid sodium bismuthate, they resulted in stripping of the americium. This is probably due to the slow oxidation kinetics encountered when using bismuthate as an oxidant, coupled with fast reduction of americium in the organic phase. Consequently, reduced americium was stripped in these bismuthate-containing scrubs, simply because the contact time did not allow for the re-oxidation of any reduced americium. However, a flowsheet concept was proposed that consists of bismuthate oxidation followed by filtration, a single extraction contact, rerouting of the raffinate to the oxidation tank, followed by a second contact, and then acid stripping to recover the extracted americium, with a 99% americium yield.

Also during FY 2012, continued investigations of the electrochemical oxidation of americium were performed. To prepare Am(V) or Am(VI), it is first necessary to prepare Am(IV) from electrolyzed Am(III) solution. However, the very high oxidizing potential and the rapid disproportionation of the tetravalent oxidation state require the use of complexing agents. Researchers have reported electrolytic americium oxidation only in phosphoric acid and phosphotungstate (PW) solution. The use of water-soluble organic complexing agents such as dimethylglyoxime and 1-hydroxy-ethane-1,1-diphosphonic acid (HEDPA) have not been successful. CV has identified a single oxidation and two reduction peaks as being solution-phase redox reactions that only occur in Am-spiked phosphoric acid or PW solution. The oxidation states prepared have not been positively identified. Researchers have initiated work with the University of North Carolina, Chapel Hill, to take advantage of their expertise in electrochemistry to resolve this difficult problem.

Ion Exchange Approach to Minor Actinide Separation

D. T. Hobbs, david.hobbs@srnl.doe.gov*; and*
A. Clearfield (Texas A&M)

During FY 2012, experimental work focused in the following areas: (1) testing lanthanide affinity of titanosilicate and multiwall carbon nanotube materials in dilute nitric acid, (2) measuring the rate of uptake of lanthanides by sodium titanates, (3) determining if lanthanides could be eluted from sodium titanate ion exchangers, (4) investigating methods to oxidize americium in dilute nitric acid with subsequent ion exchange performance measurements of metal phosphonate and sodium titanate ion exchangers with the oxidized americium, and (5) examining MA/lanthanide separations under alkaline conditions.

Three titanosilicate ion exchangers were synthesized and determined to have high affinities for lanthanide ions at near neutral pH conditions. Carbon nanotubes and nitrogen-doped carbon nanotubes exhibit low, but measureable affinities for lanthanide ions in dilute nitric acid solutions (pH 3 and 6). Testing indicated that the rates of lanthanide uptake by sodium titanates are very fast at pH 6 with monosodium titanate exhibiting faster uptake and higher capacity than that observed for SrTreat®. Experiments indicated that lanthanides could be eluted in good recoveries from sodium titanate ion exchangers using 0.1 M nitric acid. In contrast, elution of lanthanides from the sodium titanates using tetrakis-(2pyridylmethyl)ethylene-diamine and diethylene triaminepentaacetic acid proved ineffective.

Testing indicated that stable solutions of Am(V) could be produced by treating dilute perchloric or nitric acid solutions of Am(III) with sodium peroxydisulfate and calcium hypochlorite. Good separation of the oxidized Am(V) from other actinides and lanthanides was achieved using both metal(IV) phosphonate hybrid or sodium titanate ion exchangers. For example, Table 4 shows the distribution ratios and separation factors obtained in experiments investigating the separation of Am and Cm in dilute nitric acid.

Initial testing indicated that sodium titanate ion exchangers have very high affinities for Am, Cm, and lanthanides under alkaline conditions. Addition of ozone during the contact time with the sodium titanates reduced the uptake of americium and cerium by the ion exchangers. This finding suggests that Am(III) was oxidized to Am(V) or Am(VI) and Ce(III) to Ce(IV) by the ozone.

Table 4. Distribution values and separation factors for AmO_2^+ and Cm^{3+} with hybrid metal(IV) phosphonate and sodium titanate ion exchangers in dilute nitric acid

Material	K_d AmO_2^+	K_d Cm^{3+}	SF Cm^{3+}/ AmO_2^+
H-Zr-hybrid	62 ± 3.1	96 ± 4.8	1.6 ± 0.11
Na-Zr-hybrid	85 ± 4.3	1300 ± 65	15 ± 1.1
H-Sn-hybrid	120 ± 6.1	1,600 ± 80	13 ± 0.93
Na-Sn-hybrid	220 ± 11	4,400 ± 220	20 ± 1.4
MST	167 ± 17	18,700 ± 933	112 ± 11
SrTreat®	109 ± 5	15,400 ± 769	142 ± 7

Future Progress

In the coming two years, the Sigma Team will be moving toward a team milestone to demonstrate a laboratory-scale americium separation in 2015. While it remains to define the requirements of this milestone, it is anticipated that it will likely entail a demonstration flowsheet of Am separation with simulated feed using prototype small-scale engineering equipment. Based on the progress to date, three technology concepts are being considered as candidates for demonstration:

- *Advanced TALSPEAK*—Using a new combination of extractant and aqueous complexant(s), the emerging technology offers a flatter pH dependence and faster kinetics than the original TALSPEAK process. It will be developed further to formulate the solvent, investigate the extraction and stripping behavior of all metal species involved, and design an optimal flowsheet.
- *ALSEP*—By comparison to similar concepts using a combination of two extractants promoted in other countries, the americium/lanthium separations

(ALSEP) concept offers a flatter pH dependence, likely faster kinetics, and higher Am/Ln separation factors. Criteria for selecting the best combination of extractants will be established, followed by collection of the needed data, extractant selection, and flowsheet development. An option for a selective Am/Cm separation via a selective Am strip will be considered.

- *Selective Am(VI) Extraction*—A suitable method of oxidation will be selected, and the appropriate flowsheet will be developed with an eye on the question of stability of Am(VI) under conditions of the extraction. A cross-flow filtration loop will be set up and tested to determine the feasibility of sodium bismuthate as a possible chemical oxidant.

While the maturation of the above technology concepts will require certain projects to incorporate an applied component to their work scope, the Sigma Team will maintain its science-based approach. Even as applied efforts proceed in the Sigma Team, projects will continue to seek understanding of the underlying chemical principles in hypothesis-driven inquiry: An understanding of the chemical and radiolytic stability of dithiophosphinic acid extractants will be sought, along with identifying conditions for extraction from one molar nitric acid. Ion exchange materials will be sought that operate at low pH and that exhibit selectivity for An/Ln or Am/Cm separation. Radiolytic stability of the higher oxidation states of Am will be characterized, and various chemical and electrochemical methods for Am oxidation will be investigated. Interactions between combined extractants in a single solvent system will be elucidated, and alternative combinations for ALSEP type separations will be pursued. The principles underlying selective Am(III) complexation vs. Cm(III) remain to be fully revealed, and better complexants need to be developed. A dedicated effort to computationally design and test a new family of mixed-donor extractants for An/Ln separation will enter a phase of experimental testing of synthesized candidate compounds. Systems of interest overall will include mainly acidic media, especially nitric acid, and work on alkaline conditions will be phased out.

In summary, the Sigma Team will continue on its course of science-based inquiry according to its original aims to provide the scientific basis for An/Ln and Am/Cm separations. However, the needs of FCRD to begin to demonstrate emerging technology concepts has led to new priorities within the Sigma Team to mature its most promising candidate systems. This new orientation means addressing an additional set of questions related to developing working prototypes. While pursuing such objectives, the Sigma Team will continue to consider altogether new ideas and alternative concepts.

References

1. Arm, S. T., C. Phillips, and A. Dobson. Industrial Application of GNEP Solvent-Extraction Processes. In *Solvent Extraction: Fundamentals to Industrial Applications. Proceedings of ISEC 2008 International Solvent Extraction Conference*; Tucson, AZ, Sept. 15–19, 2008; Moyer, B. A., Ed.; The Canadian Institute of Mining, Metallurgy and Petroleum: Montreal, 2008; Vol. 1, pp 709–714, 2008.
2. Braley, J. C., J. C. Carter, S. I. Sinkov, K. L. Nash, and G. J. Lumetta. The Role of Carboxylic Acids in TALSQuEAK Separations. *J. Coord. Chem.* 2012, *65*, 2862–2876.
3. Braley, J. C., T. S. Grimes, and K. L. Nash, Alternatives to HDEHP and DTPA for Simplified TALSPEAK Separations. *Ind. Eng. Chem. Res.* 2012, *51*, 629–638.
4. Boullis, B. Future Nuclear Fuel Cycles: Prospects and Challenges. In *Solvent Extraction: Fundamentals to Industrial Applications. Proceedings of ISEC 2008 International Solvent Extraction Conference*; Tucson, AZ, Sept. 15–19, 2008; Moyer, B. A., Ed.; The Canadian Institute of Mining, Metallurgy and Petroleum: Montreal, 2008; Vol. 1, pp 29–41.
5. Carelli, M., F. Franceschini, E. Lahoda, and B. Petrovic. In proceedings of the *WM2011*

Conference; American Nuclear Society: Phoenix, AZ, 2011, Paper 11452.

6. Gelis, A. V., G. F. Vandegrift, A. Bakel, D. L. Bowers, A. S. Hebden, C Pereira, and M. Regalbuto. Extraction Behaviour of Actinides and Lanthanides in TALSPEAK, TRUEX and NPEX Processes of UREX+. *Radiochim. Acta* 2009, *97*, 231–232.

7. Herbst, R. S., P. Baron, , and M. Nilsson. Standard and Advanced Separation: PUREX Processes for Nuclear Fuel Reprocessing. In *Advanced Separation Techniques for Nuclear Fuel Reprocessing and Radioactive Waste Treatment*; Nash, K. L., Lumetta, G. J., Eds.; Woodhead Publishing: Oxford, 2011, pp 141–175.

8. Hill, C. Overview of Recent Advances in An(III)/Ln(III) Separation by Solvent Extraction. In *Ion Exchange and Solvent Extraction*; Vol. 19; Moyer, B. A., Ed.; Taylor and Francis: Philadelphia, 2010; Chap. 3.

9. Hill, C. Development of Highly Selective Compounds for Solvent Extraction Processes: Partitioning and Transmutations of Long-Lived Radionuclides from Spent Nuclear Fuels. In *Advanced Separation Techniques for Nuclear Fuel Reprocessing and Radioactive Waste Treatment*; Nash, K. L., Lumetta, G. J., Eds.; Woodhead Publishing: Oxford, 2011, pp 311–362.

10. Laidler, J. J. An Overview of Spent-Fuel Processing in the Global Nuclear-Energy Partnership. In *Solvent Extraction: Fundamentals to Industrial Applications. Proceedings of ISEC 2008 International Solvent Extraction Conference*; Tucson, AZ, Sept. 15–19, 2008; Moyer, B. A., Ed.; The Canadian Institute of Mining, Metallurgy and Petroleum: Montreal, 2008; Vol. 1, pp. 695–701.

11. Lumetta, G. J., B. M. Rapko, P. A. Garza, , B. P. Hay, R. D. Gilbertson, T. J. R. Weakley, , and J. E. Hutchison. Deliberate Design of Ligand Architecture Yields Dramatic Enhancement of Metal Ion Affinity. *J. Am. Chem. Soc., Comm. Ed.* 2002 *124*, 5644–5645.

12. Lumetta, G. J., J. C. Carter, A. V. Gelis, and G. F. Vandegrift. Combining octyl(phenyl)-N,N-diisobutyl-carbamoylmethylphosphine oxide and bis-(2-ethylhexyl)phosphoric acid extractants for recovering transuranic elements from irradiated nuclear fuel. In *Nuclear Energy and the Environment Symposium*; ACS Symposium Series 1046, Washington, DC, 2010a; Chap. 9, pp. 107–118.

13. Lumetta, G. J., A. V. Gelis, and G. F. Vandegrift. Review: Solvent Systems Combining Neutral and Acidic Extractants for Separating Trivalent Lanthanides from the Transuranic Elements. *Solvent Extr. Ion Exch.* 2010b, *28*(3), 287–312.

14. Moyer, B. A. *Sigma Team for Minor Actinide Separation Annual Report*. AFCI-SEPA-PMO-MI-DV-2009-000180, Oak Ridge National Laboratory: Oak Ridge, TN, September 30, 2009.

15. Moyer, B. A. *Sigma Team for Minor Actinide Separation FY2010 Annual Report*. FCRD-SEPA-2010-000125, Oak Ridge National Laboratory: Oak Ridge, TN, September 30, 2010.

16. Moyer, B. A. *Sigma Team for Minor Actinide Separation FY 2011 Annual Report*. FCRD-SWF-2011-000273, Oak Ridge National Laboratory: Oak Ridge, TN, September 29, 2011.

17. Nash, K. L., C. Madic, J. N. Mathur, and J. Lacquement. Actinide Separation Science and Technology. In *The Chemistry of the Actinide and Transactinide Elements.* 3rd ed.; Morss, L. R., Edelstein, N. M., Fuger, J., Katz, J. J., Eds.; Springer: Dordrecht, 2006; Vol. 4, Ch. 22, pp 2622–2798.

18. Nigond, L., N. Condamines, P. Y Cordier, J. Livet, C. Madic, C. Cuillerdier, C. Musikas, and M. J. Hudson. Recent Advances in the Treatment of Nuclear Wastes by the Use of Diamide and Picolinamide Extractants. *Sep. Sci. Tech.* 1995, *30*, 2075–2099.

19. OECD Nuclear Energy Agency, *Actinide and Fission Product Partitioning and Transmutation, Tenth Information Exchange*

Meeting; Mito Japan, October 6–10, 2008; NEA No. 6420, ISBN 978-92-64-99097-5; Organisation for Economic Cooperation and Development: Paris, France, 2010.

20. OECD Nuclear Energy Agency, *Actinide and Fission Product Partitioning and Transmutation, Eleventh Information Exchange Meeting*; San Francisco, CA, USA, November 1–4, 2010; NEA No. 6996, ISBN 978-92-64-99174-3; Organisation for Economic Cooperation and Development: Paris, France, 2012.
21. Regalbuto, M. Alternative Separation and Extraction: UREX+ Processes for Actinide and Targeted Fission Product Recovery. In *Advanced Separation Techniques for Nuclear Fuel Reprocessing and Radioactive Waste Treatment*; Nash, K. L., Lumetta, G. J., Eds.; Woodhead Publishing: Oxford, 2011, pp 176–200.
22. Runde, W. H., and B. J. Mincher. The higher oxidation states of americium: preparation, characterization and use for separations. Chem. Rev. 2011, *111*(9), 5723–5741; dx.doi.org/10.1021/cr100181f.
23. Salvatores, M., and G. Palmiotti. Radioactive waste partitioning and transmutation within advanced fuel cycles: Achievements and challenges. *Progr. Part. Nucl. Phys.* 2011, *66*, 144–166.
24. Tachimori, S., and Y. Morita. Overview of Solvent Extraction Chemistry for Reprocessing. In *Ion Exchange and Solvent Extraction*; Vol. 19; Moyer, B. A., Ed.; Taylor and Francis: Philadelphia, 2010; Chap. 1.
25. Todd, T. A., and R. A. Wigeland. Advanced separation technologies for processing spent nuclear fuel and the potential benefits to a geologic repository. In *Separations for the Nuclear Fuel Cycle in the 21st Century*; Lumetta, G. J., Nash, K. L., Clark, S. B., Friese, J. I., Eds.; American Chemical Society: Washington DC, 2006; Vol. 933, pp 41–55.
26. USDOE, *Nuclear Energy Research and Development Roadmap, Report to Congress*, U.S. Dept. of Energy, Office of Nuclear Energy: Washington, DC, April 2010a.
27. USDOE, *Research Objective 3 Implementation Plan: Developing Sustainable Fuel Cycle Options*, FCRD-TIO-2011-000025, DOE Office of Nuclear Energy: Washington, DC, December 2010b.
28. Wigeland, R. A., T. H. Bauer, T. H. Fanning, and E. E. Morris. Separations and transmutation criteria to improve utilization of a geologic repository. *Nucl. Technol.* 2006, *154*, 95–106.

This page intentionally left blank.

CHAPTER 6
OFF-GAS SIGMA TEAM

CHAPTER 6: OFF-GAS SIGMA TEAM

R. T. Jubin, jubinrt@ornl.gov

Effects of Sorbent Aging on Iodine Adsorption

R. T. Jubin, jubinrt@ornl.gov, and S. H. Bruffey

Storage of Reduced Media

Experiments were undertaken this year to determine optimal storage conditions for silver modenite (Ag^0Z). During exposure to ambient air, Ag^0Z can absorb some moisture, while the reduced silver in the mordenite may experience aging. At ORNL all Ag^0Z material, including samples loaded with iodine, are currently stored under a blanket of argon. To evaluate the effectiveness of this method, a charge of silver-zeolite (AgZ) was reduced. The AgZ was dried under argon at 230°C for ≈48 hr. After drying, reduction was carried out using a stream of $4\%H_2/96\%N_2$. The oven temperature remained at 230°C for the duration of the run. After 5 days, the reduction was terminated, and each sample was transferred to a glass vial. Portions of this Ag^0Z charge were stored under three conditions: argon blanket, N_2 blanket, and ambient air. These samples have been stored for 5 months. Each portion of Ag^0Z will be loaded with iodine under identical loading conditions, and the effects of storage atmosphere on initial loading rate and total I_2 capacity will be determined. These tests are currently in progress and will be reported in early FY 2013 along with recommendations for storage of AgZ test media.

Aging of Silver Functionalized Aerogel

In an off-gas system, any capture material will be exposed to a gas stream for months at a time. This gas stream may be at elevated temperature and could contain water, NO_x gas, or a variety of other constituents comprising the dissolver off-gas stream in a traditional nuclear fuel reprocessing plant. For this reason, it is important to evaluate the effects of long-term exposure, or aging, on proposed capture materials. One material under consideration is silver-functionalized silica aerogel. Aerogels are being produced at PNNL and distributed to other labs for testing. For initial aging studies conducted at ORNL, a very simple feed gas of dry air at 150°C was used. Based on the results of these studies, sequentially more complex simulated feed gases may be used for future aging experiments.

The aged aerogel material was loaded under conditions identical to previous studies in FY 2011. The material was first dried under 2-L/min N_2 for 16 to 24 hr at 150°C. No weight loss was observed in this step. After drying, iodine loading was initiated at 56 ppm under 10.3-m/min superficial velocity. The weight of the sample was monitored continuously, and when no further weight gain was observed (generally after 7+ days) the loading was allowed to continue for an additional 18 to 24 hr prior to the termination of iodine flow. The sample was then purged under 10.3-m/min dry air for 24 hr. Loading curves are shown in Figure 40. Final observed weight gains for each sample are seen in Table 5.

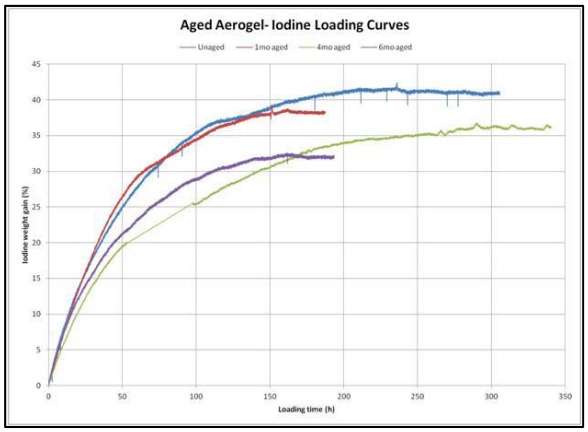

Figure 40. Iodine loading curves for aged aerogels.

Table 5. Observed iodine loadings for aged aerogels

Aging time (month)	Weight gain (%)
0	40.80
1	38.23
4	35.99
6	31.97

The iodine loading was well behaved, and the resulting curves can be expected to accurately reflect total iodine loading on the aged materials. The 4-month aged aerogel appears to load at a lower rate than the 0-, 1-, and 6-month aged aerogels. This may correspond to use of a different thermogravimetric analysis (TGA) for that sample and should not affect final observed weight gain. It was concluded from these studies that aging an aerogel under a dry air stream for up to 6 months can decrease its iodine capacity by 9%. Iodine loading of the aerogels under these test conditions appears to change the physical characteristics of the aerogels. The particles begin to clump together and turn from black to light gray.

Restoration of Capacity Lost During Through Aging

Results from recent studies[1] have shown that Ag^0Z loses a significant amount of iodine capacity when exposed to dry or moist air streams. To determine whether that capacity can be regained through a second silver reduction, a reduction of four aged Ag^0Z samples was completed using samples of 1- and 4-month dry air aged Ag^0Z and 1- and 4-month humid air aged Ag^0Z. The same reduction apparatus as used for the partial reduction work described in Section 2.3 was utilized. Initially the aged Ag^0Z was dried under argon at 230°C for ≈48 hr. After drying, reduction was begun using a stream of $4\%H_2/96\%N_2$ at 230°C. After 5 days, the reduction was terminated, and each sample was transferred to a glass vial and covered with argon.

Iodine loading of these samples is in progress. Loading tests are conducted on the TGA apparatus. Iodine concentration in the feed gas is 25 ppm, superficial velocity is 10 m/min, and operating temperature is 150°C. Initial results show that a significant amount of capacity can be regained through a reduction after humid aging (Figure 41). It remains to be determined if aged Ag^0Z loaded with iodine will retain that iodine during the reduction process.

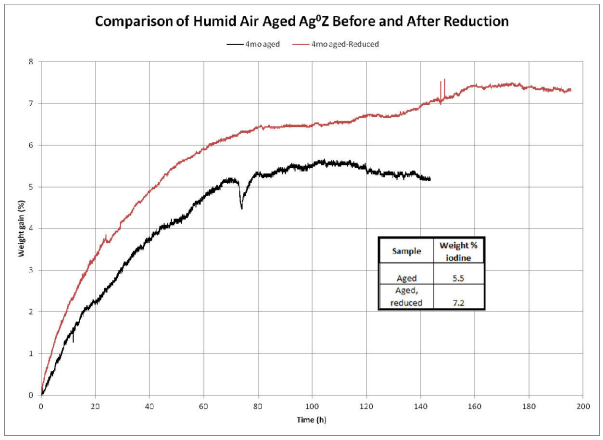

Figure 41. Comparison of the iodine adsorption on moist air aged AgZ and reduced moist air aged AgZ.

References

1. Jubin, R. T. 2011a. Report of the FY 2011 Activities of the Off-Gas Sigma Team, FCRD-SWF-2011-00306, September 2011.

Effects of Silver Mordenite Pretreatment

R. T. Jubin, jubinrt@ornl.gov, and S. H. Bruffey

Earlier work has been shown that silver mordenite has a greatly increased capacity for iodine when all the silver in the material is reduced to silver metal. Chapman et al. [2010] reported that during the hydrogen reduction of AgZ, a portion of the silver migrated within the zeolite structure, that is, through the 8- and 12-member rings and formed small clusters of elemental silver. With time, under continued reducing conditions, a portion of these clusters migrated to the zeolite surface and coalesced as larger nanoparticles. The practical effect of this silver migration on the iodine capacity of the reduced Ag°Z remains unclear. It is not currently known which of these silver sites is preferred for iodine loading in terms of (1) iodine silver reaction and (2) AgI stability. One hypothesis was that the most accessible reaction site would be on the zeolite surface. A second hypothesis was that the most stable AgI waste form would be where the iodine reacts with the silver in the internal structure of the zeolite. It was further hypothesized that by limiting the extent of the reduction, the silver migration to the surface could also be limited. Additionally, the procedure for reduction

has not been optimized to ensure that the Ag^0Z produced has the highest potential iodine capacity.

To begin to explore the first hypothesis, samples of freshly reduced Ag°Z (no aging) with various stages of iodine loading were prepared at ORNL and sent to SNL in June 2011. It is expected that a change in the relative ratios of the alpha and gamma forms of AgI as the iodine loading increases will be observed. Results from the pair distribution function (PDF) analysis method taken at the Advanced Photon Source (APS) X-ray data are reported in Section 6.3.

Other studies by the Sigma Team conducted in FY 2010 and FY 2011 have shown a significant decrease in iodine capacity with increased aging. The cause of this is hypothesized to be the oxidation of silver to AgO. It is not known if all silver sites are equally impacted. To begin the process of understanding the aging process and its impact on iodine capture, a similar series of tests utilizing the APS as described in Section 5.2 are being conducted with aged Ag°Z. In this series, a set of 11 partially iodine-loaded and aged Ag°Z were prepared. This set included both dry-air and humid-air aged materials. Target elemental loadings were 1, 2, 5, and 7 wt%. A portion of each sample was shipped to SNL for x-ray analysis at the APS.

To address the second and third hypotheses, researchers have undertaken a series of tests that will examine the effects of partial reduction on the iodine loading capacity and on the subsequent waste form. Process parameters that are relevant to the reduction include temperature, reductant concentration, and time.

The aim of this study is to investigate both fundamental and applied aspects of the reduction of AgZ. Fundamental studies include XRD and scanning electron microscopy (SEM). High-energy X-ray scattering will be performed by collaborators at Sandia National Laboratory (SNL). Applied studies will focus on optimization of the reduction procedure and iodine loading studies of Ag°Z.

To answer questions regarding the reduction process, the reductions were conducted in a manner that results in a "partial" reduction of AgZ; that is, the AgZ was reduced over periods of time ranging from 1 hr to 10 days, and examined as a function of reduction time. Reductions were performed in a reducing gas mixture of 4% H_2–96% N_2. The column containing the sorbent to be reduced is placed in a laboratory oven. The column contains seven trays, which hold the sorbent and can each be removed individually from the column.

Iodine loading of partially reduced AgZ was conducted in two TGAs. These systems are described in the *FY 2011 Report of the Off-Gas Sigma Team*.[1] Loading was conducted at 10-m/min superficial velocity, with a feed gas containing 25 ppm iodine in dry air.

A total of six reduction runs were completed. These runs were conducted at three different temperatures, ranging from 75°C to 230°C. Sampling times varied from 1 hr to 10 days.

Selected samples were loaded with iodine. Table 6 lists the samples loaded and their final loadings as determined with neutron activation analyses. These were sent to SNL for further analysis with high-energy X-ray scattering. The results from these analyses are discussed in Section 6.3. Typical TGA curves for the loading of I_2 on the sorbent from reduction run 1 are shown in Figure 42.

Table 6. Partially reduced partially loaded AgZ samples sent to SNL

Designation	Reduction Time (h)	Target I_2 Loading (%)	I_2 loading after air purge (%)	Reduction Run
FY12-032	1	1	0.99	1
FY12-018	1	Maximum	1.70	1
FY12-031	4	1	1.15	1
FY12-019	4	Maximum	2.38	1
FY12-022	4	Maximum	1.85	2
FY12-029	8	1	1.64	2
FY12-026	8	2	2.32	2
FY12-030	8	3	2.71	2
FY12-024	8	Maximum	3.43	2
FY12-034	12	1	1.78	1
FY12-033	72	1	1.86	2

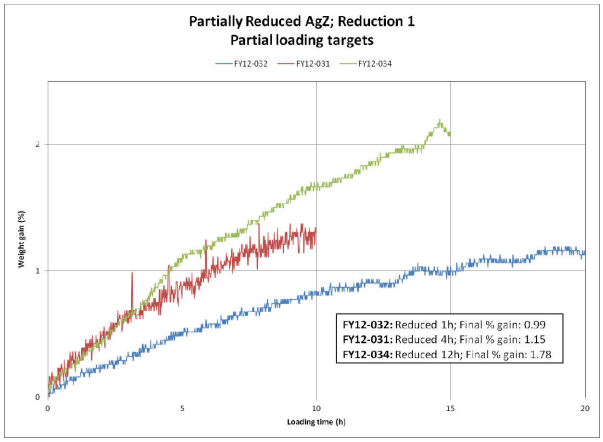

Figure 42. Iodine loading curves for partially reduced AgZ from reduction 1, partial target loadings.

Samples from reduction 1 (230°C) were analyzed with XRD. As expected, the amount of Ag0 increased with reduction time. By holding the amount of silicon at 10% in the XRD refinements, the relative percent of silver was determined and reported in Table 7.

Table 7. Refined weight % with constant addition of silicon

Time (hr)	Partially reduced AgZ		
	Silver (wt %)	Mordenite (wt %)	Silicon normalized to 10 wt %
1	0.0	13.2	
4	1.3	12.0	
12	2.5	13.7	
24	2.4	12.6	
68	3.0	13.7	

As stated earlier, the practical effect of this silver migration on the iodine capacity of Ag°Z remains unclear. These preliminary results would appear to indicate that the partially reduced Ag°Z has a lower iodine adsorption rate and a potentially lower total capacity. Future work should be continued with efforts to determine the impact of the iodine loading on these partial reduced materials and the determination of any impact on the subsequent waste forms that are produced.

References

1. Jubin, R. T. 2011a. Report of the FY 2011 Activities of the Off-Gas Sigma Team, FCRD-SWF-2011-00306, September 2011.
2. EPA. 2010a. Chapter 40. Environmental Protection Agency: Part 61–National Emission Standards for Hazardous Air Pollutants. Subpart H—National Emission Standards for Emissions of Radionuclides Other Than Radon from Department of Energy Facilities, 92 - Standard. 40CFR61.92. U.S. Environmental Protection Agency, Washington, DC.
3. EPA. 2010b. Protection of Environment: Chapter I–Environmental Protection Agency (Continued), Part 190_Environmental Radiation Protection Standards for Nuclear Power Operations. 40CFR190.10. U.S. Environmental Protection Agency, Washington, DC.
4. Gombert, D. 2007. Global Nuclear Energy Partnership Integrated Waste Management Strategy Waste Treatment Baseline Study - Volume I, GNEP-WAST-AI-RT-2007-000324, (September 2011).
5. NRC. 2012. Chapter 10, "Energy: Part 20 - Standards for Protection against Radiation," 10CFR20. U.S. Nuclear Regulatory Commission, Washington, DC.
6. Rosnick, R. 2007. CAP88-PC Version 3.0 User Guide, Environmental Protection Agency, Washington, DC.

Analysis of Iodine Loaded and Partially Reduced Silver Mordenite

T. M. Nenoff, tmnenof@sandia.gov,
and K. W. Chapman

Silver (Ag) nanoparticles supported on porous zeolites, in particular Mordenite (MOR), are used in the capture of radioactive iodine gas (I_2). The porous crystalline structure of the zeolite allows for the incorporation of Ag and/or AgI either in the pores or on the surface of the crystallites (see Figure 43). The ability to have physical retention of the iodine (as silver iodide, AgI) inside the pores adds security of retention of the radiological

element during mechanical or thermal treatments. The retention of the ^{129}I containing gas is of importance as it is a long-lived isotope and a fission gas product of nuclear fuel recycling processes, with a preferential absorption in the thyroid. AgI polymorph formation is strongly dependent on the structure and distribution of the Ag particles within the zeolite prior to iodine introduction. Accordingly, a comprehensive understanding of the Ag particle formation is key to controlling the structure and reactivity. Both thermal dehydration of water adsorbed within the zeolite pores and chemical reduction can contribute to Ag-particle formation in Ag-exchanged zeolites.

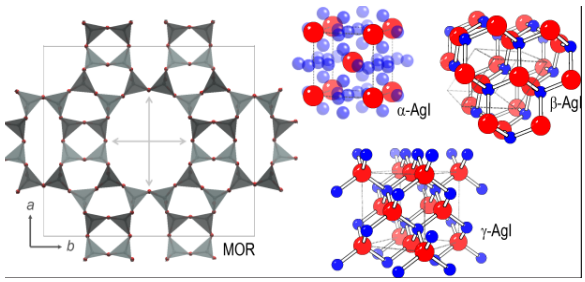

Figure 43. left; MOR pore structure; right, polymorphs of AgI.[2]

Both absorbed water and charge of silver valence (e.g., Ag^0 vs. AG^{1+}) affect silver cation mobility and, thus, have the potential to impact cluster and particle growth kinetics. Thermal dehydration during the high temperature reduction reaction and/or changes to the pore surface, may affect cation mobility in the partially reduced material. Therefore, researchers are undertaking a complex structure analysis of the role of these different factors on the ability for Ag-MOR to retain iodine from the gas.

Due to the limited availability (on an industrial scale) of commercial synthetic Ag-MOR, ORNL has provided SNL with a reference material MOR zeolite that is silver exchanged (Ionex Type Ag 900, Molecular Products); it is a non-uniformly crystalline version of the zeolite but available in industrial scale quantities. Differential PDF data were obtained by direct subtraction of the reference PDF containing only MOR correlations to isolate the contribution from the supported Ag species.

Samples of Ag°-MOR exposed to I_2 gas under varying conditions were prepared at ORNL and sent to SNL for structural analysis. SNL, in collaboration with ANL, performed crystallographic studies to understand the role of Ag°-MOR preparation on iodine capture.[1] In weight loading studies, subnanometer α-AgI clusters form preferentially at low I_2 concentrations with the γ-AgI, only forming at higher I_2 concentrations (see Figure 44, top). In aging studies at variable weight loadings, there are no clearly defined product patterns with respect to aging humidity vs. dryness[3] (see Figure 44, middle). In silver reduction studies (partial vs. fully reduced silver), the data indicates for less than 8 hours reduction processes, there is no evidence of Ag° formation/remaining; in samples reduced for greater than 8 hours, there is evidence of γ-AgI formation (see Figure 44, bottom).

This data provides guidelines to ORNL and INL in the methodology needed to prepare AgZ (Ag-MOR) for incorporation into the low temperature glass waste form reference material studies to be carried out at SNL in FY 2013. Furthermore, SNL will continue the joint tests with ORNL and INL studying and optimizing the reduction time and temperature of Ag-MOR through continued structural studies at the APS at ANL. All of these results will continue to support the effort to develop a report on the expected speciation of iodine, impacts to iodine capture, and proposed revisions to test protocols.[4] Further details are reported by Nenoff et al, in FCRD-SWF-2012-000274.[5]

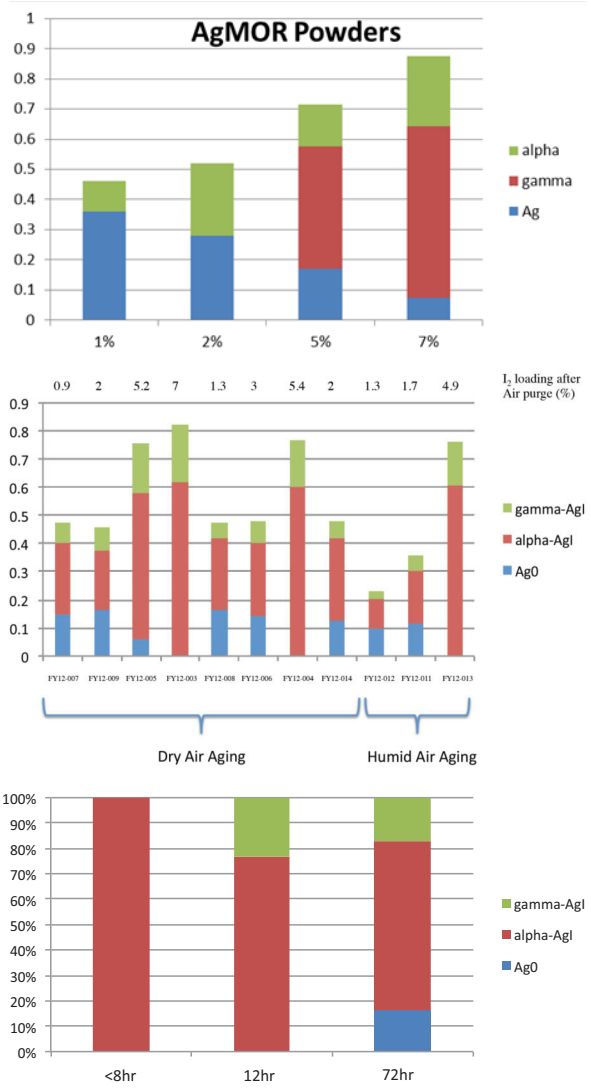

Figure 44. AgI polymorph determinations via PDF structural studies on AgI-MOR samples; (top) weight loading studies; (middle) aging studies; (bottom) Ag reduction studies. Ag° = reduced silver metal; gamma-AgI (>30Å); alpha-AgI (≈ 2-10Å).[2]

References

1. Memo from T. M. Nenoff to R. Jubin 01/05/2012, containing data, no associated milestone, Jubin, R. T., "Summary of FY 2012 Off-Gas Sigma Team Activities", FCRD-SWF-2012-000331 p. 42.

2. Chapman, K, P. Chupas, and T. M. Nenoff. "Radioactive Iodine Capture in Silver-Loaded Zeolites Through Nanoscale Silver Iodide Formation" J. Amer. Chem. Soc., 2010, 132 (26), 8897–8899.

3. Nenoff, T. M. "M4FT-12SN0303101 Complete analysis of I2-loaded aged/reduced Ag-MOR from ORNL" FCRD-SWF-2012-000258, June 28 2012.

4. Zhao, H., K. Beyer, T. M. Nenoff, P. J. Chupas, and K. W Chapman. "Combining Simultaneous Pair Distribution Function with Diffuse Reflectance Infrared Spectroscopy to Study Silver Particle Growth on Porous Template" 2012, submitted.

5. Nenoff, T. M., and K. W. Chapman. "Complete Analysis of I2 Loaded and Partially Reduced Ag-MOR Samples from ORNL" FCRD-SWF-2012-000274, August 29, 2012.

Silver-Functionalized Silica Aerogels for Iodine Capture and Immobilization

J. Matyáš, Josef.Matyas@pnnl.gov

Overview and Objectives

Silver-functionalized silica aerogel is being developed for the removal and immobilization of iodine from gaseous products of nuclear fuel reprocessing. High selectivity and efficient capture of gaseous iodine in combination with feasible consolidation to a durable SiO_2-based waste form containing encapsulated nano-AgI makes this aerogel an attractive choice for treating reprocessing off-gas and sequestering radioiodine. When fully developed, silica aerogel can be used both as an adsorbent and waste form to meet regulations for the release of ^{129}I from a reprocessing facility and ^{129}I disposal.

Accomplishments

Researchers were able to optimize lab-scale synthesis of Ag^0-functionalized silica aerogel and scaled up the production to 100 g per run, see Figure 45. Deep-bed sorption testing at INL of optimized functionalized aerogel under prototypic off-gas conditions yielded decontamination factors (DFs) in excess of 10 000. These DF values are more than sufficient to meet regulatory emission limits for ^{129}I.

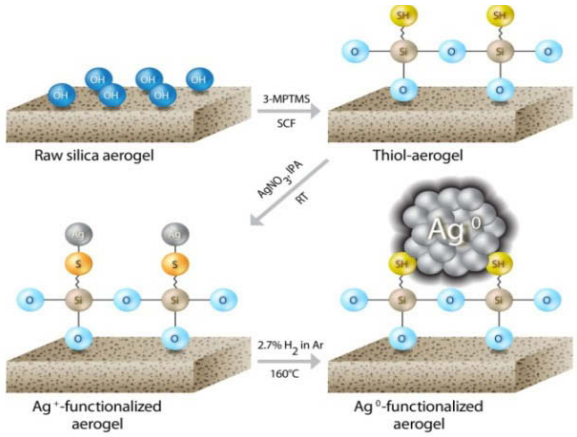

Figure 45. Schematic for production of Ag^0-functionalized silica aerogel.

In addition, dry-air aging of functionalized aerogel, which simulated the impact of long-term exposure to process gases during process idling, resulted only in a modest decrease of iodine sorption capacity (Figure 46). The 6-month aged sample exhibited an iodine sorption capacity of 32 mass%, which was 22% relative lower than that for an un-aged Ag^0-functionalized silica aerogel. In the same test with a 6-month aged silver mordenite, the loss in sorption capacity was 40% relative. In an attempt to understand this decrease in sorption capacity, researchers characterized physical properties of the aged aerogel samples with an array of analytical techniques. The results showed no detectable impact of aging on the aerogel microstructure or the silver nanoparticles in the aerogel, including their spatial distribution and morphology.

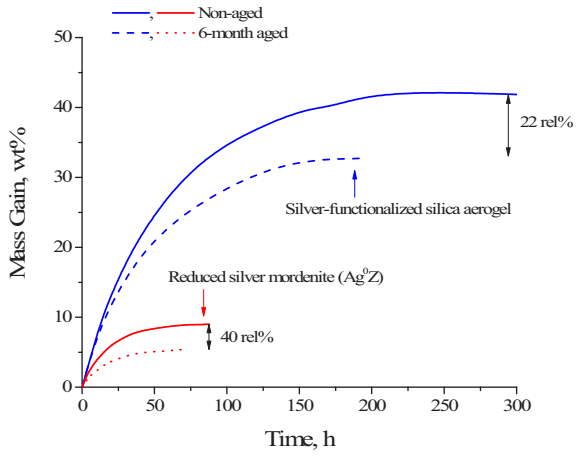

Figure 46. Sorption performance for non-aged (solid lines) and 6-month aged (dash and dot lines) Ag0-functionalized silica aerogel and silver-reduced mordenite.

Our densification studies on raw silica aerogel granules demonstrated that 15-min pressureless sintering at 1200°C results in dense granules with a density of 2.2×10^3 kg/m^3, approximately 80% of quartz density. Low-pressure hot-pressing (< 29 MPa) at 1200°C accelerated consolidation process and decreased the pore size and volume.

Deep Bed Iodine Adsorption Testing

N. Soelberg, nick.soelberg@inl.gov

Deep-Bed Iodine Test System

The term "deep-bed" implies the use of laboratory-scale fixed beds that contain specified depths of solid iodine sorbent granules in tests that emulate (on a small scale) actual fixed bed adsorption conditions. The deep-bed test system has the capability to generate synthetically blended gas mixtures designed to emulate a separations process off-gas stream (such as a dissolver off-gas stream and contain inorganic I_2 and methyl iodide (CH_3I, a surrogate for organic forms of iodine species). The process gas flows at specified compositions and flow rates through up to four separate sorbent beds of specified depths that are maintained in a temperature-controlled oven. Gas sampling of the process gas upstream and downstream of each bed, and gravimetric analysis of the sorbent, are used to measure adsorption efficiency, capacity, and mass transfer zone (MTZ) depths. These tests also generate data to support adsorption modeling, and generate iodine-laden sorbents in gram-quantities that can be used for waste form studies.

FY 2012 Test Results

Deep-bed iodine sorption tests for both silver-functionalized Aerogel (AG) and AgZ sorbents were performed during FY 2012. Figure 47 shows the sorbent beds used in tests and the color change for "natural" AgZ sorbent before and after a sorption test. The AG color also changed during the adsorption tests, from an initial rusty-red-black mix to a grey-yellow-black mix.

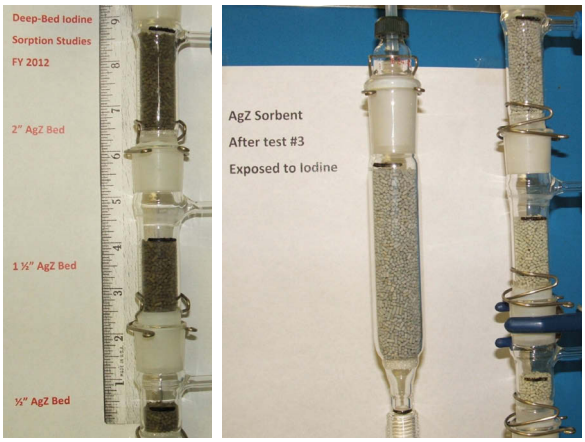

Figure 47. "Natural" silver zeolite sorbent in the deep-bed test system before and after adsorption.

Figure 48 illustrates the results of one of the deep-bed AG tests. Initial adsorption efficiencies are typically high. Off-gas I_2 control efficiencies exceeding 99.99% (DFs exceeding 10,000) were demonstrated for AgZ and AG. These control efficiencies are high enough to meet U.S. regulatory air emission limits for reprocessing facilities.[2]

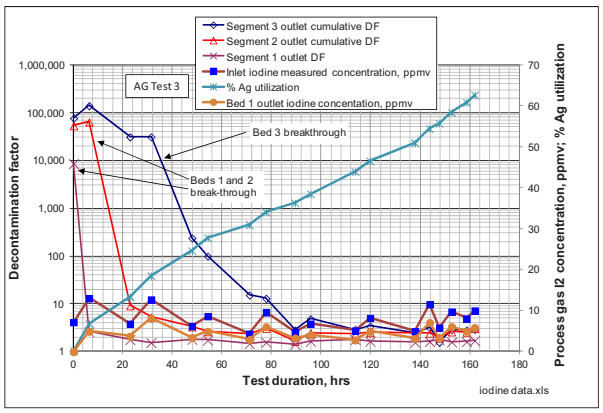

Figure 48. Typical silver-functionalized Aerogel test results.

As test time progresses, and depending on the inlet iodine gas concentrations, iodine breakthrough in the shallow Bed 1 typically occurs quickly; the control efficiency approaches zero (and the DF approaches 1) more slowly. Downstream, deeper beds reach breakthrough and saturation even more slowly.

This is consistent with typical MTZ theory for fixed sorbent beds (Figure 49), where the zone of active adsorption (the MTZ) progresses from the front to the back of the bed over time. However, these tests have indicated that the depth of the MTZ increased over time from initially 0.5-4 inches, to over 4 inches, depending on initial iodine concentrations.

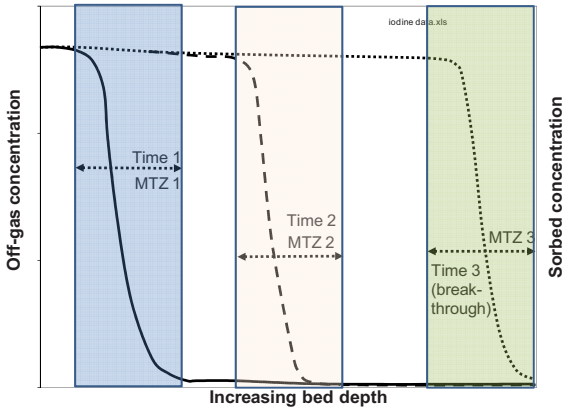

(a) Theoretical MTZ.

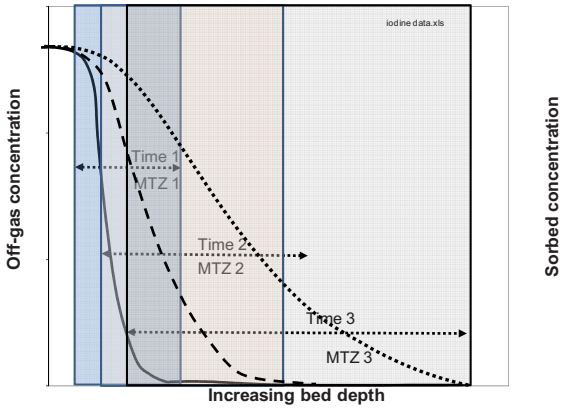

(b) MTZ that increases in depth over time.

Figure 49. MTZ progression in a fixed sorbent bed over time.

Figure 50 shows iodine loading on the sorbents and silver utilization (based on the chemisorption reaction $2Ag + I_2 = AgI$). According to the gas-phase iodine measurements, 100% silver utilization was approached or exceeded for some of the tests. The loading of iodine on the sorbents averaged ~10 wt% for AgZ and over 20 wt% for AG for the test durations. These loadings are higher than have been estimated or assumed in some prior studies (such as only 2-6.9 wt% in the earlier Integrated Waste Management Study[1]). The silver utilization was calculated using a silver content of 11.9 wt% Ag for the AgZ and 30 wt% Ag for the AG.

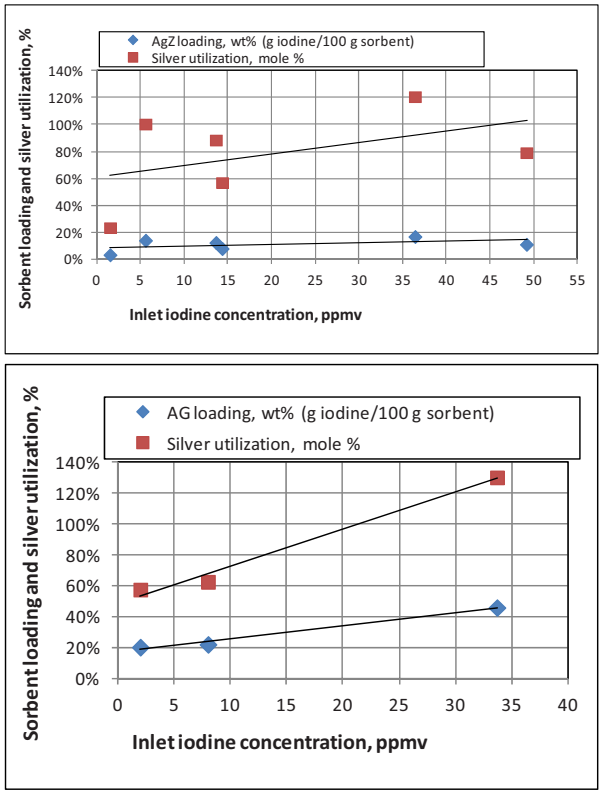

Figure 50. Iodine loadings and Ag utilization based on the inlet and outlet gaseous iodine measurements.

Most of the sorbed iodine was tightly held in the sorbents. As shown in Figure 51, less than 0.6 w% of the sorbed iodine was desorbed during post-test purging from the AgZ; and less than 0.005% of the sorbed iodine was desorbed during post-test purging from the AG.

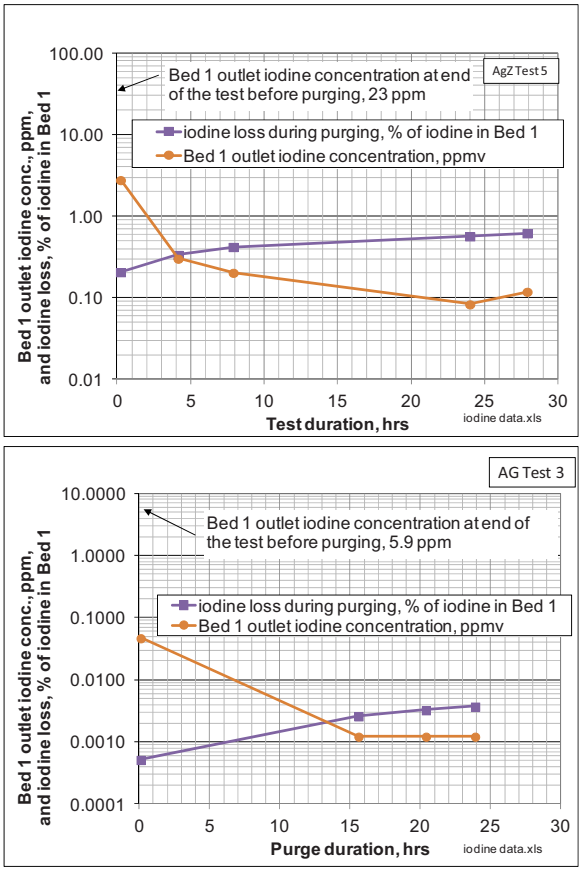

Figure 51. Desorption of sorbed iodine from AgZ and AG.

References

1. Gombert, D. II, "Global Nuclear Energy Partnership Integrated Waste Management Strategy," GNEP-WAST-WAST-AI-RT-2008-000214, May 2008.

2. Jubin, R. T, N. R. Soelberg, D. M. Strachan, and G. Ilas, "Position Paper on Practicable Performance Criteria for the Removal Efficiency of Volatile Radionuclides," FCRD-SWF-2012-000091, INL-EXT-12-25410, March 30, 2012.

Chalcogen-Based Aerogels for Iodine Capture and Immobilization

B. Riley, brian.riley@pnnl.gov, J. Chun, and W. Lepry

Chalcogen-based aerogels, or *chalcogels*, are a unique type of high porosity material that show promise as a sorbent for gaseous iodine. The chalcogen backbone in a chalcogel has an inherent affinity for iodine; thus, these materials do not

require functionalization (with silver or other agents) to bind iodine. Many different chalcogel compositions are possible and each has different properties such as interlinking connectivity, available surface area, and temperature stability. All of these materials are porous but some more than others. Considering that these materials are very lightweight, the main challenges associated with this research pertain to making a form that is useful for gaseous capture and immobilization. A collaborative effort with INL has produced a chalcogel-polymer hybrid material with increased mechanical rigidity at the expense of available surface area (Figure 52). These hybrid materials have been fabricated with a few different chalcogel chemistries and will be evaluated in FY 2013 for iodine capture efficiencies.

Figure 52. Chalcogel-polymer hybrid granules.

Initially, chalcogel materials containing Pt (Pt-Ge-S) were investigated because those formulations were readily available and easily investigated. In FY 2012, two families of chalcogels without Pt have been studied at PNNL and include Mo-S (CoBiMoS, CoCrMoS, CoNiMoS) and Sn-S formulations. All of these compositions show good iodine capture efficiencies in streams with low iodine concentrations (Figure 53). Although all of the chalcogels performed well at first, the capture efficiency of the MoCoNiS chalcogel dropped off considerably after 4–8 hrs. The SnS chalcogel performed very well throughout the entire duration of the test.

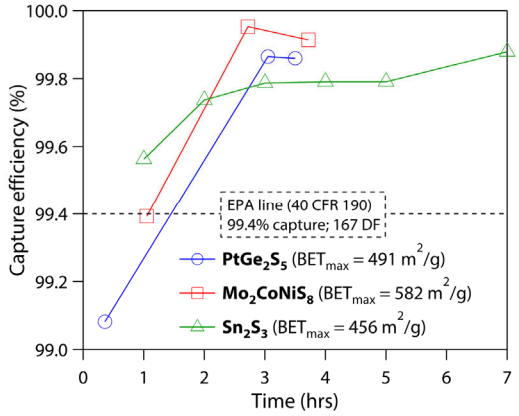

Figure 53. Chalcogel iodine sorption efficiency in 4 ppm iodine (in air).

In FY 2013, this work will include collaboration with Northwestern University through an NEUP project. This collaboration will help us evaluate the several different chalcogel chemistries Northwestern University has fabricated to date and help us direct the research towards the most promising candidate materials. The Kanatzidis Group at Northwestern University pioneered the early work with these materials and has extensive facilities for fabrication and characterization.

Iodine / Tritium Co-Adsorption

B. B. Spencer, spencerbb@ornl.gov

The purpose of this study was to evaluate tritium (water) adsorption on AgZ and to evaluate the impact of the co-adsorption of water on subsequent iodine adsorption on AgZ, that is, any change of iodine capacity in the presence of water.

In traditional nuclear fuel reprocessing plants the primary source of effluent gases containing iodine and other volatiles is the dissolver. Nitric acid dissolution of UNF releases volatile components including iodine (as I_2 or CH_3I), tritium (as HTO), ^{14}C (as carbon dioxide), xenon, and krypton (e.g., ^{85}Kr). The tritium remains in the aqueous dissolver solution and spreads throughout the aqueous systems of the plant. The other volatiles mostly escape the dissolver solution and are mixed with nitric oxide (NO), nitrogen dioxide (NO_2), and processing cell gas (e.g., air) that leaks into the reduced pressure dissolver. This happens primarily at the isolation valves between the dissolver and shear (or voloxidation). Use of the

air or oxygen voloxidation process upstream of the dissolver is being considered as a method to remove the tritium from the fuel before it is introduced to the aqueous systems. In the simplest version of this process, the fuel is oxidized from UO_2 to U_3O_8, releasing most of the tritium (as HTO) in the fuel material and significant fractions of the iodine (as high as 5%), carbon, xenon, and krypton. Because voloxidation is a dry process, the off-gas does not contain large quantities of water vapor, and since no acid is used, there is no NO_x.

Typical methods to sequester and control release of these volatiles include silver-impregnated zeolites to recover iodine, caustic scrubbers to recover carbon as a carbonate, and zeolite molecular sieves to recover the noble gases and tritiated water. These operations can be used in various combinations to treat dissolver off-gas and voloxidizer off-gas either separately or as a mixed off-gas stream. The sequence of these operations also becomes important and is dependent on which process the off-gas system supports. Alternative new processes, such as electrochemical processing, will produce off-gas streams containing similar volatile radionuclides, but the chemical species may be different. In addition, there could be other semivolatiles arising from the fuel and different process or carrier gases. A more complete understanding of the characteristics of the AgZ is needed before applying it to the different fuel processing systems just described.

Tests using a nominal 25.4-mm-diameter by 180-mm-high column of AgZ were performed to evaluate the impact of the co-adsorption of water on subsequent iodine adsorption. Reduced AgZ (Ag°Z) was prepared at about 230°C in the presence of hydrogen. Under gas compositions similar to those expected for dissolver off-gas, the AgZ adsorbs 2% to 3% water by weight. Temperature measurements within the column media indicate the passage of the water sorption front because the temperature rises markedly upon rehydration of the mordenite (see Figure 54). The water adsorption front moves through the column at over two orders of magnitude faster than does the iodine sorption front. The velocity of the water sorption front can be tracked by temperature measurements at different positions along the length of the column and is confirmed by the measured moisture breakthrough with an overall water balance.

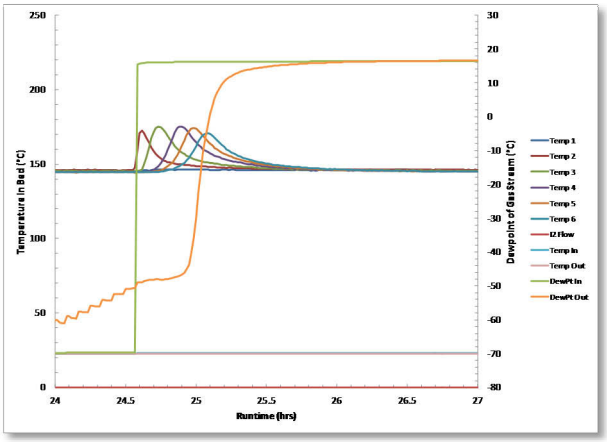

Figure 54. Temperature profile during water co-adsorption onto AgZ.

No temperature rise in the bed due to sorption of iodine was measured, likely because the iodine concentration is too low to produce sufficient thermal energy. Neutron activation analysis of the iodine-loaded bed was used to determine overall iodine loading; a value of about 4.8% for the material used in the experiments was obtained. Saturation of the column with water appeared to have no effect on the iodine capacity of the AgZ. Sampling of the effluent gas to determine iodine concentration was performed to evaluate potential changes in the breakthrough curve. Analysis of these samples is pending.

Determination of Baseline Iodine Waste Form Performance Characteristics

T. M. Nenoff, tmnenof@sandia.gov

One thrust of SNL's waste form research program is to develop effective iodine capture materials that can be flexibly utilized in a variety of repository or storage scenarios. Currently, I_2 sorption by Ag-mordenite zeolite is commonly considered the capture process for radiological iodine gas from experimental waste streams. Long-term storage will require a waste form that is compatible with either I_2 gas or iodine occluded/encapsulated capture material, and is chemically, mechanically and radiologically durable for long storage times commensurate with

the Iodine decay period. A material of interest is a Glass Composite Material (GCM) waste form that was developed by Sandia National Laboratories; the U.S. Patent was recently issued.[1,2] It is an inhomogeneous composite assemblage of low temperature sintering Bi-Si-Glass, Ag flake, and iodine capture material (e.g., AgI-mordenite), see Figure 55.

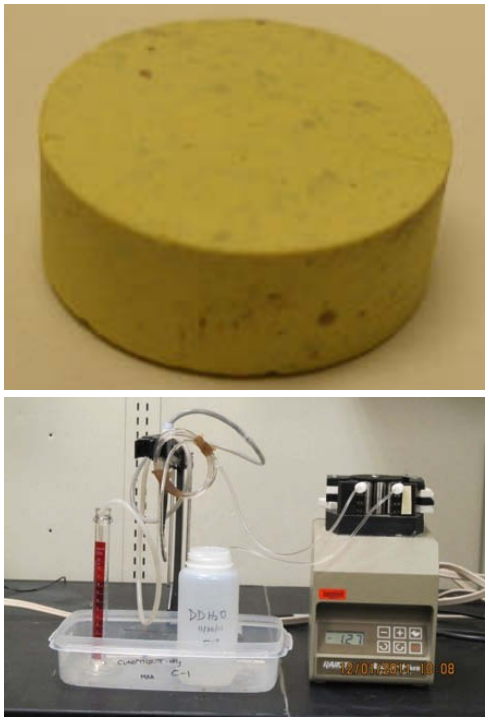

Figure 55. top, CGM of AgI-MOR/Glass/Ag, 0.5 inch diameter; bottom, Single Pass Flow Through Test set up.

In an effort to establish the baseline performance of this material, upon which to compare all other current and future iodine waste forms, it is important to establish both the chemical durability of the Bi-Si-Glass and the iodine release from the inhomogeneous GCM of AgI-MOR/Glass/Ag. Similarly, dissolution rates of the GCM can be compared against other candidate waste form materials, including ceramics, cement, and other glass compositions. Once overall waste processing steps are agreed upon, optimal capture and waste forms can be selected.

A Single Pass Flow Through[3] test was set up at SNL, see Figure 55. For the test, 2 grams of ground (to ≈ 1μm; surface area = 3.06 m^2/g) GCM was placed in 2 ml volume reactor. Test solutions were pumped 220-340 ml/day, and run at 25 and 35°C. Iodine is released from powdered AgI-Mordenite/Ag/Bi-Si-Glass waste forms at less than 10^{-16} mol/cm^2s at 25°C and pH = 3 and pH = 8, respectively. Bi-Si-Glass dissolves at rates similar to, and possibly lower than, traditional nuclear waste glasses. Glass degradation rates increase with distance from pH~6 in either direction, similar to nuclear waste glasses. Iodine release is lower at pH 3 than at pH 8. Temperature has a relatively small effect on both glass degradation and Ag and I release; maximum glass dissolution activation energies are 30 kJ/mol (based on two points). A low-end pH, and temperature- and pH-dependent waste glass rate law will conservatively bound dissolution of Bi-Si-Glass. The rate law for iodine release from powdered AgI-Mordenite/Ag/Bi-Si-Glass waste form is: Rate (mol/cm^2s) = 3.6 x 10^{-12}exp(-3608/T_k).

Initial baseline performance studies on our AgI-MOR/Bi-Si-Glass/Ag GCM (AgI-GCM) waste form indicate that the waste form behaves on par with known glass waste forms and in fact appears to dissolve more slowly than traditional nuclear waste glass (see Figure 56). Iodine release from our inhomogeneous GCM waste is less than that of the Si and Zn constituents that comprise the glass. However, researchers stress that these data are preliminary.

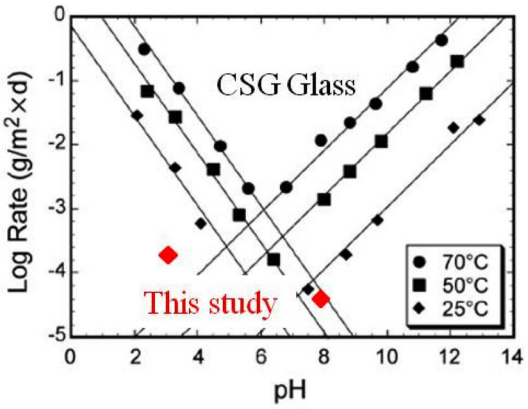

Figure 56. CSG glass degradation rates compared against silica release from AgI-GCM at 25°C and pH = 3 and 8, respectively. For normalization of GCM degradation rates to CSG rates, divide by 0.24 [4]

Follow-on and more detailed studies are required before full qualification of the AgI-GCM

waste form. After mixing, pressing and sintering the AgI-MOR + Bi-Si-Glass + Ag to form the waste form, the Ag and AgI is retained in the form of nanoparticles encapsulated in the glass, while the zeolite (MOR) is dissolved into the glass flux. Specifically, researchers will focus on better constraint of the mechanism of Bi-Si-Glass degradation; quantification of temperature dependence on degradation; establishment of controls over iodine release from AgI-MOR/Ag waste forms in isolation of glass; measurement of Bi-Si-Glass and AgI-MOR/Bi-Si-Glass/Ag degradation under unsaturated conditions; measurement of iodide sorption onto weathered Bi-Si-Glass. Further details are reported by Nenoff et al, in FCRD-SWF-2012-000172.[3]

References

1. Garino, T. J., T. M. Nenoff, J. L. Krumhansl, and D. Rademacher. "Low-Temperature Sintering Bi-Si-Zn Oxide Glasses For Use in Either Glass Composite Materials or Core/Shell 129I Waste Forms", J. Amer. Ceram. Soc. 2011, 94(8), 2412-2419.
2. Nenoff, T. M., J. L. Krumhansl, T. J. Garino, and N. W. Ockwig. "Low Sintering Temperature Glass Waste Form for Sequestering Radioactive Iodine", U.S. Patent 8,262,950, September 11, 2012.
3. Chou, L., and R. Wollast. Am. J. Science, 1985, 285, 963.
4. Nenoff, T. M., P. V. Brady, T. J. Garino, and C. D. Mowry. "Determination of Baseline Iodine Waste Form Performance Characteristics" Sandia National Laboratories, FCRD-SWF-2012-000172, June 20, 2012.

Patent Awards

1. Nenoff, T. M., J. L. Krumhansl, T. J. Garino, and N. W. Ockwig. "Low Sintering Temperature Glass Waste Form for Sequestering Radioactive Iodine", U.S. Patent 8,262,950, September 11, 2012.

Silicon Carbide for Iodine Immobilization

J. V. Ryan, joe.ryan@pnnl.gov*, W. Bennett, and D. Matson*

Background

Last FY, researchers showed that silicon carbide (SiC) is an ideal candidate for the immobilization of krypton. The same physical and chemical properties that make SiC a useful for structural components in fusion reactors[1-5], a barrier for fission product diffusion in gas-cooled fission reactors[6], and an inert matrix for the transmutation of plutonium and other TRU[7,8] also make it ideal for the immobilization of gaseous and mobile radionuclides such as iodine. Thermal diffusion of dopants in SiC requires extremely high temperatures because of the extremely low diffusivities for impurities in SiC. This low diffusivity for impurities is one of the reasons SiC is used as the fission product barrier in tri-structural-isotropic (TRISO) nuclear fuel and its use for this application has been demonstrated at temperatures over 2000 K.[9-11] Even the highly mobile helium generated in neutron-irradiated SiC is not released until temperatures above 1200 K.[12,13] Since industrial scale fabrication of SiC monoliths with physical vapor deposition (PVD) methods is a well-established technology[14-18], there is little, if any, technology development needed to produce dense, pure SiC.

Experimental Procedure

Expanding on the ion-assisted PVD technique that worked so well for the krypton immobilization proof-of-concept tests, a small PVD sputtering chamber (Figure 57) dedicated to this project was assembled from surplus components. A Lab Companion model ON-01E oven was purchased to enable heating of the thermally activated I_2 source within the gas stream. Three Metronics Dynacal I_2 sources with permeation rates of 2465.7, 5307.68 and 39615.6 ng/min were purchased. The SiC was deposited using a 3-inch diameter Saint Gobain SG-90 SiC sputtering target with a 3-in Mity Mak cathode powered by an Advanced Energy PE 5000 AC power supply operating at 0.8 amp and 340-380 volts. A Denton Vacuum GD-20 power supply with neutralizer was used with a CC-104 ion

source to add the ion assist capability. The ion source power load was 0.14 amp. The chamber was configured to sputter down with the Si substrate placed below the SiC target at a 3.75" gap. The ion source was angled at 30 degrees toward the substrate.

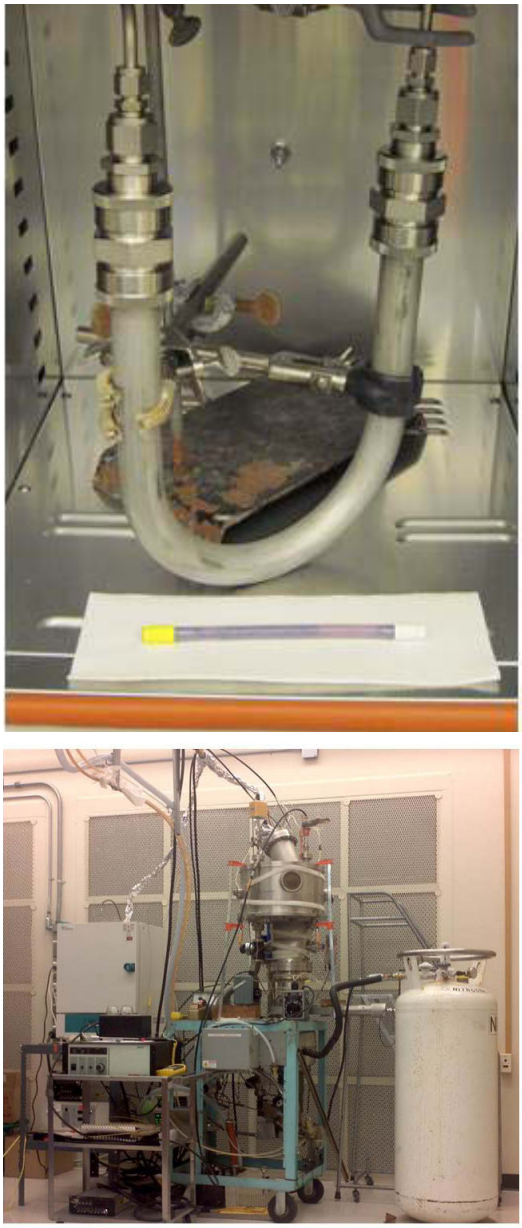

Figure 57. PNNL PVD Sputter Chamber with inset of oven interior showing sealed tube containing the thermally activated I_2 source.

Figure 58 is a schematic of the sputtering assembly. Heat tape was wrapped around the Ar/I_2 gas line to prevent I_2 from condensing in the gas line prior to entering the chamber. Coating chamber pressure during deposition was 3.6 mTorr with Ar or Ar/I_2 flow of 10 sccm. Preliminary testing of cathode and ion gun operations using pure Ar sputtering gas gave a deposition rate of 7.4 nm/min; similar to previous depositions done in our standard coating chambers.

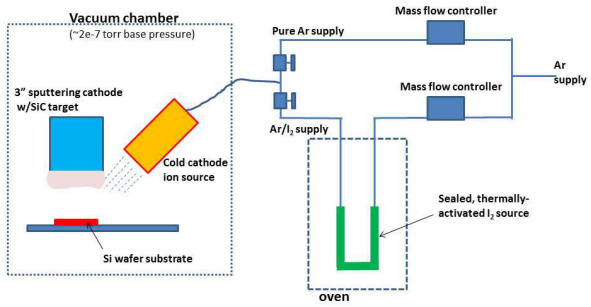

Figure 58. Schematic of the sputtering assembly.

Three depositions have been performed to date using the I_2 permeation sources (Table 8). In each case, a base layer of SiC was deposited using pure Ar to provide an adhesion layer to the Si substrate prior to the introduction of I_2 into the Ar stream. The first deposition, Run # 1G-K, utilized the 5307.68 ng/min I_2 source that thermally activated at 100°C. After the base SiC layer was deposited, the ion source was activated to start the ion-assist deposition (IAD) of SiC during which the oven and Ar/I_2 gas line were heated to 100°C. The IAD SiC deposition with Ar/I_2 was run for an additional 1 hr after reaching 100°C. The deposition rate was calculated to be 5.88nm/min for the IAD SiC Ar/I_2 layer. The second deposition, Run # 1H-K, used the same I_2 source as 1G-K. The only difference between the two coating runs was that the IAD SiC deposition was not started until the oven had reached 100°C. Because of this, the chamber was cooler when the Ar/I_2 was introduced. This may account for the low deposition rate of 2.19nm/min for the IAD SiC Ar/I_2 layer.

The third deposition, Run # 1I-K, utilized the 39615.6 ng/min I_2 source that thermally activated at 70°C. For this deposition, the oven and Ar/I_2 gas line began heating during the last third of base SiC in pure Ar deposition. The gas flow was switched to the Ar/I_2 line and the IAD SiC in Ar/I_2 deposition started. The calculated deposition rate was 3.95nm/min for the IAD SiC Ar/I_2 layer.

Table 8. Calculated deposition rates for Ar/I

Run #	Total Thickness, nm	Base SiC/Ar Thickness, nm	IAD SiC Ar/I_2 Thickness, nm
1G-K	855	502	353
1H-K	407	221	186
1I-K	948	379	569

Results

Energy dispersive spectroscopy (EDS) was performed on the samples to ascertain the presence/abundance of I_2 in the SiC deposit. Neither sample produced using the ~5K ng/min source showed evidence of iodine using this technique. The sample produced using the 40K ng/min iodine source, however, exhibited ~9.4 wt% I_2. In retrospect, if the deposition of iodine was simply a function of the iodine source concentration, the eight times more dilute iodine flow in the first tests would be expected to produce ~1 wt% iodine. This is near the detection limit of the energy dispersive analysis x-ray (EDAX), and more sensitive techniques are being applied to determine the final concentration of those samples. In addition, thermal desorption measurements will be completed with Rutherford backscattering to determine the stability of the immobilized iodine.

Although the full characterization has yet to be completed, researchers successfully demonstrated that iodine can be incorporated into a durable silicon carbide matrix, satisfying milestone M3FT-12PN03030914: Demonstrate iodine immobilization in SiC.

References

1. Fenici, P., et al., Current status of SiC/SiC composites R&D, J. Nucl. Mater. 258-263 (pt A), 215-225 (1998).
2. Nogami, S., et al., Compatibility between SiC and Li ceramics for solid breeding blanket system, J. Nucl. Mater. 386-388 (C), 628-630 (2009).
3. Zhao, J., et al., Microstructure and property of SiC coating for carbon materials, Fusion Engineering and Design 82 (4), 363-368 (2007).
4. Wong, C. P. C., et al., ITER-test blanket module functional materials, J. Nucl. Mater. 367-370 (1), 1287-1292 (2007).
5. Katoh, Y., et al., Current status and critical issues for development of SiC composites for fusion applications, J. Nucl. Mater. 367-370 A (SPEC ISS), 659-671 (2007).
6. Kim, B. G., et al., Multi-layer coating of silicon carbide and pyrolytic carbon on UO2 pellets by a combustion reaction, J. Nucl. Mater. 281 (2-3), 163-170 (2000).
7. Verrall, R. A., et al., Silicon carbide as an inert-matrix for a thermal reactor fuel, J. Nucl. Mater. 274 (1), 54-60 (1999).
8. Krstic, V. D., et al., Silicon carbide ceramics for nuclear application, Key Engineering Materials 122-124, 387-396 (1996).
9. Schenk, W., and H. Nabielek, High-temperature reactor fuel fission product release and distribution at 1600 to 1800C, Nucl. Technol. 96 (3), 323-336 (1991).
10. Schenk, W., et al., Fuel accident performance testing for small HTRs, J. Nucl. Mater. 171 (1), 19-30 (1990).
11. Nabielek, H., et al., Development of advanced HTR fuel elements, Nuclear Engineering and Design 121 (2), 199-210 (1990).
12. Sasaki, K., et al., Helium release and microstructure of neutron-irradiated SiC ceramics, Netherlands, 1991 (unpublished).
13. Sasaki, K., et al., Helium release from neutron-irradiated SiC containing 10B isotope, J. Nucl. Mater. 168 (3), 349-351 (1989).
14. Abe, K., et al., Characterization of polycrystalline SiC films grown by HW-CVD using silicon tetrafluoride, Thin Solid Films 516 (5), 637-640 (2008).
15. Jiangang, D., et al., Development of PECVD SiC for MEMS using 3MS as the precursor, from Silicon Carbide 2006-Materials, Processing and Devices. Symposium, San Francisco, CA, USA, 2006 (unpublished).
16. Saddow, S. E., et al., Effects of substrate surface preparation on chemical vapor deposition growth of 4H- SiC epitaxial layers,

Journal of Electronic Materials 30 (3), 228-234 (2001).

17. Moon, C. K., et al., Chemical-vapor-deposition growth and characterization of epitaxial 3C- SiC films on SOI substrates with thin silicon top layers, Journal of Materials Research 16 (1), 24-27 (2001).
18. Sugiyama, N., et al., Step structures and dislocations of SiC single crystals grown by modified Lely method, Journal of Crystal Growth 191 (1/2), 84-91 (1998).
19. Crum, J. V., B. J. Riley, L. R. Turo, M. Tang, and A. Kossoy. 2011. *Summary Report: Glass-Ceramic Waste Forms for Combined Fission Products,* FCRD-WAST-2011-000358, Pacific Northwest National Laboratory, Richland, WA.
20. Crum, J. V., L. R. Turo, B. J. Riley, M. Tang, A. Kossoy, and K. E. Sickafus. 2010. *Glass Ceramic Waste Forms for Combined Cs+Ln+TM Fission Products Waste Streams,* FCRD-WAST-2010-000181, Pacific Northwest National Laboratory, Richland, WA.
21. Crum, J. V., L. A. Turo, B. J. Riley, M. Tang, and A. Kossoy. 2012. "Multi-Phase Glass-Ceramics as a Waste Form for Combined Fission Products: Alkalis, Alkaline Earths, Lanthanides, and Transition Metals," *Journal of the American Ceramics Society*, 95(4):1297-1303. 10.1111/j.1551-2916.2012.05089.x.
22. Vienna, J. D., J. V. Crum, G. J. Sevigny, and G.L. Smith. 2012. *Preliminary Technology Maturation Plan for Immobilization of High-Level Waste in Glass-Ceramics,* FCRD-SWF-2012-000152, Pacific Northwest National Laboratory, Richland, WA.
23. Crum, J. V., C. Rodriguez, J. McCloy, J. D. Vienna, and C. Chung. 2012. *Glass Ceramic Formulation Data Package,* FCRD-SWF-2012-000139, Pacific Northwest National Laboratory, Richland, WA.

New Kr Adsorbents – Part 1 – INL Krypton Capture Accomplishments

T. G. Garn, troy.garn@inl.gov, M. R. Greenhalgh, and J. D. Law

Introduction

Accomplishments by the INL Kr capture effort can be segregated into three separate sub-sections which include: (1) The preparation and testing of a newly developed engineered form sorbent, (2) Collaborative research efforts with PNNL involving the testing of the Ni-DOBDC metal organic framework (MOF) and an initial attempt to make powdered chalcogel material into an engineered form using our binding process, and 3) An initial non-destructive analysis (NDA) gamma scan effort performed on the drum containing the Legacy Kr-85 sample materials. The following provides a brief description of each completed accomplishment.

Testing and Evaluation of Engineered Sorbents

Physisorption testing continued in FY 2012. A newly developed engineered form sorbent was prepared and tested in the custom designed experimental cryostat apparatus depicted in Figure 59. The apparatus is capable of testing sorbent masses ranging from 1g to 600g in a wide temperature range from 70 K to 650 K. The composition of the new sorbent consisted of a sodium mordenite converted to silver mordenite and bound with a macroporous polymer (AgZ-PAN). A patent application filed in early FY 2012 describes the preparation procedure for the newly developed engineered forms.[1]

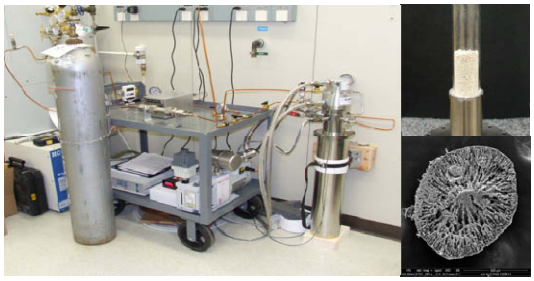

Figure 59. Cryostat test apparatus with photos of sorbent in column and EDS photo depicting material porosity.

Numerous test gas compositions were tested to determine resultant Kr and Xe capacities at 190 K and ambient temperature. Capacity results were then compared to a hydrogen mordenite sorbent prepared and tested in FY 2011(HZ-PAN). A final report published the findings for FY 2012 adsorption testing.[2,3] Table 9 includes the comparative capacity results for the two engineered forms at 190 K.

Table 9. Comparative capacity results for AgZ-PAN and HZ-PAN at 190 K.

Feed Gas	HZ-PAN Xe (mmol/kg)	AgZ-PAN Xe (mmol/kg)	HZ-PAN Kr (mmol/kg)	AgZ-PAN Kr (mmol/kg)
Kr/Xe/Air	795	468	7.4	5.3
Kr/Xe/N_2/He	636	429	7.7	8.3
Kr/Xe/He	1100	864	11	51
Kr/He	n/a	n/a	104	66
Xe/He	1460	756	n/a	n/a

The significance of this work is to develop highly porous novel sorbent materials with desirable adsorption characteristics that will provide Kr/Xe capacity data to support modeling efforts for design and scale-up of off-gas treatment plant equipment for nuclear reprocessing facilities. The necessity to contain radioactive emissions generated from volatile fission products protects the population and environment as driven by EPA regulation. The development of novel materials is driven by the need to replace the lack of available commercially engineered forms with high surface area characteristics. This potentially more viable and economic physisorption alternative can then be evaluated against the more complex cryogenic distillation process for potential nuclear off-gas treatment applications. The capture of stable Xe may also benefit from commercial marketability.

PNNL Collaboration Efforts

Collaborative efforts with PNNL off-gas sigma team members consisted of two subtasks involving the testing of the Ni-DOBDC metal organic framework (MOF) sorbent material for Kr and Xe capacity and an initial attempt to make powdered chalcogel material into an engineered form using our patent pending binding process.

The initial evaluation of the MOF material was completed. The capacity results for Kr and Xe at room temperature were reported to PNNL staff and considered to be in excellent agreement with initial PNNL results using their test method.[4]

The second task completed at the INL in FY 2012 was a scoping effort to bind chalcogel powders supplied by PNNL with our macroporous polymer into an engineered form. The chalcogel powder was successfully made into an engineered form with resultant spherical bead diameters of 1.5-2 mm (see Figure 60). As new materials are developed for capturing and immobilization of the volatile radionuclides, the requirement to use engineered forms is critical for process operation success.

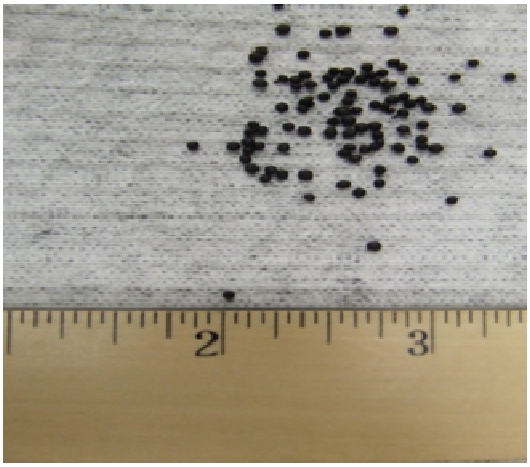

Figure 60. Photo of the engineered form of the chalcogel material.

Non-Destructive Analysis of Kr-85 Legacy Samples

Samples destined for disposal as a direct result of decontamination and decommissioning (D&D) of target Idaho Nuclear Technology and Engineering Center (INTEC; formerly the Idaho Chemical Processing Plant [ICPP]) facilities were secured, retrieved and stored for future use. These samples were generated from research efforts performed in the late 1970's to capture and immobilize Kr-85 on zeolyte 5A molecular sieve material and Hot Isostatically Pressed (HIPed) for waste form evaluations. The significance of securing theses samples is to eventually analyze the contents to retrieve historical Kr-85 decay information supporting waste form development needs, specifically to measure the effect of the build-up of the decay product rubidium on the adsorbent structure and overall performance after more than three half-lives of Kr-85 decay.

A Strategy for Analysis of Legacy Kr-85 Samples completed in FY 2011[5] documented a structured three-stage outline for analyses of the legacy samples. Stage one of the strategy was to obtain a gamma scan on the outer drum containing the samples. This gamma scan was completed in FY 2012 utilizing an ORTEC® Detective high purity Germanium detection system. As was expected, the prominent gamma emitting isotope present in this drum is Kr-85. Results from the gamma scan are also reported in the FY 2012 final report.[1]

New Kr Adsorbents – Part 2 – Metal Organic Frameworks

P. K. Thallapally, praveen.thallapally@pnnl.gov*, J. Liu, and D. M. Strachan*

Materials were developed and tested in support of the SWFC. Specifically, materials are being developed for the removal of xenon (Xe) and krypton (Kr) from gaseous products of nuclear fuel treatment. During FY 2012, three metal organic framework (MOF) structures were investigated in greater detail for the removal and storage of Xe and Kr from air at room temperature. In brief, metal organic framework (MOF) materials represent a new class of functional materials consisting of metal centers linked with organic building blocks to produce diverse and customizable structural frameworks These materials could augment the existing technology for the storage of ^{85}Kr in addition to the possibility of removing Xe and Kr from air at non-cryogenic temperatures — Kr is isolated in a MOF cage. One concern with the storage of ^{85}Kr in stainless-steel canisters at elevated pressures is the decay product rubidium (Rb). Rubidium is a corrosive liquid at projected ^{85}Kr storage temperatures. The use of MOFs augments this technology in two ways. First, it allows more gas to be stored in the canister at lower pressures. Secondly, the decay product Rb may be isolated from the metal canister, thereby reducing the corrosion concerns. In addition, if there is sufficient specificity that Xe and Kr could be separated from each other, then the inert Xe—the mass of which is 15 times that of Kr—would not need to be stored. Recent cost estimates indicate MOFs should have comparable costs when produced in bulk as other adsorbents.

Three benchmark MOFs—Ni/DOBDC, HKUST-1, and FMOFCu were studied for Xe and Kr adsorption with a dynamic breakthrough column method in FY 2012. These MOFs were selected for several reasons. First, all MOFs contain unsaturated metal centers, which are polar sites and estimated to be favorable for Xe and Kr adsorption. Second, the Ni/DOBDC is known to have high hydrothermal stability and higher Xe capacity than activated carbon. Third, the HKUST-1 has small aperture pores (0.5 nm) and pores with a larger diameter (15 nm) in the center, while the Ni/DOBDC has a uniform, 11-nm cylindrical pore. Investigating the effects of pore morphology on Xe and Kr selectivity for MOFs was interesting, both experimentally and theoretically. An important feature of FMOFCu is that 0.5 × 0.5-nm tubular cavities are connected through small (bottleneck) windows (0.35 × 0.35 nm) as shown in Figure 61.

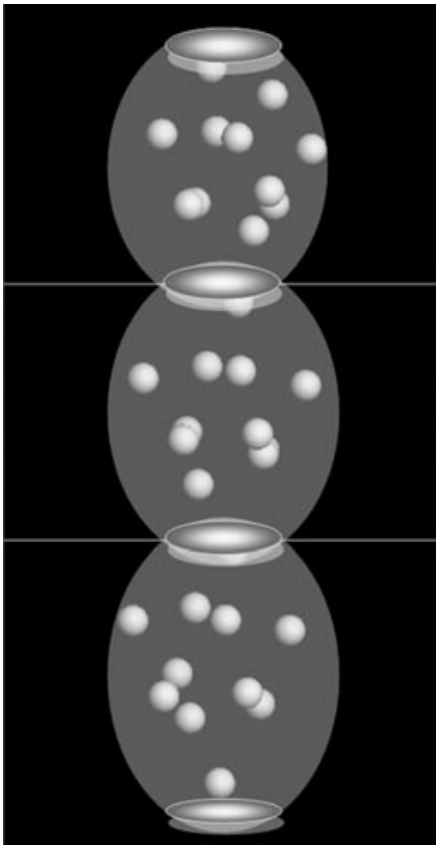

Figure 61. A schematic representation of the cavity and bottle-neck window structure of FMOF-Cu.

Although FMOFCu cages have a larger size than the kinetic diameters of Xe and Kr (0.396 nm and 0.360 nm, respectively), the research team selected this material because the connecting windows have dimensions practically similar (based on atom to atom distances) to the kinetic diameter of Kr and are smaller than the corresponding Xe diameter. Therefore, Xe diffusion into the cavities should be restricted; thus, FMOFCu should be more selective for Kr *via* molecular sieving than NiDOBDC and HKUST-1 where the connecting windows are much larger than the kinetic diameters of Xe or Kr. Breakthrough measurements on a nickel-based MOF indicate this material could capture and separate parts per million by volume (ppmv) levels of Xe (400 ppmv) from air with Kr (40 ppmv Kr, 78% N_2, 21% O_2, 0.9% Ar, and 0.03% CO_2) (Figure 62).

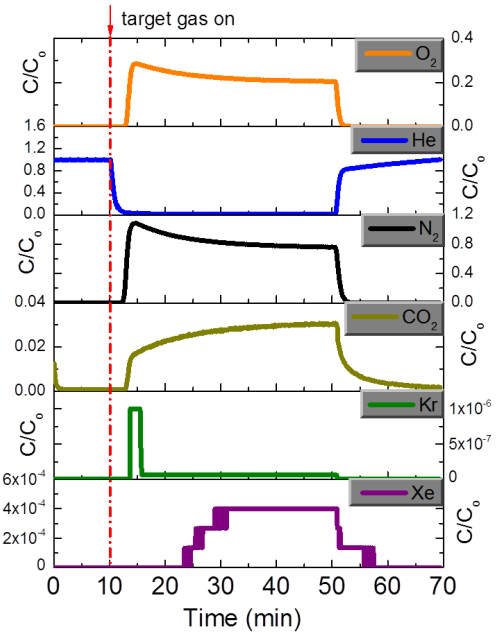

Figure 62. Xenon 400 ppmv and Kr 40 ppmv in air breakthrough curves at 25°C for the Ni/DOBDC. The flow rates are 20 sccm

Similarly, the selectivity of a fluorinated MOF can be changed from Xe > Kr to Xe < Kr simply by changing the temperature over a narrow range (-30°C) (Figure 63). Estimates were made for the cost of bulk quantities of MOFs and compared to other capture materials. For bulk quantities, these initial cost estimates showed that the costs were comparable.

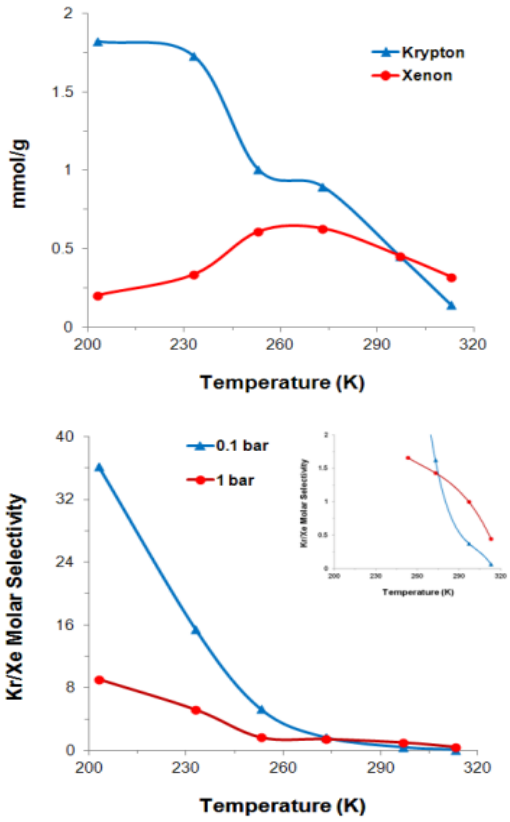

Figure 63. Adsorption of Kr and Xe as a function of temperature at 1 bar (top). The Kr/Xe selectivity in FMOFCu is inverted at 273 K (0ºC). Estimated Kr/Xe molar selectivities from pure gas isotherms as a function of temperature at 0.1 and 1 bar (bottom) (inset shows a 270–313 K temperature range).

Assessment of the Impact of Fuel Age on Capture Requirements for Volatile Radionuclides

R. T. Jubin, jubinrt@ornl.gov, D. M. Strachan, and N. Soelberg

Processing of UNF will result in the release of volatile radionuclides from the facility stack if no processes are put in place to remove them. The radionuclides that were of concern in this study were ^{3}H, ^{14}C, ^{85}Kr, and ^{129}I. The question researchers attempted to answer was how efficient must the removal process be for each of these radionuclides. To answer this question, researchers examined the three regulations that may impact the degree to which these radionuclides must be reduced before process gases can be released from the facility. These regulations are 40 CFR 61 (EPA, 2010a),

40 CFR 190 (EPA, 2010b), and 10 CFR 20 (NRC, 2012). The regulations apply to the total radonuclide release, the dose to the whole body, and the dose to a particular organ – the thyroid.

Because these doses can be divided amongst all the radionuclides in different ways and even within the four radionuclides in question, several cases were studied. These cases considered for the four radionuclides inventories produced for three fuel types – pressurized water reactor (PWR) uranium oxide (UOX), PWR MOX, and advanced high-temperature gas-cooled reactor (AHTGR) – several burnup values, and time out of reactor (herein "fuel age") extending to 200 y. Doses to the maximally exposed individual (MEI) were calculated with the EPA code CAP-88[5] and a set of referenceassumptions.

Two primary dose cases were considered. The first case, perhaps unrealistic, assumed that all of the allowable dose was assigned to the volatile radionuclides, neglecting the potential contributions from other, more sensitive, radionuclides. In lieu of this, as a second case a value of 10% of the allowable dose was arbitrarily selected to be assigned to the volatile radionuclides. The required DFs were calculated for both cases, including the case for the thyroid dose for which ^{14}C and ^{129}I are the main contributors. However, for completeness, for one fuel type and burnup, additional cases were provided, allowing 25% and 50% of the allowable dose to be assigned to the volatile radionuclides. The doses do not scale linearly for all fuel types because of the nucleonics of each fuel.

Because ^{3}H and ^{85}Kr have relatively short half-lives, 12.3 y and 10.7 y, respectively, the dose decreased with fuel age. One possible strategy for limiting the discharges of these short half-life radionuclides was to increase fuel age to take advantage of radioactive decay. Therefore, the doses and required DFs were calculated as a function of fuel age. In this document, given the above constraints and assumptions, researchers calculated the minimum ages for each fuel type that would not require additional effluent controls for the shorter half-life volatile radionuclides based on dose considerations. With respect to ^{129}I doses, researchers found that the highest dose was calculated with iodine as a fine particulate and scaled as the fraction of the total ^{129}I that was particulate. Therefore, researchers assumed for all of our calculations that 100% of the ^{129}I was particulate and allowed the user to scale our calculated doses to their needs. The working assumption was that since the CAP88 code looked at the stack discharge, this dose was down stream of the filters and had to have been formed by agglomeration or adsorption on another airborne particle.

Researchers also looked at several dose allocation cases to calculate a range of possible DFs. Allowing all of the allowable dose to be used by the volatile radionuclides is one bounding case. Subsets of this bounding case that were evaluated for select cases were (a) allowing the allowable dose to be partitioned somewhat evenly between the four volatile radionuclides and (b) allowing each volatile radionuclide to have up to 97% of the allowable dose, while the other three radionuclides were allocated only 1% of the allowable dose.

Researchers calculated the required DF values based on the whole body dose limiting case and thyroid dose limiting case and used the more restrictive of the two.

To summarize the data given in the body and appendices of this report, researchers present the data for the maximum DF values required to meet regulations in Table 10.

Table 10. Maximum DFs required for the volatile radionuclides of concern in this report

	Full dose allocation to volatile radionuclides			10% dose allocation to volatile radionuclides		
	PWR/ UOX	PWR/ MOX	AHTG R	PWR/ UOX	PWR/ MOX	AHTG R
^{3}H	25 (1 after 57 y)	160 (1 after 90 y)	42 (1 after 66 y)	600 (1 after 114 y)	720 (1 after 117 y)	585 (1 after 113 y)
^{14}C	1	1	4	10	15	30
^{85}Kr	9 (1 after 34 y)	4.2 (1 after 22 y)	9.2 (1 after 34 y)	18 (1 after 45 y)	13 (1 after 40 y)	62 (1 after 64 y)
^{129}I	380	630	650	3800	8000	6550

Figure 64 through Figure 67 show the minimum required DF values for ^{3}H, ^{14}C, ^{85}Kr and ^{129}I, respectively. These figures are based on the reference PWR UOX cases evaluated assuming that the full dose allocation was assigned to the four volatile radionuclides.

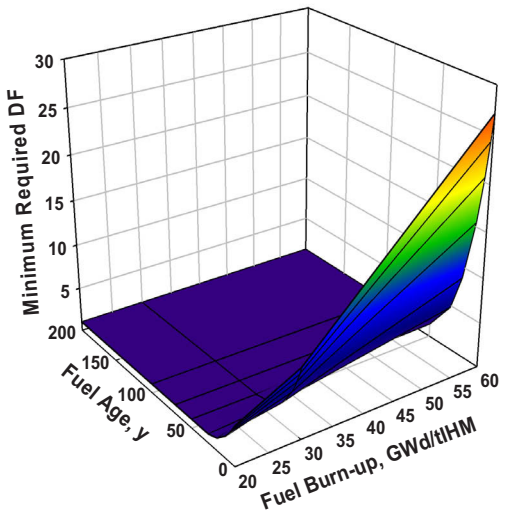

Figure 64. Minimum DF required for ^{3}H as a function of fuel age and burnup for a 1000-t/y recycle plant processing PWR UOX fuel.

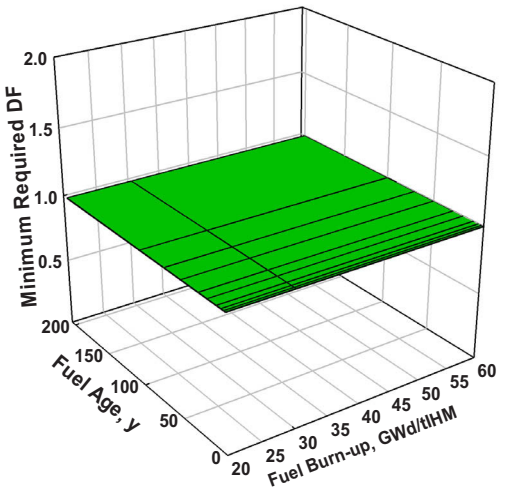

Figure 65. Minimum DF required for ^{14}C as a function of fuel age and burnup for a 1000-t/y recycle plant processing PWR UOX fuel.

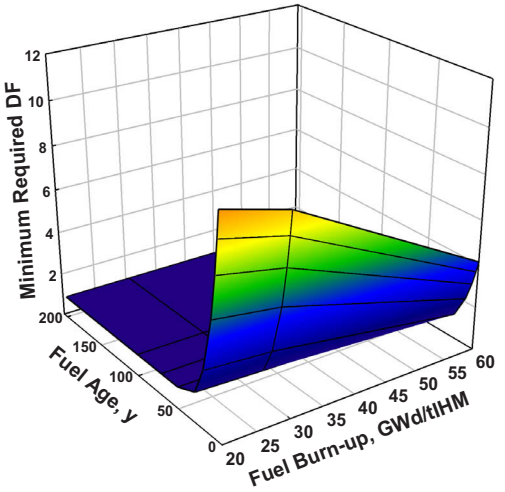

Figure 66. Minimum DF required for ^{85}Kr as a function of fuel age and burnup for a 1000-t/y recycle plant processing PWR UOX fuel.

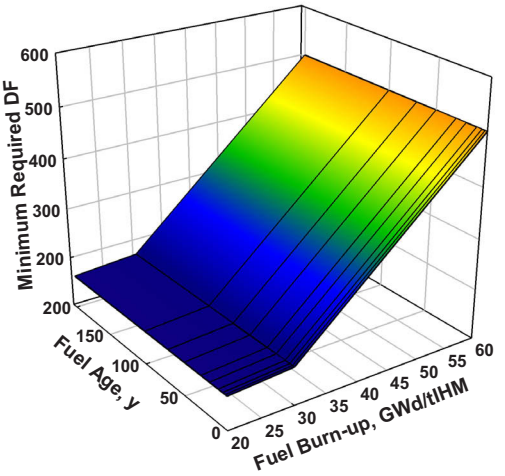

Figure 67. Minimum DF required for ^{129}I as a function of fuel age and burnup for a 1000-t/y recycle plant processing PWR UOX fuel.

The DF values shown in Table 10 and the four figures contained no engineering margin and could vary by a factor of 2 or more if different site-specific or reprocessing-facility-specific assumptions are used. In terms of establishing practicable target DF values for the capture processes under development, researchers believe that these should have been on the order of 3 to 10 times the values that result from a 25% to 50% dose allocation, that is, values that fall between those shown in the two major columns of Table

10, recognizing that at high enough fuel age the ^{85}Kr or ^{3}H control could be significantly reduced. These DF values are within the range of reported DFs for the available capture technologies for the volatile radionuclides.[3] Achieving the required ^{129}I and ^{3}H DFs is more challenging. While it can be argued that the 10% dose allocation is arbitrary, and it is, the full dose allocation is certainly too optimistic as other radionuclides will contribute to the total dose. The anticipated range is expected to be from 5% to 50% at the right half of the table. Further analysis into how potential emissions of other radionuclides in a used fuel can be controlled would have been required to refine this value.

It was clear from this study that it was possible to decrease the DF for one volatile radionuclide and increase the DF for one of the others while still maintaining the same dose to the MEI. With this in mind, it was not possible to arrive at a single target DF for one volatile radionuclide without taking into account the DFs for the other volatile radionuclides. The DF values required to limit the dose to the MEI were a function of the fuel age at the time of processing.

The sensitivity studies showed that several reprocessing facility design, operation, and location parameters can cause variations in the DF values calculated in this analysis.

- Varying stack height by a factor of 4 (from 37 m to 150 m) results in a factor of ~16 reduction in the dose to the MEI. The dose to the MEI decreases approximately as the square of the stack height.
- Changing the speciation of the ^{129}I from 100% particulate form to 30% to 70%, a range consistent with measurements from the Karlsruhe Reprocessing Plant, would reduce the ^{129}I dose to 30% to 70% of the 100% particulate value.
- Changing the stack gas velocity and temperature can affect the dose to the MEI by up to a factor of 2, depending on if the plume was momentum or buoyancy dominated, and if the stack gas velocity was varied by changing the stack diameter or the stack gas flow rate.
- Site-specific meteorological parameters can (a) cause the ^{3}H dose to vary by a factor of 2 depending on the humidity, (b) increase the dose from ^{14}C and ^{129}I by more than 10% in areas with higher precipitation, and (c) cause the dose from any of the volatile radionuclides to vary by more than 20% for different wind velocities.
- Site-specific agricultural parameters affect dose from ingestion. Changing from rural food sources to urban food sources, decreased the doses from those volatile radionuclides that play a role in the food cycle (^{3}H, ^{14}C, and ^{129}I) by 30–40%. The dose from ^{85}Kr was unchanged because it does not play a role in the food cycle.

Allowing the fuel to age before reprocessing allowed a decrease in the volatile radionuclide inventory, but only for the relatively short-lived isotopes – ^{3}H ($t_{1/2}$ = 12.3 y) and ^{85}Kr ($t_{1/2}$ = 10.73 y). However, to be effective, fuel ages would have to be on the order of 30 to 100 y, depending on fuel type and burn-up. Researchers calculated the required DF values and doses to the MEI for storage times extending to 200 y so that the user of the calculations provided here can assess this strategy. The benefit of long storage of fuel as a strategy for reducing reprocessing costs by reducing or eliminating the need to control emissions of short-lived volatile radionuclides must be evaluated against the costs of relatively long fuel storage and other impacts, such as on the recycle fuel value. Such a cost-benefit analysis was outside the scope of the current work.

References

1. EPA. 2010a. Chapter 40. Environmental Protection Agency: Part 61–National Emission Standards for Hazardous Air Pollutants. Subpart H—National Emission Standards for Emissions of Radionuclides Other Than Radon from Department of Energy Facilities, 92 - Standard. 40CFR61.92. U.S. Environmental Protection Agency, Washington, DC.
2. EPA. 2010b. Protection of Environment: Chapter I–Environmental Protection Agency (Continued), Part 190_Environmental

Radiation Protection Standards for Nuclear Power Operations. 40CFR190.10. U.S. Environmental Protection Agency, Washington, DC.

3. Gombert, D. 2007. Global Nuclear Energy Partnership Integrated Waste Management Strategy Waste Treatment Baseline Study - Volume I, GNEP-WAST-AI-RT-2007-000324, (September 2011).
4. NRC. 2012. Chapter 10, "Energy: Part 20 - Standards for Protection against Radiation," 10CFR20. U.S. Nuclear Regulatory Commission, Washington, DC.
5. Rosnick, R. 2007. CAP88-PC Version 3.0 User Guide, Environmental Protection Agency, Washington, DC.

CHAPTER 7
FUNDAMENTAL SCIENCE AND METHODS DEVELOPMENT

CHAPTER 7: FUNDAMENTAL SCIENCE AND METHODS DEVELOPMENT

Leigh Martin, leigh.martin@inl.gov

Metal Corrosion Mechanisms

C. D. Taylor, cdtaylor@lanl.gov, X-Y. Liu, D. P. Moore, and D. G. Kolman (LANL); E. Kim and K. R. Czerwinski (UNLV)

The goal of this work package has been to elucidate the thermodynamic and kinetic properties of candidate alloy waste forms and provide a fundamental science basis for the development and validation of alloy waste form materials. Researchers have taken a structured approach to the understanding of metal corrosion mechanisms according to:

1. Elucidation of the properties of the native metal alloy and intermetallic bulk compounds and their surfaces.
2. Study of water and oxygen reactivity on alloy and intermetallic surfaces.
3. Calculation of cohesive energies of metal atoms on exposed metal surfaces and, subsequently, kinetic simulation of anodic dissolution processes.
4. Construction of models for passive oxide films.
5. Validation of models complementary characterization of Fe-Tc samples via Auger electron spectroscopy (AES).

In this first phase of the project, the surface properties of the candidate alloy waste forms were evaluated using the two predominant models for the computation of materials properties: periodic band-structure calculations and quantum chemical cluster models. Researchers have also extrapolated the results of these calculations to develop many-body potentials that were applied in molecular dynamics and Monte Carlo simulations of the corrosion response of alloy waste forms. The surface science characterization work performed alongside the modeling helps direct the models to focus on the most realistic representations. Publication in the peer-reviewed literature provides an important mechanism for validation and dissemination of our findings.

First-Principles Calculations of Binary Metal Systems Containing Tc

Bulk and surface properties of Tc- or Fe-rich portions of the Tc-Fe binary alloy phase diagram were computed using density functional theory (DFT). Supercell and slab models of the alloys represented bulk alloy states and surfaces, respectively. Tc and Fe were found to have minimal degrees of mixing in the parent phases, consistent with the experimentally derived phase diagram- intermetallic phases are preferred to solid solution. The influence of oxygen on surface phase stability was then studied, with no significant impact determined for surface segregation or mixing. Oxygen adsorption changes the ordering of surface facets in Tc, such that the pyramidal phase becomes lower in energy than the prismatic phase, even with low coverage of oxygen. No evidence for increased surface segregation upon oxidation was found for solid-solutions. A potential-pH surface Pourbaix diagram was derived for Tc and H, OH and O adsorbed sub-monolayers were shown to be precursors to oxide formation (Figure 68a). Tc and Fe have similar reactivites and properties in their parent phases, and hence, also in solid-solution.

This general approach was extended to Mo-Tc binary systems, using both periodic plane-wave constructions and quantum chemical calculations of Mo-Tc metallic clusters (Figure 68b). A reference database of materials properties relevant to the Mo-Tc binary was constructed. Consequently, a framework has been laid for more detailed atomistic simulations of the Mo-Tc binary system. The surface properties of Mo and Tc low-index surface planes and atomic clusters have been determined: Mo and Tc are well miscible and likely to be closely associated in candidate alloy waste forms.

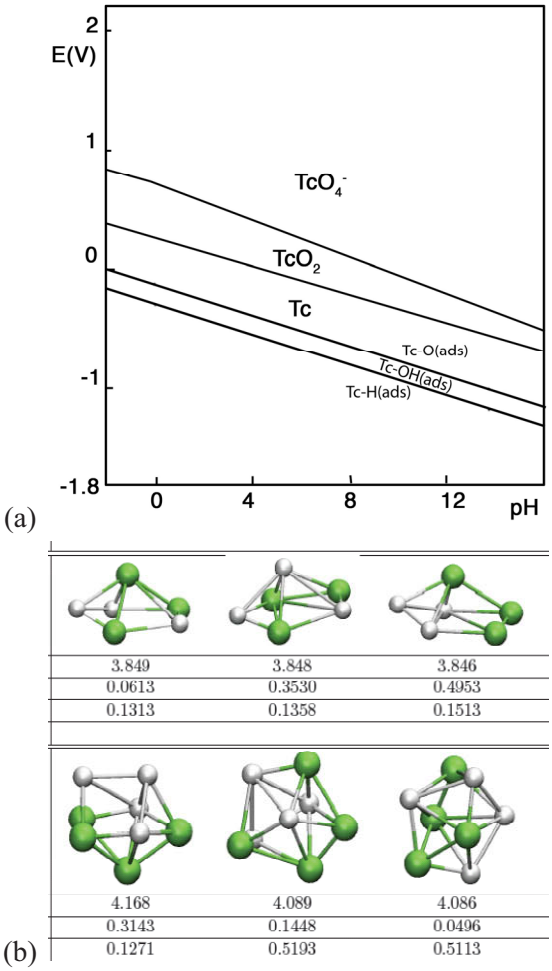

Figure 68. (a) Electrochemical phase diagrams generated using the technique developed by Taylor and Neurock for water over technetium (0001) surfaces; (b) MoTc clusters generated as part of the program to understand the nature of bonding and configurational dependence of MoTc binary alloy systems.

Development of Modified Embedded Atom Potential

Utilizing the DFT results, a modified embedded atom potential was constructed. The modified embedded atom method provides a way to study systems containing point, line and planar defects, which can be critical "weakest links", thus, serving as corrosion enablers in a material. The potential was then applied to molecular dynamics simulations of high surface area systems of iron-technetium alloys at high iron content, high technetium content and 50-50 Tc:Fe compositions (Figure 69a). Evaluation of the cohesive energy allowed us to make some inferences regarding relative corrosivity of Fe-Tc alloys as a function of surface configuration. The simulations indicated that local bonding arrangements are critical to the ultimate stability of exposed waste forms. Our analysis shows that the dependence of local cohesive energies on surface stability is not trivial, and that extra information must be taken into account (such as the relative ordering of the atoms, and their relative composition, see Figure 69b). A potential for the Mo-Tc system was developed in the same way, thus paving the way for more complex corrosion simulations to be performed on ternary Fe-Mo-Tc systems. Ni and Cr are also been included in current work.

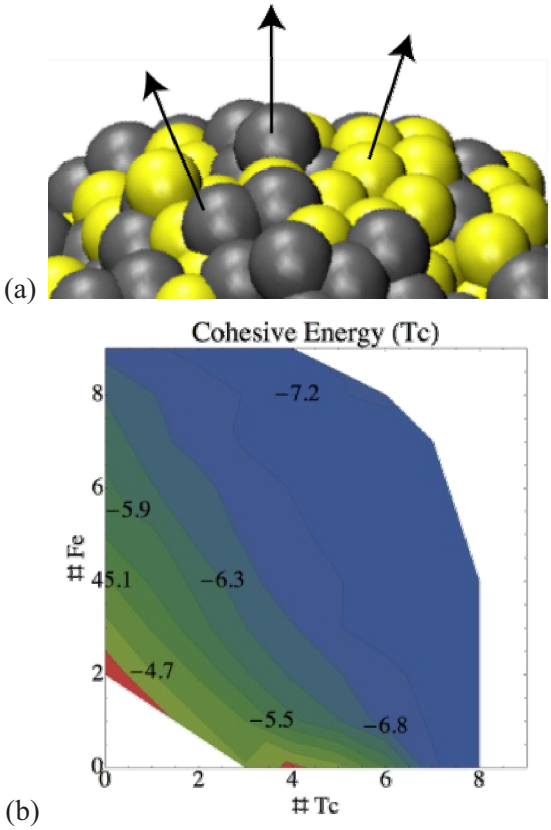

Figure 69. (a) Cohesive energies determine the relative stability of different metal atoms exposed on a candidate alloy waste form surface. (b) The instrinsic thermodynamic resistance of atoms to corrosion is a function of the number and type of nearest neighbors.

Kinetic Monte Carlo Simulations of Binary Alloy Systems

The modified embedded atom potential was applied to an innovative off-lattice kinetic Monte Carlo simulation of the active dissolution of the model alloy waste forms. The kinetic Monte Carlo

method provides a means for evaluating the types and relative severity of corrosion that such waste forms may experience as a function of composition, crystallography and surface orientation. The general scheme is illustrated in Figure 70a. Researchers found that the general suitability of Fe as a matrix for Tc depends on local phase ordering as well as alloy composition. This conclusion particularly addresses the mechanism of corrosion via active dissolution, which occurs during chemical or mechanical breach of the oxide layer.

Too much Tc destabilizes the alloy, with respect to dissolution, since Tc is destabilized in a body centered cubic lattice, preferring the hexagonally close packed phase. Further refinement of the Tc-Fe potential, using force-matching,[6,7] may be important as the current potential is fitted predominantly using the intrinsic parameters for Tc in the hexagonal close packed phase. On-going work is being performed to optimize this interaction. The mechanism of corrosion is different across distinct alloy systems and intermetallics, as seen by the types of corrosion morphologies generated by the simulations (Figure 70b).

Due to the differences in nobility between Tc and Fe, researchers find that, in the early stages of the simulation, Fe preferentially dissolves from the surface, leaving an enriched surface content of Tc. This data is consistent with electrochemical work performed at LANL on these systems,[8] as well as the formation of predominantly iron-oxide corrosion products on the reference alloy waste forms (RAW) synthesized and studied at INL.[9]

A future version of this model will be developed that includes the formation of oxide phases in a similar way to the kinetic Monte Carlo models developed by Legrand, et al.[10]

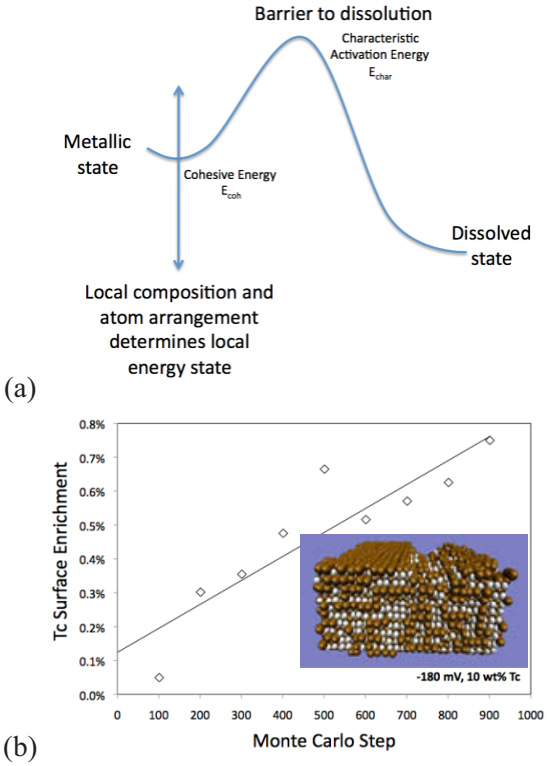

Figure 70. (a) Theoretical concept behind the relation used to estimate activation barriers from physics-based models, (b) Tc surface enrichment of the Fe solid-solution phase [Inset] Corrosion morphology obtained as outputs after the simulation of 1000 dissolution events for candidate alloy waste form.

First-Principles Calculations of Oxides of Binary Metal Systems

Researchers have proposed a general framework that consists of the four components of a corrosion system: (a) metal surfaces and bulk properties; (b) oxide properties including compatibility of alloy components with the predominant oxide films; (c) the metal/oxide interface, which can control transport properties and limiting film thickness; and (d) the oxide/environment interface, which controls corrosion rate under general corrosion conditions.

Accordingly, DFT was used to compute structural properties of Tc oxides including TcO, TcO_2, TcO_3, and Tc_2O_7. Our findings indicated that TcO_2 is the most energetically favorable form of Tc oxides, followed by Tc_2O_7. The results also showed that while TcO_3 can be plausible according to the calculated formation energy per oxygen atom, TcO is least energetically favorable. These results are consistent with surface science

studies performed to support this program at LANL. The flexibility of Tc to adopt multiple oxidation states suggests that it can be readily incorporated into oxide phases, indicative that Tc will be compatible with multiple oxide phases that form during corrosion of alloy waste forms.

The study of iron-technetium binary oxides is consistent with this result. Density functional calculations indicate that various oxides — magnetite, hematite and TcO_2 — will form depending on electrochemical conditions. Technetium incorporation into iron-oxides leads to lattice expansion, thus, technetium in iron oxide will likely be associated with free-volume defects, including vacancies, dislocations and grain boundaries. Researchers have also computed the energy of incorporation for Tc into iron oxides. Negative incorporation energies indicate that technetium, as a minority element, can incorporate into the predominantly iron oxides likely to be present on candidate alloy waste forms.

Physical properties of three spinel systems have also been investigated using DFT. While $MgAl_2O_4$ is a nonmagnetic wide-band gap insulator, both $TcCo_2O_4$ and $TcMg_2O_4$ are predicted to be metallic ferromagnetic materials (Figure 71). In future investigations, researchers will study spinel structures that can be expected to form given the compositions proposed for candidate alloy waste forms. Spinels may provide an additional means to optimize the incorporation Tc charge states into the oxide lattice.

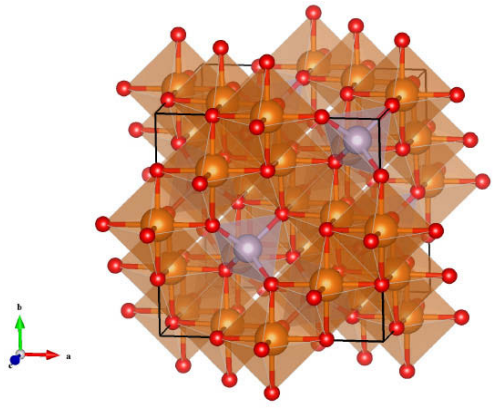

Figure 71. Cubic unit cell of stoichiometric AB_2O_4 spinel (Fd-3m, IT No. 227, Z=8). The Tc atoms (grey) and Co atoms (orange) occupy the tetrahedral sites and the octahedral sites, respectively.

Surface Science Characterization

Surface science techniques such as AES, Auger depth profiling, and orientation imaging microscopy (OIM) were applied to obtain fundamental corrosion and oxidation properties of candidate Tc alloy waste forms. AES reveals elemental and chemical state information of the materials under investigation. The technique is surface sensitive, in that it only probes the top few nanometers of the sample surface, and it is performed in a carefully controlled ultra-high vacuum (UHV) environment (based pressures of 2.5×10^{-10} Torr). Auger depth profiling is a technique where AES is combined with a surface-bombardment technique that removes surface layers sequentially. Characterization of the freshly exposed surfaces then allows the composition of the sample to be measured as a function of depth. Finally, OIM provides characterization of grain-size and orientation, including faceting and orientation of grain-boundaries. These techniques allow us to understand the nature of the candidate alloy waste form surfaces, which will benefit both the modeling portions of the program, as well as the development of electrochemical corrosion mechanisms.

Initial AES studies were performed on pure technetium metal to determine the baseline spectroscopy for the elemental technetium. Researchers have also considered the response of the system upon exposure to an oxidizing (O_2) environment. The AES results for Tc and the Tc exposed to oxygen are shown in Figure 72. The spectrum for Tc metal shows three sharp peaks with the main peak position at 245 eV. Controlled oxidation by O_2 (<100 Langmuir) shows the change in spectrum that occurs due to the formation of the oxide film. The Tc peaks broaden, and peak corresponding to oxygen appear around 500 eV. The results indicate that there is the formation of a nominal TcO_2 oxide layer on the metal surface. The relative peak heights, positions and peak shapes are consistent with an oxide of this stoichiometry (TcO_2). The baseline peaks generated for Tc and TcO_2 will be used to reference future studies with air and/or water vapor exposures at different temperatures.

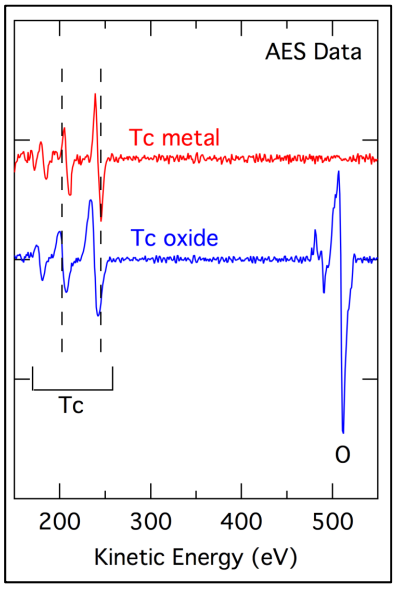

Figure 72. Auger electron spectra produced for technetium metal and technetium oxide formed upon exposure of technetium metal to oxygen under UHV conditions.

Recommendations for Waste Form Development

1. *New Experiments.* Researchers suggest two pathways for further experiments on these alloy waste forms. First, researchers propose additional characterization for the alloys being generated using electrochemical impedance spectroscopy (EIS) and ellipsometry to characterize the oxide films. Second, researchers recommend further accelerated corrosion testing to evaluate potential for loss of intermetallic precipitates (small particles embedded in a corroding Fe solid-solution matrix) and leaching out of Tc from the solid-solution phase into an aqueous medium.
2. *New Modeling Efforts.* Further development of the theory of impurity dissolution out of solid-solution and intermetallic phases using the kinetic Monte Carlo model, but further understanding the mechanism of dissolution to clarify some of the assumptions introduced in the model's development. New modeling should also begin to integrate the role of the oxide film: A theoretical understanding of oxide/environment effects is also critical to the long-term corrosion resistance of these alloys.
3. *New Waste Form Concepts.* Looking to the future, awareness of the complete corrosion mechanism will suggest active corrosion mitigation strategies. Possibilities researchers suggest for further exploration include barrier coatings that reduce mass-transport across the metal/environment interface, and Galvanically favorable composite materials (such as Ni/Tc).

References

1. Kohn, W., and L. J. Sham, Phys. Rev., 1965. 140: p. A1133.
2. Hohenberg, P., and W. Kohn, Phys. Rev., 1964. 136: p. 864B.
3. Baskes, M. I., and R. A. Johnson, Modified embedded atom potentials for HCP metals. Model. Sim. Matls. Sci. Eng. , 1994. 2(1): p. 147-163.
4. Lillard, R. S., G. F. Wang, and M. I. Baskes, The Role of Metallic Bonding in the Crystallographic Pitting of Magnesium. J. Electrochem. Soc., 2006. 153: p. B358.
5. Erlebacher, J., J. Electrochem. Soc., 2004. 151: p. C614.
6. Taylor, C. D., Cohesive relations for surface atoms in the iron-technetium binary system. J. Metallurgy, 2011. 2011: p. 954170.
7. Lee, B.-J. and M. I. Baskes, Second nearest-neighbor modified embedded-atom-method potential Phys. Rev. B, 2000. 62(13): p. 8564-8567.
8. Kolman, D., et al., Corrosion and passivity behavior of technetium waste forms, in Corrosion - National Association of Corrosion Engineers2011: Houston, TX.
9. Ebert, W. L., et al., FY 2010 Status Report: Developing an Iron-Based Alloy Waste Form, in Fuel Cycle Research and Development 2010, Argonne National Laboratory: Chicago, USA.
10. Legrand, M., et al., Three-dimensional modeling of selective dissolution and

passivation of iron-chromium alloys. Corr. Sci., 2002. 44: p. 773-790.

Thermodynamics and Kinetics of Solvent Extraction

L. Martin, leigh.martin@inl.gov

As with previous years, the Thermodynamics and Kinetics program has been a multi-national laboratory research effort including INL as the lead, Lawrence Berkeley National Laboratory (LBNL), Savannah River National Laboratory (SRNL) and ANL.

Through the combined efforts of these four laboratories, the behavior of the actinides and lanthanides in SX separation systems is being studied at a fundamental chemical level. To fully understand the factors driving the observed separations, a combination of theory and experimentation is being employed to develop a deeper understanding of the mechanisms behind these difficult separations and perhaps lead to new improved separations systems or at least more accurate models required for scale-up.

Idaho National Laboratory

The role of DTPA in trivalent actinide/ lanthanide separations has been growing recently with it implicated in TALSPEAK, modified versions of TALSPEAK and the TRUSPEAK process. To understand the mechanistic role of DTPA in any actinide/ lanthanide separations process, structural information for DTPA-metal ion complexation is required. Typically, this information is derived from precipitating crystals of interest; however, unlike ethylenediamine tetraacetic acid (EDTA), DTPA-metal complexes are extremely difficult to crystallize. This creates the challenge of studying these complexes in solution and using solution chemistry techniques and molecular modeling to develop structural models. In FY 2012, researchers began synchrotron based extended X-ray absorption fine structure (EXAFS) studies to investigate the structural properties of lanthanide-DTPA complexes in aqueous solution. Figure 73 shows the k^2 weighted EXAFS spectra and the Fourier Transformed data for Eu-DTPA at pH 3.5 in aqueous solution. Visual inspection of the Eu^{3+} and Tb^{3+} spectra show only very small differences in the data recorded. This qualitative result suggests that the coordination environments around both the Eu^{3+} and Tb^{3+} metal ion centers are the same despite the change in ionic radii.

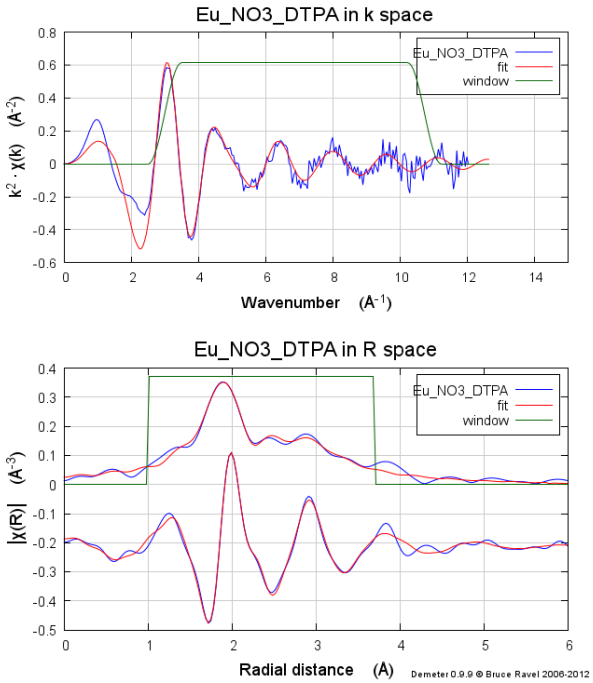

Figure 73. Eu L_{III}-edge EXAFS spectrum (k^2 weighted, top) of $Eu(NO_3)_3$ with Na_5DTPA at pH 3.5 in aqueous solution, fitted to $[Eu(DTPA)(H_2O)]^{2-}$, and Fourier transform in R space (bottom; upper plot generated from the real part of χ(R), lower plot generated from the imaginary part of χ(R)). Blue lines represent the experimental data and red lines the fit. Green line represents the area over which the fit is performed on the data.

The experimentally measured interatomic distances in these studies appear to be shorter for Ln^{3+}-DTPA coordination than previous literature reports suggest, with the Tb^{3+} complexation results showing the largest discrepancies. Although the N and O bond lengths are shorter than expected, the distances between the oxygen atoms and nitrogen atoms appear to be comparable to those predicted by molecular modeling, suggesting DTPA is coordinated in the same manner but shifted closer to the metal ion. The reported Debye-Waller (DW) factors, relating to the thermal disorder in the structure under study, were higher than expected for the DTPA-metal distances only suggesting that the DTPA binding/ exchange mechanism is considerably more complex, and perhaps more dynamic, than previous considerations. Further

study on these systems is required to fully understand the exchange dynamics of DTPA and the metal ions, structural studies alone will not produce these data.

In addition, researchers have demonstrated the direct measurement of the enthalpies of extraction using two-phase calorimetry for solvating extraction systems. This work successfully expanded the two-phase calorimetric methods developed by Zalupski and Nash. The method was developed following the extraction of europium nitrate with TOPO in toluene. A sample heat trace can be seen in Figure 74.

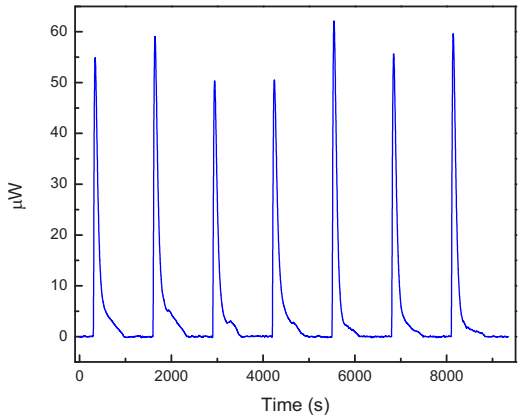

Figure 74. Power trace for the extraction of 0.025 M $Eu(NO_3)_3$ with TOPO.

Validation of the method was performed by measuring enthalpies of extraction of europium at different metal ion concentrations confirming the presence of one process during the titrations, the biphasic extraction of the europium nitrate complex to the organic phase. The $\Delta H_{extraction}$ for this system was calculated to be -34.3 ± 2.2kJ/mol. This is a reasonable result and within the excepted range reported in the literature. The greatest advantage of using calorimetry to measure these types of processes is the sensitivity of the instrument. It allows system adjustments to ensure enthalpy measurements of the metal ion extraction and not composite enthalpies of extraction (i.e., co-extraction of HNO_3 molecules).

In FY 2012, the dye xylenol orange was optimized for DTPA complexation kinetics studies with europium. This work was performed as a collaborative study with Prof. Stephen Mezyk at California State University – Long Beach (CSULB). This research was completed by utilizing a rapid-mix stopped flow UV-visible spectrometer. It was determined that the complexation kinetics for the reaction of DTPA with Eu^{3+} at pH 3.6 and 26.1°C was found to be $k_1 = (5.36 \pm 0.28) \times 10^4$ M^{-1} s^{-1}. This reaction rate is slightly faster than the result obtained for Eu-DTPA complexation determined by Martin et al. in FY 2010, $(3.06 \pm 0.36) \times 10^4$ M^{-1} s^{-1}, when using Arsenazo(III) as an indicator. This could be an indication the choice of dye in these studies has an effect on the measured rate; however, to determine this with any certainty further measurements with other metal ions is required. It is expected that in FY 2012, using the methodology developed here, these experiments will be expanded to encompass a range of lanthanide ions from La^{3+} to Lu^{3+}. Expanding this study will further develop the understanding of the importance of ionic radii and coordination number in the complexation reactions

Savannah River National Laboratory

One of the focuses of the FY 2012 research at SRNL was to understand the structures and stabilities of the aqueous phase complexes $[M^{III}(DTPA)\text{-}H_2O]^{2-}$ (M = Nd, Am) as well as the changes in Gibbs free energy for complexation in the gas phase and aqueous solution using DFT. To fully understand the chemical interactions that drive the separations, three different bonding analysis programs were used; Mulliken population analysis, Bader's Atoms-in-Molecules (AIM) approach, and Natural Bond Orbital (NBO) analysis. The results suggest that the preference of the $DTPA^{5-}$ ligand for Am over Nd is a subtle combination of effects. The electrostatic interactions draw the metal center close to the oxygen atoms, which in turn causes an increased covalency with the oxygen chelates. The nitrogen chelates provide an additional, yet small, covalent interaction but not nearly as pronounced as with the oxygen donor atoms. In other words, *both* the oxygen and nitrogen chelates may be necessary for separations. These results question the exclusive use of hard and soft acids and bases (HSAB) concepts for the design of extracting reagents and suggest that hard-soft interactions may play more of a role in the separations process than previously thought.

The basic reaction (1) for complexation can be written as,

$$M^{III} + H_5DTPA + H_2O \rightarrow [M^{III}(DTPA)\text{-}H_2O]^{2-} + 5H^+ \ (M = Nd, Am) \quad (1)$$

where M^{III}, H_2O, H^+ were optimized as the solvated species $M(H_2O)_9^{3+}$ (M = Nd, Am), H_8O_4 and $H_9O_4^+$, respectively. The change in Gibbs free energies in aqueous solution, ΔG^{o}_{solv}, can be obtained by the thermodynamic (Born-Haber) cycle as shown in Scheme 1 in terms of the free energy change in the gas phase, ΔG^{o}_{g}, and the solvation free energies of the products and reactants, ΔG^{o}_{s}. The overall reaction, as shown here, is characterized by the standard Gibbs free energy, ΔG^{o}_{solv}/kcal·mol^{-1}:

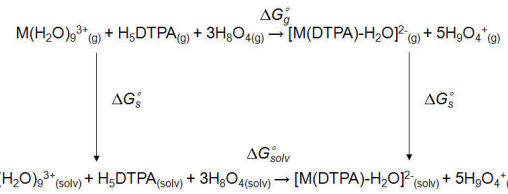

The optimized geometry, as shown using the Nd analogue in Figure 75, reveals that the coordination environment around the metal center can be defined as a distorted, monocapped, square antiprism. The non-capped base consists of the nitrogen atoms and O_1, and the remaining carboxylate oxygen atoms on the ligand form the capped plane wherein an inner sphere water molecule completes the coordination. This type of structure suggests a more hydrophilic region at the carboxylate side, in contrast to a hydrophobic region at the ligand backbone. Compared to experiment, the calculated bond lengths are longer (max ~0.1 Å) but within the standard deviation of DFT for an anionic complex with the only exception occurring with the Nd-OH_2 coordination. The optimized structures of the Nd^{III} and Am^{III} analogues are virtually identical, reflecting the similar ionic radii of both metal centers (i.e., 1.123 Å for Nd^{III} and 1.115 Å for Am^{III}). Calculated bond distances and angles of the ligand are essentially unaffected by the substitution of the metal center.

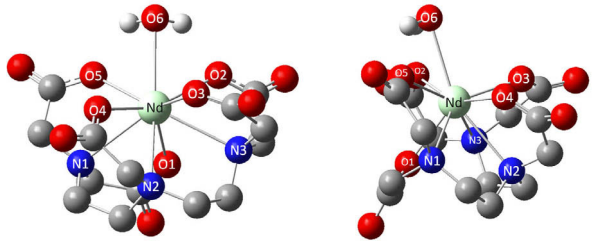

Figure 75. Front (a) and side (b) views of the optimized structure of $[Nd^{III}(DTPA)(H_2O)]^{2-}$. Hydrogen atoms on the DTPA ligand are removed for clarity.

Calculations for the free energy of complexation were based on the Born-Haber cycle in Scheme 1. The calculated changes in the Gibbs free energy in aqueous solution, ΔG^{o}_{solv}, is exergonic for both complexes with Am complexation preferred over Nd by more than 1 kcal·mol^{-1}. As expected, the calculated Gibbs free energies are similar in both the gas phase and solution because of the similar ionic radii. It is important to note that the predicted free energy difference for complexation is very small. The small energy difference in the ΔG^{o}_{solv} between the Nd and Am are rarely associated with dramatic changes in the molecular structure or properties. It is thought that weak covalent interactions between the "soft" Lewis base ligands such as nitrogen donors in $DTPA^{5-}$ and the actinides are the source for the observed complexing preference over the lanthanides. In order to understand the reasons behind preferred complexation, researchers examined the analysis results from the DFT calculations in hopes of understanding the nature of the interaction between the $DTPA^{5-}$ ligand and the metal centers (i.e., the covalency of the metal-ligand bond). To our surprise, all of the analysis methods predict that there is more covalency between O 2*p* than N 2*p* with americium. Researchers believe *both* the O and N atoms contribute to providing selectivity in the TALSPEAK process.

The present study provides a different interpretation to the preferred complexation of Am to Nd with $DTPA^{5-}$ than has been previously seen in other actinide complexes. Based on the above results, theory suggests that the preference of the $DTPA^{5-}$ ligand for Am over Nd is a subtle combination of effects: The larger radial extent of

the 5*f* orbitals causes a covalent interaction with preference for the oxygen chelates and the oxygen lone pairs are donating electron density into the formally empty 6*d* subshell to provide additional stabilization of the molecule. This interpretation is supported in combination by Mulliken population, AIM approach, and NBO analysis. In addition to that, a small amount of covalent behavior between the M-N bonds allows for additional stabilization of the Am complex.

Lawrence Berkeley National Laboratory

The primary focus of the research performed at LBNL in FY 2012 has been spectrophotometric titrations and fluorescence lifetime measurements to study the complexation of curium with the TALSPEAK ligands lactic acid and DTPA as a function of temperature. In addition to these measurements, the research performed has included measuring the heat of complexation between curium and these ligands. This thermodynamic data is not available in the open literature and is required for completing accurate models for any SX system.

Representative absorption and fluorescence spectra of the curium DTPA titrations at 25°C are shown in Figure 76. For the absorption spectra, as the concentration of the DTPA-metal ion complex increases, the intensity of the absorption bands of Cm(III) aqua ion decreases, and the corresponding absorption bands of Cm(III)-DTPA complex appear at longer wavelengths. With the presence of only one isobestic point observed during these titration experiments, it can be assumed that there is only one complex formed. This result is significantly different from the observations for Nd(III)/Eu(III) with DTPA. In these complexation systems there was evidence of the HDTPA-Nd(III)/Eu(III) species in the system. The formation constant of the Cm(III)-DTPA complex was calculated to be 21.3 ± 0.5 by analyzing the spectra collected at 25°C.

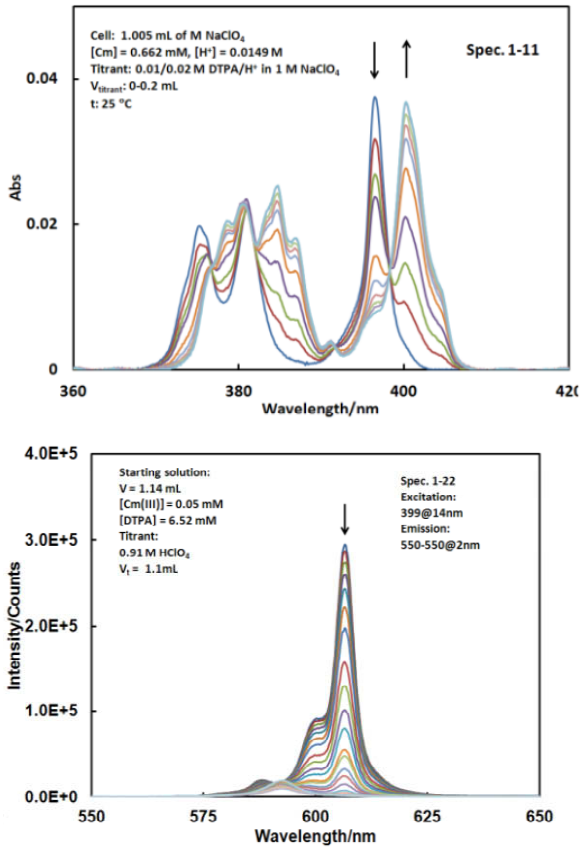

Figure 76. Representative absorption spectra (top) and fluorescence emission spectra (bottom) of Cm(III)/DTPA solutions at 25°C.

Figure 77 shows the fluorescence decay of Cm(III)/DTPA in the same set of solutions used for the measurements of the emission spectra shown in Figure 76 (bottom) at 25°C.

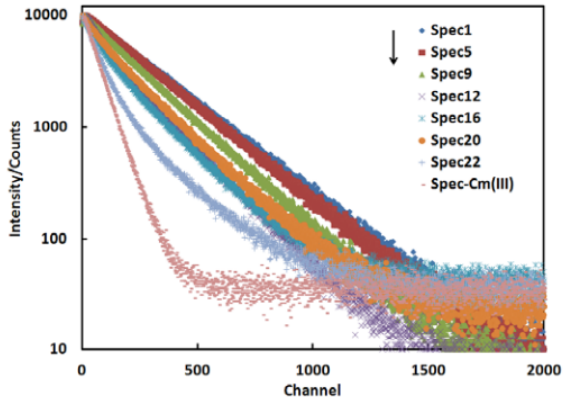

Figure 77. Fluorescence decay of Cm(III)/DTPA solutions..

As the concentration of H^+ is increased (from curves 1 to 22), more Cm(III) is disassociated

from the Cm(III)-DTPA complex and the fluorescence lifetime becomes significantly shorter. For some solutions, especially those at the higher acid concentrations, the decay is seen to be curved. As such, two exponential functions had to be used to fit the data to obtain the luminescence lifetimes (τ). This is an indication that the association/dissociation rates are relatively slower than those of the Eu(III)-DTPA system. This could be important in relation to the mechanism of extraction that drives the TALSPEAK process. By using the lifetime data from this work and the previously established linear correlation between the fluorescence lifetime and the hydration number of Cm(III) ($nH_2O = 0.63 \times \tau^{-1} - 0.29$), the hydration number of Cm(III) in the Cm-DTPA complex, was determined to be 2.05 ± 0.5, which is significantly different from the value of 1 for the Eu(III)-DTPA complexes.

The enthalpies of the complexation of Cm(III) with DTPA were determined using isothermal isothermal titration calorimetry. The measured reaction heats by microcalorimetry were used, in conjunction with the protonation and complexation constants, to calculate the enthalpies of the complexation with the computer program HyperΔH. The overall reaction was seen to be exothermic, and from the results of multiple titrations with varied Cm(III) and ligand concentrations, the enthalpies of the complexation of Cm(III) with DTPA is calculated to be -40.7 ± 2.1 kJ/mol with the formation constants measured above.

Argonne National Laboratory

The research at ANL has built on FY 2011 work in using microfluidic devices to study the kinetics of extraction in separations systems such as TALSPEAK and ALSEP. Particular focus has been paid to the stripping kinetics of americium and europium in the ALSEP process. In addition to the kinetics measurements highlighted above, the researchers at Argonne have also begun to develop a new microfluidic device that will potentially allow for oxidation state control during separations. Figure 78 shows the three piece microfluidic chip that was fabricated from two titanium chip plates sputter coated with platinum and a non-conductive FFKM perfluoroelastomer gasket to define the channel height. The top and bottom chips are used to allow electrical contact directly with the solution. The FFKM gasket insulates and separates the two electrodes.

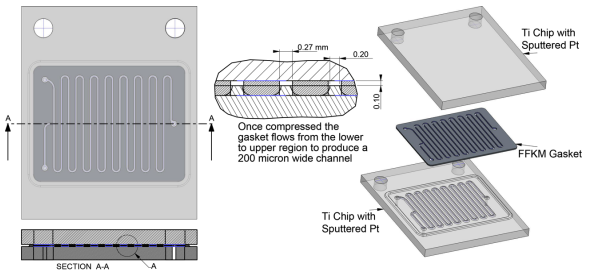

Figure 78. Schematic of the new microfluidic device to allow oxidation state control during separations

By designing a "microfluidic electrode chip" it is hoped that externally obtained oxidation states, such as AmO_2^{2+}, will be able to be maintained during kinetic analysis. This has been a particular problem that has beset research into the use of higher oxidation states of americium for SX purposes. The development of this chip may also allow for investigating the effects of controlled oxidation or reduction of metal ions during a separations process.

The fabricated chip has already been tested for the online oxidation of Ce(III) nitrate in 1 M HNO_3. The Ce(IV)/Ce(III) redox potential in 1 MHNO_3 is 1.61 V, making the couple an appropriate "cold" probe for oxidation of the actinides like Pu. In these initial tests, a significant amount of Ce(IV) was observed using UV-Vis spectroscopy after oxidation on the chip.

This microfluidic electrode chip possesses a great potential for radioanalytical applications, where a quick in-line separation of the actinides is necessary to monitor the process conditions. Also, it can be used for testing of SX chemistries with An, considering very small amounts of the actinides needed to conduct the experiments. The development of this chip will be continued into FY 2013.

Fundamental Radiation Chemistry

B. J. Mincher, bruce.mincher@inl.gov

During SX for fuel cycle applications the aqueous and organic phases are irradiated with both high LET α and low LET β/γ radiation. The deposition of this energy results in adverse effects

including degradation of ligands and changes in SX efficiency, production of radiolysis products that complex metals to decrease separation factors, and possible changes in physical characteristics of the solvent due to viscosity changes noted earlier. Components of the solvent must also have adequate radiolytic stability to ensure solvent recycle potential. The ligand decomposition yield should be sufficiently low, and the nature of the decomposition products sufficiently benign, that significant process efficiency is not lost with time and absorbed radiation dose. Therefore, a major effort in the separations campaign has been invested in understanding radiation chemical mechanisms in aerated, biphasic, acidic systems containing the ligands of most importance to the proposed future fuel cycle. Once reaction mechanisms are known, steps to mitigate damage may become possible. To fully elucidate reaction mechanisms, a program composed of a strong steady state α and γ radiolysis component, a pulsed radiolytic kinetics component and state-of-the-art analytical support are all needed.

All the program components above were used during FY 2012; however, the highlights in this report will concentrate on significant developments in α-irradiation techniques and the mass spectrometric identification of radiolysis products. A major effort was devoted to the development of α-irradiation techniques, for comparison to the γ work that has become routine for our program. To address this, α-irradiation of CMPO samples was performed using three techniques. The first was by He-ion beam irradiation. Helium ions were produced using a 9 MV FN-Tandem Van de Graaff generator with a 20 KeV plasmatron source, at the University of Notre Dame Radiation Laboratory. Particle energy was selected by varying the accelerator terminal voltage, with sufficient energy such that after passing through the cell window into the sample their energy was approximately 5 MeV. This was designed to simulate the α-particle energies produced by actinide decay.

In the second technique, CMPO samples were irradiated using ^{244}Cm, in a glovebox at INL. Curium decays by emission of a 5.8 MeV α-particle with an 18.1 y half-life. The low acid concentration was selected to minimize the extraction of curium into the organic phase, however, post-extraction organic solutions were still found to be contaminated and it was not possible to perform analyses for degradation products, although researchers have performed high pressure liquid chromatography (HPLC) to determine a CMPO *G*-value for these samples.

In the third technique, samples were irradiated with ^{211}At at Chalmers University, Göteborg, Sweden. Astatine-211 decays with the emission of an average 6.8 MeV α-particle with a 7.2 h half-life. Thus the absorbed dose to the sample is readily calculated assuming that all atoms of astatine decay prior to the analysis of the solutions. Astatine was prepared at Rigshospitalet, Copenhagen, Denmark, using a Scanditronic MC32-NI cyclotron, and delivered to Chalmers by courier. Upon receipt of the solid target it was dissolved in acid, and extracted into isooctanol solution. Small volumes of this solution were used to spike the CMPO samples for irradiation.

Figure 79 shows the degradation of CMPO versus absorbed dose, for both γ and α- irradiated samples. The density-corrected slopes of these curves are the yields of CMPO degradation ($-G_{CMPO}$). For the γ-irradiation of 0.1 M CMPO/dodecane in contact with an equal volume of 0.1 M HNO_3, the *G* value was consistent with that of pure organic solution, at about 0.18 μmol J^1.

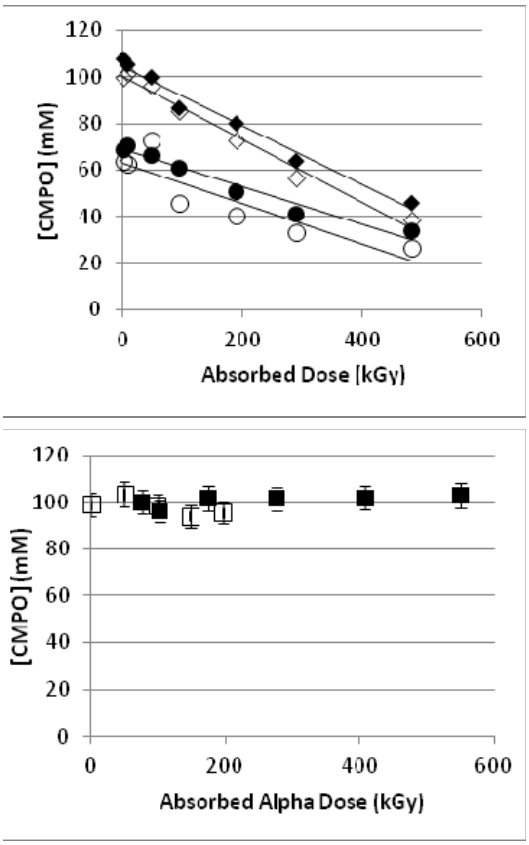

Figure 79. (top) The γ-radiolytic change in CMPO concentration for samples in the absence of the aqueous phase (closed diamonds); in contact with an equal volume of 0.1 M HNO_3 (open diamonds); in contact with an equal volume of 2 M HNO_3 (closed circles); an organic phase that was pre-equilibrated with 2 M HNO_3 (open circles). (bottom) The γ-radiolytic change in CMPO concentration for samples irradiated with ^{244}Cm in the presence of 0.1 M HNO_3 (closed boxes), and ^{211}At irradiation in the presence of a small but unknown amount of HNO_3 (open boxes). Error bars shown are ± 5%.

Also shown in Figure 79 are data for the γ-irradiation of 0.1 M CMPO/dodecane in contact with 2 M HNO_3, and for similar samples that had been pre-equilibrated with 2 M HNO_3. Pre-equilibration had the same effect on *G*-values as did contact with bulk 2 M HNO_3, and the rate of decrease in CMPO concentration (~ 0.11 μmol J^{-1}) was about half that for the neat CMPO solution. It can also be seen in Figure 79 that the initial CMPO concentration as determined by HPLC appears to be lower for the 2 M HNO_3-contacted samples. This is due to formation of the CMPO•HNO_3 complex, which was identified by mass spectrometry.

The decrease in CMPO concentration for initially 0.1 M CMPO/dodecane versus absorbed α-dose using isotopic sources is also shown in Figure 79. No change in CMPO concentration was detectable, using acid contacted isotope irradiated samples, even at absorbed doses in excess of 500 kGy. The results for the He ion beam irradiation of the pure organic phase was also performed, although only low absorbed doses could be generated by this method (data not shown). In the case of both aerated and de-aerated pure organic solution, there was again no change in CMPO concentration with absorbed dose due to He ion beam irradiations, to an absorbed dose of about 50 kGy.

A second major effort during FY 2012 was the development of state-of-the-art analytical techniques to measure the degradation products of irradiation. These techniques were also applied to α and γ-irradiated CMPO samples. The nature of the degradation products were found to depend on the presence or absence of nitric acid, and on the radiation type. ESI-MS techniques applied to 0.1 M CMPO/dodecane samples that were γ-irradiated in the absence of an aqueous phase identified octylphenylphosphinic acid as a product resulting from cleavage of the phosphorous-methyl bond. Researchers also identified phenyl-N,N-diisobutylmethylphosphine oxide, resulting from the loss of the octyl group. These compounds are probably responsible for the increasing distribution ratios measured when CMPO samples irradiated under these conditions are used in SX experiments, as shown in Figure 80.

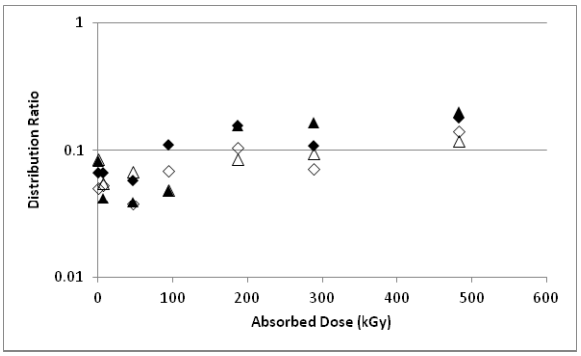

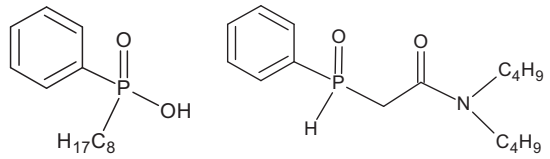

Figure 80. The SX (solid symbols) and strip (open symbols) distribution ratios of americium from 2 M HNO_3 for γ-irradiated 0.1 M CMPO/dodecane (diamonds) or for 0.1 M CMPO/dodecane γ-irradiated in contact with 0.1 M HNO_3 (triangles). The samples were diluted to a CMPO concentration of 0.016 M prior to the extraction contacts. Also shown is the structure of octylphenylphsophinic acid (top) and phenyl-N,N-diisobutylmethylphosphine oxide (bottom); the products identified by ESI-MS believed responsible for the increasing distribution ratios.

Different products were identified for CMPO γ-irradiated in the presence of HNO_3. When ESI-MS was performed on CMPO samples γ-irradiated in the presence of an equal volume of 3 M HNO_3, it was found that cleavage at the CMPO C-N bond was favored over that of the C-P bond cleavage found in neat organic solution. This resulted in production of octylphenylphosphinylacetic acid. Thus, the presence of nitric acid concentrations higher than 0.1 M, when CMPO is complexed by HNO_3, apparently favored the cleavage of the C-N CMPO bond. Under these conditions products that supported continued americium extraction were not generated, as reflected in the declining forward D_{Am} shown in Figure 81. Stripping distribution ratios continued to increase with dose when irradiated in the presence of acid, suggesting that an organic soluble acid was also being generated under these conditions, probably the reported octylphenylphosphinylacetic acid.

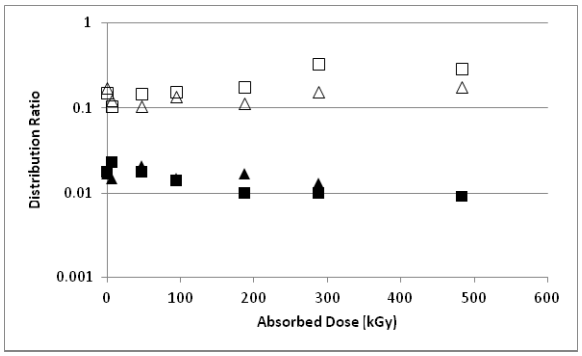

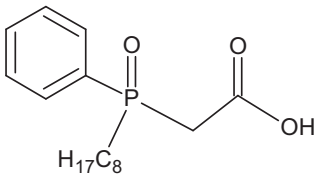

Figure 81. The SX (solid symbols) and strip (open symbols) distribution ratios of americium from 2 M HNO_3 for 0.1 M CMPO/dodecane γ-irradiated in the presence of an equal volume of 2 M HNO_3 (squares) or pre-equilibrated with 2 M HNO_3 (triangles). The samples were diluted to a CMPO concentration of 0.016 M prior to the extraction contacts. Also shown is the structure of octylphenylphosphinylacetic acid.

ESI-MS was also used to identify the main products of the α-irradiation of neat CMPO/dodecane solutions. Only He ion beam irradiated samples were analyzed to prevent radiological contamination of the specialized and expensive instrument. The main products identified for samples irradiated to 20 kGy were the amides N,N-diisobutylformamide (DIBFA), an oxygenated derivate of the formamide (oxy-DIBFA) , and N,N-diisobutylacetamide (DIBAA); indicating cleavage of the CMPO methyl C-C bond. The N,N-diisobutylformamide is believed to be a radiolysis product of N,N-diisobutylacetamide. The occurrence of aqueous-soluble amides could explain the rapid decrease in DAm at low absorbed doses for the isotope α -irradiated samples that researchers have previously reported, shown in Figure 82. Similar results were obtained for At-irradiated samples (data not shown). If these amides act as metal complexing agents they might retain their americium complexes in the aqueous phase, causing a decrease in SX efficiency with absorbed dose. Future experiments will be performed in which the effect of added amides on americium SX is investigated.

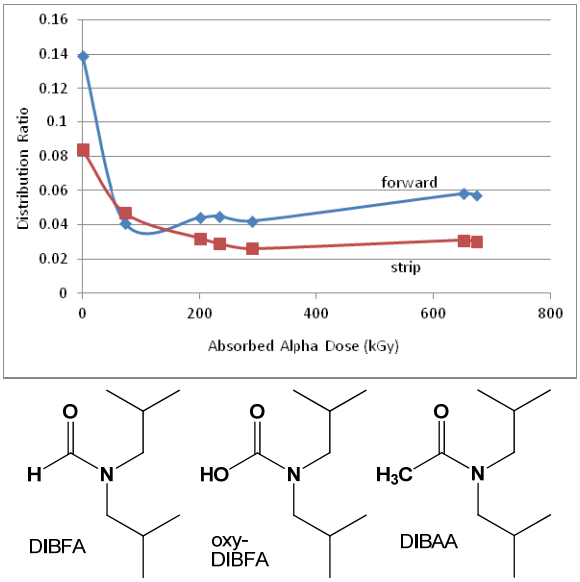

Figure 82. The americium distribution ratios from 2 M HNO_3 for forward (solid diamonds) and strip extraction (solid squares) from Cm–α-irradiated 0.1 M CMPO/dodecane when irradiated in the presence of 0.1 M HNO_3. The samples were diluted to a CMPO concentration of 0.016 M prior to the extraction contacts. Also shown are the structures of acetamide decomposition products that may hold Am in the aqueous phase during SX.

Thus, based on a combination of α and γ-irradiations combined with state-of-the-art analytical chemistry it has been possible to identify CMPO degradation products under various conditions, and to reconcile these products with their effects on SX performance. Manuscripts presenting these results in greater detail are currently in preparation.

Understanding of Decay Impacts on Waste Form Stability

Understanding of Decay Impacts on Waste Form Stability

T. M. Nenoff, tmnenof@sandia.gov, T. J. Garino, M. A. Rodriguez, and D. X. Rademacher

Pollucite ($CsAlSi_2O_6$) is a naturally occurring aluminosilicate with a zeolite-like structure. It has cubic Ia-3d symmetry and an interconnected framework of $(Al,Si)O_4$ tetrahedra with randomly distributed Al and Si ions. In addition to other potential applications, pollucite has long been under consideration as a possible host for immobilization of radioactive cesium from SNF. The primary cesium isotope, ^{137}Cs, has a high β activity due to its short half-life (30 yrs); whereas the other main cesium isotope, ^{135}Cs, is very long-lived (half-life = 2.3×10^6 yrs). Cesium decays to barium. Pollucites are excellent potential hosts for decaying ^{137}Cs since they have low Cs leach rates in aqueous environments. The pollucite framework is a small pored aluminosilicate framework and does not allow other cations to exchange for the cesium. This suggests that direct formation of pollucite from a capture material with occluded cesium as, for example, a part of spent fuel reprocessing, is a promising method to immobilize radioactive cesium cations. It is therefore necessary to understand the crystalline stability of a (Cs,Ba) substituted pollucite.

For radioactive Cs host storage, Fe-substitution of Al in the pollucite framework will potentially mimic the effects of placement of the waste form in an open environment of a repository. Also, potentially Fe^{3+} can charge reduce to Fe^{2+} to maintain charge balance during the decay of Cs^{1+} to Ba^{2+}. This coupled redox reaction, $Cs^+ + Fe^{3+} = Ba^{2+} + Fe^{2+}$ offers a charge balanced crystal chemical substitution that could help keep the phases in the waste form intact, especially if the electron sink is located near the decaying nucleus.

Since not only the stability of Cs-loaded waste forms, but also that of a potential decay product is of importance, researchers have studied the synthesis of Ba-substituted pollucites. To maintain charge neutrality, compositions with two to one replacement of cesium by barium were synthesized. Also studied was the substitution of iron for aluminum in the pollucite structure and its impact on barium incorporation. Specifically, whether or not barium could be stoichiometrically replaced for cesium with the charge imbalance being compensated by the simultaneous replacement of Al^{3+} with Fe^{2+} was investigated because this would suggest that a stable crystalline ceramic might persist throughout the decay process. The materials were synthesized using a hydrothermal process and then thermally treated to improve crystallinity. A variety of analytic techniques were used to characterize the materials.

The substitution of Ba for Cs in the pollucite lattice has been demonstrated for the first time,

using a hydrothermal synthesis technique. Only charge balanced substitution of two Cs with one Ba occurred even when an equal amount of Al was replaced by Fe. The maximum amount of Ba that could be accommodated was about 20% of the stoichiometric amount of Cs with 10% of Ba (see Figure 83).

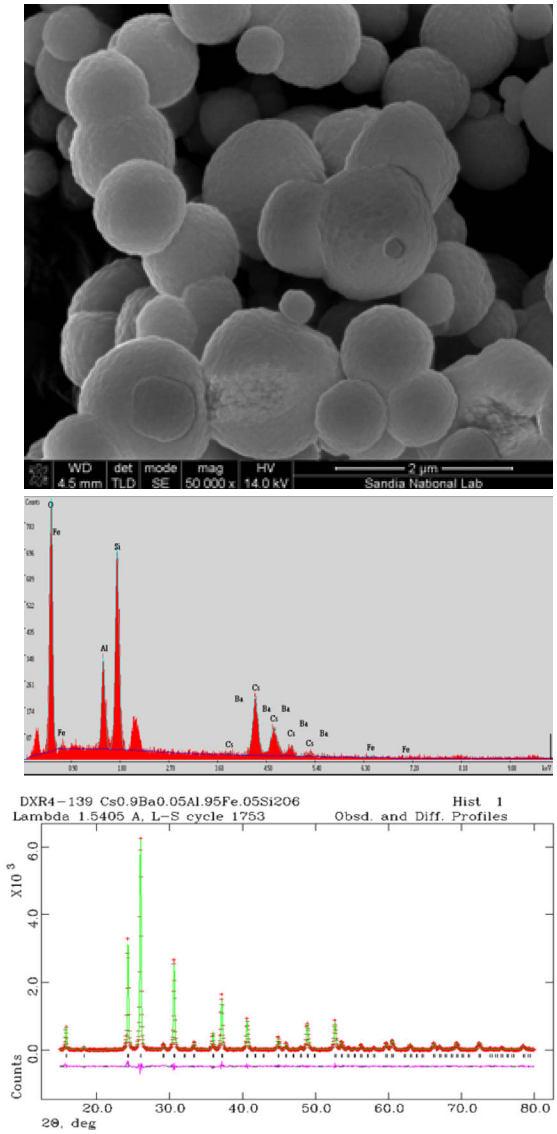

Figure 83. SEM (top) – EDS (middle) analysis of $Cs_{0.90}Ba_{0.05}Al_{0.95}Fe_{0.05}Si_2O_6$; SEM indicates one morphological phase and EDS shows the detectable presence of all expected elements: Cs,Ba,Fe,Al, Si and O. (Bottom): Rietveld refinement of $Cs_{0.90}Ba_{0.05}Al_{0.95}Fe_{0.05}Si_2O_6$, with Ba substituted on Cs site and Fe substituted on Al site (MW 4909.7 g/mol, space group Ia-3d, a = 13.673 Å, R_p = 7.99%). No impurity phases observed

Rietveld analysis showed that the incorporation of Ba caused a slight contraction of the lattice parameter and the framework bond lengths, as well as changing the framework bond angles to be closer to the tetrahedral values. See Figure 84.

The pollucite lattice has shown to be a rigid framework that does not change dramatically with substitution. This further suggests the use of the pollucite framework as a long term nuclear waste form is justified by this study as researchers have shown that it will remain stable and intact with the decay of Cs to Ba, with or without the presence of iron. These materials are suitable for further investigation of the stability of pollucite containing Ba that simulates the decay of ^{137}Cs to ^{137}Ba which occurs in a waste form. Currently, X-ray absorption near edge spectroscopy (XANES) studies are underway the ANL to determine the oxidation state of the iron substituted into the pollucite framework.

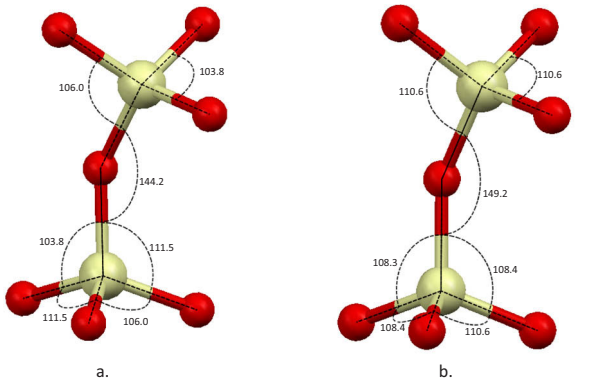

Figure 84. Framework structure fragment of (a) $CsAlSi_2O_6$ pollucite and (b) $Cs_{0.7}Ba_{0.15}Al_{0.8}Fe_{0.2}Si_2O_6$ determined from Rietveld refinement showing changes in bond angles due to Ba and Fe substitution. Smaller red spheres represent O^{2-} and the larger spheres represent either Si or Al in (a) and either Si, Al or Fe in (b) since these are randomly distributed.

Throughout this program, researchers have made pressed and heated pellets of our phase pure, substituted pollucite phases for ion implantation experiments to be carried out at PNNL by Weilin Jiang, et. al. The pellets were 0.5 inch diameter pellets that were pressed and heated at 1500°C for 1 hour. As such, researchers were successful in synthesizing, fabricating and delivering to PNNL multiple disk samples of the following compositions: $CsAlSi_2O_6$, $Cs_{0.9}Ba_{0.05}AlSi_2O_6$,

$Cs_{0.9}Ba_{0.1}AlSi_2O_{6.1}$. It is important to note that the phases with iron in the pollucite framework phases $(Cs_{0.9}Ba_{0.1}Al_{0.9}Fe_{0.1})Si_2O_6$ (a charge imbalance phase, requested by PNNL) and $(Cs_{0.9}Ba_{0.05}Al_{0.9}Fe_{0.1})Si_2O_6$ (a charge balanced phase) segregated into pollucite and minor Fe_2O_3 phase. It appears that either the pressing or the heating or a combination was the cause of this as the phase was pure after sintering at 1100°C, as determined by XRD and Reitveld refinement.

Further details are reported by Nenoff et al, in FCRD-SWF-2012-000365.[1]

References

1. Nenoff, T. M., T. J. Garino, D. X. Rademacher, and M. A. Rodriguez, "The Synthesis of Ba and Fe Substituted $CaAlSi_2O_6$ Pollucites, Sandia National Laboratories, FCRD-SWF-2012-000365.

Chemical and Charge Imbalance Induced by Radionuclide Decay: Effects on Waste Form Structure

W. Jiang, weilin.jiang@pnnl.gov; and
M. Van Ginhoven

$CsAlSi_2O_6$ Pollucite Form

As for our previous study of model waste form of $SrTiO_3$ for fission product ^{90}Sr, researchers pursued a combined theoretical/experimental approach to study of decay processes of a ^{137}Cs-containing waste form. ^{137}Cs decays to ^{137m}Ba and then ^{137}Ba by emission of a β^- particle and a γ photon or directly to ^{137}Ba by emission of a single β^- particle. This technical report focuses on our research progress on aluminosilicate pollucite ($CsAlSi_2O_6$). Researchers worked to identify the effects of the decay of ^{137}Cs on the host material.

Experimental

The experimental effort included work with a natural pollucite mineral from Marin Mineral and three types of sintered samples of undoped ($CsAlSi_2O_6$) and Ba-doped ($Cs_{0.9}Ba_{0.05}AlSi_2O_6$ and $Cs_{0.9}Ba_{0.1}AlSi_2O_6$) pollucite from Sandia National Laboratories. The Ba-doped samples were implanted with F^+ (and O^+) ions up to an atomic concentration of 5 at.% at the profile peak. The implanted anions were intended for charge compensation in the charge-imbalanced Ba-doped pollucite $Cs_{0.9}Ba_{0.1}AlSi_2O_6$. The implantation was performed at elevated temperatures (573 or 673 K) and the implanted samples were subsequently annealed in flowing Ar environments at 873, 1073, and 1423 K. The as-sintered, ion-implanted and thermally annealed samples were analyzed using a variety of experimental methods, including Rutherford backscattering spectrometry (RBS), secondary ion mass spectroscopy (SIMS), XRD, electron probe microanalyzer (EPMA) based energy-dispersive x-ray spectroscopy (EDS) and wavelength-dispersive x-ray spectroscopy (WDS), inductively coupled plasma atomic emission spectroscopy (ICP-AES), x-ray photoemission spectroscopy (XPS), helium ion microscopy (HIM), and transmission microscopy (TEM). The major results are summarized below:

- The natural pollucite sample used in this study is determined to be a single crystal, but the crystalline quality is poor and the sample is not suitable for ion-channeling study.
- The synthesized samples of $CsAlSi_2O_6$, $Cs_{0.9}Ba_{0.05}AlSi_2O_6$ and $Cs_{0.9}Ba_{0.1}AlSi_2O_6$ have a cubic pollucite structure without water. The overall composition of each sample is nearly stoichiometric. However, minor phases of Si and/or Al oxides appear to be present. Impurities of Na and Ca at low levels are identified. The pollucite grain size ranges from 100 nm to 1 μm. Microscopically, there are regions of elemental enrichment and deficiency. Barium-containing precipitates with Si and O in the 10 at.% Ba-dope pollucite are present and are located at the grain boundaries.
- High-dose F^+ ion implantation leads to amorphization of pollucite crystal even at temperatures as high as 673 K. Substantial recrystallization does not occur during post annealing up to 1073 K; A complete recrystallization of the amorphized pollucite appears to take place after annealing at 1423 K for 10 hours. Diffusion of the implanted F toward the surface is observed at 873 K, and becomes

more significant at 1073 K with F release. All F in the sample is released at 1423 K.

- Bubbles of F_2 gas are formed in F^+ ion implanted $Cs_{0.9}Ba_{0.05}AlSi_2O_6$. In contrast, no gas bubbles are found in $Cs_{0.9}Ba_{0.1}AlSi_2O_6$ under the identical implantation conditions. Even after thermal annealing at 1073 K, bubble formation does not occur. The results, together with the rather flat F depth profile in the sample after thermal annealing at 1073 K, may suggest that F implants are trapped in the structure by forming chemical bonds, such as a bond with excess Ba. The BaF^+ unit could potentially substitute for Cs^+ on the lattice site and stabilize the pollucite structure because of the charge balance. Further studies are needed to test the concept.
- The pollucite structure in the unimplanted region of $Cs_{0.9}Ba_{0.1}AlSi_2O_6$ shows a perfect Cs lattice arrangement, shown in Figure 85. This is consistent with the theoretical prediction. The material is susceptible to electron irradiation induced amorphization at electron energy of 300 keV. Since atomic displacements are unlikely to occur at the low incident energy, amorphization is attributed primarily to electronic energy deposition that leads to material decomposition (radiolysis). Near the crystalline-amorphous interface, F concentration is very small and it is yet unknown whether F and/or Ba is incorporated into the pollucite structure. Further efforts are planned to address the issue.

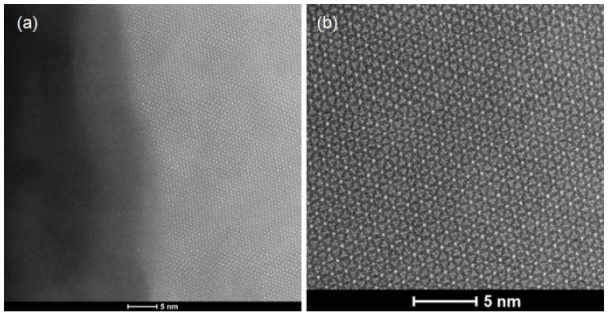

Figure 85. Atomic-level resolution HAADF TEM micrograph of (a) the crystalline/amorphous interface in F+ ion implanted Cs0.9Ba0.1AlSi2O6 pollucite on the (111) projection plane, and (b) a crystalline region near the interface.

- Ba-containing precipitates are crystalline and likely to have a structure different from pollucite. More work is required to determine the phase of the Ba-containing precipitate. An example of a precipitate is shown in Figure 86.

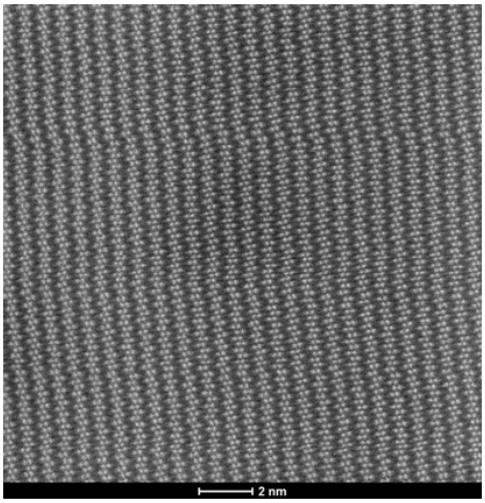

Figure 86. Atomic-level resolution HAADF TEM micrograph of a Ba-containing precipitate near the crystalline/amorphous interface.

- Cesium is diffusive in amorphized pollucite under ionizing irradiation at elevated temperatures and can be readily released from the sample. About 88% Cs in the amorphized pollucite are released to vacuum during the high-dose F^+ ion implantation at 673 K in $Cs_{0.9}Ba_{0.05}AlSi_2O_6$ and about 57% in $Cs_{0.9}Ba_{0.1}AlSi_2O_6$. However, prior to amorphization, there is no evidence from this study that shows Cs loss during ion irradiation at room temperature.
- Data from this study suggests that all the essential constituents in the amorphized pollucite are in the oxide or compound states. No evidence is found for formation of any elemental material, including Cs and Ba metals. There is also no evidence showing a valence change of all the major elements after the material is fully amorphized.

Theory

The theoretical effort focused on the atomistic simulation of pure and Ba-doped pollucite single crystals using DFT. Where possible, researchers directed the theoretical effort so as to be consistent with the ion-implantation experiments. Spin-orbit and finite-temperature effects were not included. Pollucite is a challenging material to study with electronic structure methods due both to the large unit cell (160 atoms), and the requirement to account for the disordered arrangement of Al and Si atoms in the network structure. Simulations included a careful analysis of the Al distribution, and calculations of selected defects and defect complexes.

The primitive unit cell for the pollucite structure has 16 formula units of the ideal $CsAlSi_2O_6$ composition, for a full formula of $Cs_{16}Al_{16}Si_{32}O_{96}$. The Si and Al atoms are distributed randomly throughout the pollucite framework. Researchers investigated the effect of the Al distribution by first identifying several structural subsets of the silicate network in the analogous pure SiO_2 zeolite framework, and then distributing Al atom in this network according to these structural subsets. Researchers identified five distinct Al distributions with this approach. These arrangements are shown in Figure 87. The energy differences among these five models are small, less than 0.2 eV per formula unit. Researchers conclude that the precise location of the Al ions has a minor effect on the system energetics. Researchers therefore selected a single (the lowest-energy) configuration for use in the rest of the calculations.

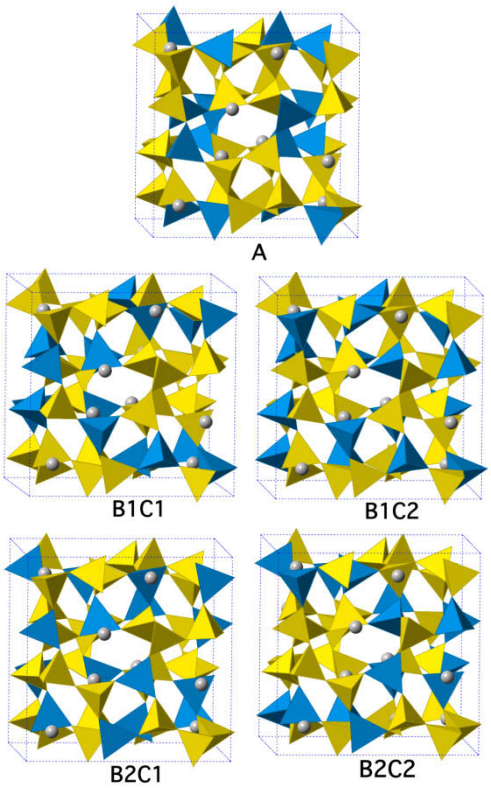

Figure 87. Aluminum distributions in pollucite. Cesium is depicted in silver, blue tetrahedra are Al, and yellow tetrahedra are Si. Oxygen atoms are not shown, for clarity. Configuration B1C2, marked with a border, is the lowest-energy structure, and was used for further investigation in this work.

The subsequent calculations included systems ranging from 1 to 16 Ba atoms substituted for Cs. Ba was either left uncompensated or was compensated by either 0 to 16 Cs vacancies, or excess interstitial oxygen, consistent with the implantation experiments. Researchers obtained optimized geometries and total energies for the full range of this defect set and all the associated reference materials (bulk Ba and Cs metal, quartz SiO_2, cubic BaO, rhombohedral Cs_2O and O_2 gas).

Results

From this initial theoretical study of aluminosilicate pollucite as a potential waste form for ^{137}Cs, the following conclusions are made:

- With the decay of Cs to Ba, the removal (or escape) of Cs is energetically unfavorable as compared to retention in the pollucite crystal. This means that as the waste form decays, remaining Cs

should stay trapped. However, information about ion mobilities is still needed. Calculations of mobilities are planned.

- The lowest equilibrium energy is achieved by precipitating half the Ba (as metal, or as BaO if oxygen is supplied by environment) so the remaining Ba(Cs) is compensated by Cs vacancies. This means that as the waste form decays, remaining Cs should stay trapped.
- Excess oxygen binds to multiple Ba atoms to form BaO or Ba_2O. An example of this quite stable interstitial defect complex, as shown in Figure 88. Additional oxygen could lead to the formation of precipitates, as seen experimentally. Additional calculations are planned to assist with study of the structure of the observed BaO precipitates.

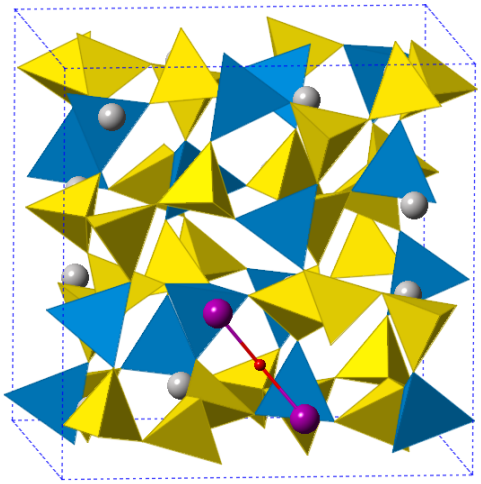

Figure 88. Compensation of Ba^{2+} by oxygen: Ba_2O complex. Colors for Si, Al and Cs are as in Figure 87. Ba is violet, and interstitial oxygen is red. Si is Network oxygen atoms are not shown. The Ba and O are covalently bonded, with Ba-O distances of 2.33 and 2.26 Å.

- Without excess oxygen it is energetically favorable for Ba to be segregated into Ba-rich regions. This is consistent with the segregation of Ba that is seen in the analysis of the Ba-doped pollucite sample provided by Sandia Laboratory.

Further investigation that includes explicit inclusion of additional excess oxygen, the presence of fluorine ions, and consideration of aluminosilicate backbone defects is needed for a complete correlation to the experimental data. In particular, a description of defect formation and evolution in crystal network is needed to explore the effects of irradiation-induced amorphization. As stated above, theoretical results show that Cs release is unlikely for intact crystalline pollucite. Based on these calculations and the experimental data, researchers hypothesize that the amorphization process is critical to the migration and release of Cs in the F^+ implanted samples. Calculation of fluorine-related and aluminosilicate network defects are planned for FY 2013.

LANL High-Temperature Solution Calorimeter

H. Xu, hxu@lanl.gov, M. Chavez, and J. Mitchell

Our work on the Setaram AlexSys-800 calorimeter transitioned from installation and performance evaluation in FY 2011 to performing measurements on standards and samples in FY 2012. Three types of experiments can be performed with this calorimeter: (1) transposed temperature drop calorimetry, (2) solution calorimetry, and (3) drop-solution calorimetry. In experiment 1, a sample is dropped from room temperature into the hot but solventless calorimeter, and the heat content, HC, is measured. This type of measurement was performed on a series of pollucite ($CsTi_xAl_{1-x}Si_2O_{6+0.5x}$, x = 0 to 1) samples in FY 2011. In experiment 2, the sample is first equilibrated in the hot calorimeter and is then dropped into the solvent, where the enthalpy of solution, ΔH_s, is measured. In experiment 3, the sample is dropped from room temperature into solvent, and the measured heat is the sum of the heat content (HC) and the enthalpy of solution (ΔH_s), which is called the enthalpy of drop solution (ΔH_{ds}). This is the type of measurement performed in FY 2012 on the same series of pollucite samples mentioned above and described below.

Drop-solution calorimetric experiments of the same four $Cs_xBa_{(1-x)/2}TiSi_2O_{6.5}$ and $Cs_xBa_{1-x}TiSi_2O_{7-0.5x}$ samples (x = 0.9 and 0.7) were conducted using molten lead borate ($2PbO{\cdot}B_2O_3$) solvent at about 973 K. The obtained heats of drop-solution (ΔH_{ds}) are listed in Table 11.

Table 11. Obtained Heats of Drop-Solution and Enthalpie of Formation from Oxides and Elements

	Heats of drop solution (ΔH_{ds}) and heats of solution in lead borate solvent at 973 K		Enthalpies of formation from the oxides ($\Delta H^{o}_{f,ox}$) and elements ($\Delta H^{o}_{f,el}$) at 298 K	
Composition	**ΔH_{ds} (kJ/mol)***	**ΔH_{s} (kJ/mol)**	**$\Delta H_{of,ox}$ (kJ/mol)**	**$\Delta H_{of,el}$ (kJ/mol)**
$Cs_{0.9}Ba_{0.05}TiSi_2O_{6.5}$	193.4 ± 4.2 (6)	36.2 ± 4.9	-146.9 ± 4.5	-3095.4 ± 5.0
$Cs_{0.7}Ba_{0.15}TiSi_2O_{6.5}$	168.4 ± 4.9 (3)	7.4 ± 5.6	-112.7 ± 5.1	-3081.4 ± 5.5
$Cs_{0.9}Ba_{0.10}TiSi_2O_{6.55}$	201.5 ± 3.0 (6)	40.8 ± 6.3	-159.5 ± 3.3	-3135.4 ± 4.0
$Cs_{0.7}Ba_{0.30}TiSi_2O_{6.65}$	161.6 ± 5.1 (5)	-3.1 ± 6.8	-119.6 ± 5.3	-3170.5 ± 5.8

* Uncertainty is two standard deviation of the mean; value in parentheses is the number of experiments.

Note that the two $Cs_xBa_{1-x}TiSi_2O_{7-0.5x}$ samples (x = 0.9 and 0.7) contain minor amounts of fresnoite, and their heat effects are ignored in these ΔH_{ds} values (as well as the heat contents, described earlier). From these data the heat contents researchers measured last year, ($H_{973} - H_{298}$), the heats of solution (ΔH_s) can be computed as $\Delta H_s = \Delta H_{ds} - (H_{974} - H_{298})$ (Table 11). In contrast to the similarity in heat content for the four compositions, both ΔH_{ds} and ΔH_s enthalpies become less endothermic with increasing Ba content or decreasing Cs content. This behavior implies an endothermic enthalpy of the Cs → Ba substitution in the Ti-substituted pollucite structure.

Using thermodynamic parameters of the constituent oxides (Cs_2O, BaO, TiO_2, and SiO_2) and our measured drop-solution data, researchers calculated the standard molar enthalpies of formation of $Cs_xBa_{(1-x)/2}TiSi_2O_{6.5}$ (x = 0.9 and 0.7) from the oxides ($\Delta H^{o}_{f,ox}$) and the enthalpies of formation from the elements ($\Delta H^{o}_{f,el}$). Similarly, the formation enthalpies $\Delta H^{o}_{f,ox}$ and $\Delta H^{o}_{f,el}$ of $Cs_xBa_{1-x}TiSi_2O_{7-0.5x}$ phases can be derived by using appropriate reaction cycles. As shown in Table 11, the enthalpies of formation from the constituent oxides ($\Delta H^{o}_{f,ox}$) of the two x = 0.9 phases are more exothermic than those of the two x = 0.7 phases, regardless of the specific charge-coupled substitution mechanism. In other words, with increasing Ba content and decreasing Cs content, the thermodynamic stability of these Ba/Ti-substituted pollucites appears to decrease with respective to their component oxides. Hence, from the energetic viewpoint, the Cs → Ba substitution mechanism in these phases may be operating at up to a certain extent. These thermochemical measurements, together with our synchrotron XRD results, thus provide important insights into the effects of the $^{137}Cs \rightarrow {}^{137}Ba$ decay on the phase stability of these waste form materials.

Non-Ideality in Solvent Extraction Systems

P. Zalupski, peter.zalupski@inl.gov, L. Delmau, T. G. Levitskaia, and M. Nilsson

Solvent extraction proceeds in non-ideal environments. The distribution of a solute between two liquids is closely guided by its thermodynamic interactions with the solvent molecules. Pure liquid does not possess long-range order and thus a liquid molecule diffuses freely, despite exerting forces on its near molecular neighbors. When a solute enters a liquid it disrupts its order, searching to regain its thermodynamic stability through multiple chemical interactions. At this stage of infinite dilution, where no interactions between the solute molecules exist in solution, the solution obeys both Raoult's law for the solvent and Henry's law for the solute.[1] If two immiscible solvents are in contact and a solute is infinitely diluted in both solvents, the equilibrium is re-established until the chemical potential of a solute is the same in both phases. The difference in the chemical potentials of the solute drives the mass transfer across the liquid-liquid interface. As such any chemical interaction that disrupts the chemical potential of a solute in both liquid phases may be regarded as non-ideal, and will affect the equilibrium state.

As increasing amounts of solute enter the solvent environment an opportunity for solute-solute interaction grows. Under such conditions the standard chemical potential may no longer approach its standard state of ideal infinite dilution. In this case the activity of a solute depends not only on its concentration, but is also related to the excess chemical potential, resulting from various non-ideal terms such as electrostatic

and/or dipole interactions, solvation effects, mixing terms, etc. That departure from ideal behavior – when solute molecules interact – is expressed by the means of the activity coefficient. To establish liquid-liquid distribution equilibrium between two complex liquid phases, where solutes do not behave ideally, the chemical potentials, but also the activities of all components have to be the same. This additional requirement imposes a thermodynamic demand on the liquid-liquid distribution equilibrium that originates solely from the "extra," non-ideal interactions. At such conditions, where the distribution of a solute between two liquid phases no longer obeys Nernst's distribution law, the proper thermodynamic discussion of phase transfer equilibrium may only be accomplished when sufficient knowledge of non-ideal behavior of solutes in solution is present. Furthermore, the ability to predict the extent of the mass transfer of a solute at equilibrium in such two-phase systems is complicated because the distribution of the solute is not constant.

Non-ideal behavior in solutions always complicates accurate representation of mixtures when modeling a chemical system. A theoretical representation, i.e., model, is particularly challenging when modeling chemical systems as complex as those encountered in aqueous partitioning processes for actinide recycling from dissolved UNF. This research effort illustrates how non-idealities obstruct accurate modeling of separations based on liquid-liquid distribution of the metal between two immiscible phases, i.e., SX. The overarching objective of the project seeks to build experimental capabilities to enable studying fundamental physical properties of solutions. Such inquiry builds thermodynamic knowledge of complex mixtures, allowing better numerical representation, and, as a result, greater accuracy of computational prediction.

The research plan for "Non-Ideality in Solvent Extraction" orbits three main pillars: experimental inquiry into physical chemistry of liquid phases, building thermodynamic models of mixtures of interest to SX and computational prediction using the computer program SXFIT. Several FY 2012 accomplishments are highlighted here to illustrate progress made in those three topics. The significance of each accomplishment to the overall goal of this effort will also be discussed.

PitzINL

The program PitzINL was constructed (Simon Clegg, University of East Anglia) to use the compiled sets of equilibrium equations and the initially accumulated library of Pitzer parameters to model Eu^{3+} complexation by DTPA in a system containing an electrolyte and a buffer. The Pitzer model is used to calculate activity coefficients, and the Pitzer interaction parameters can be changed by the program user. The DTPA protonation and complexation equilibria can be calculated either with activity coefficients from the model, or using concentrations of the species present in electrolyte mixtures. The development of this computational capability illustrates the whole "building-from-the-ground-up" approach when constructing accurate thermodynamic models of solutions. The initial calculations performed in FY 2012 using this program allow tracking aqueous activities of various components in a Eu^{3+} / H^+ / Na^+ / NO_3^- / H_2Mal / $HMal^-$ / DTPA / H_2O system, where Mal describes malonate, based on Pitzer ion-interaction theory. When a model was used to estimate activity effects present across a pH dependency study for TALSPEAK-type system the changes in the activity of free europium ion matched the typically observed decreasing trend of its liquid-liquid distribution as illustrated in Figure 89. Each time the thermodynamic model for this aqueous electrolyte mixture is refined through the addition of new Pitzer ion interaction parameters, the calculations will be re-visited to observe the effects on the ion activities. This approach will indicate the importance of certain ion-ion interactions in the overall thermodynamic model. Such sensitivity analysis was performed based on theoretical calculations. The arrival of new Pitzer parameters should agree with those. New Pitzer parameters are currently being collected using three experimental methods: (1) isopiestic equilibration studies, (2) water activity measurements, and (3) ionic strength dependencies for equilibrium constants.

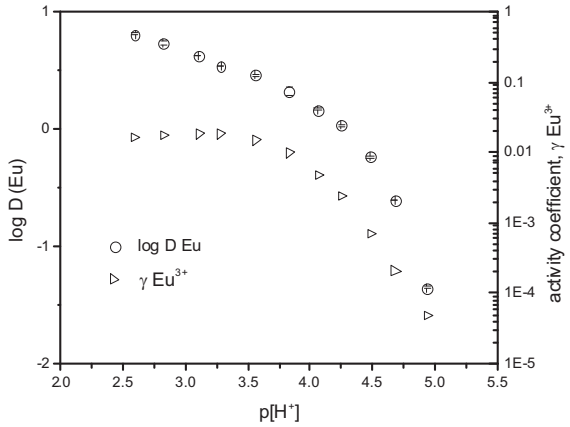

Figure 89. Activity effects of free europium ion.

SXFIT

This project originated based on the needs of a computational package SXFIT.[12] This computer program relies on an iterative fitting procedure, which allows the identification of an equilibrium model for the distribution of a solute in a liquid-liquid system. Since the validity of SXFIT minimization routines relies heavily on the accurate thermodynamic models developed for the complex solutions involved in a two-phase system, the means for gauging the physical chemistry of non-ideal solution behavior needed particular attention. To account for solution non-idealities the program uses Pitzer ion-interaction theory to calculate activity coefficients in aqueous electrolyte mixtures and regular solution theory to describe solute-solute and solute-solvent interactions in the non-aqueous environment. Thus the experimental efforts focus on: (1) studying the thermodynamic properties of mixtures, to (2) represent them theoretically, and (3) acquire a library of thermodynamic parameters that specifically describe a particular system. In a nutshell, the project evaluates the predictive capabilities of SXFIT computational package based on the progressive expansion of new thermodynamic information on the solution non-idealities present in liquid-liquid systems.

In FY 2012 a graphic user interface was developed for SXFIT (James Leighton, ORNL) to upgrade the user-friendly appearance of the package (Figure 90). The graphical user interface (GUI) is platform independent and was tested successfully on a Mac and on a Windows machine. This new development may broaden the user pool, which inevitably would expand our evaluations of the predicting capabilities of the computation to different liquid-liquid distribution systems.

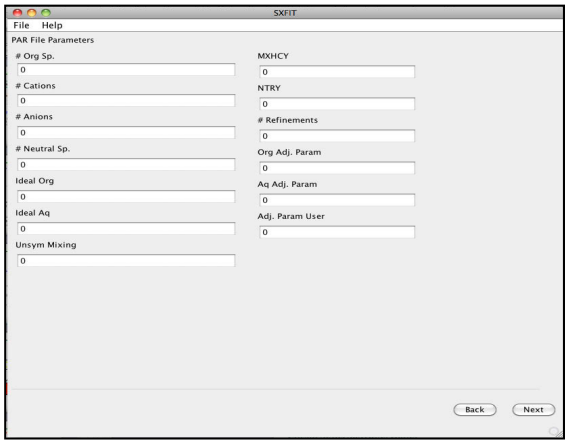

Figure 90. Graphic user interface was developed for SXFIT

Water Activity Measurements

Water activity meter monitors the partial pressure of water vapor saturation inside an experimental chamber containing the sample solution. Once the equilibrium is reached the humidity inside the chamber does not change and the partial pressure of water vapor saturation is zero. At vapor equilibrium the measured dew point temperature is translated into water activity in the solution. The water activity may be converted to the osmotic coefficient, yielding another thermodynamic means of studying electrolyte mixtures and theoretical representation using Pitzer ion interaction theory. FY 2012 efforts illustrate that the thermodynamic data collected by the combined efforts of water activity measurements and vapor pressure measurements on the most dilute mixtures matches the literature data assembled using isopiestic method. Figure 91 summarizes the observed agreement. This finding validates new experimental capability to support thermodynamic parameterization when constructing numerical representations of solutions.

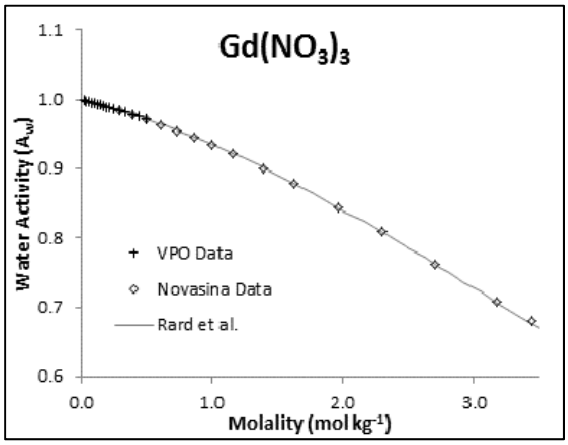

Figure 91. Water activity measurements and vapor pressure measurements on the most dilute mixtures

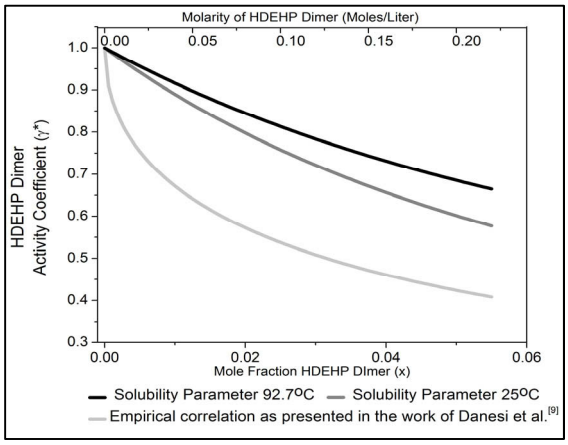

Figure 92. Comparison of the activity coefficient trend of the HDEHP dimer

Vapor Pressure Osmometry

An initial understanding of the solution behavior of the di(2-ethylhexyl)phosphoric acid (HDEHP) dimer in aliphatic diluents has been established using vapor pressure osmometry (VPO). In FY 2012 the theoretical means of obtaining the activity coefficients for the HDEHP dimer based on the collected VPO data were surveyed. Various theories were considered based on the integration of Gibbs-Duhem relation using several different simplified forms of Wohl's expansion of the excess Gibbs energy (Scatchard-Hildebrand, van Laar, 2 and 3-suffix Margules, Scatchard-Hamer). Figure 92 shows the comparison of the activity coefficient trend of the HDEHP dimer, calculated using the Scatchard-Hildebrand relation with a solubility parameter, and the trend afforded by a liquid-liquid distribution study, with the slope analysis based activity correlations.

The calculated activity coefficients follow Henry's law ($\gamma \rightarrow 1$ as HDEHP mole fraction goes to 0), which would be expected as the standard state of infinite dilution is reached. The mismatch between the thermodynamic trends determined based on the VPO data and SX is apparent, even after the adjustment for the temperature dependency to extrapolate the values to 25°C. Further studies will investigate this discrepancy and investigate the effects of aqueous pre-equilibrations, i.e., wetting of the organic solution, on the non-ideal behavior of the HDEHP dimer. However, most importantly, this study illustrates a thermodynamically sound approach toward theoretical representation of non-ideal chemistry in organic mixtures, which constitutes an important step forward considering the objectives of this collaborative effort.

The overarching objective of the collaborative efforts of "Non-Ideality in Solvent Extraction" FCRD project is to advance the ability of theoretical representation of such complex two-phase systems. The project entails surveys of the existing theory, which, together with the established new means of experimental inquiry into basic physical chemistry of liquid mixtures, might accurately represent chemistry using equations. Such mathematical description is fundamental to our goal of computational prediction of aqueous separations using models that accurately describe non-ideal behavior in the liquid phases.

References

1. Marcus, Y. Principles of Solubility and Solutions. In Solvent Extraction Principles and Practice, Rydberg, J., Cox, M., Musikas, C., Choppin, G.R., Eds., 2nd ed., Marcel Dekker, Inc., New York, USA, (2004), p. 49.
2. Baes, C. F., Jr. The Extraction of Metallic Species by Dialkylphosphoric Acids, J. Inorg. Nucl. Chem., 24, 707-720 (1962).

Contactor Modeling and SX Data for Modeling (CFD)

K. E. Wardle, kwardle@anl.gov

Introduction and Objectives

Solvent extraction (SX) process simulation tools are critical for advanced process design, evaluation, and optimization and, in turn, provide the quantitative basis for system-level evaluation of process options. Process-level simulations depend both on accurate chemical data and engineering understanding of unit operations performance over the range of process conditions. This effort seeks to deliver computational tools for simulation of SX contactor unit operations providing a pathway for prediction of key operational performance measures (e.g., stage efficiency, extent of separation) for any conditions using computational fluid dynamics (CFD). In addition, a companion experimental effort is being conducted to provide the necessary data for validation of these advanced multiphase tools.

Of the available SX equipment types, annular centrifugal contactors (ACCs) have the largest relative knowledge gap and at the same time the greatest opportunity for significant benefits due to their compact size and efficiency. While the tools developed here are generally applicable to all SX equipment types, the present focus has been on prediction of the complex flow in ACCs. CFD simulations of these devices can provide insight into improvements in design, enable operational optimization over a wider range of conditions than is currently available, and provide tools to support the confident deployment of this technology in various areas of chemical processing.

R&D Overview

As multiphase CFD methods tend to be regime-dependent, the turbulent multiphase flows in ACCs and other SX devices present a unique challenge as they inherently span multiple flow regimes from fully phase-segregated and, free-surface flow to fully dispersed multiphase flow. Successful simulation of such flows requires a computational framework capable of combining sharp interface capturing methods with multi-fluid dispersed flow modeling. In addition, droplet breakup/coalescence models are needed to capture the evolution of the droplet size distribution to predict liquid-liquid interfacial area. Experimental validation of these advanced models with detailed multiphase data from actual contactors is essential. The experimental facility used for this work consists of two different size ACCs (2-inch and 5-in rotor sizes) each customized for a variety of interrogation methods including flow monitoring and mass balancing, high-speed imaging, and for the larger contactor, electrical resistance tomography (ERT).

Accomplishments

A novel hybrid multiphase CFD solver based on the combination of an Eulerian multi-fluid solution framework (per-phase momentum equations) coupled with sharp interface capturing using volume of fluid (VOF) on selected phase pairs has been developed using the open-source CFD toolkit OpenFOAM. The solver provides unique capability unavailable in any other CFD packages and has been released as part of OpenFOAM v2.1. This tool enables three-phase, liquid-liquid-air simulations in which a sharp interface is maintained between each liquid and air, but dispersed phase modeling is used for the liquid-liquid interactions. During this fiscal year, the solver has been extended to include a reduced population balance model for prediction of liquid–liquid interfacial area. Comparison with experimental observations shows similar mixing phenomena and flow features (Figure 93). Among other investigations, simulations exploring the effect of rotor speed on droplet size have been performed and comparison with available preliminary experimental data demonstrates the ability of simulations to match experimental values.

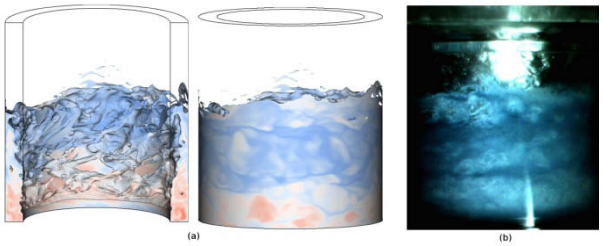

Figure 93. Comparison of snapshots from (a) CFD simulation of 3D annular mixer (left image shows cross-section view) and (b) liquid-liquid operation in an actual centrifugal contactor (CINC-V2) at a comparable overall liquid height showing similar aqueous phase (blue) striations.

The pioneering effort to apply ERT to the confined geometry of the centrifugal contactor continues to show promise for delivering useful insight into phase distributions in the mixing region and quantitative data for future validation efforts. Critical capability has also been demonstrated for measurement of dispersed phase droplet size distributions through image analysis to enable calibration of certain CFD droplet breakup/coalescence model coefficients.

CHAPTER 8
ADVANCED SEPARATION PROCESS ALTERNATIVES

CHAPTER 8: ADVANCED SEPARATION PROCESS ALTERNATIVES

R. T. Jubin, jubinrt@ornl.gov

Extractant Design by Covalency

A. J. Gaunt, gaunt@lanl.gov, E. R. Batista, S. R. Daly, G. Jarvinen, J. M. Keith, S. A. Kozimor, A. Olson, B. L. Scott (all LANL); J. R. Klaehn and D. R. Peterman (both INL)

Importance and Relevance to DOE-NE

This project aims to provide a structure-to-function understanding of actinide extractants. In turn, this new knowledge can be used to feed into the design process for extractants in actinide separation concepts for the nuclear fuel cycle. Specifically, experiments are focused upon elucidating the role of electronic structure and covalency in metal-extractant bonding and how subtle differences can impact actinide selectivity. The research entails a multi-disciplinary approach that integrates chemical syntheses, single-crystal structural determination, K-edge X-ray Absorption Spectroscopy (XAS), and DFT calculations.

Description of Results

Our results in FY 2012 showed that extractant electronic structure and orbital mixing can be correlated with the extractant's separation factors. Complex electronic interactions in $S_2PR_2^{1-}$ ligands were characterized by evaluating the experimental S K-edge XAS data using high-powered electronic structure calculations, including ground state-DFT and a linear response theory (TD-DFT). In general, studying a series of dithiophoshinate salts $(PPh_4)[S_2PR_2]$ whose conjugate acids provide systematically varying Am/Eu separations factors, enabled us to methodically evaluate the effects of P–S orbital mixing as a function of (*1st*) the position of the CF_3 substituent on the aryl group (ortho, meta, para) and (*2nd*) the electron-donating ability of the substituent at the ortho position (CF_3, Me, MeO). These results enabled us to identify "special" electronic structure properties that appear to correlate with the Am/Eu separation factors, and prompted a DFT study focused in predicting a new series of dithiophosphinic acids that researchers propose will exhibit very high actinide selectivity.

A series of fully characterized $S_2PR_2^{1-}$ molecules were prepared to provide a benchmark series that were used in systematic S K-edge XAS experiments and TD-DFT calculations. Specifically, researchers synthesized seven new $[PPh_4][S_2PR_2]$ complexes (R = methyl, phenyl, *p*-$CF_3C_6H_4$, *m*-$CF_3C_6H_4$, *o*-$CF_3C_6H_4$, *o*-MeC_6H_4, *o*-$MeOC_6H_4$) and found that the structure of $S_2P(o\text{-}CF_3C_6H_4)_2^{1-}$, an excellent MAs extract, is distinct from $S_2PR_2^{1-}$ anions that exhibit poor An/Ln selectivity (Figure 94).

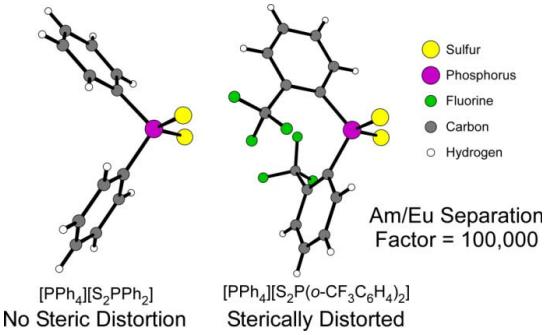

Figure 94. The structure of $S_2P(o\text{-}CF_3C_6H_4)_2^{1-}$ compared to $S_2PR_2^{1-}$ anions

The results of the ligand sulfur K-edge XAS spectroscopy identify clear correlations between electronic structure and the ability of certain dithiophosphinates to remove MAs from lanthanides present in UNF (Figure 95).

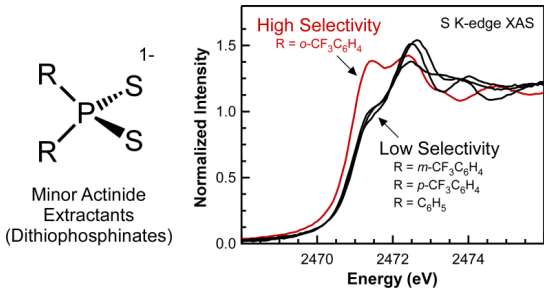

Figure 95. Correlations between electronic structure and the ability of certain dithiophosphinates to remove MAs from lanthanides

Researchers established this correlation by systematically analyzing seven dithiophosphinates whose performance in lanthanide/actinide separations is well documented and range – for reasons previously not understood – from highly effective to ineffective. The study reported here provides data that helps explain why the *ortho*-substituted $S_2P(o\text{-}CF_3C_6H_4)_2^{1-}$ is an exceptional actinide extractant, and identifies crucial structure-to-function relationships in dithiophosphinates that may prove useful in guiding the design of new extractants for advanced nuclear fuel cycles. In general, researchers find that the *ortho*-CF_3 substitution in $S_2P(o\text{-}CF_3C_6H_4)_2^{1-}$ inhibits rotation of the aryl groups, thereby holding the $S_2P(o\text{-}CF_3C_6H_4)_2^{1-}$ in a geometric configuration that appears electronically poised for selective actinide binding, a concept that is commonly referred to in bioinorganic chemistry as an entatic state. Trapping the arene groups in this geometric configuration increases orbital mixing between the arene groups and the S_2P core. In essence, this more effectively delocalizes the negative charge on S over the entire $S_2P(o\text{-}CF_3C_6H_4)_2^{1-}$ molecule, making it "softer" than $S_2PR_2^{1-}$ analogues where the arene groups are free to rotate out of the actinide-binding entatic state.

Interpretation of the complicated spectral contributions from both 5*f* and 6*d* orbitals in the actinide systems is not straightforward and pushes the very limits of computational capabilities in actinide science. Researchers needed to conduct additional measurements on simple transition metal dithiophosphinate complexes (Figure 96).

Researchers have revealed that the Ni complex containing the exceptional MA extractant $S_2P(o\text{-}CF_3C_6H_4)_2^{1-}$ has UV-Vis transitions assigned to metal-ligand bonding that are shifted by up to 1100 cm^{-1} relative to other $Ni[S_2PR_2]_2$ compounds (R = *m*-$CF_3C_6H_4$, *p*-$CF_3C_6H_4$, and Ph), whose spectra are nearly identical. This spectral difference, manifests itself in the unique purple color of the $Ni[S_2P(o\text{-}CF_3C_6H_4)_2]_2$ complex, and suggest that $Ni[S_2P(o\text{-}CF_3C_6H_4)_2]_2$ has an unusually large HOMO/LUMO gap due to the unique ligand electronic structure. The increased highest occupied molecular orbital (HOMO)/lowest unoccupied molecular orbital (LUMO) gap for $Ni[S_2P(o\text{-}CF_3C_6H_4)_2]_2$ is interpreted as arising from increased covalent mixing in the Ni–S σ bonds formed between the Ni $3d_{xy}$ orbitals and the S 3*p* lone pairs. These same S 3*p* lone pairs are likely those involved in M–S σ bonds with MAs, if covalent mixing is present.

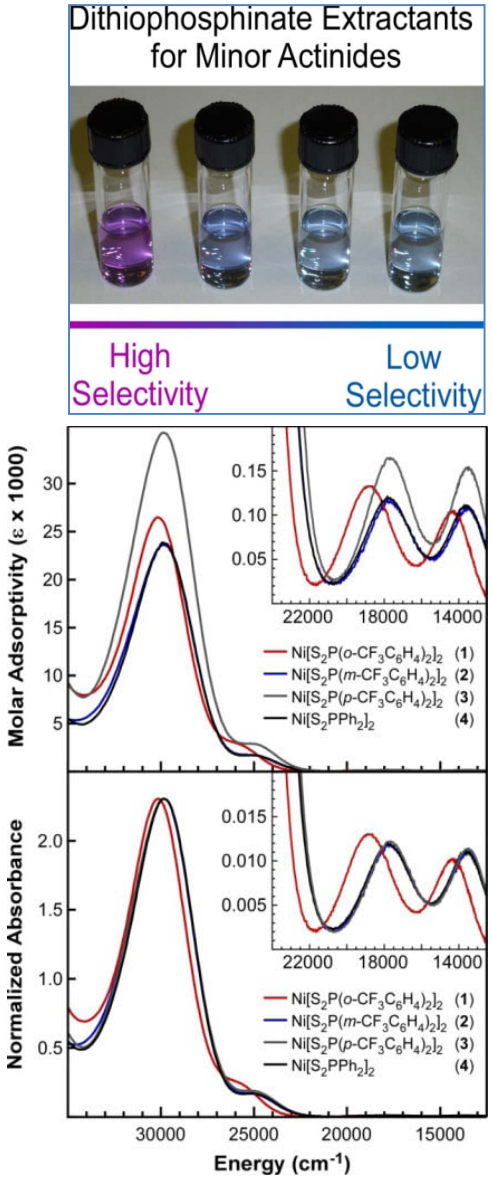

Figure 96. Simple transition metal dithiophosphinate complexes

Using all of the knowledge learned above researchers are now predicting the selectivity and electronic structure of new proposed molecules. It appears that the orientation of the aryl group has profound effect on the "softness" and Am^{3+}-extracting ability of the $S_2PR_2^{1-}$ ligand framework.

Researchers surmise that constraining the arene groups, or "tethering them together," in the correct orientation would augment softness, and concomitantly improve Am/Eu separation factors. Hence, researchers have conducted a series of DFT calculations on dithiophosphinates (Figure 97) with constrained arene groups and identified a series of molecules where the amount of S 3p character is more effectively delocalized over the arene systems. The proposed tethered ligands (1–4) can be accessed in three steps from 1,1'-bisaryl-2,2'-dibromides using established synthetic procedures, and these efforts are now underway to isolate these new molecules, measure their electronic structure by XAS, and test their Am/Eu separation factors by SX tracer studies at INL.

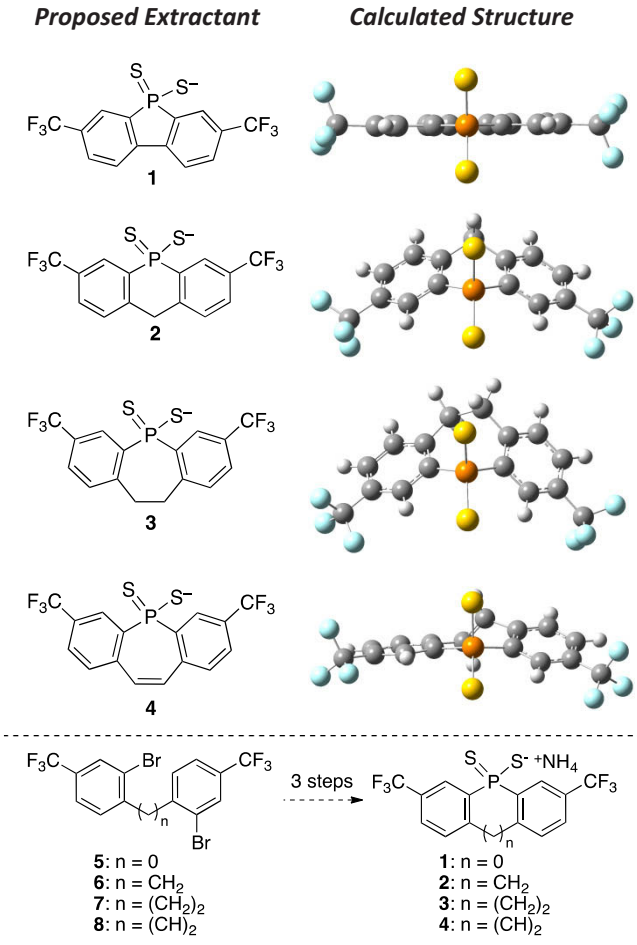

Figure 97. DFT calculations on dithiophosphinates

Conclusion

These results demonstrate the importance of using ligand K-edge XAS and TD-DFT calculations as tools for innovation in understanding extractant behavior. Ultimately, this research strategy will facilitate rational design of extractants based upon electronic structure-to-function relationships, and researchers expect to be able to apply this technique to additional donor atom extractants such as oxygen and nitrogen.

Aqueous Electrochemical Separations

A. V. Guelis, guelis@anl.gov

The goal of this study was to identify areas where electrochemical processes can be used to achieve an efficient process for used fuel treatment with minimal generation of secondary waste streams. Anodic dissolution of used fuel and simultaneous cathodic recovery of $UO_2 \cdot xH_2O$ from aqueous chloride and sulfate media have been studied using depleted uranium oxide pellets. Proof -of –principle tests have demonstrated that electro-dissolution of UO_2 and reduction/precipitation of UO_2 on the electrode surface is a feasible method for the used fuel treatment. In FY 2012 researchers have tested the dissolution of crushed UO_2 pellets in an apparatus utilizing a very large anode along with intense stirring and heating. In those tests, a reasonable dissolution rate was accomplished. Noticeable amounts of UO_2 were recovered on the bismuth cathode. The raffinate solution would be treated by ion exchange/SX for MA/Lanthanide group separation.

Transformational Ionic Liquid Separation Systems

B. A. Moyer, moyerba@ornl.gov, and S. Dai

The hypothesis under investigation in this project is first that acidic ionic liquids (ILs) can dissolve oxides of actinides, initially UO_3 as a potentially useful test case, and second that the dissolved oxide can be electrodeposited to either the metal or an insoluble lower oxidation state oxide. The basic concept being explored is shown in Figure 98.

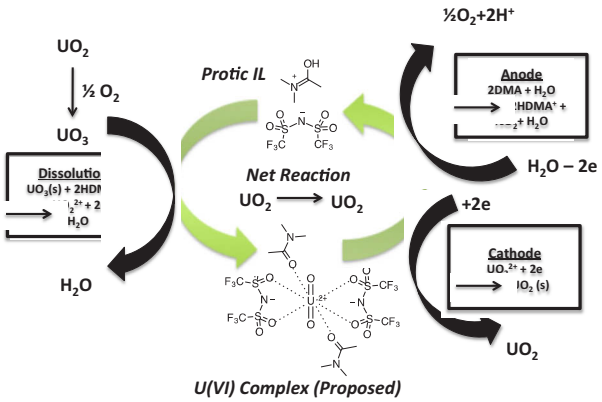

Figure 98. Proposed cycle of dissolution of UO_3 using amide based acidic IL, producing dissolved UO_2^{2+} cation that is solvated by DMA and NTf_2^-, and electrodeposition of UO_2 in the presence of an aprotic IL [EMIM][NTf_2].

The proposed concept has similarities to the pyrochemical treatment of UNF using molten salts. Among other advantages, ILs potentially allow the process to take place at much lower temperatures. The key result from FY 2012 work is summarized as follows:

> *A tandem dissolution and electroreduction of UO_3 was demonstrated. The dissolution employs the acidic IL N,N-dimethylacetimidium bis(trifluoromethanesulfonimide), while 1-ethyl-3-methylimidazolium bis(trifluoromethanesulfonimide) served as the diluent. These two species are completely miscible and promote uranyl ion solvation in the same system. Bulk electrolysis performed at –1.0 V yields a dark brown-black amorphous uranium dioxide deposit (UO_2) on the cathode, which may be annealed at high temperature to crystalline UO_2. Further studies have confirmed that the IL used in the dissolution may be regenerated in the anode compartment by water oxidation. Since water is released on dissolution of UO_3, the regeneration of the acidic N,N-dimethylacetimidium ion at the anode by water oxidation closes the conceptual process cycle.*

In this work, researchers are exploring the potential of ILs for electrodeposition of actinides in used-fuel recycle applications. One of the unique properties of ILs in comparison with traditional solvents is their electrical conductivity, opening the door to electrochemical separations of metals at low temperatures. Even more far-reaching is the potential to combine electrochemical separations with other separation steps, such as a prior dissolution of metals into the IL followed by direct electrodeposition. In this work, researchers explore this particular idea, taking as an initial example the dissolution of UO_3 followed by electrodeposition to UO_2, a potential form of uranium for fuel fabrication. As a prototype system for study (see Figure 98), this system makes sense in the context of processing used oxide fuel following a voloxidation step that brings the uranium up to UO_3. Although there are many outstanding and difficult questions to be addressed for practical application, the objective in this project has been limited to an initial demonstration of a closed conceptual process cycle together with a preliminary characterization of the component processes.

The dissolution and electroreduction process involves the use of the acidic IL *N,N*-dimethylacetamidium bis(trifluoromethane sulfonyl)imide ([DMAH][NTf_2]) in a non-acidic IL diluent, 1-ethyl-3-methylimidazolium bis(trifluoromethanesulfonyl)imide ([EMIM][NTf_2]). The acidic IL cation is simply a protonated form of *N,N*-dimethylacetamide (DMA). By spectrophotometry, the stoichiometry of the dissolution was shown to involve the reaction of two moles of $DMAH^+$ with one mole of UO_3 to give one mole of UO_2^{2+} cation. Presumably, the uranyl cation is solvated by the two molecules of DMA that are liberated, though the presence of added DMA slows the dissolution rate. On the other hand, one mole of water is liberated, which tends to accelerate the dissolution rate. The water is driven off prior to electroreduction at 115–130°C. Similar results have been achieved for two other amidinium based ILs.

Controlled-potential electroreduction using a Pt gauze working electrode at –0.8 V versus Ag reference electrode results in deposition of amorphous UO_2. After electrolysis for 24 h at 120°C, a blackish-brown deposit is observed on the working electrode and also in suspension in

the IL. The deposited material exhibits a featureless powder XRD pattern, but upon annealing under argon at 900°C, the typical pattern of UO_2 as cubic uranite is obtained. Based on the collected amount of UO_2 measured gravimetrically and the number of coulombs passed, the Faradaic efficiency of electrodeposition was found to be at least 80%. The electrochemical mechanism of the electrodeposition is complex and under investigation. Results from cyclic voltammetric scans show an initial quasi-reversible one-electron reduction process that researchers assign to the $UO_2^{2+/+}$ couple. The fate of this species involves at least two pathways, believed to be further reduction at the electrode to give UO_2 and disproportionation in solution. The latter reaction could account for the UO_2 that is suspended in solution.

NMR and acid-base titration analysis suggested that the acidic IL consumed during the dissolution of UO_3 can be quantitatively regenerated in the anode compartment by water oxidation. In a separate electrochemical experiment, water was added to the working electrode compartment containing the IL [EMIM][NTf_2] and DMA. Upon applying an oxidizing potential at a Pt gauze electrode, the quantitative formation of the $DMAH^+$ cation was shown by NMR spectroscopy and titration. This result demonstrated that a closed process cycle is possible with regeneration of the acidic IL ready for reuse.

Combination of Hard and Soft Donor Ligands for Actinide Co-extraction from UREX Raffinate

P. Zalupski, peter.zalupski@inl.gov, D. Peterman, and D. Ensor

The richness of actinide redox chemistry, spanning a +3 to +6 range in aqueous acidic solutions, presents a challenging obstacle to a single-step, total actinide recovery from mixtures containing metals of diverse chemical behavior. Hard donating ligands, such as those containing oxygen atoms like tributyl phosphate, bind metal ions classified as hard Lewis acids based on purely electrostatic interactions. As such the ionic binding is governed by the overall charge density on the metal ion.[1] The strength of such interaction increases as the charge density increases. In UNF mixtures the hexavalent uranyl ion, and tetravalent plutonium are easily coordinated by hard donors such as TBP.

The charge density for a trivalent actinide such as americium is not sufficient to efficiently interact with TBP, requiring a reagent of higher basicity.[2] In a UREX+ process, a bifunctional carbamoylphosphonate reagent fulfills that role, affording an equally strong interaction with lanthanides and actinides of similar charge density. Grouped f-elements require a final An/Ln differentiation step to recover Am and Cm. Furthermore, the management of neptunium and plutonium relies on redox state adjustments to guide their final destinations in a 2-phase system.[3] Thus, aqueous-based separation of all actinides from dissolved UNF requires multiple steps - each predominantly relying on charge-controlled (ionic) interactions. A proposed UREX+ separation scheme may include up to 5 independent SX cycles.[4]

A slightly greater degree of polarization of 5*f* orbitals for actinides, relative to their 4*f* lanthanide counterparts, offers an alternative chemistry that is effective when targeting a selective An isolation. Here, the enhanced spatial extension of those *f*-orbitals encourages some contribution from covalent binding with complexants that contain atoms such as nitrogen, sulfur or chloride.[2] Polarized, electron-rich orbitals of such functionalities may partially overlap with 5*f* and 6*d* orbitals of actinide ions offering a certain degree of direct, covalent bonding interaction. This is a current justification for multiple demonstrations of highly efficient An/Ln separations using SX reagents containing soft donor groups such as N or S.[5-7]

An advanced separations alternative concept proposed here attempts to combine the coordination chemistry of both hard and soft donor ligands in an attempt to demonstrate the feasibility of significant simplification of the UREX+ scheme. The proof-of-principle feasibility study for the single-step co-extraction of all actinides from simulated aqueous streams resembling UREX raffinates has been completed.

Following an initial step of bulk uranium removal (together with technetium) an actinide co-extraction step separates all remaining 5*f* elements away from aqueous mixtures of fission products.

The chemistry chosen for this demonstration is based on a synergistic combination of an ion-exchanging SX reagent (soft) with the solvating phase-transfer compound (hard) to enhance the efficiency of metal ion recovery from aqueous acidic media.

Figure 99 shows the chemical structures of hard and soft donor reagents chosen for a solvent recipe. Bis(o-trifluoromethylphenyl) dithiosphosphinic acid (abbreviated as compound "1") is a liquid cation exchanger that offers the soft characteristics of sulfur. Trioctylphosphine oxide (TOPO) is a neutral, hard-donating, solvating extractant, which participates in the metal ion complexation. Its enhancement in the lipophilicity of a formed metal complex increases its thermodynamic stability in the non-aqueous environment, and, consequently, allows a "boost" in the distribution of the metal into the organic phase.

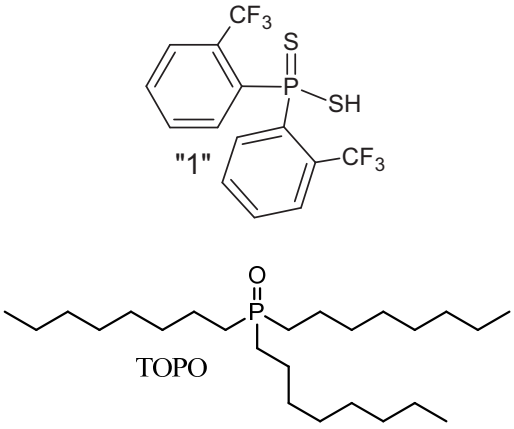

Figure 99. Chemical structures of bis(o-trifluoromethylphenyl)dithiosphosphinic acid (compound "1") and trioctylphosphine oxide (TOPO).

An organic mixture of 0.1 M "1" / 18 mM TOPO / toluene was chosen as the optimal condition to proceed with the demonstration. This solvent composition allows efficient separation of Am from Eu at an aqueous pH of 1. Multiple determinations of Am and Eu partitioning were performed using several batches of compound "1," yielding consistent results (D_{Am} = 10.8 ± 0.5 and D_{Eu} = 0.15 ± 0.02). The separation factor between Am and Eu for those conditions is 74 ± 4. All lanthanides have been shown to remain in the aqueous phase of 0.1 M HNO_3 / 0.9 M $NaNO_3$, whereas americium was extracted into the organic phase. The lowest observed separation factor was 42 for americium and holmium. Studies on the phase transfer kinetics for both spherical and linear dioxo actinyl cations illustrated that equilibrium is established in less than a minute of phase contact.

Further tests demonstrated a complete removal of all actinides (UO_2^{2+} - Cm^{3+}) from 0.5 M HNO3 using an organic mixture of 0.5 M "1" / 0.1 M TOPO / toluene. All studies on the feasibility of this concept cannot be listed here, as those results progressively tested actinide partitioning behavior as the complexity of the aqueous phase grew. The final results, summarized in Table 12, illustrate the overall behavior of all metal ions in the liquid-liquid system of the highest complexity.

Table 12. Distribution ratios for all metal ions present in the UREX raffinate simulant solution used as an aqueous phase in the feasibility study. Organic phase was 0.5 M "1" / 0.1 M TOPO / FS-13.

Metal	D ± 2σ	Metal	D ± 2σ
Am	10.1 ± 3.8	Ce	0.039 ± 0.006
Eu	0.036 ± 0.001	Nd	0.025 ± 0.007
U	109 ± 52	Sm	0.025 ± 0.002
Np	quantitative	Eu	0.021 ± 0.002
Pu	40 ± 3	Gd	0.011 ± 0.008
Ba	no extraction	Y	0.003 ± 0.003
Cs[#]	0.006 ± 0.008	Ag	12.7 ± 0.7
Rb	0.005 ± 0.004	Cd	69 ± 31
Sr	0.006 ± 0.006	Pd	75 ± 4
Zr	1.06 ± 0.06	Rh	0.092 ± 0.008
La	no extraction		

[#]distribution ratio was too low to accurately determine using ICPMS method

Table 12 lists the distribution results for actinides (UO_2^{2+} – Am^{3+}) and fission products resulting from the equilibration of 0.5 M "1" and 0.1 M TOPO in trifluorophenyl sulfone (FS-13)

diluent and the aqueous UREX raffinate simulant, whose composition is summarized by Table 13.

Table 13. Aqueous composition of UREX raffinate simulant used in the study.

Ion	Concentration	Ion	Concentration
H^+	0.50 M	Sm^{3+}	0.75 g/L
Ba^{2+}	0.51 g/L	Eu^{3+}	0.03 g/L
Cs^+	0.55 g/L	Gd^{3+}	0.04 g/L
Sr^{2+}	0.18 g/L	Y^{3+}	0.12 g/L
Rb^+	0.086 g/L	Ag^+	0.02 g/L
Zr^{4+}	0.97 g/L	Cd^{2+}	0.03 g/L
La^{3+}	0.31 g/L	Pd^{2+}	0.38 g/L
Ce^{3+}	0.60 g/L	Rh^{3+}	0.13 g/L
Nd^{3+}	1.04 g/L		

As expected Ag^+, Cd^+ and Pd^{2+} reported to the organic phase. Rhodium's behavior follows those of other fission products, indicative of higher charge density due to the trivalent oxidation state. The observed extraction of zirconium, as expected in liquid-liquid systems containing organophosphate extractants, will have to be addressed using an oxalic acid as a holdback reagent in the scrub solution. Perhaps the most important take-home message from this complex distribution system is the overall actinide behavior in presence of other soft metal ions, which compete with Ans for coordination by ligand 1. Actinide behavior is still preserved as all maintain their preference of the partitioning into the non-aqueous environment. Excellent separation between Am^{3+} and Eu^{3+} was still maintained at 284. All mass balances for the metal ions studied radiometrically (Am-243, U-233, Pu-239, Np-237 and Eu-154) were excellent (±10%).

Complete single-step separation of uranium, neptunium, plutonium and americium from aqueous mixtures containing 0.5 M nitric acid and a total fission product content of 5.5 g/L (45 mM) has been demonstrated. Organic solvent that accomplishes the co-extraction consists of a synergistic mixture of a soft donor: bis(o-trifluoromethylphenyl)dithiosphosphinic acid and a hard donor: trioctylphosphine oxide, in the aromatic diluents: toluene and FS-13. Separations tests using FS-13 as a diluent enhanced the differentiation between Am and the lanthanides, which stretches the window of flexibility for this liquid-liquid approach.

References

1. Choppin, G. R., and M. P. Jensen, Thermodynamics and kinetics of actinide complexation. In Morss, L. R., Edelstein, N. M., Fuger, J. (eds.) The chemistry of the actinide and transactinide elements, pp. 2524-2621. Springer, Dordrecht, The Netherlands (2006) Vol. 4.
2. Nash, K. L., C. Madic, J. N. Mathur, and J. Lacquemont, Actinide separation science and technology. In Morss, L. R., Edelstein, N. M., Fuger, J. (eds.) The chemistry of the actinide and transactinide elements, pp. 2622–2798. Springer, Dordrecht, The Netherlands (2006) Vol. 4.
3. Herbst, R. S., P. Baron, and M. Nilsson, Standard and advanced separation: PUREX processes for nuclear fuel reprocessing. In Nash, K.L., Lumetta, G.J. (eds.) Advanced separation techniques for nuclear fuel reprocessing and radioactive waste treatment, pp. 141-175. Woodhead Publishing Ltd., Cambridge, UK (2011).
4. Regalbuto, M. C., Alternative separation and extraction : UREX+ processes for actinide and targeted fission product recovery. In Nash, K. L., Lumetta, G. J. (eds.) Advanced separation techniques for nuclear fuel reprocessing and radioactive waste treatment, pp. 141-175. Woodhead Publishing Ltd., Cambridge, UK (2011).
5. Diamond, R. M., K. Street, Jr., and G. T. Seaborg, An ion-exchange study of possible hybridized 5f bonding in the actinides. J. Am. Chem. Soc. 76, 1461-1469 (1954).
6. Zhu, Y., J. Chen, and R. Jiao, Extraction of Am(III) and Eu(III) from nitrate solution with purified Cyanex 301. Solvent Extr. Ion Exch. 14, 61-68 (1996).
7. Kolarik, Z., U. Mullich, and F. Gassner, Extraction of Am(III) and Eu(III) nitrates by 2-6-di-(5,6-dipropyl-1,2,4-triazin-3-

yl)pyridines. Solvent Extr. Ion Exch. 17, 1155-1170 (1999).

Volatilization Methods

Advanced Voloxidation using Nitrogen Dioxide

G. D. DelCul, delculgd@ornl.gov, J. A. Johnson, R. D. Hunt, B. B. Spencer, E. D. Collins, and R. T. Jubin

Introduction

A novel dry head end process based of NO_2/O_2 mixtures to convert the fuel to a fine powdered form that can selectively chosen to be U_3O_8, UO_3, or a nitrate by selecting the processing conditions is being successfully developed. The process removes volatile, and some semivolatile, fission products from the UNF to prepare it for further separations. The NO generated as a result reconverts to NO_2 in the presence of oxygen. In a closed loop application NO_2 is continuously regenerated (except minor process losses) and the actual reagent to be fed is oxygen.

The dry powder generated can be readily interfaced with an aqueous based process, fluoride volatility, and electrochemical separations. The process is well suited for oxide based fuels such as LWR (PWR and boiling water reactor [BWR]) and heavy water reactor (HWR) fuel (Candu) and it may also be used for sodium bonded metallic fuel.

Initial laboratory studies with simulants and authentic used fuel have been performed and show the potential of the process, and concepts for implementation have been developed that indicate significant improvements compared to conventional voloxidation. These improvements include oxidation at lower temperatures and shorter processing times, near complete removal of the more problematic species (e.g., iodine) plus the already mentioned selectivity of the species produced. In the case of interfacing the dry head-end with aqueous separations, the UO_3 or nitrate products will dissolve readily without gas evolution (fumeless) in low concentration nitric acid (0.3M and above) or carbonates for UO_3, or directly into organic extractants such as TBP for the nitrate product. The fumeless dissolution coupled with a closed loop NO_2 regenerative system has the potential for significantly reduce the off gas volume by several orders of magnitude (e.g., a few m^3 per tonne of fuel compared to around 1000 m^3 per tonne for conventional voloxidation and high acid dissolution of U_3O_8).

Description of the Process

A mixture of NO_2 and O_2 is used as the oxidant at lower temperature. The product generated is a fine powder that can be selected to be U_3O_8, UO_3, or uranyl nitrate according to conditions used. NO(g) readily reacts with O_2 during cooling to regenerate NO_2. In essence, NO_2 acts as a catalyst with O_2 being the consumable reagent. The reactions are faster than air or O_2 oxidation at temperatures >500°C

Figure 100. $3UO_2$+ 2 NO_2(g) = 2 NO(g) + U_3O_8 (Brown to black)

Figure 101. U_3O_8+ NO_2(g) = NO(g) + 3 UO_3 (Red)

Figure 102. 2 UO_3 + 8 $NO_2(g)$ + $O_2(g)$ = 2 $UO_2(NO_3)3NO$ (yellow-green); 2 NO(g)+ $O_2(g)$ = 2 $NO_2(g)$ (NO_2 regeneration)

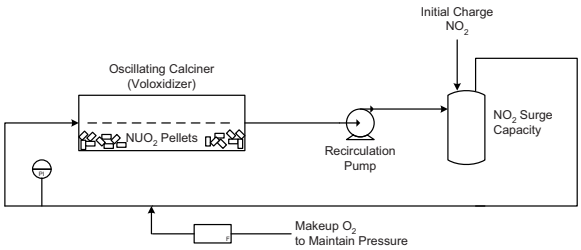

Figure 103. Simplified flow sheet to test NO_2 catalyzed oxidation (i.e., regenerative system)

Accomplishments

Successful Demonstration of Regenerative NO_2 Voloxidation at 1 kg scale including Six 100g Runs

The purpose of this task was to (1) obtain experimental data on the NO_2-voloxidation and nitration process using unirradiated surrogate materials, (2) construct nitration test equipment capable of handling batches of UNF at the 1-kg scale, and (3) test the operability of the equipment before installation in a hot-cell.

Seven runs of actual testing with unirradiated UO_2 pellets were successfully completed. Six runs were conducted at a 100 g-scale. One run was completed at 1 kg-scale. In all cases, the oxygen to uranium ratio of the product was slightly above 3.0. The overall tests were very successful showing the processes to be very efficient, reliable, and forgiven. No problems were encountered and the closed loop system proved to be very stable. No recharging of NO_2 was needed to complete all of the runs. The only losses were during the evacuation of the sample chamber at the completion of each run. The system was operated with excess liquid N_2O_4/NO_2 in the surge tank. Under these conditions, the system operating pressure is mostly governed by the sum of the vapor pressure of the NO_2 in the surge tank and the partial pressure of oxygen.

Figure 104. Kilogram-scale voloxidizer

Successful Demonstration of NO_2 Voloxidation of Authentic Commercial Fuel from the Dresden Reactor

Several very successful experiments using Dresden BWR UNF (24 GWD/MT burnup, 34-year decay) were performed to find if the reactions with UNF produce similar results as those with simulants. All results with authentic fuel were very similar to the surrogates, the nitrated product was determined to be hydrated uranyl nitrate in place of uranyl nitrosyl nitrate as in the surrogate work. The difference is attributed to a reaction with atmospheric water since the hot samples were handled in air inside the hot cell and glove boxes.

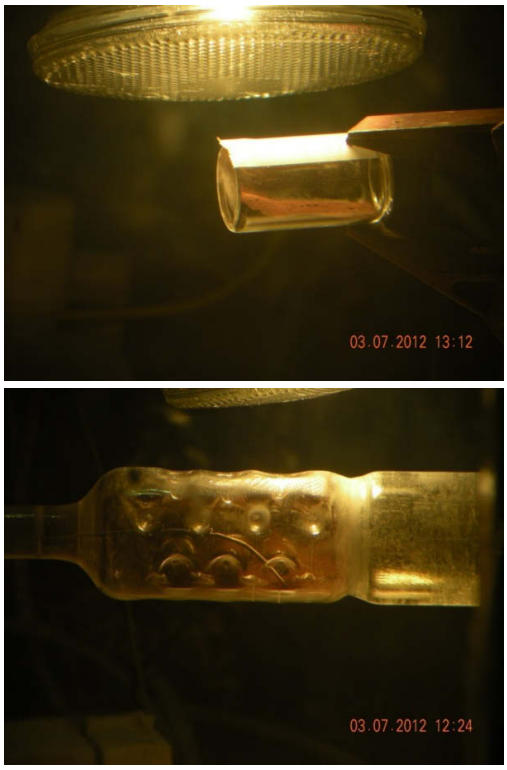

Figure 105. UO_3 product from Dresden fuel

Nitration of the Voloxidized Fuel Powder and Direct Dissolution in Tributyl Phosphate

The nitration of UO_2 unirradiated pellets and authentic fuel was tested successfully. A small batch of surrogate uranium fuel containing selected, simulated fission products (Rb, Sr, Y, Zr, Cs, La, Ce, Pr, Nd, Sm, Eu, Ba and I) was nitrated using NO_2 and contacted with 30% TBP. The sample readily dissolved leaving behind a small amount of solid residue of alkaline, alkaline earth species and zirconium.

Figure 106. Nitrated surrogate uranium fuel

Removal of Iodine

Iodine, which is mostly present in the spent fuel as CsI, is released as I_2 vapor. As shown in Figure 107, NO_2 readily reacts with NO_2 to form $CsNO_3$ and releasing iodine per the following reaction:

$$2CsI + 4NO_2(g) \rightarrow 2\ CsNO_3 + 2\ NO + I_2(g)$$

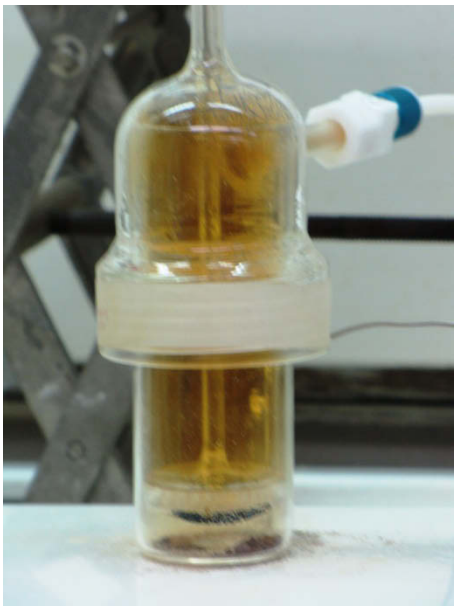

Figure 107. NO_2 reaction to release iodine

To test the reaction in the presence of UO_2 and to quantify the iodine release, 1 g batches of depleted uranium oxide spiked with 10 mg CsI with 27 µCi of ^{125}I were reacted with NO_2. The mixtures were analyzed by gamma spectroscopy at 35 keV before and after reaction. It was found, after initial oxidation of the UO_2 to UO_3 in a stationary system, 5.7% of the iodine remained in the system. The material was then treated further in a rotary calciner for two hours. It was determined that 1.2% of the original iodine remained.

Hot test showed high removal but with significant uncertainties due to analytical problems. After prolonged storage, only ^{129}I is present in used fuel. Our hot tests were done using a few grams of authentic fuel. The analytical determination of the ^{129}I in the samples before and after treatment is very difficult as the signal is very low and comparable to background and interferences. Given the analytical uncertainty the actual removal is in the range from 65% to higher

than 90%. More sensitive methods are being developed to better ascertain the removal efficiency and allow for the optimization of the process.

Fluoride Volatility Reprocessing – NF_3 Method

B. McNamara, bruce.mcnamar@pnnl.gov

It has been shown that, as a result of the difference in the volatility of the fluorides of the actinides and transition metal fission products, the gas-fluoride technology possesses all prerequisites for efficient removal of fission products from U and Pu. The fluorinating agents typically used (i.e., F_2, HF, and ClF_3) to produce the desired volatility are highly toxic and have the highest hazard ratings. Researchers have been investigating nitrogen trifluoride as the fluorinating agent because of its relatively low chemical toxicity, low room temperature reactivity hazard. The resulting lower transportation and storage costs, facility set up and use costs, reagent recycle costs, and user friendly nature of the gas make it a fluorine replacement with great advantage not only with these operational issues, but also with respect to human and environmental exposure.

While it is quite likely that NF_3 could be more safely used for flame fluorination for instance in place of F_2, researchers recognized early in our studies a difference between the behavior of NF_3 and literature reports of F_2/HF fluorinations of used fuel. Researchers investigated an NF_3-based fluoride volatility process where differences in temperature associated with formation of volatile actinide and fission product fluorides would be used to separate fuel constituents: essentially a temperature programmed desorption approach. As presented in Figure 108, NF_3 is used to fluorinate used-fuel that has been pretreated by voloxidation to convert the UO_2 matrix to U_3O_8. The fluidized bed reactors are held at a temperature required to selectively volatize one or a set of fission products. The separations of fission products from U and Pu can be quite effective as is demonstrated further below.

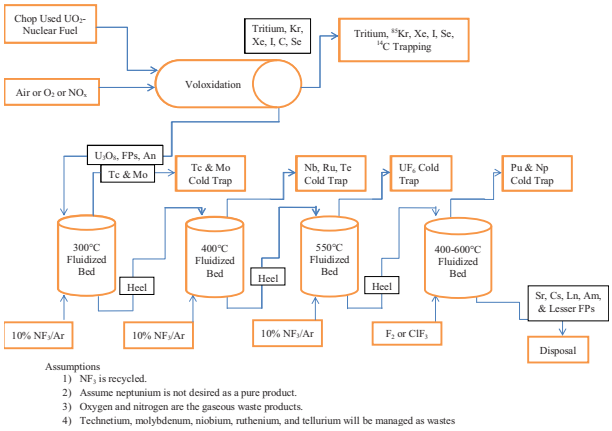

Figure 108. Voloxidation of the fuel is followed by selective temperature desorption of volatile transition metal fluorides then UF_6, NpF_6, and finally PuF_6.

The effort carried out in FY 2010 through 2102 produced several complete data sets concerning the reaction of NF_3 with actinides and transition metals. The results are now the subject of articles in the peer-reviewed literature, with additional manuscripts currently under review. Several conferences and workshops were attended by group members. Briefly, these topics covered general characterization of the thermal reactions of NF_3 with UNF constituents and characterization of the reaction products[6,7], reaction of NF_3 with uranium and plutonium metals[3], efficient separation of uranium from MOX fuel using NF_3 [7], conversion of NpO_2 to NpF_6 using NF_3 [1], a comparison of the reaction of F_2 and NF_3 with UO_2 using a modified shrinking core model[2], and finally, thermal characterization and speciation by Raman spectroscopy of volatile molybdenum and technetium products using NF_3.[4] Also, our observation of the catalytic effects of a high yield fission product, ruthenium, on NF_3 fluorination is currently under review as a patent application.

Highlights

Thermal Profiles of Relevant Used-Fuel Components

Figure 109 compares volatilization of TcO_2 at 265°C to that of UO_2 with exposure to NF_3 at 425°C. At 265°C, the reaction to form solid UO_2F_2 does not begin before the Tc is quantitatively removed. Molybdenum and other transition metals were shown to behave in a similar manner. For 0.02 wt% mixtures of TcO_2 in solid UO_2, in

particular, researchers demonstrated Tc removal down to 10^{-7} g Tc/ g UO_2 by exposure of the mixture to NF_3 for 1 hour at 300°C. The results demonstrate that low level isotope separations of intimate mixtures can be achieved with NF_3 exposure.

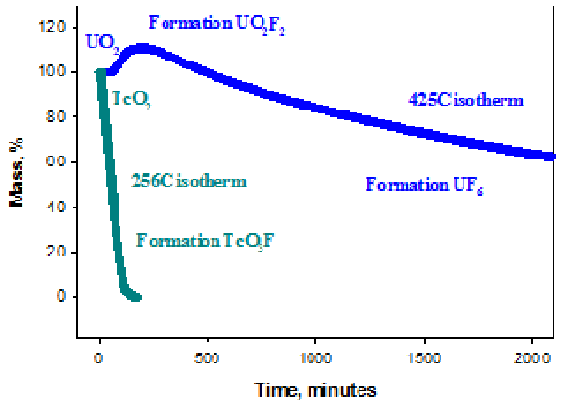

Figure 109. Volatilization isotherm of UO_2 at 425°C is compared to that of TcO_2 at 265°C.

Quantitative Separation of Uranium from MOX $(U_{0.8}Pu_{0.2})O_2$ using NF_3

Isothermal experiments between 400 and 550°C where PuO_2 was exposed to 10% NF_3/Ar did not produce volatile PuF_6. The inability to volatilize plutonium with NF_3 encouraged an experiment, the results of which are displayed in Figure 110, that demonstrated complete uranium removal from MOX $[(U_{0.8}Pu_{0.2})O_2]$ up to 630°C with no Pu carry over.

The mass curve (indicated) shows that uranium was quantitatively separated from the MOX solid, leaving a heel of PuF_4 of about 25 mass%. No uranium was found in the residual PuF_4 product by EDS analysis (Figure 110b) or in the XRD powder pattern (99.9% uranium removed). Because MOX is a solid solution of uranium and plutonium oxide, the result suggests that very good separations using NF_3 may be achieved for MOX and likely other solid oxide matrices.

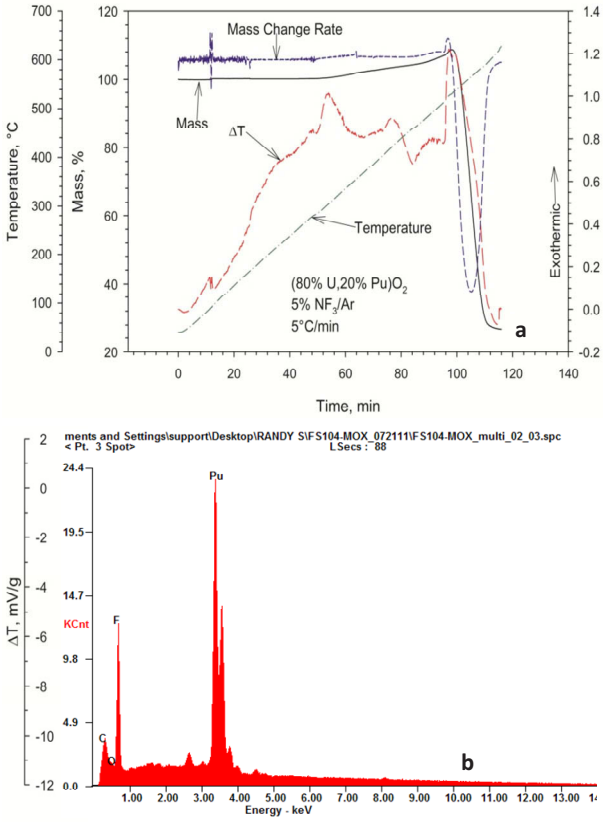

Figure 110. (a) % NF_3/Ar on $(U_{0.8}\ Pu_{0.2})O_2$ as measured by TG and DTA. The mass curve (indicated) shows quantitative uranium removal. (b) EDS analyses for U in the residual PuF_4 product.

Gas-Solid Reaction Kinetics Considerations

Gas-solid reaction kinetics play an important role in achieving the goal of separating fuel constituents from each other. Physical models that properly describe the reaction kinetics include reaction at the phase boundary, diffusion through an intermediate product barrier, nucleation and growth, and autocatalysis. In FY 2010–2012 such models were elucidated for the reactions of NF_3 with U, Np, Pu, and Tc. These models were an important breakthrough in our understanding of gas-solid reactivities and are critical to applications for processing of nuclear fuels with *any* gas phase reagent, for their ability to predict fluorination behavior. Three manuscripts that describe models of the reactions of NF_3 with NpO_2, UO_2, U, and Pu metal are in preparation for submission near the end of 2013.

Catalytic Effect of RuO_2 and CoF_2 on NF_3 reactions of UO_2, NpO_2, and PuO_2

Researchers have demonstrated that RuO_2 lowers the onset of fluorination of NpO_2 and UO_2 a full 100°C relative to that with no additive. Additionally, it appears that Pu (PuF_6) mobility becomes possible near 300°C using NF_3 whereas this was not observed without the added catalyst. The plot in Figure 111 shows that the reaction of NF_3 with pure PuO_2 to produce PuF_4 took significantly more of time and that the entire reaction profile for the RuO_2/PuO_2 mixture is perturbed. The observation should be applicable to reagents such as ClF_3, BrF_3, BrF_5, etc., such that Pu mobility could be enhanced at lower temperature.

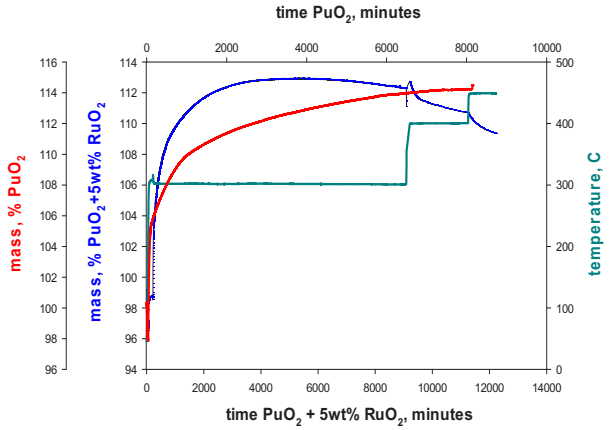

Figure 111. Comparison of the isothermal reaction of NF_3 with PuO_2 at 450°C and with a 5 wt% mixture of RuO_2 and PuO_2 at 300, 400, and 450°C.

References

1. Casella, A., R. Scheele, B. McNamara, and A. Kozelisky. 2013. "Gas Solid Reaction Model for the Conversion of NpO_2 to NpF_6 using NF_3" *in* preparation for submission to J*ournal of Nuclear Science and Technology*.

2. Casella A, R. Scheele, B. McNamara, and A. Kozelisky. 2013. "Comparison of the reaction of F_2 and NF_3 with UO_2 using a Modified Shrinking Core Model" in preparation for submission to *Journal of Nuclear Science and Technology*.

3. McNamara, B., R. Scheele, A. Kozelisky, and M. Edwards. 2009. "Thermal Reactions of Uranium Metal, UO_2, U_3O_8, UF_4, and UO_2F_2 with NF_3 to Produce UF_6." *Journal of Nuclear Materials* 394:166-73.

4. McNamara, B., S. Sinkov, A. Casella, R. Scheele, A. Casella, and D. Neiner, Fluorination of Uranium and Plutonium Metal by Nitrogen Trifluoride: Evidence for Elusive UF_2, in preparation for submission to *Journal of Physical Chemistry*, 2012.

5. McNamara, B., S. Sinkov, C. Soderquist, and . Scheele. 2013. "Thermal Characterization and Speciation by Raman Spectroscopy of Volatile Molybdenum and Technetium Products using NF_3" in preparation for submission to *Journal of Inorganic Chemistry*.

6. Scheele, R., B. McNamara, A. Casella, and A. Kozelisky. 2012(a). "On the Use of Thermal NF_3 as the Fluorination and Oxidation Agent in Treatment of Used Nuclear Fuels." *Journal of Nuclear Materials* 424:224-36.

7. Scheele, R., B. McNamara, A. Casella, A. Kozelisky, and D. Neiner. 2012(b). "On the Use of Thermal NF_3 as the Fluorination and Oxidation Agent in Treatment of Used Nuclear Fuels: Fluorination of Cobalt, Yttrium, Zirconium, and Lanthanide (Sans Promethium) Oxides" accepted *Journal of Fluorine Chemistry*, 2012.

Sulfur Hexafluoride Treatment of Used Nuclear Fuel to Enhance Separations

J. Gray, joshua.gray@sml.doe.gov, R. Torres, M. Martinez-Rodriguez, J. Becnel, P. Korinko, B. Garcia-Diaz, T. Adams

Reactive Gas Recycling (RGR) technology development was initiated at SRNL, with a stretch-goal to develop a fully dry recycle technology for UNF. This approach is attractive due to its potential for targeted gas-phase treatment steps that reduce the footprint and secondary waste volumes associated with traditional aqueous separations, so long as the fluorinators employed in the reaction are recycled for use in the reactors or are optimized for conversion. Fluorination via SF_6 can be used to address multiple fuel forms and downstream cycles. The process can be free-standing, incorporated into an aqueous process (e.g., modified FLUOREX) or integrated with a pyro

treatment to be used in advanced gas reactor designs such metal- or gas-cooled reactors. The experimental results in the past year indicated that the majority of the fission products form stable solid fluorides and sulfides, while a subset of the fission products form volatile fluorides such as molybdenum fluoride and niobium fluoride. These results agree with earlier thermodynamic predictions. Additional kinetic analysis was performed on selected fission products. A key result was the verification that SF_6 requires high temperatures for direct fluorination and subsequent volatilization of uranium oxides to UF_6, and thus is well positioned as a head-end treatment for other separations technologies, such as the volatilization of uranium oxide by NF_3 and other advanced pyrochemical separations

The primary effort during the program focused on using thermogravimetric (TGA) data to characterize the kinetics and proposed reaction mechanisms of SF_6 with various fission product surrogate materials in the form of oxides and metals. Previous TGA results indicated that the majority of the characterized fission product surrogates formed stable solid fluorides and sulfides at temperatures up to 750°C. Solid-state reaction kinetics were studied by following the weight change of the sample. Different experiments were conducted in which either (1) the sample was heated in the presence of SF_6 from room temperature or (2) heated in Ar until reaching a high temperature isotherm, at which point the SF_6 gas flow was turned on. The weight change data was converted to a normalized form called conversion fraction (α), which ranges from 0 to 1 and is a measure of reaction progress as a function of time or temperature (Eqn. 1, left). Using this conversion fraction, a variety of solid-state kinetic models were applied to the experimental TGA results to identify potential reaction mechanisms of the fission products without requiring detailed analysis of Arrhenius-style kinetic parameters [5-6]. (Eqn. 1, right) The f(α) can be deduced through kinetic analysis to suggest the mechanism, without requiring the calculation of the k(T) parameters.

$$\alpha = \frac{W_{initial} - W_t}{W_{initial} - W_{final}} \quad , \quad \frac{d\alpha}{dt} = k(T) f(\alpha) \qquad (1)$$

As an example, application of these models to the TGA mass profiles of Gd_2O_3 (Figure 112, top), shows that the fission product initially follows a 3rd order reaction kinetics, after which the material experienced diffusion limitations, consistent with Jander (D_3) and Ginstling-Brounshtein (D_4) models. Further characterization by XRD (Figure 112, bottom) confirmed the formation of GdF_3 as the primary product. These results suggested that the formation of GdF_3 follows readily on the oxide surface until saturation, at which point the product acts as a diffusion barrier for further fluorination of the core powder. Similar characterization has been performed on additional fission product surrogates of interest in UNF separation schemes. An expanded use of the analyses discussed here to multi-component systems will help in designing an overall engineering process for fluoride volatility involving sulfur hexafluoride.

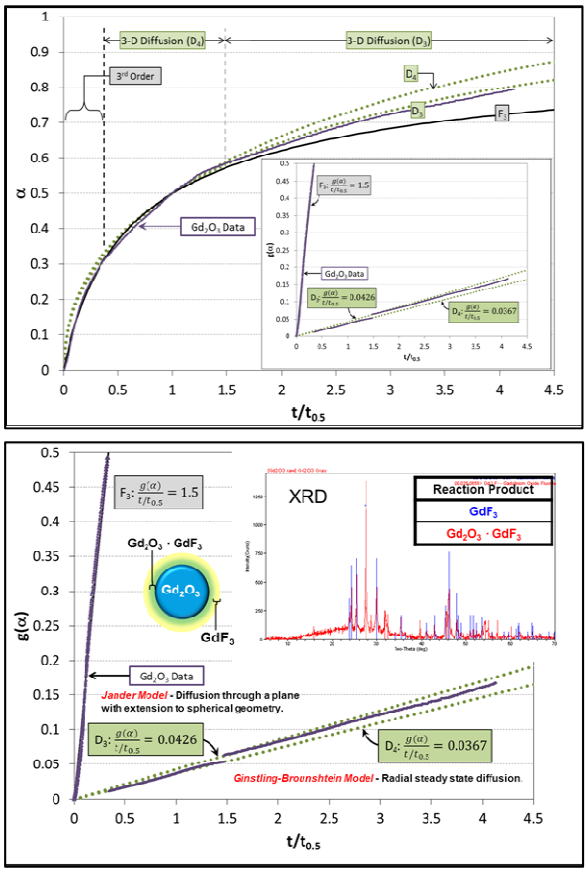

Figure 112. (top) Proposed transport mechanisms during the fluorination of Gd_2O_3 with SF_6, (bottom) Proposed reaction mechanisms for Gd_2O_3 with XRD

The results of the research at SRNL on fluoride volatility showed that SF_6 treatment renders all anticipated volatile fluorides studied to be volatile and all non-volatile fluorides studied to be non-volatile, with the notable exception of the uranium oxide stocks that were available at SRNL. This offers an excellent opportunity to use this fluorinating agent for head-end separations treatments because:

1. SF_6 can be used to remove volatile fluorides from a UNF matrix while leaving behind uranium oxides. A secondary agent such as NF_3 would follow to separate a UF_6 stream, leaving other compounds in the bottom ash pan such as PuF_4, SrF_2 and CsF.
2. Since uranium oxide is not separated by volatilization upon reaction with SF_6 at moderately high temperatures ($\leq 1000^oC$), this fluoride volatility approach may be well-suited for head-end processing for Gen IV reactor designs where the LWR is treated as a fuel stock. For this fuel form, it is not desired to separate the uranium from plutonium.
3. It is likely that removal of the volatile fission products from the uranium oxide should simplify both traditional and next generation pyroprocessing techniques.
4. SF_6 treatment to remove volatile fission products, with or without treatment with additional fluorinators, could be used to simplify the separations of traditional aqueous processes in similar fashion to the FLUOREX process.

A flow diagram was developed in ASPEN$^+$ to explain a potential reprocessing scheme, wherein SF_6 exposure would be followed by another process for further conditioning. One such process that could be introduced would be further reaction with NF_3. This scheme is shown in Figure 113. PNNL has shown that UF_6 will readily form from exposure to NF_3 at temperatures of approximately 440°C, which should more cleanly separate the uranium out from this solid product without any potential contamination of species such as molybdenum, niobium, rhenium, rhodium or other similar elements. This should also leave the plutonium at the bottom of the fluorination reactor along with other radioactive species such as Cs and Sr which may have advantages for implementation. Note that this scheme also assumes separation and recycle of fluorinating agents in both fluorination steps, to minimize the wastes to the treated.

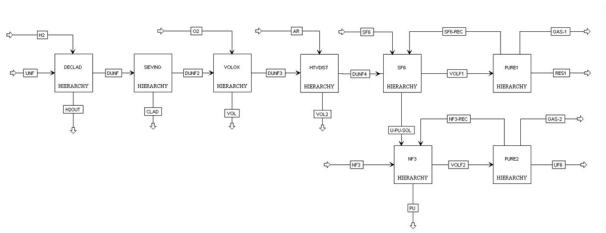

Figure 113. Process Diagram for combined SF_6 and NF_3 Separations Process which Includes Fluorinating Agent Recycle

Another possibility would be to integrate fluoride volatility approaches with pyrochemical methods, in order to remove fission product and actinide contaminants prior to electrochemical separation. A group at SRNL is currently developing an alternate pyrochemical approach for treatment of UNF using non-traditional salts, as opposed to a chloride salt electrolyte. This process can incorporate a fluoride donor, such as NF_3 or SF_6, to render the formation of volatile UF_6 under controlled electrochemical conditions. Thermodynamic calculations have indicated that this process is theoretically thermodynamically spontaneous and should allow for controlled separation of UNF component materials.

Halogenation

B. Westphal, brian.westphal@inl.gov

Background

The oxidative processing of used LWR fuel has been researched extensively since the early-1960's and is currently being proposed by the Korean Atomic Energy Research Institute (KAERI) for recycle of fuel via pyroprocessing. The benefits of the technology hinge on the selective removal of onerous fission products such as cesium, technetium, and iodine. Unfortunately the rare earth fission products remain and can contribute adversely to reactor neutronics upon recycle. The purpose of this research would be to target rare earth removal following the oxidation cycle by a halogenation reaction (with chloride or

bromide) that would allow for the removal of the rare earths by vaporization according to the following reaction:

$$RE_2O_3 + 6\ NH_4X = 2\ REX_3 + 6\ NH_3 + 3\ H_2O \quad (1)$$

where X = Cl or Br and RE = La, Ce, Nd, Sm, or Eu. Vaporization of the resultant rare earth halides can be achieved at similar temperatures as the oxidative step, thus utilizing the same equipment for both oxidation and halogenation. Current flow sheets for recycle of used LWR fuel contain multiple process steps and/or pieces of equipment wherein this technology could be performed in a singular piece of equipment (rotary kiln) capable of all the operations. Additionally, the halogenation of rare earth oxides has been investigated for mineral and scrap recovery processes but the application to UNF would be unique. The research as proposed would allow the removal of volatile fission products in order to recycle used LWR fuel for multiple cycles.

Experimental

Three experimental activities were investigated during FY 2012:

1. Surrogate testing at Montana Tech with rare earth oxides to determine optimum conditions for chlorination by Jerry Downey and Diane Bell,
2. Surrogate testing at the INL with uranium oxides, rare earth oxides, and ammonium halogens to determine the degree of uranium halogenations by Cal Morgan and Brian Westphal.
3. Rare earth precipitation testing using irradiated LWR fuel in the HFEF by Brian Westphal.

The research performed for the experimental activities is summarized below.

Montana Tech Surrogate Testing

Multiple experiments have been performed with rare earth oxides and chlorinating agents to determine the optimal operating conditions for the chlorination and removal of rare earths. One piece of equipment operated in two modes (stationary and rotary) has been utilized for these experiments with temperatures up to 1100°C. Variables tested include chloride source (HCl gas or ammonium chloride) and amount, argon flow rate, reaction time, temperature, carbon addition, and the ratio of rare earth (both neodymium and samarium) oxide to chloride source. Analyses for these experiments have included XRD and gravimetric measurements.

The major challenge during surrogate testing with HCl(g) has been the formation of a non-volatile rare earth oxychloride species that results in the incomplete removal of the rare earths. Although reaction (2) below is the goal for chlorination of the rare earth oxides, reaction (3) is possible given the conditions present during testing:

$$Nd_2O_3 + 6\ HCl = 2\ NdCl_3 + 3\ H_2O \quad (2)$$

$$Nd_2O_3 + 2\ HCl = 2\ NdOCl + H_2O \quad (3)$$

The highest removal of rare earths during testing with HCl(g) was only approximately 20% with considerable evidence, via XRD, of oxychloride species in the residual products.

Testing with ammonium chloride resulted in considerably more removal of rare earths, up to 97%, according to the following reaction:

$$Nd_2O_3 + 6\ NH_4Cl = 2\ NdCl_3 + 6\ NH_3 + 3\ H_2O \quad (4)$$

The optimum parameters for removal were 600 ml/min for argon with two processing regimes; one for reaction (318°C) and one for distillation (1000°C). A minimum of 60 minutes at both the reaction and distillation temperatures was recommended to maximize rare earth removal. Oxychloride formation was observed but was avoided using the optimized conditions.

INL Surrogate Testing

Following on the favorable results from the previous year's testing with ammonium bromide, further experiments were performed with rare earth oxides (La_2O_3 and Nd_2O_3) and NH_4Br under an argon atmosphere in the furnace shown in Figure 114. Similar to equation (4), ammonium bromide should react with rare earth oxide to form a volatile bromide species of rare earth according to equation (5). It was believed that the air atmosphere during the previous year's tests altered the results, i.e., favored the formation of oxybromide species.

$$Nd_2O_3 + 6\ NH_4Br = 2\ NdBr_3 + 6\ NH_3 + 3\ H_2O \quad (5)$$

Figure 114. Tube furnace utilized for testing at the INL

Given in Table 14 is a summary of the initial experiments under argon with varying temperatures and argon flows. For the first two tests, it was noted that the loss of NH_4Br due to sublimation (450°C) may have affected the results and the temperature for follow-on tests was lowered. Tests #3 and #4 produced high yields and confirmation by XRD of no oxybromide species. For tests #5-7, the temperature of the furnace was increased after a reaction temperature of ~350°C to 1000°C to distill the rare earths as volatile bromides. Tests #8 and #9 repeated previous tests with high yields although reaction of the silica boat was noted for test #9. For test #10, reaction of the silica boat was noted again and the loss of NH_4Br at the reaction temperature caused incomplete yields. An Inconel 600 crucible was fabricated and used for test #11 but the depth of the crucible most likely affected the results, i.e., insufficient argon flow over the reactants to remove excess water vapor.

Table 14. Results of experiments with La_2O_3, Nd_2O_3, and NH_4Br under Ar

Test	RE Oxide	Final Temp. (C)	Argon Flow (ml/min)	Yield* (%)	Notes
1	La	425	450	79	Ar flow or temperature too high
2	La	420	400	90	Ar flow or temperature too high
3	Nd	360	200	97	XRD results show no oxybromide
4	La	340	200	94	XRD results show no oxybromide
5	La	1000	150	72	Air ingress causing oxybromide
6	Nd	1000	150	4	Air ingress minimized but evaporation of bromide
7	La	1000	150	88	Air ingress causing oxybromide
8	Nd	360	150	99	Repeat of Test #3
9	La	360	150	88	Reaction with boat
10	Nd	1000	150	5	Reaction with boat and evaporation of bromide
11	Nd	1000	150	63	Inconel boat was too deep

* Percent of expected reaction from oxide to bromide based on weight measurement

A water wash of the residual material was performed and analyzed by Inductively Coupled Plasma-Optical Emission Spectrometry (ICP-OES) for tests #8 and #9 confirming the high yield values in Table 14. The optimum conditions derived during this phase of testing were a reaction temperature near 350°C for at least 60 minutes under an argon flow of 150 ml/min. The high temperature runs were problematic in the reaction of the silica boats and air leakage of the system.

Testing with uranium oxide (U_3O_8), rare earth oxides, and ammonium bromide was performed in the furnace shown in Figure 114 in a hooded area of the Analytical Laboratory. Given in Table 15 is a summary of those tests including results. For the first three tests, the ratio of La_2O_3 and Nd_2O_3 relative to U_3O_8 was greater than that expected for a moderate burnup (~50 GWd/t) LWR fuel to determine feasibility. The ratio in the second three tests was more prototypical of actual fuel. The amount of ammonium bromide for all tests was in excess of equation (5) to allow sufficient quantities as reactant. The reaction temperatures were slowly raised to the values shown in Table 15 to prevent sublimation of the NH_4Br prior to reaction. Argon flow rates were lowered to 50 ml/min at the reaction temperature for tests #4 through #6 in an attempt to avoid the loss of NH_4Br. As before, the reaction of the silica or quartz boat was observed and different materials were tested. For tests #3 and #6, the distillation portion of the test was not performed in order to discern whether the product from the reaction portion of the experiment was a bromide or oxybromide.

Table 15. Summary of experiments with La_2O_3, Nd_2O_3, NH_4Br, and U_3O_8 under Ar

Test	NH4Br (g)	La2O3 (g)	Nd2O3 (g)	U3O8 (g)	Reaction Temp. (Cel)	Ar Flow (ml/min)	Boat Material	Distill Temp. (Cel)	RE Reacted (%)	U Reacted (%)
1	0.239	0.019	0.036	1.097	~400	150	Silica	1000	<1	<0.1
2	0.492	0.010	0.034	1.847	~300	150	Silica	1000	<2	<0.1
3	0.420	0.019	0.038	1.150	~300	150	Silica	NA	~97	<1.0
4	0.118	0.004	0.007	1.119	250	50/200	Inconel	1000	<1	<0.1
5	0.203	0.007	0.013	1.142	250	50/200	Pt	1000	<1	<0.1
6	0.198	0.007	0.012	0.662	250	50	Pt	NA	~49	4

With the high temperatures of the distillation cycle during tests #1 and #2, the amount of rare earths reacted was minimal as detected by ICP-OES on a water wash of the distilled material. Analyses following a water wash of the solid material remaining after test #3 did confirm a significant reaction had occurred assuming the rare earth bromides are water soluble. Thus, the formation of the oxybromide must be occurring

between the reaction and distillation portions of the tests. Tests #4 and #5 reduced the reaction temperature and argon flow to assure the presence of NH_4Br as a reactant. Obviously from the results, the rare earth oxides were not converted to bromides either due to the distillation temperature or the lower reaction temperature and/or argon flow. If sufficient argon flow is maintained across the reactants, water should be swept away from the reactants, thus preventing oxybromide formation. Another factor to incomplete reaction may be the quantity of rare earth oxides for these tests as compared to tests #1 through #3. Based on the results of test #6, it is assumed that the flow of argon was insufficient to prevent the formation of oxybromide species as determined by ICP-OES analyses of the residual material. Continued testing will increase the argon flow to reduce the formation of oxybromide followed by a distillation temperature of 1000°C with a platinum boat to prevent deleterious side reactions.

Irradiated LWR Testing

A test was performed in the declad and oxidize (DEOX) furnace located in HFEF with irradiated LWR fuel (BR-3) that had been previously oxidized to U_3O_8 at 500°C and taken to 1200°C for volatile off-gas removal. Following off-gas removal, the fuel was also taken to 1250°C and 1300°C under a static argon atmosphere during FY 2011 in an attempt to precipitate or segregate rare earth oxide nodules from the solid solution U_3O_8 matrix. Although these phases have been documented [P. Taylor, U.S. Patent 5,597,538], the specific conditions necessary for their formation were not clearly defined. Precipitation of the rare earth nodules was not evident in FY 2011 as determined by SEM/ wavelength dispersive analysis (WDA) examinations. The most recent test was performed again at 1300°C for six hours but under an air flow of 1 scfh to promote the decomposition of U_3O_8 to UO_2 and thus, the segregation of rare earth oxides. The crucible assembly shown in Figure 115 was utilized for this test. Air was supplied down the tubing and into the base of the alumina crucible where it was then allowed to pass back up through a porous disc covered with approximately 50 g of BR-3 fuel. The flow of air across the fuel should enhance the formation UO_2 (fluorite phase) by removing the oxygen produced during the decomposition of U_3O_8 (orthorhombic phase). As mentioned, the fluorite phase is enriched with the rare earth nodules. Confirmation by microscopy of rare earth segregation was not performed in FY 2012 due to time constraints but is planned in the near term.

Figure 115. Crucible assembly used for the 1300°C test in DEOX furnace with air

Summary

The purpose of the research program was to investigate the halogenation of rare earth oxides in used LWR fuel with subsequent removal via distillation. Scoping studies at Montana Tech with representative rare earth oxides and various chlorinating agents showed promising results, particularly with ammonium chloride as the chlorinating agent. Optimum conditions were specified for the chlorination and removal of rare earths with ammonium chloride during these studies. Testing at the INL with representative materials including ammonium bromide and uranium oxide gave mixed results; reasonable success converting the rare earth oxides to bromides but removal of the rare earth bromides by distillation at higher temperatures has not been as successful. Testing at the INL with irradiated LWR fuel was not completed pending confirmation of the rare earth precipitation from the U_3O_8.

Supercritical CO_2 Separations

A. Farawila, anne.farawila@pnnl.gov

Current liquid-liquid extraction processes used in recycling irradiated nuclear fuel rely on (1) strong nitric acid to dissolve uranium oxide fuel, and (2) the use of aliphatic hydrocarbons as a diluent in formulating the solvent used to extract uranium. The nitric acid dissolution process is not

selective. It dissolves virtually the entire fuel meat which complicates the UREX process. In addition, a solvent washing process is used to remove TBP degradation products, which adds complexity to the recycling plant and increases the overall plant footprint and cost.

A liquid or supercritical carbon dioxide (l/sc -CO_2) system was designed to mitigate these problems (Figure 116). Indeed, TBP-nitric acid complexes are highly soluble in l/sc -CO_2 and are capable of extracting uranium directly from uranium oxide (UO_2, UO_3 and U_3O_8) powders. This eliminates the need for total acid dissolution of the irradiated fuel. Furthermore, since CO_2 is easily recycled by evaporation at room temperature and pressure, it eliminates the complex solvent washing process.

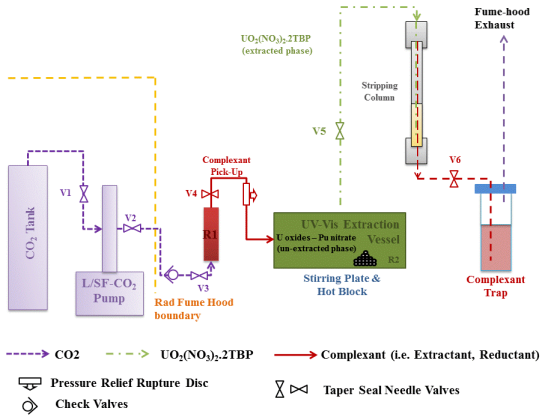

Figure 116. Schematic of the SFE system with stripping column

The extraction system and our online monitoring capability using UV-Vis absorbance spectroscopy directly in sc-CO_2 are shown in Figure 116 and Figure 117. The setup consists of a syringe pump that pressurizes, regulates and delivers CO_2 to the system. The reactor cell (R1) is a 7.5 mL column with an entry and an exit for the fluid at each end. The extractant (TBP-nitric acid complex) is delivered to this R1 cell at the start of an experiment via a syringe. The high-pressure extraction cell (R2) is where the uranium oxides are delivered prior to extraction. R2 fits inside an aluminum hot block and its temperature is controlled by a regulator using a thermocouple inside the cell. R2 also doubles as a UV-Vis cell [S.I. Photonics, Tucson, AZ], where fiber optics are used to measure the absorbance of the fluid and its components under pressure. The cell path-length between the fiber optics was measured to be 0.7 cm. The cell can also be stirred using a traditional magnetic stirrer inside the cell that is controlled by the stirring plate on which the hot block sits.

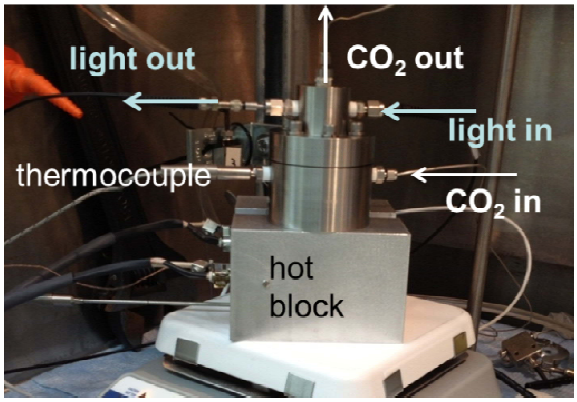

Figure 117. Extraction cell (R2, on top of the hot block for better view) with online monitoring

For this project, researchers demonstrated:

1. A reprocessing scheme starting with the selective extraction of uranium from solid uranium oxides into a TBP-HNO3 loaded sc-CO_2 phase,
2. Back extraction of uranium into an aqueous phase, and
3. Conversion of recovered purified uranium into uranium oxide.

The purified uranium product from step 3 can be disposed of as low level waste, or mixed with enriched uranium for use in a reactor for another fuel cycle.

Using this system, researchers determined the UREX efficiencies and kinetics for different oxides and under different physical and chemical conditions: l/sc -CO_2 pressure and temperature, and TBP/HNO_3 complex used. Figure 118 shows $UO_2(NO_3)_2(TBP)_2$ solubility in CO_2 measured by UV-Vis at different temperature settings vs. pressure (top) and density (bottom). At 40°C, [U] reaches a plateau after 3500 PSI as all the $UO_2(NO_3)_2(TBP)_2$ is dissolved in the CO_2 phase. At 50°C and at 60°C the solubility increases with pressure (and density). At 25°C, where CO_2 is liquid, not supercritical, the solubility is lower and varies little with increasing pressure. At 60°C, the added benefit of the higher temperature is

overcame by the loss in density, and therefore the pressure needs to go to ~4000 PSI to reach the solubility measured at 40 and 50°C. The setting at 50°C and 2900 PSI offers the best compromise, as more than 90 % of the complex is dissolved while keeping the pressure at a reasonable level. This setting was therefore used for the rest of this study.

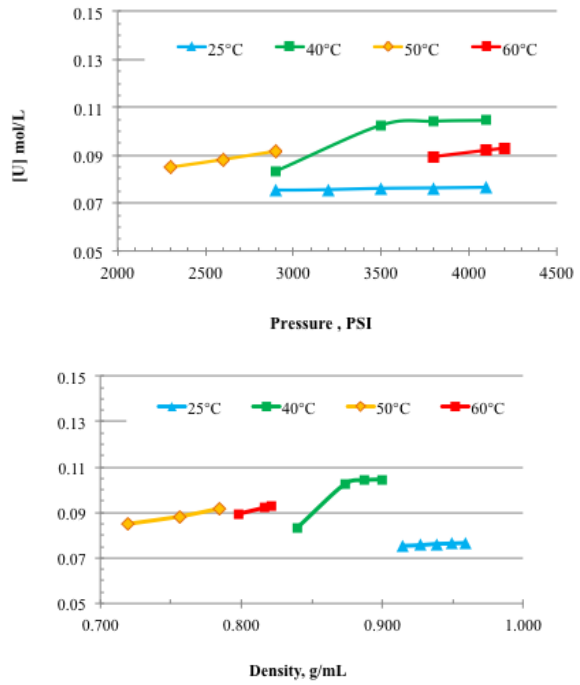

Figure 118. Uranium concentration in CO_2 measured by UV-Vis at different temperature settings vs. pressure (top) and density (bottom).

Additional dissolution experiments showed that the composition of the TBP-nitric acid complex is an important dissolution factor. The complex with the higher nitric acid to water ratio (i.e., $TBP(HNO_3)_{1.8}(H_2O)_{0.4}$) dissolve more uranium (Figure 119, top) than complexes with lower ratios (i.e., $TBP(HNO_3)_{0.8}(H_2O)_{0.4}$ or $TBP(HNO_3)_{0.4}(H_2O)_{0.7}$). The former complex was therefore used for the rest of this study. Figure 119 (bottom) shows the dissolution of different oxide in sc-CO_2 using the optimized settings previously discussed (50°C and 2900 PSI, $TBP(HNO_3)_{1.8}(H_2O)_{0.4}$ complex). UO_2 and UO_3 are dissolved in CO_2 with fast kinetics while U_3O_8 dissolution reached a plateau at a third of the expected absorbance. This low recovery is certainly due to the crystal structure of the oxide.

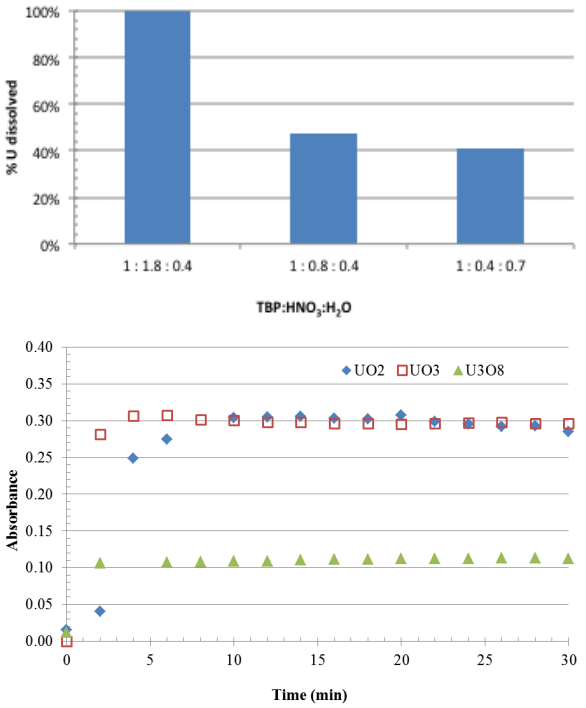

Figure 119. (Top) % uranium dissolved in sc-CO_2 (2900 PSI, 50°C) using different TBP/nitric acid complexes. (Bottom) Dissolution of 0.3 g of different uranium oxide in sc-CO_2 at 50°C and 2900PSI using 2mL of $TBP(HNO_3)_{1.8}(H_2O)_{0.4}$

To complete the extraction and recovery cycle, researchers then demonstrated uranium back extraction from the U-TBP loaded sc-CO_2 phase into an aqueous phase. Different stripping solutions were investigated. The best stripping solution was chosen for its ability to quantitatively recover uranium from the dense U-TBP-CO_2 phase into a small aqueous volume. Researchers demonstrated that a solution of ammonium carbonate ($(NH_4)_2CO_3$, 2 mol/L) was able to quantitatively recover uranium. However some precipitates are formed in the process. To eliminate the precipitate, researchers used hydrogen peroxide, which react with carbonates to form peroxymonocarbonate ions and with uranyl carbonate to form the uranyl peroxo-carbonato complex, both more soluble in the aqueous phase.

Another aspect of this project was to limit proliferation risks by either co-extracting uranium and plutonium or by leaving plutonium behind by selectively extracting uranium. Researchers reported that the former is easily achieved, since plutonium is in the tetravalent or hexavalent

oxidation state in the oxidizing environment created by the TBP-nitric acid complex, and is therefore co-extracted. The latter is more challenging, as a reductant or complexant to plutonium has to be used to selectively extract uranium. After undertaking experiments on different reducing or complexing systems (e.g., AcetoHydroxamic Acid (AHA), Fe(II), ascorbic acid), oxalic acid was chosen as it can complex tetravalent actinides (Pu, Np, Th) in the aqueous phase while allowing the extraction of hexavalent uranium in the sc-CO_2 phase.

Finally, researchers show results using an alternative media to commonly used aqueous phases: ILs. Researchers show the dissolution of uranium in ILs and its extraction using sc-CO_2 with and without the presence of AHA. The possible separation of trivalent actinides from uranium is also demonstrated in ILs using neodymium as a surrogate to trivalent actinides and diglycolamides as the extractant.

In conclusion, researchers were successful in demonstrating UREX into supercritical fluids, and its back extraction and recovery as uranium oxide. Researchers also showed the selectivity of this method for uranium, by inhibiting plutonium and neptunium co-extraction with uranium. Finally, researchers showed that ILs could also used as a supporting media for the separations. This technology has low environmental impact and would enable sustainable fuel cycles by greatly reducing the amount of liquid waste generated.

Reference

1. Farawila, A. F., M. J. O'Hara, H. Z. Taylor, C. M. Wai, and Y-J. Liao, Report # PNNL-21590 submitted to DOE/FCRD in July 2012, "Selective Extraction of Uranium from Liquid or Supercritical Carbon Dioxide"

Functionalized Ultra-Porous Ceramic Nanofiber Membranes

T. M. Nenoff, tmnenof@sandia.gov

This project focused on the methodology, characterization, and preliminary results of developing thermally stable ultra-porous polycrystalline ceramic nanofiber membranes as nuclear waste separation and sequestration scaffolds for nuclear fuels, in particular Modified Open Cycles (MOC). By combining a modified sol-gel chemistry and coaxial electrospinning, amorphous TiO_2 nanofibers were first obtained by electrospinning, and subsequently converted to anatase fibers with controllable interior porous structures via calcination without changing their morphology. Researchers anticipate that by crushing the fuel and performing a simplified heating and/or hot gas extraction process, researchers will be able to separate out the volatile fission products (e.g., Cs, Sr, Rb) and poisons (e.g., Xe) by using such ceramic nanofiber membranes as specific absorbent materials, which subsequently can be disposed in encapsulated glass waste forms. Functionalized ceramic nanofiber membranes are being examined for gas separations for these various dry separations options, as an innovative one-step extraction process in modified open fuel cycle.

The electrospinning technique is an electrostatically induced assembly process, and is an efficient, inexpensive, and scalable approach to synthesize nanofibers. In a typical electrospinning process, a viscoelastic polymer solution is ejected from a metallic nozzle under a strong external electric field. Electrostatic charges are therefore built up on the surface of the polymer solution. When the repulsive force between these charges overcomes the surface tension of the fluid, an electrified liquid jet is induced, which is uniaxially and extensively stretched to form continuous thin fibers and gets deposited on the collection screen. The morphology and diameter of the electrospun fibers depends upon material properties, including molecular weight, viscosity, electrical conductivity, and surface tension of the solvent, as well as operational conditions, including strength of the electric field, feeding rate, separation distance between source and collector, and humidity.

There are two unique morphological characteristics of porous nanofiber membranes: porous open structures that provide low resistance to mass transport, and large volumetric surface area that provide high efficiency of target-absorbent fiber membrane interaction. One can also extend this method to process many different types of ceramic nanofibers by simply changing the sol-gel precursors, including the

technologically important metal oxides TiO_2, SiO_2, Al_2O_3, V_2O_5, ZrO_2, $MgTiO_3$, CeO_2, SnO_2, $BaTiO_3$, or MOXs. Enhanced affinity and selectivity to the radionuclide contaminants of interest can be achieved by functionalizing the porous surface of the nanofiber membranes with both chemisorption and physisorption, and porous nanofibers can serve as excellent support for other extremely high surface area nanomaterials (MOFs, zeolites, etc).

Researchers demonstrated a successful method of producing porous titania nanofibers through a modified sol-gel technique in conjunction with coaxial electrospinning.[1] Polycrystalline nanofibers made of anatase TiO_2 were chosen to demonstrate the concept, and subsequent functionalization was added onto the fiber membranes to study the iodine separations and glass encapsulation in final waste forms. In particular, researchers successfully functionalized the nanofibers with Ag nanoparticles for iodine sorption studies as proof of concept for gas capture at lower temperatures. See Figure 120. Upon exposure of the Ag-TiO_2 nanofibers to I_2 gas at 90°C, the nanofibers formed AgI-TiO_2 during the I_2 capture. This is the proof of concept for functionalization of the nanofibers and use in volatile off gas capture.

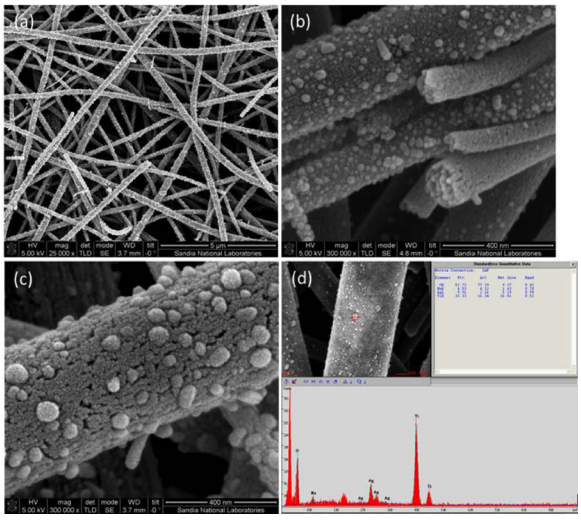

Figure 120. (a)-(c) SEM of Ag deposited on TiO_2 fibers by citrate reduction method. (d) EDX spectrum indicating the presence of Ti, O, and Ag peaks.

The next step was the functionalization of the nanofibers with MOFs for both initial iodine capture and then for our project target of high temperature MOC off gas capture, such as Xe. Researchers successfully synthesized nanocrystallites of ZIF-8 MOF (used by us in I_2 capture studies), and then incorporated those nanocrystals into the TiO_2 nanofiber electrospinning (see Figure 121). Our next planned experiments were to be in both I_2 and Xe gas capture. However, due to programmatic changes, this project is not funded for FY 2013 and all experimentation has stopped. Detailed results on the nanofibers experimental work are reported by Liu, et. al., in FCRD-SWF-2012-000359 and SAND2012-8025.[2]

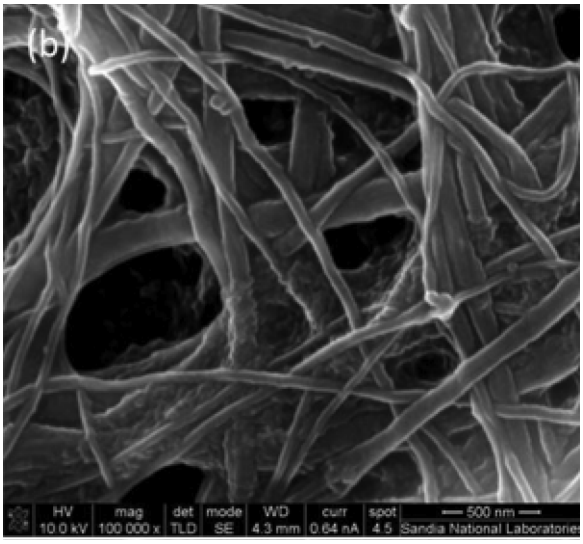

Figure 121. SEM of MOF-TiO_2 composite fiber membranes; ZIF-8 crystallites are cubic in shape and imbedded in the fibers.

This invention could have a direct impact on the spent fuel separations as it could significantly reduce the cost and complexity of reprocessing, provide a much simpler plant with a small footprint and small number of waste streams. It will also be an important element of an integrated energy and waste management policy.

Complimentary advanced modeling and simulation studies based on neutronic characterization of SNF in a simplified MOC were also carried out. In particular, the focus was on the SNF reprocessing using Atomics International Reduction-Oxidation (AIROX) or the enhanced oxidation/ chlorination process. These processes remove varying amounts of gases and volatile species from spent reactor fuel without requiring aqueous separations. This study examined recycle

of the residual fuel in reactors after blending with fresh uranium oxide fuel. The overall goal of this work was to determine if simplified modified open fuel cycles are feasible and to help target the specific elements which should be removed using the gas sorption/separations ceramic nanofibers.[3]

References

1. Nenoff, T. M., and H. Liu, "Nanoporous Ceramic Nanofiber Membranes for Highly Selective Gas/Ion Capture", Sandia Technical Advance for U.S. Patent, SD# 12197, Dec 2011.
2. Liu, H., N. Bell, B. B. Cipiti, T. G. Lewis, D. F. Sava, and T. M. Nenoff, "Functionalized Ultra Porous Titania Nanofiber Membranes" Sandia National Laboratories, SAND2012-8025; and FCRD-SWF-2012-000359.
3. Lewis, T. G., et al., "Modified Open Cycle Modeling". FCRD-SWF-2012-000259, July 2012; and SAND2012-5456, July 2012.

Patents

1. Nenoff, T. M., and H. Liu, "Nanoporous Ceramic Nanofiber Membranes for Highly Selective Gas/Ion Capture", Sandia Technical Advance for U.S. Patent, SD# 12197, Dec 2011.

CHAPTER 9
ADVANCED WASTE FORMS

CHAPTER 9: ADVANCED WASTE FORMS

J. D. Vienna, john.vienna@pnnl.gov

Ceramics

Ceramics for HLW Raffinate

K. S. Brinkman, kyle.brinkman@srnl.doe.gov,
and M. Tang

Ceramic (or crystalline) waste forms incorporate the radionuclides in the waste as part of the crystal structure. As such, ceramic forms are tailored to create certain minerals (i.e., unique crystalline structures) that will host the radionuclides by binding them in their specific crystalline network. Tailoring of a ceramic waste form is based on the knowledge that there are many naturally produced minerals containing radioactive and non-radioactive species very similar to the radionuclides of concern in wastes from fuel reprocessing. The research conducted in this work package is aimed at taking advantage of the long term thermodynamic stability of crystalline ceramics to create more durable waste forms (as compared to HLW glass) in order to reduce the reliance on engineered and natural barrier systems. Durable ceramic waste forms that incorporate a wide range of radionuclides have the potential to broaden the available disposal options and to lower the storage and disposal costs associated with advanced fuel cycles. Assemblages of several titanate phases have been successfully demonstrated to incorporate radioactive waste elements, and the multiphase nature of these materials allows them to accommodate variation in the waste composition. Recent work has shown that they can be successfully produced from a melting and crystallization process

SRNL and LANL have focused on developing crystalline ceramic waste forms to incorporate the combined cesium, strontium, lanthanide, transition metal (CS/LN/TM) waste streams of interest. Crystalline phases consisting of perovskite, hollandite, pyrochlore, zirconolite, and powellite phase assemblages were targeted by a melt and crystallization process. FY 2012 activities included (1) developing a reference ceramic formulation, (2) continued synthesis of select individual phases hollandite focusing on Cs incorporation (3) initiating data collection in support of potential melting demonstration, and (4) evaluating the radiation stability of single and multi-phase ceramic waste forms.

Figure 122a displays the microstructure of an optimized hollandite waste form obtained after a melt and crystallize process. XRD analysis indicated the presence of a single crystalline phase and EDS chemical analysis confirmed Cs incorporation into the crystalline structure resulting in an approximate stoichiometry of $Ba_1Cs_{0.4}Cr_{1.2}Al_{0.2}Fe_1Ti_{5.7}O_{16}$. Figure 122b displays the microstructure and EDS chemical analysis regions of a multi-phase waste form incorporating the combined CS/LN/TM waste streams of interest. The spots labeled in Figure 122b correspond to regions that were chemically analyzed by EDS. The XRD phase analysis and EDS chemical analysis results used together to identify the crystalline phase analyzed present in the spots labeled in Figure 122b; these results are listed in.Table 16.

Table 17 displays the reference ceramic composition that will serve as the basis for further FY 2013 development and testing. The principal difficulties encountered during processing of the "reference ceramic" waste form by a melt and crystallization process were the incomplete incorporation of Cs into the hollandite phase and the presence of secondary Cs-Mo non-durable phases. In the single phase hollandite system, these issues were addressed in this study by refining the compositions to include Cr as a transition metal element and the use of Ti/TiO_2 buffer to maintain reducing conditions.

(a)

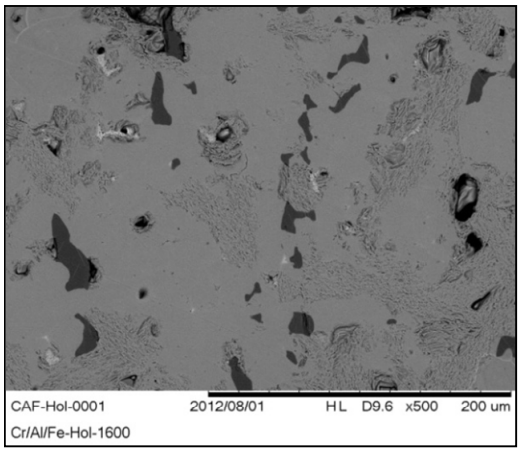

(b)

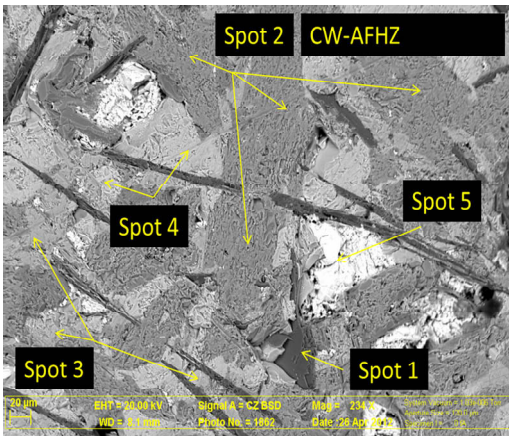

Figure 122. Backscattered Electron Micrograph of a Polished Surface of Sample (a) Single Phase Hollandite ($Ba_1Cs_{0.4}Cr_{1.2}Al_{0.2}Fe_1Ti_{5.7}O_{16}$) and (b) Reference Ceramic Multi-Phase Waste Form

*Table 16. Summary Crystalline Phases in Figure 1(b) (*Crystalline phases determined from XRD measurements and EDAX elemental analysis)*

Spot	Crystalline Phases
1	Al_2O_3
2	Hollandite- $BaAlTi_5O_{14}$
3	Zirconolite-$CaZrTi_2O_7$
4	Perovskite- $CaTiO_3$
5	Powellite $(Ba,Ca)MoO_4$

Table 17. Reference Ceramic Compositions (wt%)(Fe and/or multivalent transition metal)*

Composition	wt %	Targeted Phase
Waste	24	
Al_2O_3	7	*Hollandite*
TiO_2	51	*Hollandite, Perovskite, Zirconolite*
CaO	2	*Zirconolite*
BaO	10	*Hollandite*
$*Fe_2O_3$	6	*Hollandite*

An examination of the viscosity of crystalline ceramic waste form melts as a function of temperature and composition is especially important when considering industrial scale melt processing. The temperature window where flow will occur as well as the critical temperature where crystallization proceeds must be determined. Figure 123 presents the results of initial investigations into the viscosity versus temperature relations for crystalline ceramic waste form melts. A nominal sample composition of CS/LN/TM 11 was chosen for initial characterization, which closely resembles the reference ceramic composition. As shown in Figure 123, the melt is very fluid above 1400°C, with a relatively low viscosity that had little temperature dependence. The melt crystallized rapidly when cooled to between 1350 and 1400°C, which locked up the viscometer and prevented further measurement. The sample was then reheated to approximately 1500°C for a final viscosity measurement. After crystallizing and remelting, there was no change to the measured viscosity value at 1500°C. These initial experiments indicate that the pour spout must be maintained above 1400°C to avoid flow blockages due to crystallization for this composition.

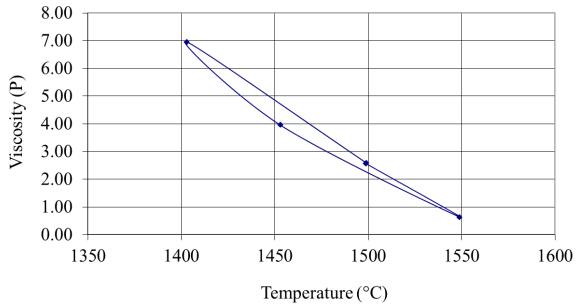

Figure 123. Viscosity (P) versus Temperature (°C) for Crystalline Ceramic Waste Form

LANL performed a series of *in situ* electron irradiations using 300-keV electrons generated in a Tecnai F30 transmission electron microscope (TEM) in the Electron Micrsocopy Laboratory. By focusing electrons in the TEM beam on certain crystalline phases of the waste forms, it was possible to simulate radiolysis effects that might be experienced by crystalline ceramic waste forms. Figure 124 shows the impact of electron irradiation on a powellite $BaMoO_4$ melt and crystallized sample. In-situ electron irradiation studies indicated that both $CaMoO_4$ and $BaMoO_4$ powellite phases exhibit radiation stability up to 1000 years at anticipated doses with a crystalline to amorphous transition observed after 1×10^{13} Gy. Additional *in-situ* electron irradiations simulating radiolysis effects indicated hollandite undergoes a crystalline to amorphous transition after a a radiation dose of 10^{13} Gy, which corresponds to approximately 1000 years at anticipated doses (2×10^{10}-2×10^{11} Gy). Dual-beam ion irradiations employing light ion beam (such as 5 MeV alpha) and heavy ion beam (such as 100 keV Kr) studies indicate that reference ceramic waste formsare radiation tolerant to the β-particles and α-particles, but are susceptible to a crystalline to amorphous transition under recoil nuclei effects.

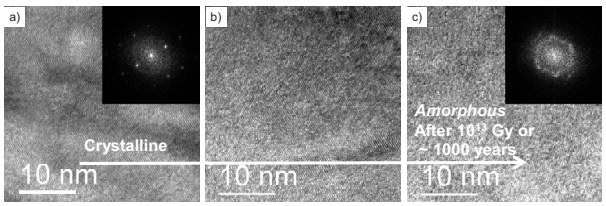

Figure 124. High-Resolution TEM Images Reveal Crystalline to Amorphous Transition in (Ba,Ca)MoO_4 Powellite phase after 10^{13}Gy or ~ 1000 years of self-irradiation.

Initial FY 2013 activities will begin by targeting an alternative waste stream with lower Mo content (3% instead of 14%). This new composition, which includes the refined hollandite target phase with Ti/TiO_2 buffer additions, will be melted in air, argon, and a 1%H_2 balance argon atmosphere. The phase formation and secondary phase content will be evaluated with particular attention paid to Cs and Mo elemental partitioning. In addition to melt processing, alternative fabrication routes are being considered including Spark Plasma Sintering (SPS) and HIP. This work is part of collaborative activities with Alfred University as part of a DOE-NEUP program on advanced waste forms and the Australian Nuclear Science and Technology Organization (ANSTO). In addition, compositions will be developed and fabricated in FY 2013 with a new baseline waste stream including TRU actinide elements. The principal goal of FY 2013 activities remains to demonstrate both the composition and processing for incorporating combined Cs/Sr, lanthanide, and transition metal (Mo,Zr), and TRU elements into crystalline ceramic waste form with promise of higher waste loading and durability as compared to a borosilicate glass (BSG) baseline.

Ceramics for Tc

T. Hartmann, thomas.hartmann@unlv.edu, A. J. Alaniz (UNLV); M. Tang, G. Jarvinen (LANL); and K. Sickafus (UT)

At UNLV, researchers continued our experimental work regarding the incorporation of Tc-99 into ternary oxides of different structure types. Hereby, researchers were testing our previously synthesized ceramic Tc-waste form candidates for solid solution formation with tin (Sn) and tellurium (Te). In this endeavor samples of the following stoichiometry were fabricated by conventional dry chemical synthesis: pyrochlores ($Nd_2Tc_{2-2x}Sn_xO_7$, $Nd_2Tc_{2-2x}Te_xO_7$), perovskites as ($SrTc_{1-x}Sn_xO_3$), and a layered perovskites ($Sr_2Tc_{1-x}Sn_xO_4$), while varying the Sn (or Te) to Tc ratio from $0\leq x\leq 1$ in steps of x=0.25.

The synthesis of the ternary pyrochlores in the solid solution system $Nd_2Tc_{2-2x}Sn_xO_7$was successful and e.g., the $Nd_2(Tc_{0.5}Sn_{0.5})_2O_7$ pyrochlore is well crystallized and its lattice parameter was refined to a = 10.52639(5) Å,

which is in a reasonably good agreement with the expected value. On the other hand the ternary pyrochlores in the system $Nd_2Tc_{2-2x}Te_xO_7$ did not show significant solubilities for tellur and the lattice parameter of the "$Nd_2(Tc_{0.5}Te_{0.5})_2O_7$" pyrochlore specimen was refined to a = 10.40428 (4) Å, which is only slightly smaller than the pure $Nd_2Tc_2O_7$ pyrochlore phase (a = 10.40629(3) Å). Also TeO_2 has shown itself as not compatible with the used Pt envelopes at 1100 °C and significant corrosion of the Pt foils was observed.

For the solid solution system $SrTc_{1-x}Sn_xO_3$ (orthorhombic space group *Imma*) and based on the results of least square lattice parameter- and Rietveld structure refinement, isomorphic substitution of up to 25 at.% Sn^{4+} for Tc^{4+} was observed, while solid solution formation by substituting Tc for Sn in the $SrSnO_3$ lattice (orthorhombic space group *Pbnm*) is very limited and below 2 at.%.

Also the isomorphic substitution of Sn for Tc in the $Sr_2(Tc_{1-x}Sn_x)O_4$ lattice (tetragonal space group *I/4mmm*, K_2NiF_4 structure type) is limited and a maximum substitution of 23 (±5) at % Sn for Tc can be postulated. On the other hand, measurable isomorphic substitution of Tc for Sn in the $Sr_2(Tc_{1-x}Sn_x)O_4$ lattice was not observed.

Researchers furthermore entertained an engineering senior student design project with three students from mechanical-, electrical-, and computer engineering to complete the prototype development of a remotely operated hot uniaxial press (RoHUP). This RoHUP device is designed to fabricate dense, gram-size Tc-99 bearing ceramic as waste forms and features electronic control and feedback systems to set and monitor the parameters for pressure, load, and temperature. The RoHUP operates wirelessly via portable computer using Bluetooth® technology and will be installed in a standard atmosphere controlled negative pressure glove box to address the growing demands of radiation safety, and also to allow for sintering under inert conditions (e.g., under Ar, He, N_2). This RoHUP can be utilized for a broad range of applications such as the synthesis and fabrication of e.g.(1) novel ceramic waste forms, (2) advanced oxide dispersion fuels, (2) specimen of air-sensitive systems, (3) metallic alloys, (4) specimen applying (nano) powder metallurgy, (5) cladding-fuel diffusion couples.

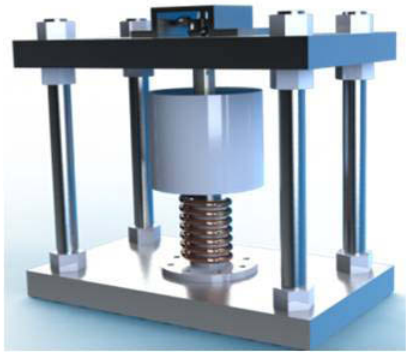

Figure 125. Conceptual drawing of the RoHUP device with a vertical split tube furnace

LANL is developing tailored ceramic waste forms to incorporate various fission product waste streams. *Ruddlesden-Popper* phases, $A_{n+1}B_nO_{3n+1}$ with A^{2+} = (Sr, Ba) and B^{4+} = (Ti, Ru, Tc), are attractive because researchers should be able to incorporate two highly radioactive fission products, such as ^{90}Sr and ^{99}Tc, simultaneously in one crystalline phase.

A hot-forging technique (see Figure 126) has been used to obtain the n = 2 ($Sr_3Ti_2O_7$) and n = ∞ ($SrTiO_3$) members of Ruddlesden-Popper phase $Sr_{n+1}Ti_nO_{3n+1}$.

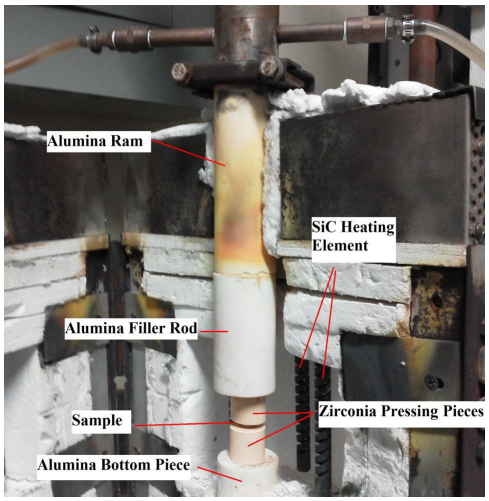

Figure 126. Hot-forging set up.

Pure phase and high density (>95% theoretical) samples were achieved (see Figure 127). These polycrystalline samples were irradiated with 200 keV He ions to a fluence of 2×10^{17} ion/cm^2 (corresponding to a peak dose at 5

dpa) at room temperature to study radiation damage effects.

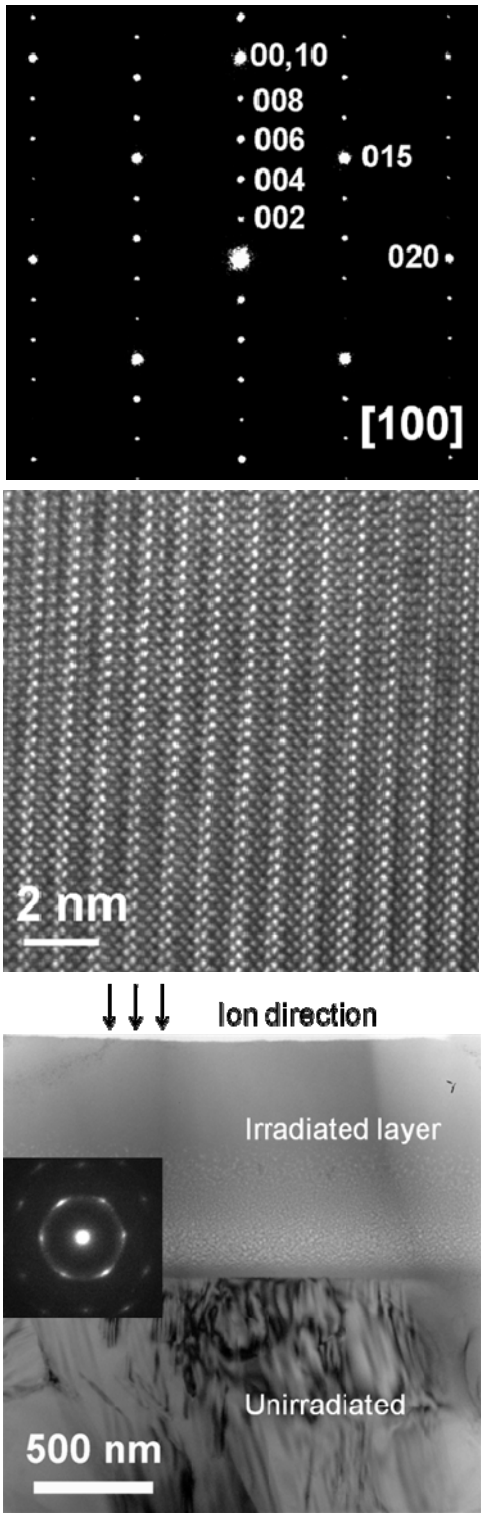

Figure 127. TEM observation of $Sr_3Ti_2O_7$. Left and middle are select area diffraction pattern and high resolution image for pristine sample; right is cross-sectional bright field image for He irradiated sample.

A detailed microstructural investigation on pristine and irradiated samples was performed using grazing incidence X-ray diffraction (GIXRD) and TEM. Three phenomena are revealed upon comparing pristine versus irradiated samples in Figure 128. First, both compounds interplanar lattice spacings increased after irradiation. Second, peak broadening suggests incredibly small crystalline domains due to irradiation (TEM results confirmed that initial microsized grains were refined into nano-size grains, micrograph not shown here). Third, experiment results reveal an amorphization in irradiated $Sr_3Ti_2O_7$, while no amorphous is observed in irradiated $SrTiO_3$ (to our knowledge, it is a very high dpa without amorphization, perhaps a record for perovskite).

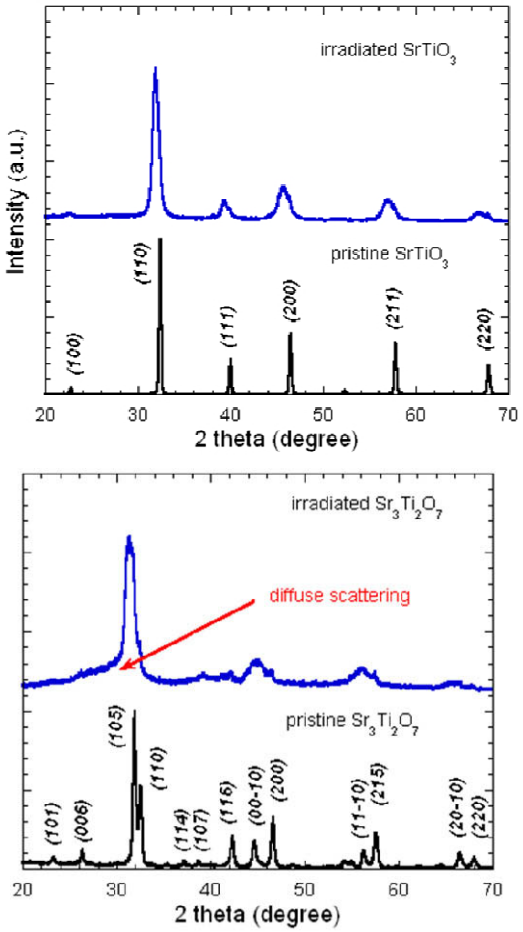

Figure 128. GIXRD measurements for $SrTiO_3$ (top) and $Sr_3Ti_2O_7$ (bottom) before and after He irradiation.

Initial FY 2013 activities will begin with characterizing heavy ion 600 keV Kr irradiated these above two samples, and comparing with

light ion 200 keV He irradiation. Researchers will try to incorporate other fission products, like Mo/Tc into prevoskite phase, and test their radiation stability.

Glass Ceramic Waste Form Development

Glass Ceramic Waste Form Development

J. V. Crum, jarrod.crum@pnnl.gov, C. Rodriguez, J. McCloy, and B. J. Riley (PNNL), and M. Tang (LANL)

Multiphase BSG ceramic is being developed for immobilization of the HLW raffinate stream generated during separation of UNF [Crum et al. 2011; Crum et al. 2010]. The proposed glass ceramic waste form consists of powellite, oxyapatite, Ln-borosilicate, and a BSG matrix. Development work to date has focused on laboratory testing to characterize phase assemblage, thermal and irradiation stability, and short term static leach testing.

This year, work transitioned to focus on creation of a technology maturation plan (TMP) to direct future waste form development activities, formulation for the first ever melter test of these glass ceramics, and documenting glass ceramic formulation work in the literature [Crum et al. 2012b]. Summaries and accomplishments of these major actives are given below.

A TMP was generated this year to plan/guide development of the glass ceramic waste form [Vienna et al, 2012]. An expert panel was convened to identify the critical technology elements (CTEs), rate their current technology readiness levels (TRLs), and activities required to advance the TRLs to levels 4 then 6. The CTEs identified were: (1) waste feed mixing, sampling, and analysis, (2) feeding, melting, and pouring, (3) glass ceramic formulation, (4) canister cooling and crystallization, and (5) canister decontamination. CTEs 1–4 were rated at TRL level 1, while canister decontamination has been demonstrated up to TRL 4. The TMP was utilized to plan development, processing, and preliminary engineering work for FY 2013.

In preparation of the melter test, the processing properties of three candidate glass ceramics were characterized. Viscosity, electrical conductivity, and crystallinity were each examined as a function of temperature, providing the necessary information for a selection of an optimal candidate reference formulation, as documented in a data package [Crum et al. 2012a]. Listed below are some of highlights of the melter run support work.

The viscosity of the glass ceramic exhibits roughly Arrhenius behavior above ~ 1120°C, similar to glass. Below this temperature, rapid crystallization results in dramatic increases in viscosity (Figure 129) and a change from Newtonian- to Bingham-like rheology. These data show that the glass ceramic can be processed as a single phase melt similar to BSG melter technology at temperatures above 1250°C. Second, viscosity data shows that crystals precipitate/dissolve in <10 minutes at crucible scale.

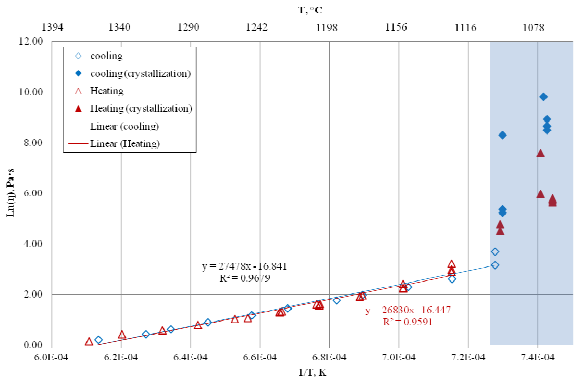

Figure 129. Arrhenius viscosity relationship of GC-Mo-Li-6.25 glass ceramic. The blue shaded region denotes the temperature range where the rheology is significantly impacted by crystallization.

Electrical conductivity was found to be a critical property because of the limited amount of light alkali (Li, Na, and K) in the waste form relative to typical BSG waste forms. A new glass ceramic was formulated (ID# GC-Mo-Li-6.25) with added alkali to increase conductivity into an acceptable range (10 - 60 S/m) at the target operating temperatures of 1250 - 1350°C, shown in Figure 130.

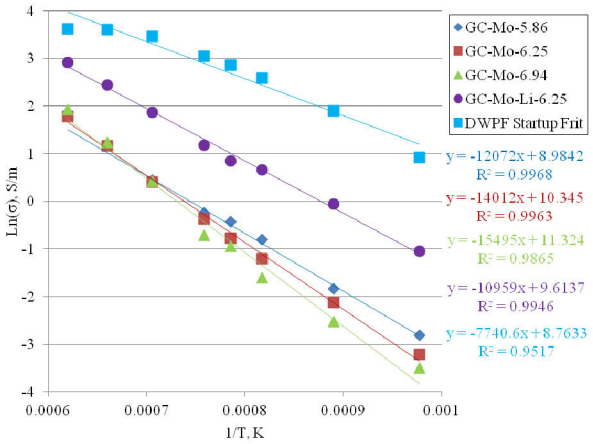

Figure 130. Arrhenius electrical conductivity relationship of glass ceramics compared to the DWPF-startup standard glass.

Thermal history is also a critical parameter to achieve the target crystalline phases in the glass ceramic waste form. The candidate glass ceramic was surprisingly flexible to cooling rate, showing no impact on targeted crystalline phases achieved or their concentrations. Only crystal size was impacted over the range of cooling rates tested in the lab, 4× (small crystals) to 0.25× (large crystals) shown in Figure 131, where × = centerline cooling rate of a 2" diameter canister.

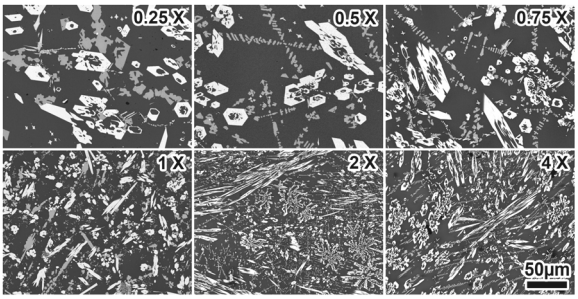

Figure 131. Backscattered electron images (500×) of GC-Mo-Li-6.25 slow cooled at various rates (0.25×, 0.5×, 0.75×, 1×, 2×, and 4×), where× equals the cooling rate at the centerline of a 2' diameter can.

Glass Ceramic Stability

M. Tang, mtang@lanl.gov

LANL focus on characterization and testing procedures on the single- and multi-phase glass ceramics to further develop the glass ceramic waste form for an immobilization HLW raffinate stream. FY 2012 activities include: (1) Characterize glass ceramic waste forms and single phase glass ceramics from PNNL and test their radiation stability, thermal stability, and mechanical properties; (2) Develop model (compositionally simple) glass ceramic waste forms and test their durability and stability.

Characterization, and Stability Testing of Glass Ceramics from PNNL

FY 2012 focused on further characterization and stability test of single phase glass ceramic waste forms and combined glass ceramic waste forms. Selected glass ceramics were subjected to electron and dual ion beam irradiation to simulate self-radiation and test their radiation stability. Thermophysical properties (including thermal conductivity, thermal diffusivity, specific heat capacity) of combined glass ceramic waste forms were measured.

Self-radiation damage and elevated temperature due to decay heat are significant issues for the long term stability of glass ceramic waste forms. Most of the self-radiation in a waste form incorporating fission products is due to beta particle and gamma emission. These emissions cause radiation damage primarily via ionization processes, because both beta and gamma particles induce substantial electronic excitations in a target material. Preliminary evaluations of the radiation damage tolerance of select glass ceramic waste forms were undertaken by subjecting samples to ion beam irradiations using accelerators, and electron irradiation using TEM. Light ions and electrons provide a useful means to examine ionization effects because they deposit nearly all of their energy in solids via electronic loss processes; and heavy ion are used to simulate energetic recoil nuclei interaction which involves *ballistic* processes. Compared with the self-radiation dose rate (10^4–10^5 Gy/h) expected in Cs/Sr waste forms, the high dose rates of electron irradiation using electron microscopes (10^{11}–10^{13} Gy/h) and highly ionizing ion beams (such as protons or helium) using accelerators (10^7–10^8 Gy/h) offer the capability to study radiation effects over the ionizing dose range of interest on laboratory time scales. Available γ sources and doping with short-lived isotopes, such as ^{134}Cs, are not able to achieve the necessary dose level, due to the low dose rate or dopant level.

In the case of nuclear waste in a repository, significant heating is possible: self-heating from β-decay of fission products can result in initial storage temperatures greater than 200°C for non-U.S. commercial HLW glass [Weber et al., 1998]; at desired high waste loadings, storage temperature of Cs/Sr waste forms could be up to 1000°C [Weber et al., 2009]. In our study, the measured sample temperature rise under ion beam irradiations at room temperature is ~10°C; while, the calculated temperature rise from electron-beam-heating is between 10–50°C, depending on different theoretical models and target materials.

Figure 132 is a TEM/electron irradiation study for single phase Oxyapatite sample at room temperature; the electron-beam was operated at 300 keV. High resolution TEM images and inset fast Fourier transforms (FFT) indicate Oxyapatite still keep good crystalline phase after a radiation dose of 10^{13} Gy, which is equivalent to roughly 1000 years of self irradiation dose for a highly loaded Cs/Sr waste form(Weber et al., 2009).

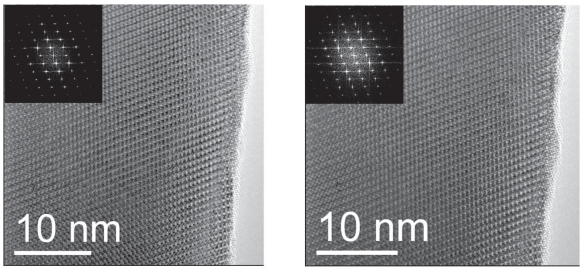

Start (~0 Gy) *(~10^{13} Gy)*

Figure 132. High resolution TEM/electron irradiation results of oxyapatite.

Figure 133 shows XRD patterns obtained from a sample of composition GC-4 before and after the dual beam irradiation at room temperature, 5 MeV alpha (He-light ion) beam with a fluence of 1×10^{17} ions/cm^2 (corresponding to a dose of 5 GGy) and 600 keV Kr (heavy ion) with a fluence of 2.5×10^{15} ions/cm^2 (corresponding to a dose of 4 dpa) sequentially. Sample GC-4 was the first attempt to evaluate a glass ceramic approach for the CS+LN waste streams, which is the highly crystallized multi-phase glass ceramic with the following crystalline phases: oxyapatite($Sr_xNd_{(10-x)}Si_6O_{26}$), RE-borosilicate($Gd_3(BSiO_6)(SiO_4)$), celsian($Ba_xSr_{(1-x)}Al_2Si_2O_8$). There is little difference in the relative intensities among the peaks in the spectra between the pristine and alpha irradiated samples. However, after combined light and heavy ion irradiation damage, the spectra changes significantly and an increased amorphous regime (near 2θ = 24-34°) not present before irradiation. As stated above, these dual beam irradiation results indicate that these materials are radiation tolerant to the β–particles and α-particles, but susceptible to amorphous under recoil nuclei effects.

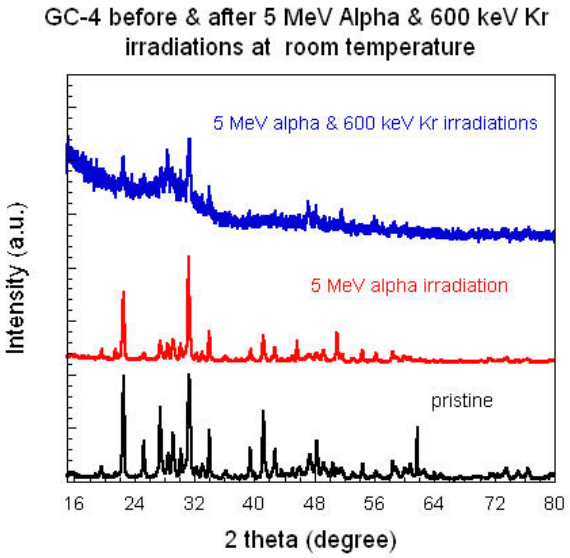

Figure 133. XRD results of GC-4 before and after He & Kr irradiations

Accurate thermophysical properties (thermal conductivity, heat capacity, thermal diffusivity) as a function of temperature are critical to engineering analysis of nuclear materials including nuclear energy waste forms. These properties are important in determining the thermal gradients in a waste form during its fabrication, storage, transport and geological disposal. Thermophysical properties of glass ceramic waste forms provide very useful information on the glass melting, forming process, and crystalline phase formation.

Four kinds of glass ceramic waste form materials with different compositions and waste loadings from PNNL, including GC-4 (no Mo), GC-Mo-5.85, GC-Mo-6.25, GC-Mo-6.94, were prepared for thermophysical properties measurement. Specific heat capacity of glass ceramics was measured from room temperature to

1000°C at the heating rate of 20 °C/minute and cooling rate of 20°C/minute. As illustrated in Figure 134, the heat capacity of GC-4 shows typical Debye temperature dependence; all Mo-glass ceramics contain mid-range glass transition (T_g~600°C), and second glass transition starts ~ 900°C. The glass transition temperature, T_g, is consistent with the thermal diffusivity changes in the same temperature range. Thermal diffusivity of the glass ceramics was measured from room temperature to 1000°C using LFA. As shown in Figure 134, thermal diffusivity showed a reduction in thermal transport observed following glass transition (T_g~600°C) of Mo-glass ceramics.

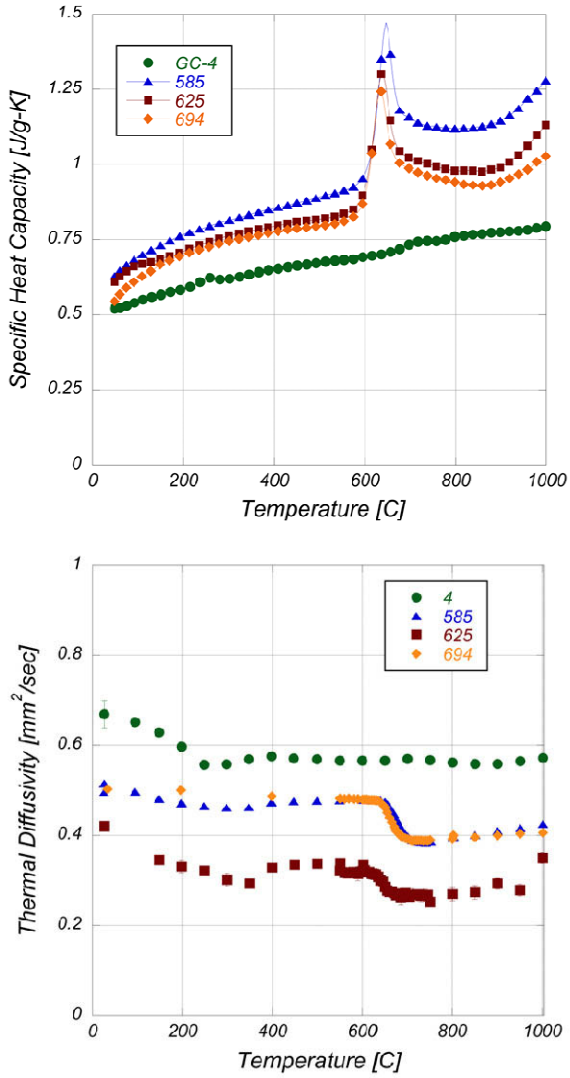

Figure 134. Thermophysical properties on glass ceramics.

Nd-Mo-Borosilicate Glass-Ceramic: Synthesis, Characterization and Response to Ionizing Radiation

LANL is developing glass ceramic waste forms to incorporate CS/LN/TM high Mo waste streams. In particular, researchers fabricate compositionally simple (model) glass ceramic waste forms, in which researchers incorporate just a few fission products. This reductionist approach will make it possible to readily characterize glass ceramic microstructures and to identify the nature of the crystalline inclusions. In FY 2012, new BSG-ceramic with high content of Mo and Nd was synthesized and thoroughly characterized. Behavior of material after it was subjected to 5 MeV He^+ was investigated. 5 MeV He^+ was chosen since it deposits most of the energy as ionizing radiation rather than as nuclear stopping and therefore can be used to simulate self-radiation damage in advanced nuclear waste-forms. As a result of irradiation, slight Mo reduction occurred together with increased number of crystalline precipitates. Those results are interesting for understanding the behavior of systems with high Mo and Nd content such as nuclear waste-forms demonstrating an influence that ionizing radiation can have on the chemistry and microstructure of the waste forms.

Figure 135 shows XRD patterns of as-prepared quenched and slowly cooled Nd-Mo samples, and 5 MeV He irradiated quenched sample.

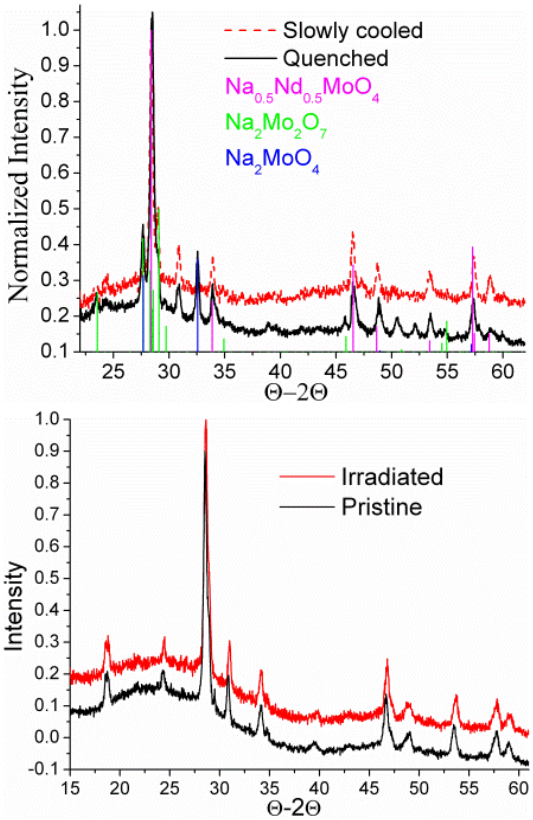

Figure 135. XRD Θ-2Θ scans show the phase composition of as-prepared samples (top) and structural evolution before / after irradiation (bottom).

As seen in the Figure 135, these samples consist of amorphous and crystalline phases, and the phase compositions of crystalline fraction being similar after either quenching or cooling. Since Mo was determined to be 6-valent, the crystalline phases were identified as $Na_{0.5}Nd_{0.5}MoO_4$ and $Na_2Mo_2O_7$. Their mole ratio was about 2:1. XRD results also reveal no remarkable structural difference in quenched sample before and after ion irradiation. SEM images (Figure 136) showed that the microstructure changed during the course of irradiation. Specifically, the size of small crystalline precipitates around bigger islands increased significantly after irradiation.

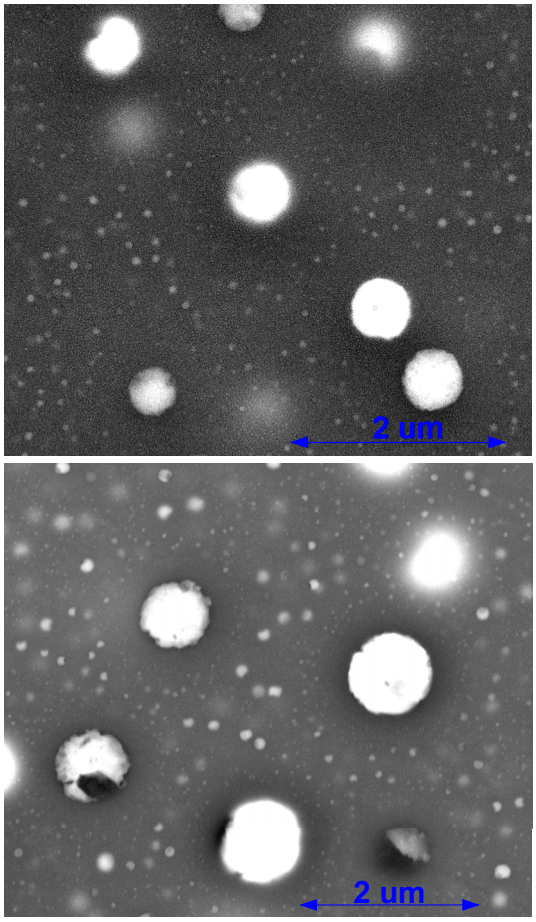

Figure 136. SEM images of quenched glass ceramics before (top) and after (bottom) irradiation. The size of crystalline islands increases during irradiation.

Results of X-ray photoelectron spectroscopy (XPS) measurements on pristine and irradiated material are shown in Figure 137. In a qualitative comparison of the Mo3d peaks, it is seen that the irradiated sample shows a higher fraction of reduced Mo species (more spectral weight at lower binding energy) after prolonged sputtering with 1 keV Ar+. Due to long sputtering time, a steady state sputter damaged layer is achieved. Therefore, since both irradiated and reference pristine materials were subjected to same conditions it could be assumed that different degree of Mo reduction originates from the original irradiation.

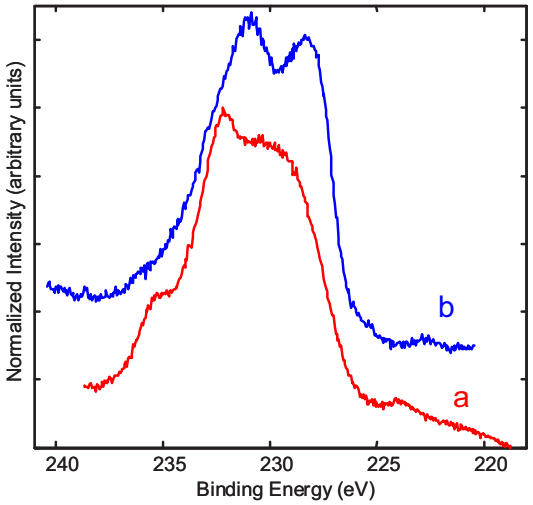

Figure 137. XPS of Mo3d states for quenched material after long sputtering with 1 keV Ar^+ at grazing incidence to achieve a thin steady state sputter damaged layer: a) pristine material, and b) irradiated material. Note the irradiated materials have a qualitatively higher fraction of reduced (lower binding energy) Mo species.

Zirconium Recycle

E. D. Collins, collinsed@ornl.gov

In late 2011, technical assistance was obtained from two industrial expert teams with experience in manufacture of Zircaloy fuel rod cladding. This was arranged by means of contracts with the industrial assistance program in DOE-NE. The two industrial teams made site visits for observations of the experimental equipment and facilities, and for technical discussions with the experimenters. Both teams provided information describing the industrial-scale processes used to purify zirconium, convert it to zirconium tetrachloride salt, and then convert the salt to purified zirconium metal "sponge." The purified metal is vacuum arc melted, and alloying agents are added. Finally, metallurgical processes (heating, extruding, rolling, and milling with intermittent annealing steps) are used to fabricate Zircaloy fuel cladding tubes (Figure 138).

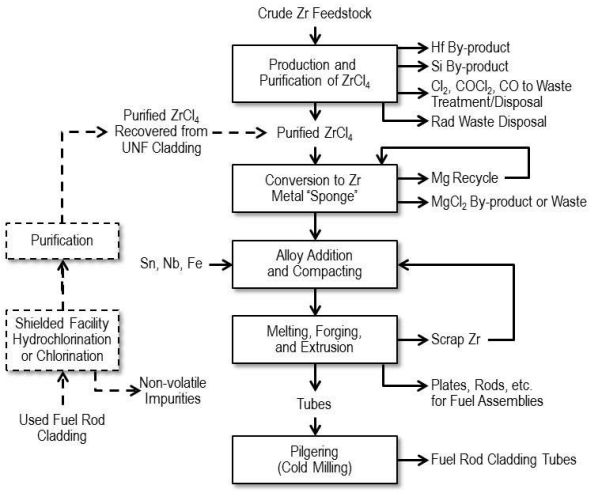

Figure 138. Potential inclusion of purified recycle zirconium into the process for zirconium alloy cladding manufacture.

For the processing of UNF cladding containing highly radioactive contaminants, there are additional requirements that must be considered. These include (1) the need for simplified and robust processes that may be operated in a hot cell type environment, at least up to the point where the highly radioactive fission and activation products are separated from the zirconium, (2) recovery and treatment of the residual ash after the zirconium is volatilized, permitting return of the actinides to the fuel recycle plant for recovery and prevention of losses, and (3) recovery and sequestration of volatile radioactive gases that may be released from the cladding, for example tritium.

Several advantages were identified for changing the process for zirconium recovery and purification from the initially considered iodination to hydrochlorination or chlorination. These advantages included (1) a direct connection to existing industrial processes by producing purified zirconium tetrachloride from the UNF cladding (Figure 138), (2) elimination of the need for the recovery process to include a process step to convert the purified zirconium salt to zirconium metal, and (3) use of gaseous HCl or Cl_2 at atmospheric pressure as reagents, permitting good flow rate control.

Even though the hydrochlorination process is less exothermic and does not create as many volatile impurity species as the chlorination

process, an issue for an industrial application of the hydrochlorination process in a radiochemical operation is the hydrogen generated in the off-gas by the reaction:

$$\text{Zr clad} + 4\ \text{HCl} \xrightarrow{350°\text{C}} \text{ZrCl}_4 \uparrow + 2\text{H}_2 \uparrow$$

Whereas, hydrogen is not generated by reaction with the chlorination process

$$\text{Zr clad} + 2\ \text{Cl}_2 \xrightarrow{350°\text{C}} \text{ZrCl}_4 \uparrow$$

In addition, the hydrogen generated in the off-gas from the hydrochlorination process complicates the separation and retention of tritium that is released from the UNF cladding. Therefore, the chlorination process was selected for further development for recovery/purification of zirconium from UNF cladding.

In late FY 2012, a test of the chlorination process was made using a single 12 g cladding hull obtained from a UNF fuel rod after shearing and leaching in nitric acid to dissolve the fuel. The hull sample represented that typically obtained in current reprocessing plants, and contained radionuclides in similar concentrations as found in extensive characterization studies by the French CEA. The major radionuclide was ^{137}Cs and the hull sample gamma emission was 3 mSv. The 12 g hull sample was placed into a glass reaction tube and dried at 350°C in a flowing stream of argon. Chlorine gas was admitted and the exothermic reaction began, causing the temperature to rise to ~420°C during the initial 10-minute period. Thereafter, the chlorine feed rate was decreased as necessary to reduce the reaction temperature to ~360°C for the remaining ~100-minute period, after which the hull residue was reduced to ~0.5 g of dusty powder. The product salt collected in the cyclone condenser was decontaminated from ^{137}Cs by a factor of 600, from all beta emitters by a factor of 278, and from the gamma radiation by a factor of >30. These results indicate the feasibility of decontamination that can be achieved by the chlorination process after optimization and scale-up to industrial-scale levels. Studies planned during FY 2013 will be initiated to continue the process development.

Based on information learned from site visits to industrial plants that recover and purify zirconium from natural materials, a preliminary process design illustrated in Figure 139 was conceived.

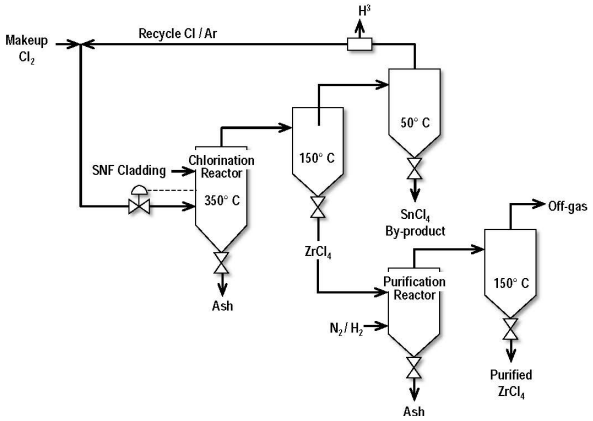

Figure 139. Diagram for Planned Chlorination Process

This process design will be used for near-term process development testing. Reactor design is more dependent on the physical characteristics of the specific feed stock (i.e., washed hulls or intact fuel rods). Modifications to improve either the reactor and/or process design are expected to be derived from planned experimental tests, modeling studies, engineering calculations, and scale-up tests.

After the decision in FY 2012 to use the chlorination process, alternative applications to UNF recycle flow sheets were identified. These include: (1) washed hulls after shearing and removal of the oxide fuel by dissolution in nitric acid as is done in current reprocessing plants; (2) washed hulls after shearing, voloxidation treatment to convert the ceramic UO_2-based fuel pellets to a finely-divided U_3O_8- or UO_3-based fuel powder, separation of the fuel powder by screening, and acid washing of the hulls; or (3) chemical decladding of intact UNF assemblies or fuel rods (Figure 140).

In summary, based on previous test results and process analyses, future work will begin and be focused on (1) use of chlorine as the chlorinating agent and (2) use of the preliminary processing design illustrated in Figure 139.

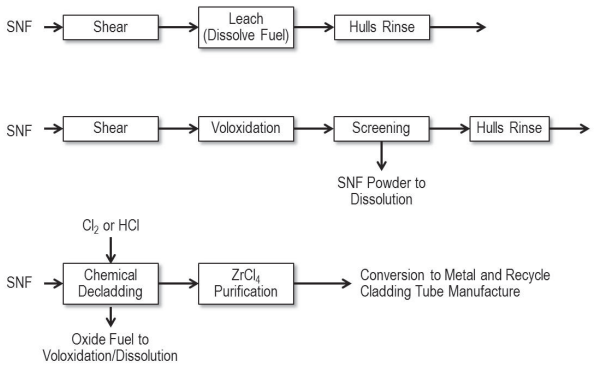

Figure 140. Potential Flowsheet Applications

Epsilon Metal Waste Form Development

J. V. Crum, jarrod.crum@pnnl.gov, D. M. Strachan, and M. Zumhoff

Epsilon metal (ε-metal) is a Ru, Pd, Rh, Tc, and Mo metal phase that is naturally formed in irradiated fuel. The name originates from the region within the Rh+Pd – Mo – Ru+Tc ternary phase diagram [Leykamp, et al. 1985]. This metal is being developed as a waste form for the treatment of undissolved solids (UDS; high noble metals, Tc, Zr, and Mo), soluble Tc, and noble metal waste streams generated during aqueous reprocessing of UNF [Strachan et al. 2010; Strachan et al. 2011]. Epsilon metal particles will be present in the real waste steam because they form in the fuel during irradiation and are, for the most part, expected to survive reprocessing. These elements are troublesome to process in an oxide waste form, BSG, glass-ceramic, or ceramic because of their limited solubility leading to low waste loading in the waste forms. In addition, Tc volatility during oxide waste form fabrication process is a major concern. Plus, the ε-metal waste form out performs glass in terms of durability and it can be fabricated using only the waste (no additives).

Prior work on the ε-metal waste form showed that the hexagonal close packed epsilon phase could be successfully fabricated by arc melting [Strachan et al. 2010]. However, the UDS contains a significant fraction of oxides, namely ZrO_2, which compromise the arc melting process, resulting in a low density, heterogeneous waste form. In addition, arc melting leads to some volatility of the low melting constituents, especially Pd.

For these reasons, a commercial processing literature review study was performed to indentify and rank commercially available fabrication technologies to produce the epsilon metal alloy with oxides as a cermet [Rohatgi and Strachan 2011]. The three top ranked commercial technologies were microwave sintering (MS), SPS, and HIP. These were tested in FY 2012 using a non-radioactive surrogate waste composition where Re was substituted for Tc [Crum et al. 2012]. The composition of the ε-metal waste form was tested at three levels of oxides (0, 17.5, and 35 mass % of ZrO_2) to encompass the projected range of oxides in the waste stream due to separations variability. Samples were batched and prepared for processing at PNNL and shipped to commercial vendors for processing by MS, SPS, and HIP. After which, sample morphology, phase assemblage, and bulk density were all evaluated. These tests were done to make a preliminary assessment of the three technologies and do not represent an optimized process.

The results from tests clearly show dense monolith forms of ε-metal alloy were produced with SPS and HIP, with up to 35 mass% ZrO_2 (Figure 141).

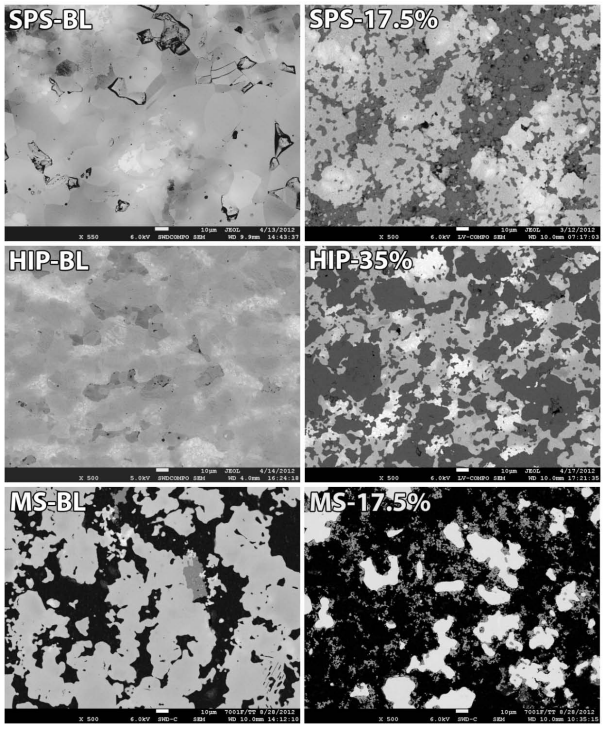

Figure 141. Backscattered electron scanning electron micrographs of spark-plasma (SPS), hot isostatic pressing (HIP), and microwave sintering (MS) epsilon alloy with ZrO_2 (17.5 or 35 mass %) and without (baseline = BL). Metal alloy is white or light gray, molybdenum carbide is medium grey, ZrO_2 is dark gray, and porosity is black.

Minimal porosity (black regions in micrographs) is observed in the HIP and SPS samples, where as MS samples show significant voids. Bulk density measurements of the samples show similar results for the three methods: SPS (87–94% dense), HIP (>90% dense), and MS (55–61% dense). XRD shows the five individual metals (Mo, Ru, Rh, Pd, and Re) alloy into the major phases, ε-metal (hexagonal close packed structure), and α-metal (cubic close packed structure), while ZrO_2 remains stable as an oxide during processing. For SPS, some Mo reacted with the graphite die to form Mo_2C as a minor phase at the outer surfaces of the pellets. The presence of ZrO_2 was expected to be a hindrance in the consolidation process, but it appears to only hinder the use of MS while slightly improving the formation of the ε-phase in SPS. In conclusion, SPS and HIP successfully produced dense, mostly reacted (>90% ε-metal HCP alloy) ε-metal containing 0, 17.5, and 35 mass% ZrO2, even though the samples started out as the five individual metals (Mo, Pd, Re, Rh, and Ru). These results show that the UDS and soluble Tc can be immobilized in durable cermet waste forms at 100% waste loading with two commercially available processes.

This page intentionally left blank.

CHAPTER 10
WASTE FORM PRODUCTION

CHAPTER 10: WASTE FORM PRODUCTION

J. D. Vienna, john.vienna@pnnl.gov

Cold Crucible Induction Melter Tests to Produce a Simulated Non-Radioactive Glass Ceramic High Level Waste Form

V. Maio, vince.maio@inl.gov

Summary

Engineers and scientists at the INL successfully prepared for and completed a series of non-radioactive DOE-NE sponsored tests validating the process-ability of a simulated glass-ceramic (GC) HLW form utilizing Cold Crucible Induction Melter (CCIM) technology. This first-of-a-kind result proves that the unique features (e.g., no exposed refractory, no in-melt electrodes, higher temperatures, higher throughput, uniform mixing, smaller foot print and bottom drain) inherent in the design of CCIMs (in contrast to the presently deployed Joule Heated Ceramic Melters or the Hot Walled Induction Melters) are well suited for producing advanced GC HLW forms. GC waste forms have qualities superior (e.g., higher waste loadings, greater long term durability, higher decay heat load tolerance) to those of the current HLW waste form baseline; BSG.

Purpose

The major objective of the tests was to demonstrate the processability of glass-ceramic waste forms in a CCIM (see Figure 142). A melter feed simulating a liquid UNF reprocessing waste (e.g., raffinate from a next generation aqueous-based actinide separation method) was used but was not optimized for water and nitrate content. This simulated CCIM feed/waste contained surrogates for the alkaline and alkaline earth fission products (e.g., mostly Cs, Sr), the transitional metal fission products, and the lanthanide fission products – all beta decayers – as well as the long half life, alpha decaying trace actinides not removed from recycling.

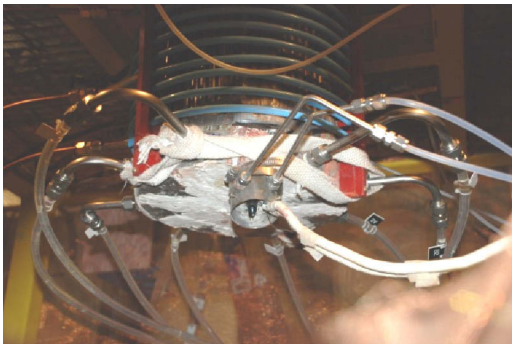

Figure 142. The INL's pilot-scale CCIM with its bottom assembly highlighted. Note the bottom turn of the lower induction coil in blue and the cooled cylinder (annulus) drain. The white inside the outer drain pipe is the inner drain tube heater and the dark material represents the onset of melter content draining as material in the drain line decreases viscosity and starts slumping upon heating

Experimental

Prior to the test run, the appropriate glass additives (as determined earlier by PNNL) were mixed with the surrogate HLW liquid and fed as a slurry to the INL's pilot-scale 10.4 diameter CCIM pilot plant located in Bay W-1 of INL's Idaho Engineering Development Facility (IEDF). Before feeding the simulated waste slurry, the CCIM was first preloaded with a solid amorphous starting bed reflective of the feed composition (i.e., a pre-melted, quenched and grounded HLW surrogate containing glass additives). Based on prior and current year small-scale melting studies conducted at PNNL, heat-up and melting of the initial solid charge in the larger scale CCIM pilot plant at INL was then initiated using a titanium ring. When the entire bed was molten at the desired melt temperature, feeding of the slurry feed commenced at rates from ½ to ~1 kg/hr. When stable CCIM operations were achieved, the system operated in a planned manner at a set RF frequency to induce and couple to the lower-than – normal conductivity of the melt. Tapping of the drain pour was than undertaken to produce three 4" diameter glass-ceramic waste logs (cylinders) varying in height from about 6 to 8 inches.

Specifically, the simulated waste was melted in the CCIM at 1300–1350°C, tapped at 1200–1275°C (see Figure 143) and poured into graphite canisters equipped with thermocouple trees. The molded pours were then cured with prescribed post controlled cooling (under three separate cooling scenarios) to ensure formation of the following dispersed crystalline phases in a continuous glass matrix: Pollucite, Powellite, Oxyapatite, and Ln Borosilicate (see Figure 144).

Figure 143. A pour of the molten glass ceramic from the INL bench scale CCIM. Note at the bottom of the photo the accurate positioning of the insulated heaters and molten waste collection canister to ensure catching the melt

Figure 144. A look Inside the INL's Pilot-Scale CCIM Containing a Fraction of the Crushed Starting Bed and a Segment of a Previously Formed Glass Ceramic that has been Melted and Cooled. Note the different layers and colors of the glass ceramic segment indicating the formation of both amorphous and crystalline phases

Theses phases -which were verified based on follow-up analysis- exclusively contained the Mo and various surrogate actinides and fission products with both higher durability and an overall higher waste loading. See the elemental dot map in Figure 145.

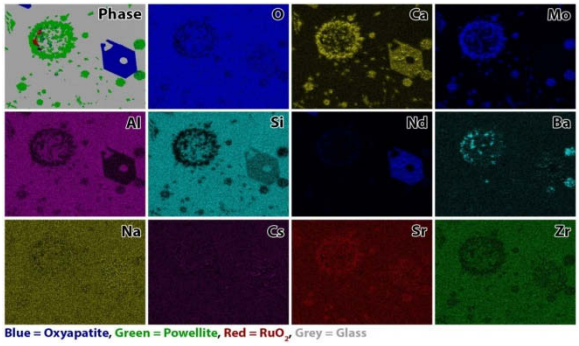

Figure 145. The elemental dot map. As desired, note the positioning of the Mo and Nd Elements in the Powellite and Oxyapatite respectively.

Results

Collectively the pilot-plant tests demonstrated and/or advanced the capabilities of the CCIM system in the following processing and design areas:

- The ability to start and stop several CG pours at elevated temperatures to reach the low viscosity level required for gravity flow and achieve this pour without repeated plugging or bridging in the drain tube The pours were also completed within specific uninterrupted durations to avoid improper canister filling (e.g., under filling, the creation of voids in the waste form and/or over flowing). Figure 146 provides side and top views of two completely cooled glass-ceramic pours achieved with two different cooling rates.

Figure 146. Side and top views of two completely cooled glass-ceramic pours

- The ability to accomplish a variety of post CCIM draining activities as is required for producing a glass ceramic waste form. These activities included controlled cooling and casting of the waste form after tapping and pouring and in-situ monitoring of the waste form's temperature profile using thermal couple trees while under a cooling period (see Figure 147).

Figure 147. The Mobile Apparatus Designed and Built for this Test to Provide the Insulated and Controlled Cooling of Three Separate GC Pours from the INL's Pilot Scale CCIM

- The ability to initiate and couple inductively to a recalcitrant melt due to its unique conductivity and sustain the initial melt during the formation of ceramic phases in the melt. Compared to pure glass melts, the challenge of melt sustainability is a result of the crystal's latent heat of fusion, higher viscosity, lower conductivity, and significant yield stress.
- The ability to consistently feed (and measure the feed rate) of a slurry representative of the feed tank waste as well as keep the slurry feed adequately mixed in the feed tank for the duration of the test. The ability to slurry feed proves that HLW feeds to the CCIM do not necessarily have to be pre-calcined to a solid-which can be efficient for melting but problematic in terms of solids handling and the concentration of radioactivity
- The ability to build a cold cap (even with a dilute feed) and break up that cold cap (with an air bubbler) on a routine basis when it affects the feed flow into the melt.
- The obtaining of initial scale-up parameters in terms of melter dimensions, drain size and canister diameter.

CHAPTER 11
WASTE FORM PERFORMANCE OVER GEOLOGIC TIMESCALES

CHAPTER 11: WASTE FORM PERFORMANCE OVER GEOLOGIC TIMESCALES

Bill Ebert, ebert@anl.gov

Metal Waste Forms

W. Ebert, ebert@anl.gov, J. Fortner, T. Cruse (ANL); L. Olson (SRNL); S. Frank (INL); D. Kolman, G. Jarvinen (LANL); and E. Buck (PNNL)

Work is in progress to develop a steel-based metallic waste form for immobilizing reprocessing wastes that can be produced by directing melting the fuel wastes with either cladding hulls present in the waste stream, as in the case of electrometallurgical processing, or added steel, as in the case of aqueous wastes. Fuel wastes dissolve in the molten steel and become incorporated into a small number of durable intermetallic and solid solution phases. The assemblage of phases that forms provides flexibility to accommodate a wide range of waste stream compositions in a small number of phases, which greatly simplifies performance modeling for long-term system assessments and waste form consistency requirements for waste acceptance. A conceptual degradation model has been developed for calculating the release of radionuclides from alloyed waste forms based on a two-step mechanism of oxidation and dissolution. Well-established analytical models that were developed for steel corrosion are being applied to waste form degradation, and experimental methodologies drawing on and combining standard electrochemical and immersion techniques are being coupled with microscopy to evaluate the corrosion behavior of these multi-phase alloys having micrometer-sized domains. The results of experimental activities in FY 2011 and early FY 2012 have provided confidence in both the modeling and experimental approaches, and the present focus and main objective of planned FY 2013 testing is on generating data bases needed to parameterize and implement the degradation model.

Much of the developmental work was performed with RAW-1, which was formulated to represent the immobilization of fuel wastes in the minimum amount of steel required to dissolve the wastes and incorporate the waste elements in durable iron intermetallic phases. Several other reference alloys will be formulated and used in experiments to study the processing, characteristics, and corrosion behavior of potential metallic waste forms made with reprocessing wastes from aqueous and pyrochemical operations. Table 18 summarizes the RAW materials that have been or will be formulated for use in testing.

Table 18. Summary of RAW materials for model development

Material ID	Waste Stream	Purposes
RAW-1(Re)	Aqueous	Method development; ID constituent phases
RAW-1(Tc)	Aqueous	Tc distribution and host phases; corrosion behaviors of individual phases; phase boundary and coupling effects; Tc release behavior
RAW-2(UTc)	Aqueous & EChem	Dispositions of U and Tc; effects on phase composition and corrosion behavior
RAW-3(UTc)	EChem	Dispositions of U and Tc; effects of U and HT9 on phase composition and corrosion behavior
RAW-4(UTc)	EChem	Four materials (4a–4d) to expand composition range of EChem waste forms
EWF-1(Tc)	Aqueous & EChem	Direct processing of metal wastes without added steel

These alloys have been formulated to represent a wide range of nominal waste stream compositions alloyed with various amounts of steel (e.g., sodium-cooled fast reactor cladding hulls) and additives. The concentrations of fuel wastes in the aqueous and EChem waste streams are expected to be similar, and the primary difference is expected to be the presence of steel cladding in the EChem wastes and the absence of steel cladding in the aqueous processing wastes; waste steel from other sources must be added to process the aqueous wastes. Alloys are also being

made with variations of these compositions to study the effects of key elements on the constituent phase assemblage and corrosion behavior.

The test materials in Table 18 represent waste forms made with a wide range of added steel. The initial tests were conducted with RAW-1 that was initially made with Re as a surrogate for Tc and then with Tc. Alloy RAW-2 was made with U and Tc in FY 2012 for use in tests to be conducted in FY 2013. Alloys RAW-1 and RAW-2 represent waste forms made with the least amount of added steel (Type 316L) that is necessary to incorporate all waste elements in iron-based constituent phases. Alloy RAW-3 was formulated in FY 2012 to represent nominal EChem waste with HT9 cladding; it is planned to be made for testing in FY 2014. Alloy RAW-4 includes several alloys that were made during development of the metal waste form for EBR-II wastes and will be used in FY 2013 testing activities. Alloy EWF-1 is a surrogate for the epsilon phase that forms in oxide fuel. It represents direct processing of metallic fuel wastes (without steel cladding) and will provide a limiting composition for evaluating the applicable range of the alloy waste form degradation model. It is planned to be made and used in FY 2013 testing activities. Compositional variants of these reference alloys have been made to study the effects of key waste components and additives.

Effect of Cr Content on Waste Form Passivation

L. Olson, lonnie.olson@inl.gov

Alloys with Cr contents ranging from 0 to 30 at% Cr were prepared in FY 2011 as variations of RAW-1 to evaluate the effect of Cr content on the alloy corrosion resistance and the possible benefit of additional Cr in the waste form. It was determined that Cr in excess of that in the stainless steel did not improve the durability and resulted in a brittle alloy. Work with these materials continued in FY 2012 to study the effects of Cr on the passivating role oxide layers on long-term corrosion. Samples of the alloys were subjected to hydrothermal tests to generate oxides at the surface and evaluate the effect of the Cr content on the passivation behavior. Some of the corroded alloys were examined with SEM and EDS to quantify the extent of corrosion and the nature of the oxides formed over specific phases. Others were fashioned into electrodes for electrochemical measurements. Figure 148 shows SEM images of cross sections of alloys with 0 at% and 14 at% Cr (which is the Cr content of RAW-1). In the alloy made with 0 at% Cr, attack of the Fe solid solution and Mo-Fe intermetallic phases was observed to penetrate as deep as ~200 µm into the sample (Figure 148, top). Only thin iron oxide layers (0.2 µm to 0.5 µm) were observed on the surfaces of all the Cr-bearing alloys (e.g., Figure 148, bottom). The thickness did not correlate with the Cr content and the composition appeared to be uniform over all constituent phases. No indication of preferential attack of particular phases was evident in any of the Cr-containing alloys.

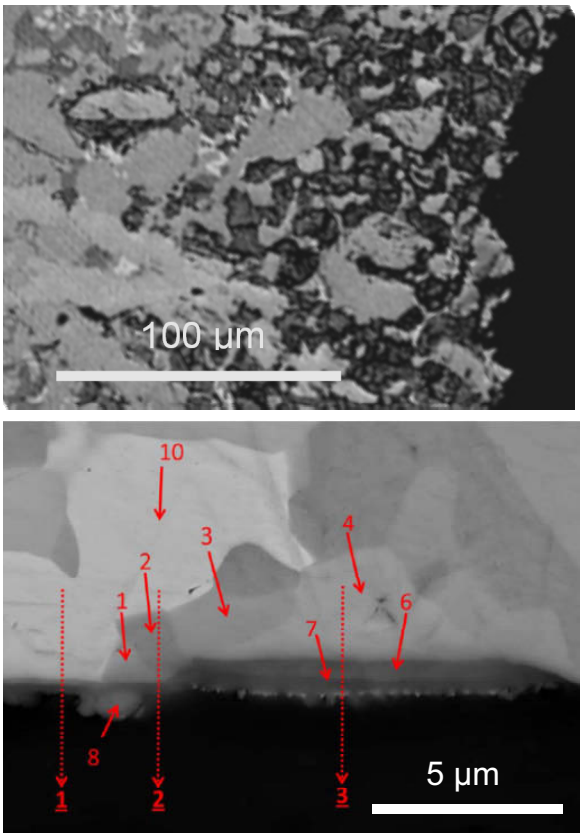

Figure 148. SEM images of cross-sectioned alloys with 0 at% Cr (top) and with 14 at% Cr (bottom).

DSC Analysis of RAW-1 and RAW-1(Cr) Alloys

S. Frank, steven.frank@inl.gov

Alloy RAW-1(Re) and the variant alloys made at SRNL with different Cr contents were analyzed

with differential scanning calorimetry while heating to above the melting point and then cooling. Figure 149 shows replicate scans with RAW-1(Re) and scans for the alloys made with 5, 20, 25, and 30 at% Cr.

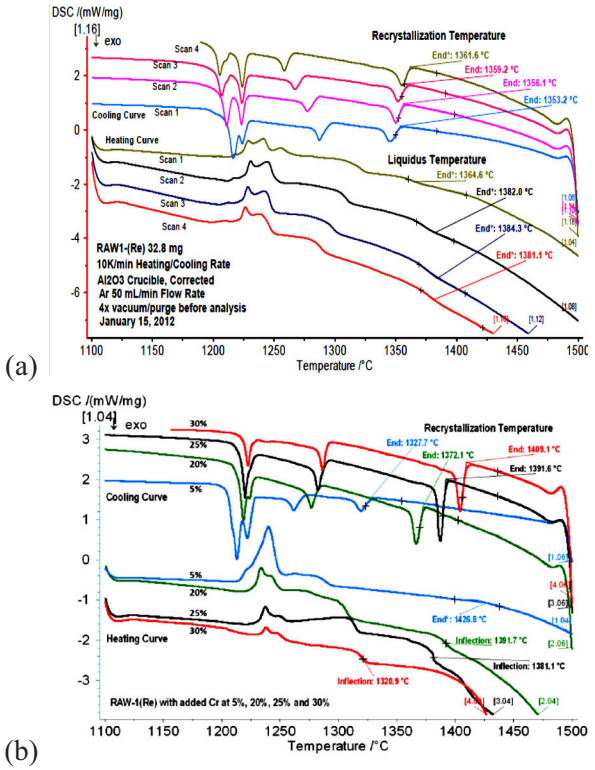

Figure 149. Differential scanning calorimetry scans for (a) RAW-1(Re) and (b) variants of RAW-1 with Cr contents of 5% (blue), 20% (green), 25% (black), and 30% (red).

The heating curves show exothermic peaks where the constituent phases melt and the cooling curves show endothermic peaks where each constituent phase precipitates from the melt. Shifts in peaks during repeated analyses indicate minor changes in phase compositions. The Cr content has the greatest effect on the phase with the highest precipitation temperature and the amount of the phase with the lowest precipitation temperature. SEM analyses indicate these are the MoFe intermetallic and the iron solid solution phases, respectively. This information is useful for developing processing controls and for understanding the distributions of waste elements among the different constituent phases.

Microscopic Characterization of RAW-1(Tc)

E. Buck, edgar.buck@pnnl.gov

The structures and compositions of constituent phases in the alloys being studied are being characterized with transmission electron microscopy to better understand the physical effects of incorporating radionuclides and changes that occur as the alloys corrode. The two predominant phases in RAW-1 are $MoFe_2$ and $ZrFe_2$ intermetallics. Analyses indicate that Tc is incorporated into the $MoFe_2$ intermetallic but not the $ZrFe_2$ intermetallic, and that the $MoFe_2$ intermetallic has a cubic structure.

Model Development and Corrosion Experiments with RAW-1(Tc)

W. Ebert, ebert@anl.gov, T. Cruse, and J. Fortner, ANL

Various experimental methods are being used to quantify the effects of environmental conditions on the performance of alloyed waste forms to support development and application of a waste form degradation model. The objective of the model is to provide source terms for radionuclides that are immobilized in alloyed waste forms for use in performance models for engineered disposal systems. The degradation model that is being developed is based on an oxidative dissolution mechanism in which metallic elements must first be oxidized to soluble oxidation states and then those oxides dissolve to release ions (including radionuclides) into solution in a transportable state. The oxidation step, the dissolution step, and the transport step can all limit the release of radionuclides, and all are sensitive to many environmental variables. The key variables for the oxidation step are the potential at the waste form surface, which is established by the environmental redox conditions (i.e., the Eh), and the chloride concentration (for steel-based alloys); the key variables for the dissolution step are pH, Eh, and temperature; the key variables for transport are groundwater advection, solubility, and sorption. The modeling and experimental work underway in the waste form behavior activities is focused on the oxidation and dissolution steps, and on the release behaviors of Tc and U. Transport is being addressed in modeling and simulation activities within the SWF and UFD Campaigns.

The alloyed waste forms of interest are multi-phase materials with four or five constituent phases. The approach taken in the degradation model is to represent waste form corrosion and radionuclide release as the sum of the contributions of the constituent phases. The current density that is measured in electrochemical tests is related to the sum of the corrosion rates of the constituent phases, where the current for each phase is related to its corrosion rate through Faraday's Law. The dependence of the current density on the potential at the alloy surface is modeled using the Butler-Volmer equation and key environmental effects are modeled using modeling methods developed for stainless steels by Anderko [2001].

Several electrochemical measurements were made in a wide range of environments and to study the corrosion behavior of alloyed waste forms and the release of Tc. The corrosion current density measured in Potentiodynamic tests with RAW-1(Tc) in several electrolyte solutions that were either air-saturated (representing oxidizing environments) or purged with argon to remove dissolved oxygen (representing reducing environments) are shown in Figure 150. The current densities shown in Figure 150a were measured using Tafel analysis. The corrosion behavior is fairly insensitive to the environment under oxidizing conditions and only moderately sensitive in reducing conditions. Additional tests were conducted in a range of NaCl concentrations. The results of Potentiodynamic scans are shown in Figure 150b. Although the corrosion potential varies with the NaCl concentration, the shapes of the curves and the corrosion current densities are similar, but do not correlate analytically with the NaCl concentrations. A key observation of the scans is that the corrosion current densities are all fairly constant over the potential range 0.1 to 0.6 V.

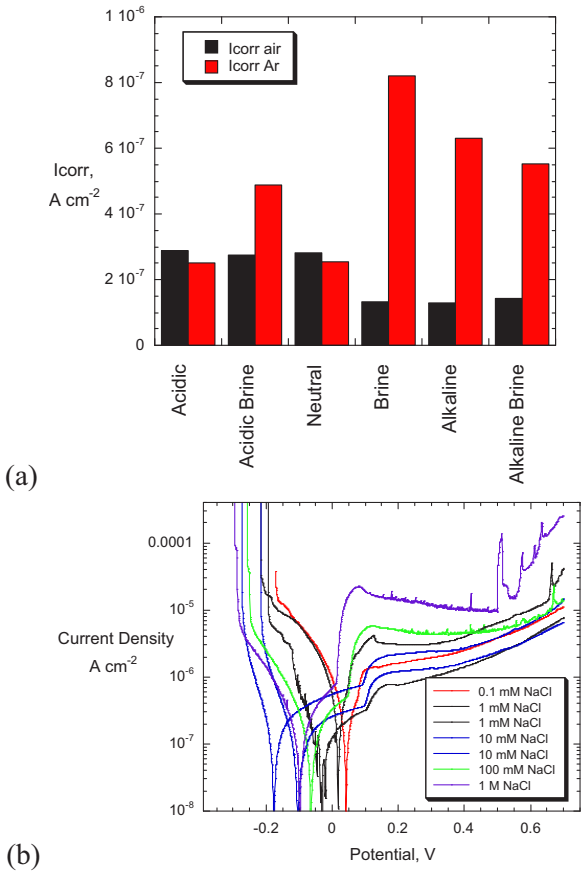

Figure 150. (a) Tafel analyses of RAW-1(Tc) in various electrolytes and (b) Potentiodynamic scans with various NaCl concentrations.

Potentiostatic hold experiments were performed to study the preferential dissolution of constituent phases. Figure 151a shows results of Potentiodynamic scans performed on the freshly prepared surface (black) and after 24-hour potentiostatic holds at 100 mV (red) and then at 200 mV (blue). The scan of the fresh surface indicates changes in the phases dominating the response at about 20 mV, 110 mV, and 140 mV. Corrosion during the potentiostatic hold at 100 mV resulted in a shift in the corrosion potential from about -110 mV to about 40 mV, a decrease in the 110 mV peak, and a new peak at about 200 mV. Further corrosion during the potentiostatic hold at 200 mV resulted in the loss of the peak at 200 mV and reestablishment of the peak at 140 mV. Examination of specific regions of the electrode surface before and after the potentiostatic holds (Figure 151b and Figure 151c, respectively) indicates that the primary effect was the generation of pits in the phase labeled 2, which

is the $ZrFe_2$ intermetallic. Analyses of the solutions after the hold did not indicate significant Tc release, which is consistent with the fact that the $ZrFe_2$ intermetallic phase does not host Tc.

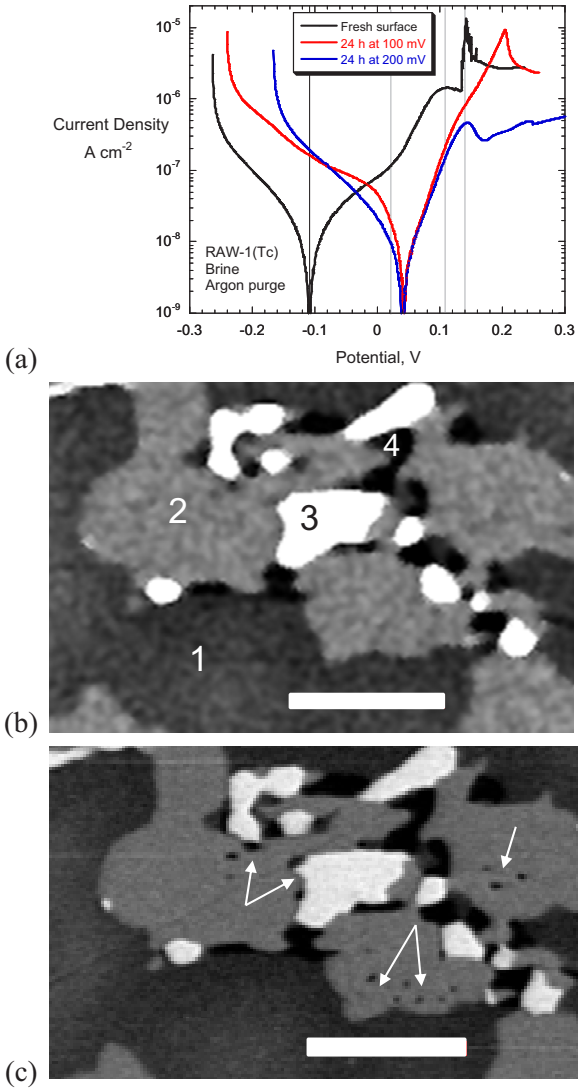

Figure 151. (a) Potentiodynamic scans of RAW-1(Tc) fresh surface (black), after 24 h potentiostatic hold at 100 mV (red) and 200 mV (blue), SEM photomicrographs of surface (b) before potentiostatic holds and (c) after potentiostatic holds. Arrows locate dissolved regions.

Corrosion tests were conducted with RAW-1(Tc) at 200ºC in which several samples of the alloy were immersed in demineralized water or suspended in humid air. The solution was completely replaced every 2 or 3 weeks and the test continued. The recovered solutions were analyzed to track the release of Tc and other components over time and evaluate the kinetics. Samples are being removed occasionally from each test for surface analysis with tests continuing with the other samples. Figure 152 shows some initial results. The releases of Tc and Mo in both the humid air and immersion tests are slowing with time. The curves show power law fits with greater fractional release under humid air conditions and time dependencies ranging from 0.317g Tc/g alloy in the immersion test to 0.553g Tc/g alloy in the humid air test. SEM examination of a cross sectioned sample shows a thin layer ~0.5 µm of predominantly iron oxide to have formed after about 120 days. A small amount of TcO_2 was detected in the layer by XANES analysis performed at grazing incident and exit angles. The XANES analyses also indicated that Mo and Tc occupy equivalent sites in the $MoFe_2$ intermetallic phase.

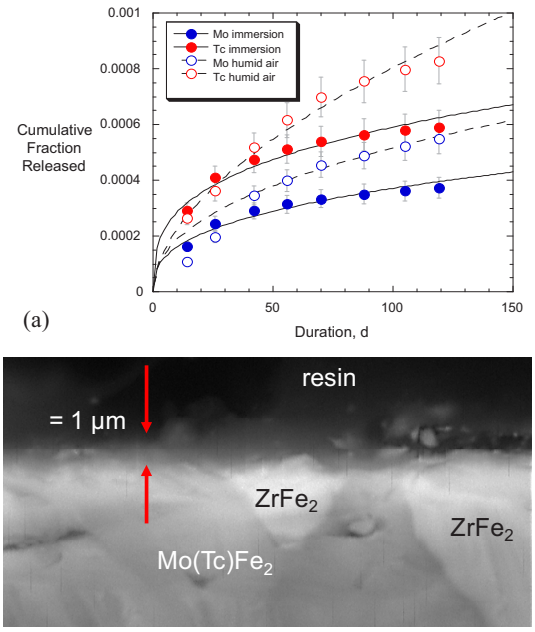

Figure 152. Results of corrosion tests with RAW-1(Tc): (a) release kinetics of Tc and Mo, and (b) thin oxide layer formed after 140 days in humid air test.

These results illustrate the experimental approach being taken to evaluate the corrosion behavior of alloyed waste forms. The electrochemical measurements needed to parameterize the parts of the degradation model quantifying the oxidation reactions are coupled with solids analyses that are used to identify the constituent phase(s) giving rise to the electrochemical response and with solution analyses that are used to quantify the release of Tc

and other radionuclides and represent the dissolution part of the degradation model. By conducting potentiostatic experiments over a range of potentials and in various electrolyte solutions, researchers can map out the corrosion behavior over the range of possible environmental conditions in disposal systems of interest. Conducting tests with the other RAW alloys will provide a range of relative surface areas of the constituent phases and may provide a waste form composition term that can be added to the degradation model. To this end, the alloy RAW-2 was made and characterized to support future testing and alloy RAW-3 waste formulated.

References

1. Anderko, A., P. McKenzie, and R. D. Young. (2001). "Computation of Rates of General Corrosion Using Electrochemical and Thermodynamic Models." Corrosion, 57 (3), 202-213.

Fabrication and Characterization of RAW-2

S. Frank, steven.frank@inl.gov, and J. Fortner (ANL)

RAW-2 was fabricated to study the disposition of Tc and U in the constituent phases and for use in laboratory testing activities planned for FY 2013 to study their release behaviors as the alloy corrodes. RAW-2 was formulated to represent waste forms with fuel wastes and minor amounts of residual uranium from separation processes. The relative amounts of waste elements and Type 316L steel approximate the highest practical waste loading for electrometallurgical wastes. Figure 153 is an SEM photomicrograph of RAW-2 showing the representative microstructure and identifying the four major constituent phases. Phases 1 and 2 host U and phases 3 and 4 host Tc.

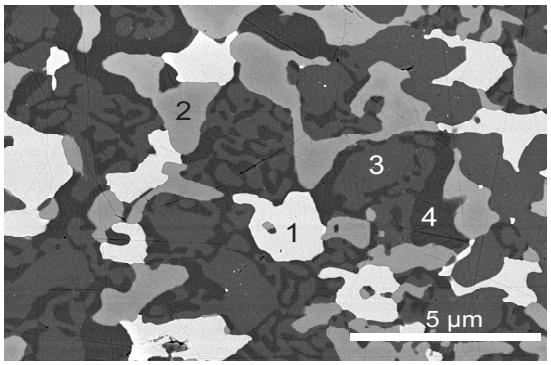

Figure 153. SEM micrograph showing the microstructure of RAW-2.

Analysis with SEM/EDS indicated that, although the compositions of the constituent phases are generally uniform across the ingot, there is some variance in composition within each domain. Figure 154 shows the relationships between the components in the four phases relative to the U and Tc concentrations. These results show the compositional flexibilities of these phases to accommodate wide ranges of U and T concentrations within and between different waste streams.

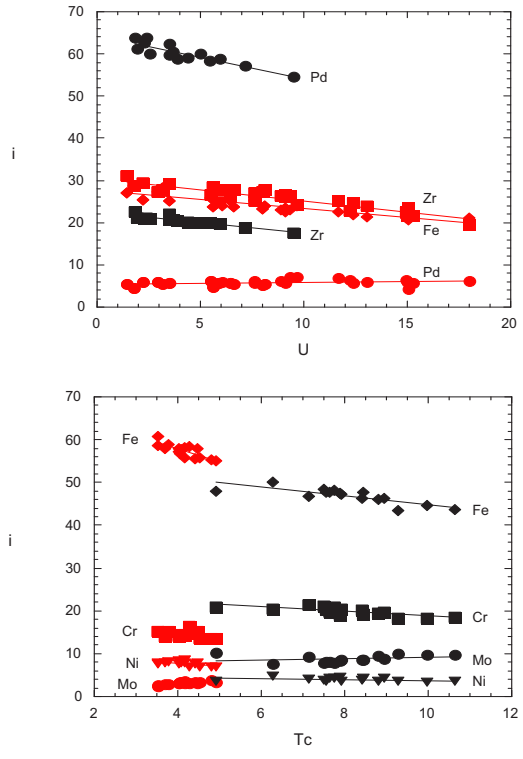

Figure 154. Composition ranges measured for (a) Phase 1 (black) and Phase 2 (red) and (b) Phase 3 (red) and Phase 4 (black), in mass%.

Tolerance to Oxides in Waste Streams

S. Frank, steven.frank@inl.gov

The ability to fabricate alloy waste forms from waste streams with high oxide contents, such as the UDS waste from aqueous fuel dissolution, and the capacity of the alloy to accommodate the oxides were investigated. Figure 155 shows an SEM photomicrograph of an alloy made from a mixture of Type 316L stainless steel, Zr, Mo, and 30 mass% ZrO_2 as a surrogate for waste oxides. It is expected that many oxides would be reduced to metals during processing, but not ZrO_2. Intermetallics similar to those that form in RAW-1 were observed to be intimately mixed with regions of ZrO_2. The alloy was highly fractured, which is probably due to the lack of an iron solid solution phase to absorb stresses. Only about half of the steel was mixed with the waste with the other half placed on top of the mixture with the expectation that it would flow through the waste mixture during processing. Although that did not happen, enough steel was available in the mixture to consolidate the waste form. Although the formulation would need to be adjusted, these scoping experiments demonstrate the tolerance of the method and waste form to oxides in the waste stream.

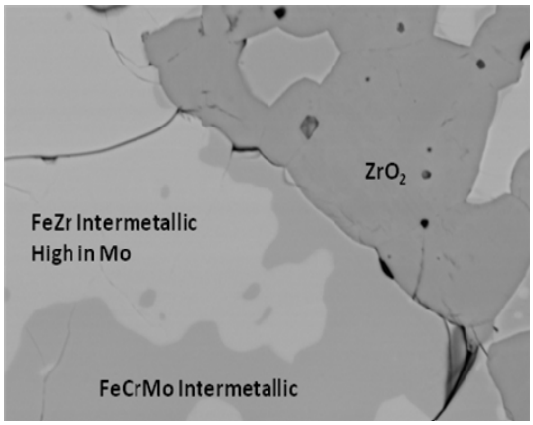

Figure 155. SEM photomicrograph of alloy made with 30% ZrO2.

Formulation of RAW-3

L. Olson, lonnie.olson@inl.gov

Reference alloy RAW-3 was formulated to represent waste forms for wastes from electrometallurgical reprocessing of fast reactor fuel with HT9 ferritic-martensitic steel made with a minimal amount of added Zr. The other prototype waste forms were made austenitic 316 stainless steel. To provide a scientific basis for the formulation, surrogate waste forms were made and analyzed to determine the minimum Zr:U ratio that can be used to sequester U into durable phases in an alloy waste form with a minimal amount of added Zr and to optimize waste loading. The evaluation of the waste forms focused on presence or absence of residual uranium and the phase assemblage produced in a full melt and furnace-cool thermal process.

The criteria used in formulating the RAW-3 composition were: (1) accommodate all constituents in HT9 ferritic steel, which is the most likely cladding material to be in an advanced fast reactor, (2) accommodate all U in intermetallic or solid solution phases, with no pure or nearly pure U metal phases, (3) minimize the Zr/U ratio to increase waste loading for U contents expected to result from advanced pyroprocessing methods, (4) a small number of constituent phases, (5) a uniform distribution of constituent phases on the scale of 0.2 mm^2, and (6) flexibility in waste loading. While all of these criteria were not quantified due to the scoping nature of this work, none of the criteria were violated based on the analyses completed to-date, and will likely be verified upon further examination.

Alloys were made with Zr/U ratios of 2Zr:1U, 1Zr:1U, and 1Zr:3U using 316L and HT9 steels, and with 1Zr:1U at waste loadings of 9 and 21 mass% using HT9. Re was used as a surrogate for Tc. Figure 156 shows the microstructure of alloy made with the 1Zr:1U mixture at 9 mass% with HT9 and a high magnification image of the phases hosting U. The compositions of the three major phases measured in the 1Zr:1U, 2Zr:1U, and 1Zr:3U alloys are summarized in Table 19. The relative amounts of the ZrFe and PdUZr intermetallic that form are sensitive to the relative amounts of Zr, Pd, and U in the alloy. Since the same ZrFe intermetallic phase forms in the 2Zr:1U and 1Zr:1U alloys, this phase assemblage provides a "buffer" that can accommodate a wide range of U contents.

The formulation of RAW-3 is based on an estimated ratio of fuel wastes similar to that used in the formulation of prototype waste forms

RAW-1 and RAW-2 with a conservative amount of residual U in the electrorefiner waste. The elemental formulation is given in Table 20 (on a mass basis) and corresponds to 85.5 mass% HT9 cladding, 10.5 mass% fuel wastes and 4.0 mass% residual U wastes. An ingot of RAW-3 will be made in the future for use in corrosion tests.

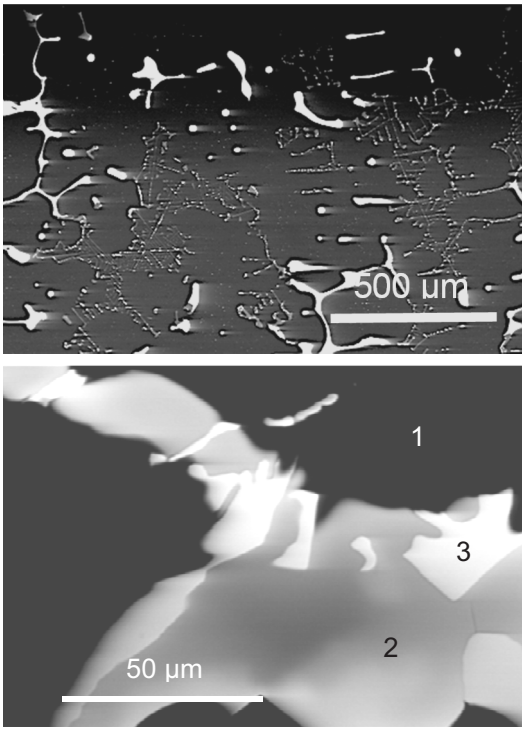

Figure 156. Microstructures of alloys with 1Zr:1U made with HT9 steel.

Table 19. Compositions of major phases in alloys made with HT9, in atomic%

	Cr	Mn	Fe	Ni	Zr	Mo	Ru	Rh	Pd	Re	U
Phase 1: Iron solid solution											
2Zr:1U	12.8	2.2	80.4	0.4	0.0	1.8	0.9	0.4	0.3	1.0	0.0
1Zr:1U	12.2	2.3	80.4	0.4	0.0	1.8	1.2	0.5	0.3	0.9	0.0
1Zr:3U	Not analyzed										
Phase 2: ZrFe intermetallic											
2Zr:1U	2.4	0.9	57.3	1.7	20.9	1.1	1.1	4.9	3.3	0.0	6.4
1Zr:1U	2.2	1.0	55.3	1.7	19.9	1.4	1.1	7.2	2.9	0.0	7.5
1Zr:3U	Not detected										
Phase 3: PdUZr intermetallic											
2Zr:1U	0.6	0.0	5.6	1.3	12.5	0.8	0.0	0.0	62.1	0.0	17.1
1Zr:1U	0.0	0.0	4.9	1.8	12.5	0.9	0.0	0.0	61.1	0.0	18.8
1Zr:3U	1.0	0.0	3.8	1.1	0.4	0.0	0.0	0.0	66.8	0.0	26.8

Table 20. Elemental composition of RAW-3, in mass%

	Cr	Mn	Fe	Ni	Mo	Si	W	V	C	Zr	Ru	Pd	Tc	Rh	U
HT9a	10.2	0.6	72.2	0.5	1.0	0.3	0.4	0.3	0.2	–	–	–	–	–	–
waste	–	–	–	–	2.0	–	–	–	–	1.5	1.7	1.8	1.6	1.7	4.0
total	10.2	0.6	72.2	0.5	3.0	0.3	0.4	0.3	0.2	1.5	1.7	1.8	1.6	1.7	4.0

[a] Equivalent to 85.5 mass% HT9.

Iron-Technetium Alloys

D. Kolman, kolman@lanl.gov

Several compositionally simple single phase alloys are being studied to help interpret composition effects on the distributions of radionuclides and corrosion behaviors of constituent phases in multi-phase materials and to support atomistic modeling activities. Various amounts of technetium were alloyed with iron to generate of compositions 0, 10, 50, 90 and 100 wt% Tc in Fe to study the effect of Tc concentration on the corrosion behavior. Samples were exposed to dilute H_2SO_4 solutions to measure the corrosion rate in acidified ground waters. Results suggest that corrosion rates are high for the alloys with 0 and 5 wt% Tc (about 7 mpy), but 10X lower for the 50, 90 and 100 wt% Tc materials, even though passivity is not observed. The lowest corrosion rates were measured for the 50 wt% Tc alloy, suggesting both the chemical and microstructural effects of alloying affect the corrosion behavior. The formation of a nonpassivating film was inferred from EIS analyses. High-vacuum measurements indicate the formation of TcO_2, which was predicted to passivate the surface. The fact that the electrochemical measurements did not indicate passivation suggests that either different surface films formed in the electrochemical experiments and under high-vacuum or the predicted passivating effect of TcO_2 is not correct. Both measurements and model simulations indicated that Fe dissolved preferentially to Tc in these binary materials.

Glass Waste Forms

J. Ryan, joe.ryan@pnnl.gov, D. Strachan, D. Schreiber, and J. Neeway, PNNL; C. Crawford and J. Marra, SRNL; W. Ebert and J. Fortner, ANL

Research activities are focused on three areas: elucidating the processes involved in waste glass corrosion, understanding and modeling the effects of alteration phase precipitation on the glass dissolution rate, and evolving the glass degradation and radionuclide release model to quantify the long-term impact of these processes. A key remaining question is the role of transport mechanisms through alteration phases that form on the surfaces of corroding glass. Some models

invoke a diffusion barrier that limits the access of water and the continued dissolution of glass. Detailed knowledge of the location, composition, evolution, and function of such a transport barrier would enable incorporation of this process into the dissolution rate models. Identification and characterization of the altered surface-layer is complicated by several factors. First, the evolution of the alteration layer(s) is a slow process that is affected by many variables, including pH, solution chemistry, and the test conditions. Second, once formed, the alteration layers are fragile and can be disrupted through physical damage by handling and changes in solution chemistry. New experimental methods and sophisticated analytical techniques are being developed and applied to characterize the generation of these layers, the diffusion of ions through these layers, and the continued glass dissolution kinetics with precision that was not previously achievable. These advanced techniques are being used to characterize naturally weathered archaeological glasses as analogues along with laboratory test samples. New approaches to optimizing and standardizing the use of experimental results to parameterize modeling and simulations are being developed.

Laboratory tests have indicated that the dissolution rate of many waste glasses increase abruptly by several orders of magnitude and coincides with the formation of mineral alteration phases. The fact that researchers cannot currently predict under what conditions this acceleration occurs has required conservatively low estimates of the glass waste form service life in a repository. Work is in progress to identify (1) the process responsible for the sudden increase in the glass dissolution rate, (2) the processes controlling the continued high dissolution rate, (3) the conditions that trigger and maintain the increased rate, (4) the incorporation of these effects into a glass waste form degradation model to account for the increase in dissolution rate, and (5) the approaches that can be taken to avoid rate increases. Understanding the cause and providing a scientific basis for why an increase will or will not occur under disposal conditions is an important aspect of assuring waste glass performance. Identifying the conditions under which an increase could occur and the impact of the resulting increased rate will allow for more reliable predictions of waste glass performance. Three testing activities were conducted in FY 2012 to address these topics: tests to measure the relative importance of diffusion and dissolution under high reaction progress and prior to the formation of the alteration phases that cause increased dissolution rates; tests to characterize the solutions and solids immediately before and after the onset of the rate increase; and tests highlighting the effects that conditions after the increase have on the resulting rate, which often called “Stage 3.”

Many of the on-going research activities are being coordinated with work being conducted internationally by a contingent of researchers in an organized effort to elucidate the mechanism, kinetics, and long-term modeling of waste glass degradation and radionuclide release. The DOE has spearheaded the organization and coordination of the effort to reach international consensus on waste glass degradation during geologic disposal.

In the summaries that follow, researchers highlight distinct efforts to develop the understanding necessary to predict the long-term corrosion rate of glass in disposal conditions. Each of these activities contributes a piece to the puzzle that is being solved by the international community as a whole. The details of how each of these activities, along with those activities being performed by our international partners, fit together to solve the one problem are describe in detail by Ryan et al. (2011).

References

1. Ryan, J. V., et al. 2011. *Technical Program Plan for the International Technical Evaluation of Alteration Mechanisms (I-Team)*, PNNL-21031, Pacific Northwest National Laboratory, Richland, WA.

Glass Dissolution Rate Law and Alteration Product Precipitation Kinetics

D. Strachan, denis.strachan@pnnl.gov, and J. Neeway

The reaction affinity model of glass dissolution couples kinetic terms describing the intrinsic dissolution rate at temperature and pH with a thermodynamic term describing the deviation of the system from pseudo-equilibrium between the glass and its alteration products. It is

important to have a proper expression for the intrinsic glass dissolution rate and the effects of temperature and pH. Separate empirical fitting parameters are currently used to achieve fits for dissolution under acid and alkaline conditions. An examination of the possible values for the intrinsic rate constants for acid and alkaline conditions found that the ratio of these constants can be based on the dissociation constant for water. Recognizing this, it is possible to write the rate expression with a single intrinsic rate value and a term involving the sum of the activities of H^+ and OH^- that may be used for the entire pH range over which the rate mechanism is valid. Much of the literature suggests that the same mechanism appears to be valid from acidic to alkaline conditions. Even better agreement can be achieved if the equation contains a third term for reaction with molecular water. This rate expression was used to explain illite {ideally $(K,H_3O)(Al,Mg,Fe)_2(Si,Al)_4O_{10}[(OH)_2,(H_2O)]$} dissolution (Kohler et al., 2003). These observations have large implications about the dissolution mechanism. For example, if there are three independent activation energies, it might suggest that there are three rate limiting steps in the mechanism, each dominant over different ranges of pH. Alternatively, the activation energies could be different if the active species (e.g., H^+) have catalytic activity. The three-term expression is

$$R = A_H \exp\left(\frac{-E_{AH^+}}{RT}\right) a_H^y + A_{H_2O} \exp\left(\frac{-E_{AH_2O}}{RT}\right) + A_{OH} \exp\left(\frac{-E_{AOH^-}}{RT}\right) a_{OH}^z$$

where A_H, A_{H2O}, and A_{OH} are the pre-exponentials (rate constants) for hydronium ion, water, and hydroxide, respectively; a_H and a_{OH} are the H^+ and OH^- activities and the exponents y and z are the order of the reaction with respect to these species, respectively; and E_{AH}, E_{AH2O}, and E_{AOH} are the activation energies of the rate-limiting reaction involving the solution species H^+, H_2O, and OH^-, respectively(J/mol); R is the gas constant (J/(K·mol)).

In addition to modeling the intrinsic dissolution rate with the above equation, modeling has also been performed to examine the effect of the relative rate of glass dissolution to the precipitation rate for a secondary phase (in this case, the zeolitic phase, analcime [ideally, $Na(AlSi_2O_6)\cdot H_2O$]) on glass durability. These kinetics calculations were performed with rate equations for glass dissolution and analcime precipitation that are similar to the above equation, but with one intrinsic rate value across the pH range. To study this effect, a range of intrinsic values (A in the above equation) were used for both glass dissolution and analcime precipitation. Along with changes to A, the effect of glass composition was also studied. Figure 157 shows an example of how the glass dissolution rate is affected by changes in the intrinsic rate constant for glass at fixed A for analcime precipitation. Even with this simplistic model, results suggest that the dissolution rate is perturbed in the presence of the precipitate, but the durability of the glass is ultimately controlled by the glass phase; i.e. the presence of the secondary phase merely causes a brief increase in the dissolution rate and the rate eventually slows. This result has been observed in many experiments in which the precipitation of a zeolite phase occurs, but experimental evidence has also shown that some glasses completely dissolve after the onset of secondary phase formation. The results from these model calculations suggest that the presence and composition of the gel layer is important in controlling the glass dissolution rate. Results from calculations performed with varying glass compositions indicate that glasses perform poorly if they are high in Al and Na, two elements that are necessary in the formation of zeolitic phases, such as analcime.

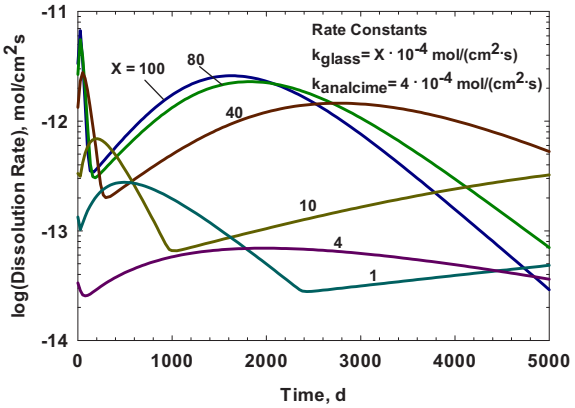

Figure 157. Results from modeling of the effects of changing the glass dissolution rate with a fixed analcime pre-exponential term for glass dissolution rate.

References

1. Köhler, S. J., F. Dufaud, and E. H. Oelkers (2003). "An experimental study of illite dissolution kinetics as a function of pH from 1.4 to 12.4 and temperature from 5 to 50 degrees C." *Geochimica et Cosmochimica Acta* **67**(19): 3583-3594.

Advanced Characterization and Isotope Experiments

J. Ryan, joe.ryan@pnnl.gov

It is critical to understand the transport of ions through mature alteration layers, but isolating this mechanism without chemically perturbing the system is quite challenging. To solve this difficult problem, glasses with the same nominal elemental compositions were synthesized in FY 2010 with different isotopic abundances and allowed to corrode under nominally the same conditions for about one year. Both monolithic glass coupons and glass powder were included in each test. Following the development of a mature alteration layer, the solutions were swapped. In this way, the solution and the glass/alteration products have different isotopic signatures but the overall chemical compositions are nominally the same. The changes in the isotope concentrations in the solid coupons and the solutions each were independently monitored. The migration of individual isotopes through the monolith corrosion products was monitored. In this manner, reaction and transport to and from solution have been and continue to be evaluated without chemical or physical disruption.

The analyses of these test specimens (solid and aqueous) require techniques with sufficient sensitivity to reliably characterize the isotopic distribution in these solid specimens and solutions. In the case of solid specimens, the isotopic sensitivity must be combined with sub-nanometer through millimeter spatial resolution. Atom-probe tomography (APT) is an analytical technique that combines three-dimensional, sub-nm spatial resolution with single-atom sensitivity for all elements independent of atomic number. While the technique has focused traditionally on electrically-conductive metallic specimens, the technique can also be applied to non-conductive specimens through laser-assisted field ionization. In FY 2012, researchers successfully demonstrated the application of APT to describe interfaces within the corrosion layer and between the corrosion layers of a reference nuclear waste glass (SON-68). This was not only the first demonstrated use of the technique for this application, but it was also the first use of APT on multicomponent glasses of any type. While the development of APT for this use took some effort and time, it is a major improvement for the field of glass science and will lead to advancements in materials science for glass materials as a whole.

Through these experiments with APT, researchers have gained an extremely detailed and unprecedented view of the interfacial area where glass corrosion is occurring, as shown in Figure 158. Researchers observed a very sharp interface where the boron and sodium are released from the glass and another further toward the solution where the network silica rearranges because of dissolution and condensation reactions; these are the interfaces between regions IV/III and III/II in Figure 158, respectively. This is a major change from the assumptions foremost in many models. In surface reaction driven models the assumption is a single reacting front, in ion-exchange models there is a diffuse reacting front. Here researchers find more than one distinct fronts as well as different diffuse interfaces for each mobile ion. Several prior assumptions are challenged by these results. The interface where boron and sodium are released from the glass is far sharper than detectable in the past with the less sensitive techniques available up to now. This sharpness puts the question of boron diffusion to rest, as the interface is too sharp to be a diffusion front. The study of silicon transport by isotope tracking showed that there is little barrier to silicon transport into and out of the gel area, contrary to the theories behind transport-limiting models. In addition, researchers found that lithium penetrates quickly, easily, and deeply into the "unreacted glass" (deeper than hydrogen penetration), showing a depth of effect previously unknown in glass research and confirming that the transport of ions depends strongly on the ion in question. The combination of these observations shows that models of radionuclide release from glass must contain more complexity than currently assumed.

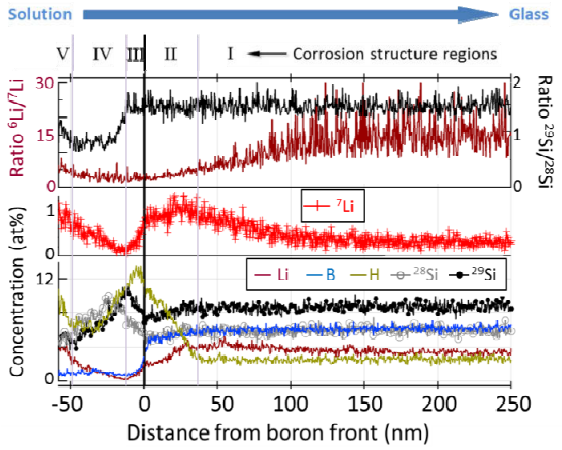

Figure 158. Atom probe tomography (APT) of a 1-year corroded SON68 glass.

Characterization of Ancient Glasses

J. Ryan, joe.ryan@pnnl.gov, and D. Strachan

Archaeological glasses offer a very long time data point for understanding ambient temperature glass corrosion processes. These conditions result in extremely slow kinetics, kinetics that would be difficult to observe in the laboratory even in the longest of experiments. Therefore, laboratory experiments are intentionally accelerated to achieve measurable results in reasonable time frames. Having long-time data points from "experiments" not subjected to accelerating techniques is invaluable both for evaluating the mechanisms operating over those times and for comparing and contrasting the data with those gathered from accelerated tests. In addition, knowledge of the chemistry of the surrounding soil can help bound the conditions (temperature, water flow, and ground water composition) under which the glasses were corroded. This information is critical to the accurate modeling of glass performance over geologic time to the interpretation of results from the laboratory experiments and for model validation.

Several Roman (~3rd century AD) glasses from three archaeological sites have been characterized: the shipwreck of the *Iulia Felix*, located off the coast of Italy (courtesy of our colleagues at University of Padova); a shipwreck from near Embiez Island in the Mediterranean Sea off the coast of southern France (courtesy of our colleagues at CEA); and a Roman villa at the ancient city of Aquileia with glasses buried in soil (courtesy of our colleagues at University of Padova). Because the environment and corrosion time of the shipwreck samples are known, these glasses provide valuable insights into the long-term effects of ion exchange, the prominence of the gel layer in long-term dissolution, and the effects of alteration products on the long-term behavior. Researchers successfully mounted and evaluated specimens of each glass. With X-ray tomography (Figure 159), researchers were able to provide a common 3-D reference for sample analysis.

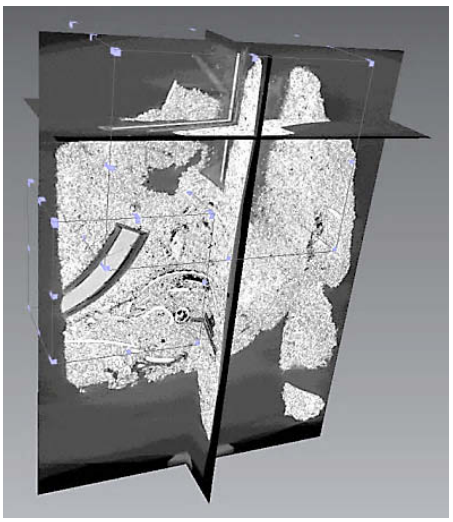

Figure 159. X-ray tomography of Iulia Felix glasses in contact with the surrounding sediment. This technique allows the accurate position referencing of sample data for use in larger-scale models.

Researchers have found signs of an ion-exchange layer (Figure 160) and striking differences in corrosion from glasses with only minor differences in composition. Glasses with colorants and minor (but critical) differences in network formers were only 30-75% as corroded as the colorless glasses. In addition, results from geochemical modeling of the interaction between the encrusting sediment and the glass in contact with sea water indicated that the presence of the sediment influenced the dissolution of the glass and the dissolving glass influenced the alteration phases on both the glass and the sediment. The modeling found that a complete picture of the precipitating phases is critical to being able to model the observed behavior. Only by allowing a minor phase observed with coupled XRD and

SEM characterization were researchers able to show the changes in the encrusting sediment relative to loose sand of the same composition.

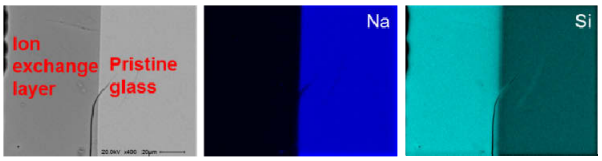

Figure 160. The depth of the ion exchange layer, shown in this SEM image (left) and EDS composition maps for a colorless sample, was found to vary based on composition. This effect, which will be more extensively probed in FY 2013, will help develop versatile models for ion exchange proclivity with changes in glass formulation.

Work planned for next year will focus on establishing the ion-exchange parameters, linking the composition and alteration phase changes through geochemical modeling, and exploring the role of water access to corrosion progress. The samples recovered from terrestrial sites will provide a data point for samples that have experienced intermittent contact with water, but, have not yet been analyzed sufficiently. In addition, researchers will use a summer student to make a comparable series of glasses to those found at the *Iulia Felix* site and see if the observed differences in corrosion behavior can be reproduced in the laboratory.

Synthetic PRI

J. Neeway, PNNL

An existing theory to explain glass alteration kinetics is the existence of a passivating reactive interphase (PRI), which may limit the transport of glass forming species from the pristine glass to the bulk solution. This layer must be extremely thin, and is hypothesized to exist between the pristine glass and the gel layer. Although some results suggest that such a layer is unlikely to form, researchers need to try and generate the material that is likely to form at the glass-solution interface to understand its properties. The properties of this material and its contribution to the corrosion mechanism are unknown, mainly because such a thin layer is very difficult to interrogate.

A joint DOE/CEA project was begun to synthesize a bulk version of this hydrated glass layer and facilitate characterization of its physical and chemical properties. Experiments have consisted of machining ~180 µm thick coupons of the SON-68 reference HLW glass and reacting them in duplicate, along with 75-150 µm glass powder, at 90°C, in a solution saturated with H_4SiO_4 (saturated with respect to amorphous silica). The solutions were buffered at pH values of 4, 7, and 9, as well as one experiment with an unbuffered H_2O. These experiments were performed in a flow-through configuration so that the solutions were dilute with respect to other components needed to form typical secondary phases. In silica-saturated conditions ion-exchange is theorized to be the dominant corrosion mechanism, thus, in this controlled experiment, a PRI is expected to form.

Because of the long-term nature of the experiment, few results are available. However, one coupon, corroded in H_2O, was removed from a reactor after 66 days of corrosion and exhibited an alteration layer approximately 1 µm thick. There was evidence of secondary phases at the surface, indicating that the conditions were not sufficiently dilute to prevent their formation, but they have not yet been characterized. Their effect on the majority of the leached layer has not been determined, but the phases appear to only populate the surface. Solution data, obtained for the slowest reaction condition (water), suggest it may take ~10 years for the leached region to reach the center of the coupon. However, the experiments performed with the pH 4 and 9 solutions may be finished much faster because of the more corrosive conditions.

Solution Exchange Tests

W. Ebert, ebert@anl.gov

Questions regarding the process controlling the long-term kinetic behavior of glass dissolution remain, specifically whether it follows the root-time dependence of a diffusion-controlled process, continues to vary in response to the solution composition, or maintains a constant rate. Solution replacement tests were conducted with SON-68 glass in solutions with Si concentrations near the saturation level. These tests were designed to maintain a nearly constant average reaction affinity over each sampling interval to distinguish the relative importance of diffusion and reaction to glass dissolution. To distinguish between testing artifacts and the release mechanism, tests were

conducted at different exchange frequencies and with solutions containing different Si concentrations. The results indicate that releases of B and Li follow root-time kinetics initially, but both evolve to linear release kinetics as the reaction continues. The change in kinetics is clearly observed in the experiments by the response to changing the solution exchange frequency to either shorter or longer intervals and to changing the solution composition. For example, Figure 161 shows the results for two tests conducted in a 0.33 M SiO_2 solution. Results from a test with fresh glass conducted with a 1-day exchange frequency show non-linear behavior (Curve 1). Curve 2A shows the non-linear results of a test conducted with five exchanges at a frequency of 14 days (see inset). Curve 2B shows that the dissolution of the same test specimen used to generate Curve 2A follows linear kinetics after the exchange frequency was increased to 1 per day. (That is, the specimen had reacted 1675 hours when Test 2B was initiated, and 1819 hours when Test 2C was initiated.) Curve 2C shows the results for continuation of that test with a 1-day exchange frequency using a 0.23 M SiO_2 solution. The specimen remained wet at each solution exchange. The release remains linear, but at a slightly higher rate in the leachant with the lower Si concentration. Whereas the non-linearity during the initial dissolution in Test 2A was due to mass transport through the developing surface alteration layer, the non-linearity seen beyond the first few exchanges was probably due to the small increase in the Si concentration over the 14-day exchange interval. This is evidenced by the linear response when the exchange frequency was increased to 1 day (Curve 2B). The predominance of the solution control was confirmed by the higher rate measured when the leachant with a lower Si concentration was used (Curve 2C). However, the dissolution rates measured as shown in Curves 2B and 2C were about eight-times lower than the rates measured with those solutions in tests with fresh glass and a 1-day exchange frequency. This is attributed to the mass transport effect becoming nearly constant as the layer matures.

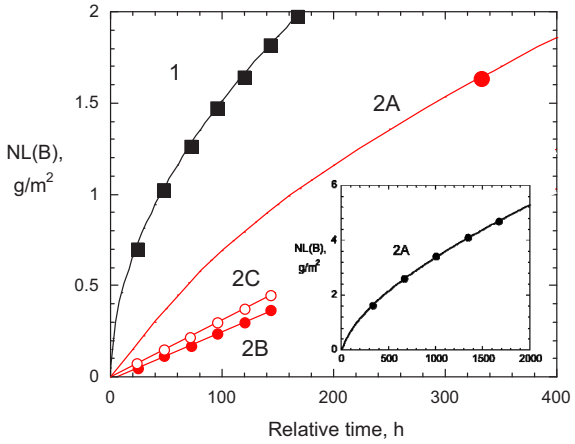

Figure 161. Results of solution replacement tests in two SiO_2 solutions with two exchange intervals. Curve 1, 1-d exchange interval; Curve 2A, 14-d exchange interval; Curve 2B, 1-d exchange for the test specimen from 2A after 70-d of testing; Curve 2C, 1-d exchange in 0.23 m Si, specimen from 2B after a total of 76 d.

The observed change in kinetics is opposite to the behavior seen previously in tests with very low Si concentrations, where the releases evolved from initially linear kinetics to a root-time dependence over time. It was hypothesized at that time that structural changes in the near-surface region occurred to provide a transport barrier to water accessing reactive sites. Tests in solutions with low SiO_2 concentration were dominated by the effects of the developing surface acting as a diffusion barrier such that the releases of B and Li slow with the reaction time. How quickly the layer forms is affected by the SiO_2 concentration in the leachant and the exchange frequency. The increase in the SiO_2 concentration that occurred over the test interval due to glass dissolution became significant for exchange frequencies greater than a few days and also affected the dissolution rate. In the current tests in solutions with high Si concentrations, the change in the near-surface region of a fresh glass specimen occurred rapidly (i.e., within the first few solution exchanges) such that the dissolution rate became controlled primarily by the solution after short reaction times; albeit coupled with an essentially constant transport model coefficient imposed by the layer. The observed behavior of initial linear reaction-controlled dissolution, intermediate diffusion controlled kinetics, and long-term linear kinetics sensitive to the solution composition is consistent

with that seen previously in long-term product consistency tests (PCT) with the same glass.

Although both diffusion and affinity-controlled dissolution reactions impact the long-term glass corrosion behavior, these tests indicate that the net kinetics is linear and the rate is controlled by the solution composition. This conclusion applies to the glass + water system, but may not apply when alteration phases form and become coupled with the glass dissolution kinetics through the solution. The relative importance of mass transport and reaction kinetics may change in such a coupled system.

Stage 3 Dissolution (S3D) Tests

C. Crawford charles.crawford@srnl.doe.gov, and J. Marra, SRNL; and W. Ebert and J. Fortner, ANL

A novel test method was used to study the corrosion behavior of the AFCI reference waste glass. This glass was developed during the AFCI to account for a high Mo waste stream, giving a reference composition to estimate waste loading in glass and defining a reference set of properties including durability. It was nearly immediately determined to have significantly better short-term and poorer long-term durability than the HLW reference glass (SON-68). It was therefore included as a composition studied in all long-term durability testing to help understand how two glasses with similar compositions could perform so differently in corrosion tests. Tests on the AFCI glass were performed by imposing conditions under which the sudden increase in the dissolution rate has been observed: a solution with high concentrations of dissolved glass components (and high pH), the presence of alteration phases, and the presence of a clay layer overlying an alkali metal and boron-depleted glass surface. The alteration phases were generated in vapor hydration tests (VHT) conducted at 200ºC, which provided specimens of AFCI glass with a thick crust of mature alteration phases. Different amounts of alteration phases were generated by reacting glass coupons of different sizes. The source solution was prepared in static tests with crushed glass conducted for about four months to generate a highly concentrated solution nearly saturated with respect to the suite of alteration phases that eventually form in long-term PCTs and affect the glass dissolution rate. This solution was equilibrated with the VHT specimens (i.e., the alteration phases) for two weeks prior to use. The standard S3D test was conducted by placing a fresh glass coupon in a vessel with the saturated solution and a VHT specimen and reacting at 90ºC. The surfaces of the test specimens were preconditioned by conducting dissolution tests in demineralized water for 45, 72, and 196 days prior to use in the S3D tests. The S3D test was interrupted occasionally (every 2 or 3 weeks) to track the glass mass loss, which was used as a measure of the dissolution rate. Modified tests were conducted to measure the effects of the presence or absence of mineral alteration phases, the relative surface areas of the alteration phases, the glass surface area-to-solution volume ratio, and a pre-reacted surface layer on the glass. The glass and VHT specimens were separated by a Teflon grid in all but one test, which was conducted to measure the effect of direct contact between the two test specimens. At the end of each test, the solution was analyzed to provide a measure of the cumulative glass dissolution and the reacted solids (the glass and VHT specimens) were analyzed.

The primary objective of the S3D tests is to determine the relative importance of alteration phase nucleation and precipitation rates, mass transfer through solution, surface alteration (gel formation), and mass transfer through gel and clay surface layers on the glass. The insights gained will guide subsequent process-specific testing to quantify the coupling of the dissolution and precipitation kinetics for inclusion in the glass degradation model. The key results from these tests are

1. The precipitation of new phases caused the glass dissolution rate to increase rather than the continued growth of the phases that were provided on the VHT specimen. Neither the presence nor the size of the VHT specimen, which is assumed to be proportional to the surface areas of the alteration phases on it, had an effect on the glass dissolution rate. The rate-affecting phases may be precursors to the more stable phases that are present on the VHT specimens.

2. Glass dissolution in Stage 3 proceeded with linear kinetics (i.e., after the new phases formed). This conclusion is based on the measured mass changes of the glass specimens being linear with time. The rate changed midway through some tests, but remained linear. The measured mass changes represented the difference between mass loss from glass dissolution and mass gain from the precipitation of new alteration phases on the glass specimen. The change in rate was attributed to a change in the relative contributions of glass dissolution and alteration phase precipitation to the net mass change.
3. The glass dissolution rate in Stage 3 was not correlated with the Si concentrations measured in the final solutions. This suggests either that the form of the reaction affinity term that is appropriate for glass dissolution in the presence of alteration phases includes species in addition to (or other than) total Si. This is consistent with results of static tests discussed in the next section.
4. The glass dissolution rate is higher in tests conducted at lower surface area-to-volume (S/V) ratios, for both the glass and VHT surface areas, despite the initial leachant compositions being nearly saturated with respect to the suite of rate-affecting alteration phases. The difference is attributed to the effects of S/V on the efficiency of coupling the glass dissolution rate to the precipitation rate of the new alteration phases through the solution chemistry. That is, the amounts of glass that must dissolve and alteration phases that must form to affect the solution concentrations depend on S/V.
5. Alteration of the fresh glass surface (e.g., dealkalization or gel formation) is not a prerequisite for the increased rate, nor does the presence of an alteration layer measurably affect the Stage 3 rate. Successful nucleation of the alteration phases appears to be the controlling factor for the increased dissolution rate.
6. The exact suite of alteration phases that forms initially cannot currently be predicted because kinetically favored phases precipitate prior to thermodynamically favored phases. This adds uncertainty to the predicted effect of alteration phase formation on the glass dissolution rate. Although the specimens were only examined at the end of the tests (and more complete examinations are in progress), the mass loss behavior suggests the reaction conditions affecting the glass dissolution rate remained constant throughout most of the S3D tests.

Figure 162a shows an abundance of blocky (left) and fibrous (right) alteration phases that formed overlying analcime crystals on the VHT specimen used in a standard S3D test. Figure 162b shows crystallites of what appear to be the same phases that formed on the surface of a glass specimen from a S3D test conducted without a VHT specimen. Further analyses of the reacted solids (both the glass and VHT specimens) will be performed in FY 2013 for comparisons with alteration phases formed in other tests with AFCI glass. The alteration phases formed under different test conditions will provide insights regarding the evolution of the alteration phase assemblage from the kinetically-preferred suite to the thermodynamically-preferred suite of phases.

The results from these S3D tests will be combined with results from static tests at ANL and SRNL that are discussed in the two sections that follow to identify the phase or phases that affect the glass dissolution rate and determine the solution conditions required for the formation of these phases.

Measuring and modeling the precipitation kinetics of mineral phases is by itself very challenging due to simultaneous evolution of the solution chemistry, the size, surface area, and reactivities of nucleating embryos, and coupling that with the changing glass dissolution kinetics further complicates the effort. Experimental measurements are challenging due to the need to provide conditions suitable for phase nucleation and growth, while at the same time monitoring glass dissolution. These tests represent an initial attempt to control the reaction conditions and

identify the process responsible for the increase in glass corrosion. Although the experimental system was necessarily complex (relative to common corrosion test methods) to promote the coupled reaction and the results are qualitative due the abundant precipitation of two or more alteration phases, valuable insights were gained from these experiments. The results clearly indicate the primary importance of the solution composition and lack of influence of the glass surface and existing mineral phases. The precipitation of new phases triggered the increase in glass dissolution, not the growth of existing phases.

For modeling long-term waste glass behavior, these results suggest that the onset of increased glass dissolution rate can be triggered in the glass degradation model based on the attainment of critical solution conditions that are conducive the formation of rate-affecting alteration phases. This is discussed in the next section.

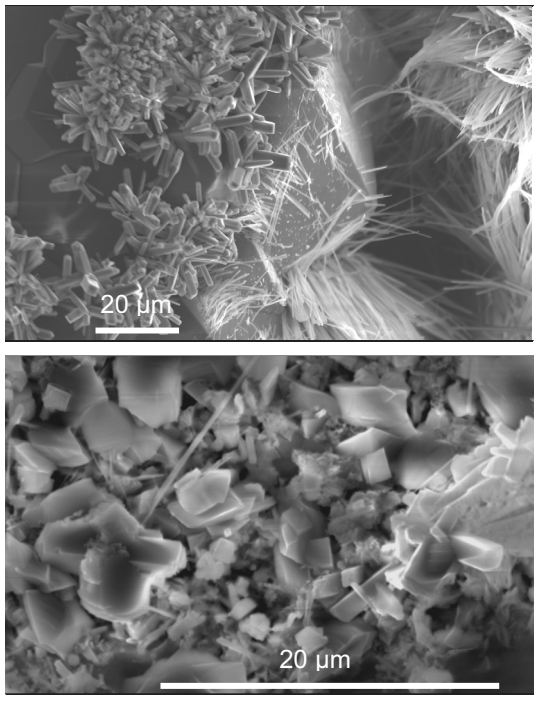

Figure 162. SEM images of tabular and fibrous alteration phases formed during S3D test: (a) overlying blocky phase on VHT specimen and (b) on the surface of a glass specimen reacted in the absence of a VHT specimen.

Static Tests to Study Onset of Alteration Phase Precipitation

J. Fortner, fortner@anl.gov, and W. Ebert

Static tests are being conducted with AFCI glass to better correlate changes in the solution composition with the initial precipitation of rate-affecting alteration phases and quantify the coupling of the glass dissolution rate with the alteration phase precipitation rate. Tests at 90ºC are in progress with alteration phase precipitation expected to occur during FY 2013. Tests are being conducted at 200ºC to produce alteration phases more quickly, to develop the analytical techniques, and to demonstrate the process. The top plot of Figure 163 shows the sudden increase in the normalized glass dissolution rate that occurs after about 40 hours under these test conditions in terms of the amounts released into solution normalized to the elemental concentrations in the glass (i.e., fractional release FR). The releases remain constant through the longest test duration of 115 hours (not shown), at which point about 60% of the glass has corroded. The matrix dissolution is quantified by the release of B and the fractional releases of other glass components into solution are compared with that of B in the bottom plot of Figure 163. Lines drawn for tests in which alteration phases had formed (tests run longer than 40 hours) show Li and Na releases to be proportional to the release of B and linear with reaction progress, but the slope of the FR_{Li} data suggest that the Li release is congruent with the B release. For Na, the slope of the line drawn through the data, being significantly lower than 1, suggest that Na is removed from the glass at a slower rate or that some of the Na is precipitating from solution. Based on results shown above, it is assumed that Na is precipitating. The FR_{Al} decreases when alteration phases precipitate due to its removal from solution. The FR_{Si} appears to shows a transient increase when the alteration phases first precipitate—at about $FR_B = 0.055$—but then decreases and remains nearly constant or increases slightly thereafter. The release of Ca to solution increases slowly, at about the same rate as Si. These results suggest that Al, Ca, Na, and Si are sequestered in the alteration phases and the solution concentrations of some or all of these could affect the glass dissolution rate when the kinetics becomes coupled with alteration phase

precipitation kinetics. Whereas the concentration of orthosilicic acid controls the dissolution rate prior to the formation of alteration phases, these results suggest the concentration of aluminum in particular (and perhaps silicon) could limit the coupled kinetics of the system through the precipitation kinetics of one or more of the alteration phases. Additional testing is needed to evaluate the role of the Al and Si concentrations on the glass dissolution rate after alteration phases form.

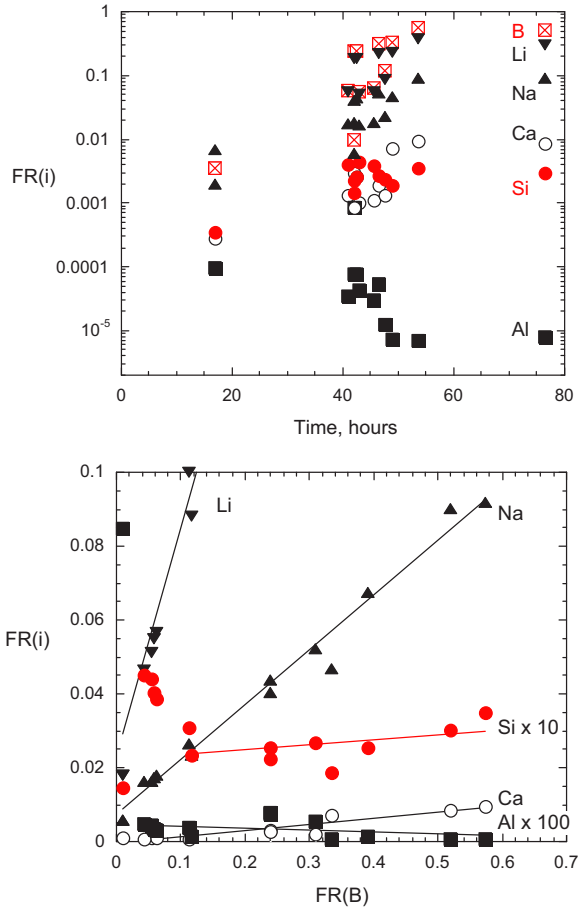

Figure 163. Fractional releases of Al, B, Ca, Li, Na, and Si as a function of time (top) and relative to the release of B after alteration phases form at 40 h (bottom).

Figure 164a shows a corroded grain of glass with a large blocky NaAl-silicate alteration phase, based on twinned morphology and composition, and a spherical Ca-silicate alteration phase. The large phase formed on the glass but broke off during SEM analysis (due to handling or electrostatic charging in the SEM). The glass particle is covered by a layer of another phase that either did not form on or has spalled from the area adjacent to the blocky phase. A small remnant of the blocky phase remained attached to the underlying glass (in the area labeled Glass). Figure 164b shows the morphology of the spherical alteration phases and underlying clay. The albite precipitation rate is expected to depend on the Na, Al, and Si concentrations and the Ca-silicate on the Ca and Si concentrations. Clay is known to form on most waste glasses without leading to the sudden increase in the glass dissolution rate, has slow precipitation kinetics, and is not considered to be an important couple. Work is planned for FY 2013 to quantify the effects of the solution composition on the coupled kinetics and determine which phase affects the glass dissolution rate.

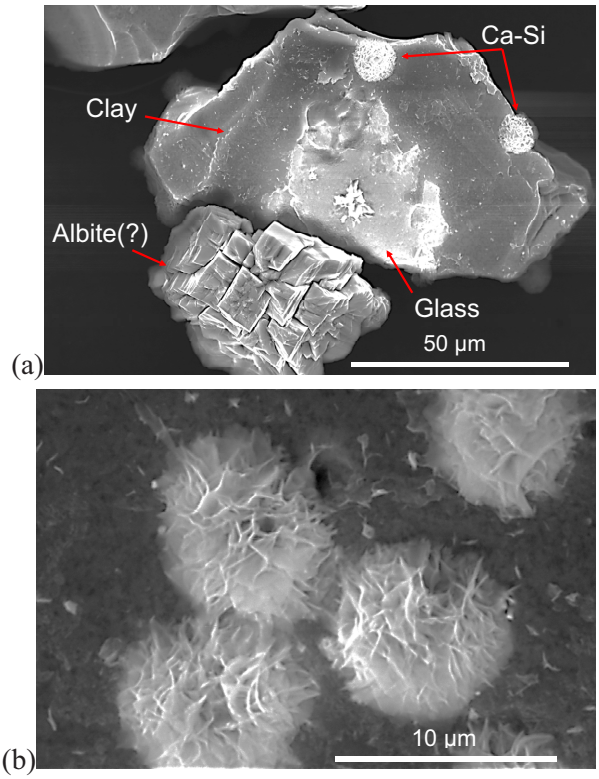

Figure 164. SEM images of blocky NaAl silicate and rosette Ca-silicate alteration phases formed during static test at 200ºC (a) glass grain with thin clay layer and alteration phases and (b) Ca-silicate rosettes and clay.

Characterization of Solids from Long-term Corrosion Tests

C. Crawford, charles.crawford@srnl.doe.gov, and J. Marra

Previous Product Consistency Testing – Method B (PCT-B) and Vapor Hydration Testing (VHT) provided some insight into the formation of alteration phase formation during corrosion of AFCI and SON-68 glasses. From FY10 to FY12, very long-term PCT-B tests were conducted at 200°C on the AFCI and SON-68 glasses to obtain additional data on alteration phase formation. These tests were conducted at 200ºC with 200-325 mesh glass particles to accelerate the build-up of dissolved glass in solution, promote the formation of alteration phases, assess their effect on the glass dissolution rate, and facilitate phase identification. An effort was initiated in FY12 to characterize the solids recovered from the very long-term PCT-Bs conducted with these glasses. After the two longest test durations of 509 and 791 days, the glass particles from each glass had become "cemented" into an aggregate. The reacted material was removed intact by first applying a thin epoxy coating to the top surface followed by core-drilling. This proved to be an effective method to recover the material intact thereby decreasing the ambiguity during microscopic analyses. In addition to identifying the suite of alteration phases, examination of the phase distributions and compositions with depth and radius provided insights regarding the possible sedimentation of phases, constriction of water transport, localized composition gradients, etc. These insights are relevant to understanding the physical and chemical effects of surface alteration layers, corrosion in tight cracks, and identifying possible artifacts of laboratory test methods with glass powders. Duplicate samples were run in the PCT-B. One of the duplicate samples was pulverized for XRD and the other was cut in half (radially), impregnated with additional epoxy, polished and examined with SEM. These samples provide a unique opportunity to study the corrosion behavior of densely packed glass grains with pore water that may have had localized compositional variations. The results of initial SEM analyses are summarized below.

The XRD analyses showed that the AFCI glass alteration phases formed quickly under these test conditions and the glass was almost completely converted to analcime and montmorillonite (clay) after 791 days. In the SON-68 glass, there was minor evidence of alteration phase formation after 28 days and distinguishable phases were observed in the sample reacted for 124 d (see Figure 165). After 791 d, SON-68 had reacted to form analcime, nontronite (clay), and a hydrated sodium aluminum silicate phase. It should be further noted that leachate concentrations in relation to exposure time correlated with the XRD data on phase formation. For example, the SON-68 leachate Al concentrations increased through 300 days and possibly reached a maximum with the concentrations decreasing by 500 days. This is supported by the results shown in Figure 165 for SON-68 that show insignificant crystalline species up to 124 days, with significantly more crystalline species present at >300 days.

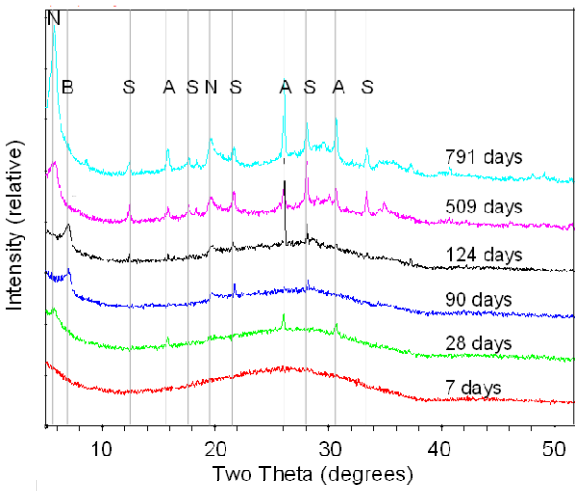

Figure 165. XRD scans of the reaction products of SON-68 glass showing secondary phase formation evolution during 200°C PCT. N-Notronite, S-0.95$Na_2O{\cdot}Al_2O_3{\cdot}$ 3.35$SiO_2{\cdot}$4.79H_2O, B-Beidellite, A-Analcime

SEM analyses coupled with EDS to facilitate elemental determinations confirmed the presence of the alteration phases identified in the XRD scans. However, the SEM analyses also revealed the presence of large inhomogeneous regions enriched in certain glass elements. Figure 166a shows a SEM image of a small region of corroded SON-68 glass and alteration phases. Small cores

of unreacted glass (feature 2) are seen surrounded by a highly porous layer (feature 4) and an encapsulating layer (features 3 and 7), which is assumed to locate the original surface of the glass grain. Fibrous alteration phases (feature 1) and spherical phases (feature 5) of a primary inclusion phase present in SON-68 glass are observed to be distributed throughout the sample. Although many interpretations of these data are possible, it is suspected that the encapsulating layers (features 3 and 7, likely nontronite) formed slowly on each grain during Stage 2 prior to the precipitation of other alteration phases, and that the porous material (feature 4) is a gel that formed quickly at the higher glass dissolution rate in Stage 3. Phases formed outside the encapsulating layers (e.g., feature 1) possibly precipitated from solution during Stage 3. Analyses are in progress to measure spatial variations in the degree of glass corrosion and the assemblage and abundance of alteration phases in cross section. The black regions in Figure 166a are voids filled with resin. These regions were probably filled with pore water during the test.

The gross distributions of some glass components show interesting patterns at scales much larger than the glass grains (note: the glass grains are nominally between 45 and 75 µm at the initiation of the PCT-B test). For example, Figure 166b is an X-ray map that shows local regions of high Cs concentration on the scale of about 1 mm. The radial nature of the concentration gradients is suggestive of a transport property. Additional studies are necessary to understand the exact nature of this gradient and element distributions in the samples.

These results provide insights into processes occurring in pore water within alteration layers formed on glass surfaces. Further analyses will be conducted in FY 2013 at both scales.

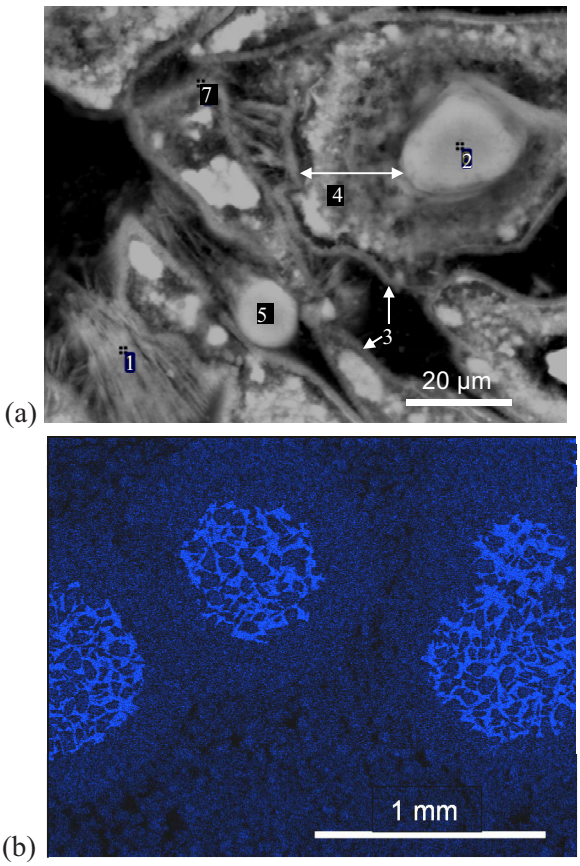

Figure 166. Polished cross section of SON-68 glass reacted 509 days showing (a) fibrous alteration phase (1), core of unreacted glass (2), exterior alteration layer (3), interior alteration layer (4), and a primary Mo inclusion (5), and (b) an X-ray map of Cs (blue), showing the inhomogeneity of the Cs distribution in an area of the specimen [unrelated to that shown in (a)].

Geometric Effects on Dissolution

J. Ryan, joe.ryan@pnnl.gov

Many laboratory test methods use powdered glasses to increase the surface area available for reaction, but the effects of the shapes of the glass particles are not taken into account. A summer study supported by the DOE Science Undergraduate Laboratory Internships (SULI) and Visiting Faculty Programs (VFP) conclusively showed that particle shape can have a large effect on the observed dissolution data. Starting with a type of glass that is much more soluble than any waste glasses, two interns and a visiting faculty member evaluated the effect of shape on dissolution at a macroscopic scale. The results of our study refute some common views about how glass particles geometrically evolve during

dissolution (see Figure 167). For example, sharp edges on glass particles have been thought to round as they corrode in water, whereas researchers observed the opposite. Exterior corners became sharper while interior corners rounded.

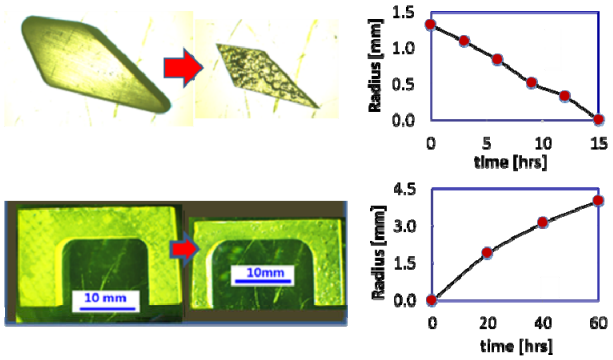

Figure 167. Results showing how various particle shapes are affected by congruent dissolution by tracking the radii of outside (top right graph) and inside (bottom right graph) corners of the test specimens shown on the left. At the start of the dissolution, all corners were very sharp; outside corners sharpened; the corners inside the "U" rounded.

In short, the congruent dissolution of glass was found to follow a geometric pattern, with dissolution taking place along a direction normal to the surface at a constant rate. Expanding on our results, a quantitative dissolution model was developed involving the concept of image pixel removal that successfully predicts the dissolution behavior for any 2-D geometrical configuration. With this model researchers will be able to calculate the effect of particle shape for future flow-through tests, producing a correction factor that could assist us in the interpretation of the results from dissolution tests. While success was achieved in calculating the effect of dissolution on these test shapes with surrogate glasses, the model was based on simple geometry and must be vetted further before application in specific conditions.

Undergraduate Student Awards

1. N. Reeves, *MS&T 2012*, 1st Place Poster.
2. M. Yamamura, *Surface Analysis 2012*, 3rd Place Poster.

Inverse Modeling

R. Williford, PNNL

The public acceptance of engineered waste packages is critically dependent upon input of glass dissolution models into field-scale fate and transport calculations. It is imperative, therefore, that robust models based on a scientific and mechanistic understanding of the processes responsible for glass degradation and radionuclide release be used to calculate the long-term behavior of a glass waste form. As defined here, a "model" would be a set of relevant chemical reactions and mass transport mechanisms that describes anything from a small portion of simplified glass corrosion layers, to the multi-layered structures found on ancient glasses, to a directional flow corrosion profile such as that found in the alteration layers on glass from a 26-year experiment recently terminated at the CEA laboratory in Marcoule, France, to full-scale nuclear glass monoliths.

Because several such models have been proposed to date, a generalized model evaluation tool is needed that allows models to be systematically and quantitatively compared to experimental data and, just as importantly, to each other. To this end, a tool to estimate model parameters and the corresponding uncertainty in model predictions is being developed. In partnership with our colleagues at CEA, researchers utilized the Parameter Estimation (PEST) code to evaluate the CEA-produced analytical GRAAL glass corrosion model with the objectives of (1) demonstrating a capability to rapidly fit model parameters to a given data base, (2) assessing model parameter sensitivities, and (3) assessing the predictive uncertainties of the GRAAL glass corrosion model. In addition, the work also will be used to guide future experimental efforts towards uncertain or particularly sensitive parameter space. For example, the GRAAL waste glass corrosion model was found to be relatively insensitive to several parameters that could be held constant to focus on other parameters that have a greater impact on GRAAL predictive accuracy, such as pH.

With the extended international collaboration on glass corrosion regularly producing detailed new information, the variety of current models

stand to be updated and extended in the coming years. With such a plethora of models originating from many technical groups with varied points of view, it seems self-evident that a capability for formalized and rapid quantitative assessment of such models is a valuable addition to the world modeling community. The tool being developed with this effort will gradually add capabilities to treat the full range of relevant phenomena from flow and thermal effects to micro-kinetic chemical reactions to package design geometries. Such a generalized tool should have a noticeable impact on the speed at which development of verified predictive glass corrosion models, radionuclide release models, and waste package designs can be completed to regulatory satisfaction with the end goal of selecting and parameterizing the model best suited to the prediction of glass corrosion in an arbitrary near-field environment.

International Simple Glass

J. Marra, jim.marra@srnl.doe.gov

Given the complexity of waste glass compositions, it is often necessary to utilize simplified glass compositions for atomistic models and to avoid interactions that complicate or prevent the use of sophisticated analytical techniques. A six-component glass was formulated by the collaborating group of international scientists as a reference glass test material providing a compromise between compositional simplicity and a useful representation of waste glasses. This glass will be used in support of efforts to closely couple first-principles theory, reactive-transport modeling, and experiments for predicting waste form behavior over geologic time scales. Tests with this so-called international simple glass will help identify dominant processes that occur at different stages of glass corrosion, develop corrosion models to represent these key processes, define model parameters values and model sensitivities, and support the integration of atomistic and continuum models into disposal site assessments. These models and approaches can then be applied to actual waste glass formulations.

Under a subcontract from the SRNL, MoSci Corporation (Rolla, MO) produced approximately 50 kg of a BSG with a nominal composition of (mass% oxide): *56.2 SiO_2, 17.3 B_2O_3, 12.2 Na_2O, 6.1 Al_2O_3, 5.0 CaO, 3.3 ZrO_2* in the form of 100 annealed blocks (nominally 5x5x10 cm and 0.5 kg). During the production of the 50 kg, two samples (Bar #221 and Bar #223) were submitted to SRNL's Process Science Analytical Laboratory (PSAL) to confirm that the compositions were within the contractual specifications. Once acceptance testing was completed, the glass bars were received by SRNL and then distributed to the EM, NE, and international glass corrosion partners at 18 institutions in 6 different countries for use in a variety of material characterization and corrosion test activities.

International Collaborative Studies on Glass Corrosion Mechanism and Modeling

J. Ryan, joe.ryan@pnnl.gov

The international collaboration on glass corrosion made strong gains in FY 2012. The detailed, peer-reviewed, multi-year plan developed last year for the NE/EM joint DOE program has inspired the international community to write an overall plan to be submitted to a peer-reviewed journal early in FY 2013. This plan describes the positions of each participant nations, outlines the goals of the collaboration, and provides details on how research is coordinated. Our Japanese, Belgian, and French partners have joined us in applying for and being accepted as a "Coordinated Research Program" by the IAEA. This program designation provides organization for future meetings, some travel funding to attend these meetings, and international recognition.

Two international face-to-face workshops and one web meeting were held to facilitate communication and collaboration of researchers within the group. The May 2012 general workshop was held in St. Louis in conjunction with a Glass and Optical Materials conference and was attended by 30 researchers from five countries. All participants exchanged and discussed recent results and organized future collaborative and coordinated efforts. A mini-workshop dedicated to modeling issues was held in June 2012 in conjunction with the Montreal Goldschmidt geochemistry conference.

As part of a CEA/DOE direct collaboration, a renowned corrosion expert from the French CEA lab, Dr. Stéphane Gin, began a 15-month appointment at PNNL in August 2012. Having Dr.

Gin working directly with us will facilitate our achieving a consensus understanding of the glass corrosion mechanism. Also, our groundbreaking FY 2012 work at the DOE-SC EMSL led to team members authoring a chapter on APT for a new book on glass characterization and to the awarding of SC-supported Science Theme User Access for FY 2013 and FY 2014. Because of this visibility, the SC facility is looking into awarding our international co-workers major access as well. Researchers will continue to explore such options in the coming years.

CHAPTER 12
FUEL RESOURCES

CHAPTER 12: FUEL RESOURCES

K. Felker, felkerlk@ornl.gov

Advanced Absorbent Development

K. Felker, felkerlk@ornl.gov

In FY 2012, key accomplishments for the Advanced Adsorbent Development task included the following: development of uranium adsorbents with higher adsorption capacities compared to current state-of-the-art adsorbents in both laboratory screening and actual seawater experiments; receipt of an R&D 100 Award for our "HiCap Adsorbents" (see Figure 168); submission of a patent application on our adsorbent technology entitled, "Fiber-based adsorbents having high adsorption capacities for recovering dissolved metals and methods thereof"; completion of many collaborative activities associated with adsorbent manufacture including the synthesis, characterization, radiation and chemical process optimization, mechanical and thermal property testing, long-term aging experiments, stability and equilibrium studies and seawater testing; and evaluation of several strategies for reducing the manufacturing cost of developed adsorbents.

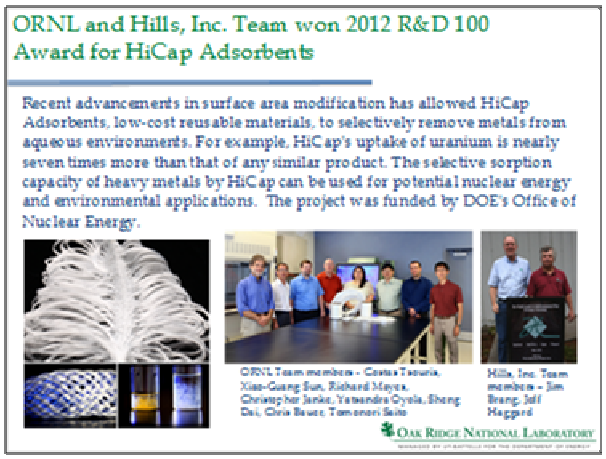

Figure 168. ORNL announcement of 2012 R&D 100 Award.

During FY 2012, the production of adsorbents having high uranium adsorption capacities continued with the development and testing of a large number of new and improved adsorbents. These adsorbents incorporated new high surface area fibers from Hills, Inc. and were processed using improved irradiation and grafting conditions at NEO Beam's irradiation facility and improved amidoximation and alkaline conditioning methods at ORNL. These same types of fibers were also successfully braided at Steeger USA to produce Japanese-like braid adsorbents and other braided forms for marine testing. New non-fiber-based adsorbent materials are also being evaluated as possible alternatives to conventional fiber-based adsorbents. In addition, new hydrophilic grafting monomers are being investigated and have recently shown promise as potential alternatives to the conventional methacrylic acid monomer. Several strategies are being evaluated for potentially reducing the manufacturing costs of the adsorbent materials including reducing the amount of co-monomers and solvents used in the grafting process, incorporating key additives in the grafting solution that may enhance grafting efficiency and inhibit co-polymerization of the grafting monomers, and minimizing the use of costly chemicals in the downstream adsorbent processing. The testing of the developed adsorbent materials has progressed from laboratory screening with synthetic seawater to testing of the most promising adsorbents with seawater at marine testing facilities. An example of adsorbent capacity progression is shown in Figure 169.

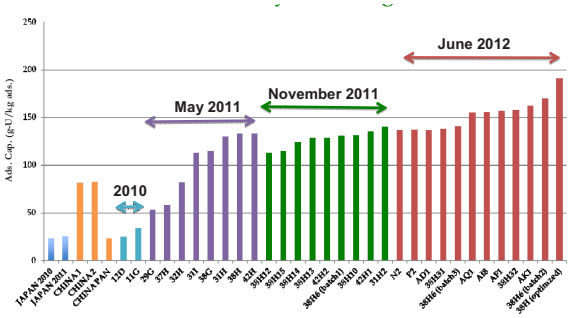

Figure 169. Uranium adsorption capacity progression over two year period.

Thermodynamic, Kinetic, and Structural Studies

In FY 2012, The studies of the thermodynamics for the complexation of uranium with the tridentate cyclic imidedioxime ligand that is hypothesized to be responsible for the efficient extraction of uranium from seawater was completed. The complexation strength, the ability to compete with carbonate, and the coordination modes were revealed with multiple techniques. The results were published in Dalton Transactions as a cover page article (see Figure 170). The complexation of uranium with the open-chain amidoxime ligand was found to be weaker than the cyclic ligand. A paper describing this data has been submitted for publication.

Figure 170. Cover page article, Dalton Transactions

Comparative studies of the complexation of transition metals (Fe, Pb, Ni, Cu) was conducted. These results increased the understanding of competition of transition metals with uranium for sorption by the amidoxime-based sorbents.

Collaboration with the Hay Group at ORNL to study an AO-related ligand was initiated. These results will help to develop a structure-property relationship that can guide the design of more efficient ligands and sorbents. A joint paper describing this activity is in preparation.

Stopped-flow kinetic studies were initiated to investigate the reaction rate between tricarbonato uranyl complex and amidoxime ligands.

Functional Ligand Development

The objective of this task is to increase uranium uptake from seawater through modification of the chelating agents that serve as binding sites in adsorbent materials. A focused theoretical and experimental research effort entails (1) evaluation of amidoxime-uranyl interactions (electronic structure calculations, organic synthesis, x-ray crystallography); (2) computer-aided molecular design of optimal chelating structures (molecular mechanics, de novo structure-based design methods); (3) preparation, characterization, and testing of chelating agents (organic synthesis, x-ray crystallography, NMR and UV-visible spectroscopy, pH titration); and (4) chemical modification to allow covalent attachment to polymeric materials (organic synthesis).

The FY 2011 studies yielded requisite criteria for application of computer-aided design methods to identify optimal architectures for ligands containing amidoxime functional groups. In FY 2012, structure-based *de novo* design methods were used to locate the optimal linkages for bis-amidoxime chelates. The top scoring architecture, Figure 171, image **1**, was selected for synthesis. In a parallel effort, electronic structure calculations were used to rank the uranyl binding affinity for a series of tridentate cyclic imidodioxime ligands, see Figure 171, images **2** and **3**. Formation constants for aqueous 1:1 ligand:metal complexes, estimated from electronic structure calculations with implicit solvation corrections, predict that **1** - **3** all exhibit high affinity for the uranyl ion when in their dianionic forms, sufficient to displace two carbonate ligands from the predominant seawater species $[UO_2(CO_3)_3]^{4-}$. Synthetic routes to **1** – **3** have been developed and each has been prepared with $-NH_2$ substituents in > 500 mg quantities. The initial strategy was to exploit the $-NH_2$ substituent as a means to covalently attach the ligand to chloromethylpolystyrene via nucleophilic substitution. Unfortunately, the amines in these compounds proved to have very low nucleophilicity and polymer functionalization by this route is not viable. An alternate strategy, involving the reaction of alkyne-substituted ligands with azide-functionalized polymers, is

now under investigation. Additional synthetic efforts are in progress to isolate hydrophilic analogs of **1** and **2** in order to allow the experimental measurement of their uranyl binding affinities.

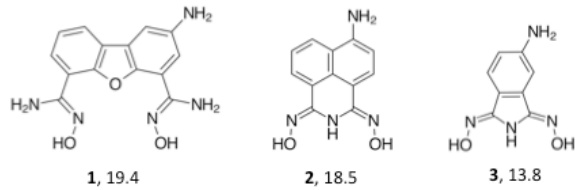

Figure 171. Novel uranyl chelates identified through computer-aided molecular design methods, 1 – 3, shown in their fully protonated, charge-neutral forms. Predicted log K values for the formation of 1:1 complexes involving the uranyl aquo ion and the dianionic form of the ligand, estimated from calculated complexation free energies, are given below each ligand.

Nanosynthesis

The progress toward nanostructured adsorbents capable of extracting uranium from seawater in 2012 saw a dramatic increase in capacity of the sorbents based on high uranyl concentration laboratory screening. Results indicated sonication-based polymerization provides a better sorbent than standard thermal polymerization. This is speculated to be due to the better mobility of monomer and initiator into the pores of the carbon materials under sonication as well as the enhanced thermal effects around the cavitation bubbles formed during sonication (Gorka, et al. *J. Mater. Chem. A*, (2013) DOI: 10.1039/C2TA01008A). However, as seen in Figure 172, challenges in matching high surface area materials with high capacity were encountered. When the largest pore size was 10 nm, the capacity was restricted. Upon increasing the pore size above 10 nm to 35, 50 or 85 nm the capacity increased dramatically. This is speculated to be due, in part, to the density of sites capable at the lower curvature radius present in larger pores, where the pore wall may mimic an external surface. As the radius of curvature increases (i.e., pore diameters decrease), the steric hindrance increases thus limiting the density of chelation sites.

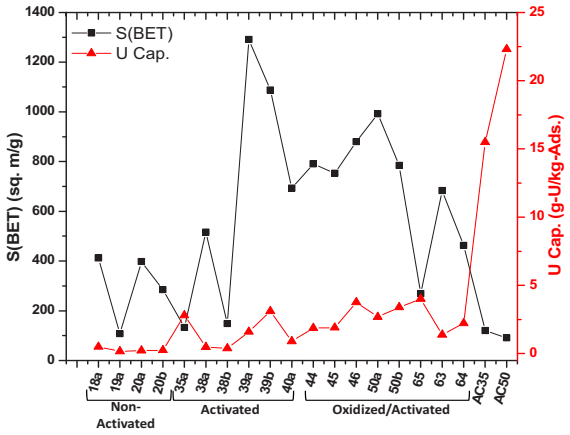

Figure 172. Surface area vs. capacity for different pore motifs

Further complicating the issue is the polymerization process itself. If the polymer grows along the pore wall (see Figure 173), this may block other polymerization sites or provide enough steric effect to slow the polymerization at other sites. Figure 173 also illustrates the effect of polymerization on the surface area and BJH pore size distribution. If non-conformal coatings on the pore walls are generated, the shape of the hysteresis loop changes to that typically observed for constricted pores (red isotherm). However, if the pore is conformally coated, the isotherm indicates no constriction (green isotherm). With conformal coatings, the pore size distribution of the mesopore is expected to shift along with the expected decrease in pore volume. This is observed in the pore width plot where a nearly 1 nm shift is observed after grafting the polymer onto the carbon.

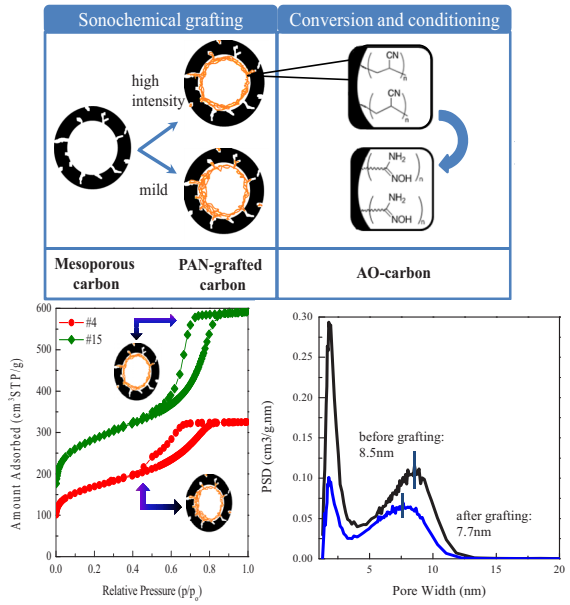

Figure 173. Schematic of the polymerization with effect on pore structure observed with nitrogen sorption

Based on work by the Ligand Design subtask, the effect of conditioning with dimethylsulfoxide (DMSO) was investigated versus the traditional potassium hydroxide (KOH) conditioning (see Table 21) with the 85 nm pore-grafted PAN sorbent. This study consisted of varying the pore motif and the conditioning step. Conditioning is required, however some questions remain about the effects of conditioning that are currently under investigation. Preliminary results indicate microporosity is not required and the effect of mesoporosity is complex, but may be required.

Table 21. Effect of conditioning as a function of pore motif

Sample	Pore regime	S_{BET} (m^2/g)	Grafting (%)	Uranium adsorption cap. (g-U/kg-ads)		
				No treatment	DMSO	KOH
85a-AO	2/10/85	260	19.1	4.8	20.9	20.5
85b-AO	2/85	283	16.2	10.3	13.4	6.5
85c-AO	85	-	10.0	6.4	**33.0**	**37.8**
85d-AO	10/85	103	14.0	7.0	**28.9**	**41.9**

In late 2012, efforts shifted to controlled living polymerization to graft long chains onto the surface. This also allows the possibility of grafting long chains of initiator onto the surface from which polyacrylonitrile will be grown in a subsequent step. Preliminary results under laboratory screening conditions are promising with capacities ranging from 16-30 g-U/kg-ads based on this approach compared to the approx. 20 g-U/kg-ads. capacity of the supplied Japanese sorbent.

Marine Testing

In FY 2012, marine testing of developed adsorbent materials began at two sites, the Marine Sciences Laboratory (MSL) at PNNL in Sequim, Washington and at the Rosenstiel School of Marine and Atmospheric Science (RSMAS) at the University of Miami in Florida. Both sites offered unique seawater testing capabilities and have researchers with extensive experience in marine chemistry, seawater testing, and trace element analysis. After an initial pre-screening with simulated seawater, the most promising adsorbent materials were selected and prepared for the marine testing. A summary of the experiments in FY 2012 at each facility are provided below.

Marine Sciences Laboratory

Several marine tests were conducted in collaboration with the MSL at PNNL (see Figure 174) using a prototype experimental setup. The first experiment was initiated in January of 2012 with seawater at 30°C, and lasted for 6 weeks. The second experiment was conducted at 20°C, and yielded a higher amount of uranium adsorbed per unit mass of the adsorbent than in the first experiment. Replicate experiments were subsequently performed to verify the adsorption results at 20°C. Comparisons of uranium uptake data at various conditions, as well as comparison of data obtained from ORNL and Japanese adsorbents are presented in Figure 175. Good reproducibility was observed, considering the data were obtained from different experimental setups and elution and chemical analysis was performed at different laboratories. Other parameters that have been investigated in the experiments conducted at PNNL include type of adsorption bed (columns vs. cartridges), packing material (beads vs. glass wool), and filtered/unfiltered seawater. The experimental setup has recently been upgraded to allow for testing of additional adsorbent material samples.

Figure 174. PNNL's Marine Sciences Laboratory in Sequim, WA.

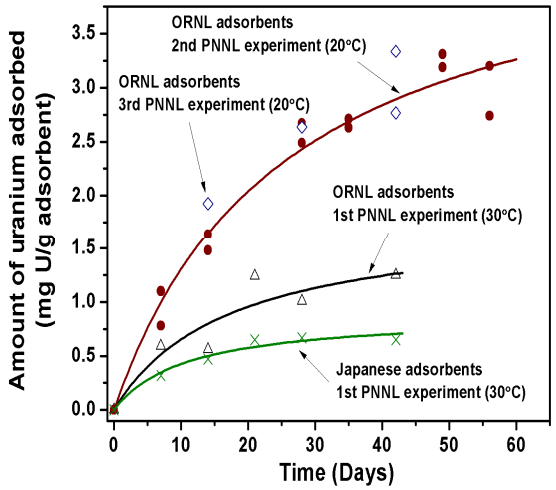

Figure 175. Uranium adsorption capacity from initial testing at MSL.

Rosenstiel School of Marine and Atmospheric Science

Marine testing at RSMAS of the University of Miami has been conducted at two sites: (1) at the RSMAS main campus and (2) on Broad Key Island, off the coast of Miami (see Figure 176). Two experiments were conducted at the RSMAS main campus February 2012 and May 2012. The first experiment was conducted with raw seawater, while the second was conducted with filtered seawater; however, biological fouling in adsorption beds was observed during both experiments. The amount of uranium adsorbed vs. time for the two experiments is shown in Figure 177.

Figure 176. The RSMAS main campus (top) and Broad Key Island (bottom).

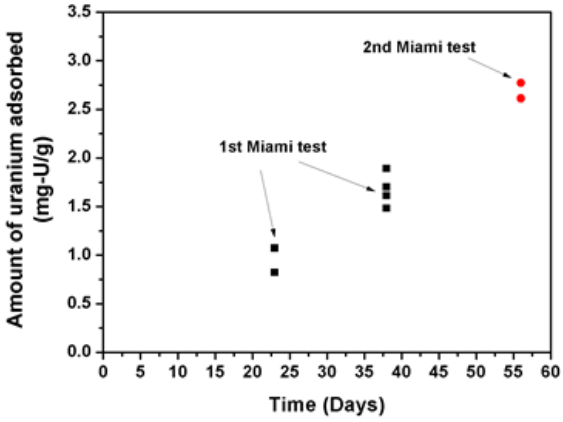

Figure 177. Uranium adsorption capacity measurements from RSMAS tests.

In FY 2012, a test site was established on Broad Key Island, located approximately 25 miles from the main campus of RSMAS. This site, operated by RSMAS, was selected because: (1) it provides access to water with minimal effects

from land discharge, and (2) RSMAS maintains research facilities on the island that could be readily used in marine testing of uranium adsorption. The first field test on Broad Key Island is planned for early FY 2013.

This page intentionally left blank.

APPENDIX
PROJECT PUBLICATIONS
FY 2007–FY 2012

APPENDIX: PROJECT PUBLICATIONS, FY 2007–FY 2012

Aqueous Reprocessing

1. Braley, J. C., J. C. Carter, S. I. Sinkov, K. L. Nash, and G. J. Lumetta. 2012. "The Role of Carboxylic Acids in TALSQUEAK Separations," *Journal of Coordination Chemistry*, Submitted.

2. Braley, J. C., T. S. Grimes, and *K. L. Nash. 2011. "Alternatives t*o HDEHP and DTPA for Simplified TALSPEAK Separations," *Industrial and Engineering Chemistry Research*, 51:628-638. dx. doi. org/10. 1021/ie200285r

3. Brigham, D., C. Badajoz, G. Cote, and K. L. Nash. 2011. "Extraction of Trivalent Lanthanides and Americium by Tri-N-Octylphosphine Oxide from Ammonium Thiocyanate Media," *Solvent Extraction and Ion Exchange*, 29(2):270-291.

4. Brown, M. A., A. Paulenova, and A. V. Gelis. 2012. "Aqueous Complexation of Thorium(IV), Uranium(IV), Neptunium(IV), Plutonium(III/IV), and Cerium(III/IV) with DTPA," *Inorganic Chemistry*, Submitted.

5. Bryan, S. A. and T. G. Levitskaia. 2007. "Monitoring and Control of UREX Radiochemical Processes," *GLOBAL*.

6. Bryan, S. A. and T. G. Levitskaia. 2011. *Solvent Degradation Mechanisms, Products, and Signatures: PNNL FY 2011 Status Report,* PNNL-20688, Pacific Northwest National Laboratory, Richland, WA.

7. Bryan, S. A., T. G. Levitskaia, A. J. Casella, J. M. Peterson, A. M. Johnsen, A. M. Lines, and E. M. Thomas. 2011. *Spectroscopic On-Line Monitoring for Process Control and Safeguarding of Radiochemical Streams.* Publisher: Woodhead Publishing Ltd; CRC Press LLC. ISBN 978-1-84569-501-9.

8. Bryan, S. A., T. G. Levitskaia, A. J. Casella, J. M. Peterson, A. M. Johnsen, A. M. Lines, E. M. Thomas, and C. Orton. 2011. "Spectroscopic On-Line Monitoring for Process Control and Safeguarding of Radiochemical Streams. " In *Advanced Separation Techniques for Nuclear Fuel Reprocessing and Radioactive Waste Treatment,* eds. K. L. Nash and G. J. Lumetta. Woodhead Publishing Ltd, Cambridge, U. K.

9. Bryan, S. A., T. G. Levitskaia, A. J. Casella, J. M. Peterson, A. M. Lines, D. E. Verdugo, and E. A. Jordan. 2011. "Spectroscopic on-Line Monitoring for Process Control and Safeguarding of Radiochemical Streams," *19th International Solvent Extraction Conference*

10. Bryan, S. A., T. G. Levitskaia, A. M. Johnsen, C. R. Orton, and J. M. Peterson. 2011. "Spectroscopic Monitoring of Nuclear Spent Fuel Reprocessing Streams: An Evaluation of Spent Fuel Solutions Via Raman, Visible, and near-Infrared Spectroscopy," *Radiochim. Acta*, 99:563-571. DOI 10. 1524/ract. 2011. 1865.

11. Bryan, S. A., T. G. Levitskaia, J. M. Schwantes, C. R. Orton, J. M. Peterson, and A. J. Casella. 2012. "Monitoring, Controlling and Safeguarding Radiochemical Streams at Spent Fuel Reprocessing Facilities, Part 1: Optical Spectroscopic Methods," *International Journal on Nuclear Energy Management and Safety*, 2012.

12. Burns, J., A. Clearfield, M. Borkowski, and D. Reed. 2012. "Pillared Metal(IV) Phosphate-Phosphonate Extraction of Actinides," *Radiochim. Acta*, 100:381-387.

13. Burns, J. D., M. Borkowski, A. Clearfield, and D. T. Reed. 2012. "Separation of Oxidized Americium from Lanthanides by Use of Pillared Metal(IV) Phosphate-Phosphonate Hybrid Materials " *Radiochim.*

Acta, Submitted. DOI: 10. 1524/ract. 2012. 1929 (in press).

14. Burns, J. D., A. Clearfied, T. C. Shehee, and D. T. Hobbs. 2012. "Separation of Americium from Curium by Oxidation and Ion Exchange," *J. Am. Chem. Soc.,* Submitted.

15. Casella, A. J., T. G. Levitskaia, J. M. Peterson, O. S. Muzaffery, M. Nilsson, and S. A. Bryan. 2011. "Raman Spectroscopy for On-Line Acid Concentration/pH Monitoring in Spent Nuclear Fuel Reprocessing," *19th International Solvent Extraction Conference*.

16. Casely, I. J., J. W. Ziller, B. J. Mincher, and W. J. Evans. 2011. "Bismuth Coordination Chemistry with Allyl, Alkoxide, Aryloxide, and Tetraphenylborate Ligands Attached to the {[2,6-(Me2nch2)2c6h3]2bi}1+ Cation," *Inorganic Chemistry*, 50:1513-1520.

17. Cipiti, B. B., V. F. D. Almeida, I. C. Gauld, J. F. Birdwell, and D. W. Depaoli. 2009. *Coupling a Transient Solvent Extraction Module with the Separations and Safeguards Performance Model,* SAND2009-6307, Sandia National Laboratories, Albuquerque, NM.

18. Cipiti, B. B. and O. Zinaman. 2010. *Separations and Safeguards Model Integration,* SAND2010-5962, Sandia National Laboratories, Albuquerque, NM.

19. Collins, E. D., D. Benker, R. J. Vedder, G. D. Delcul, and R. J. Ellis. 2012. "Macro TALSPEAK Separations of Am-Cm from Fission Products — Implications for a Single Step Separation and Advanced Fuel Cycle Irradiation of Am-Cm," *Ninth International Conference on Methods and Application of Radioanalytical Chemistry*, Kailua-Kona, Hawaii, March 25-30, 2012.

20. Collins, E. D. 2008. "Closed Nuclear Fuel Cycle Technologies to Meet near-Term and Transition Period Requirements " *Atalante*.

21. Collins, E. D. 2008. "Minor Actinide Recovery Finishing " *ISEC 2008*

22. Collins, E. D. 2007. *Preliminary Multicycle Transuranic Actinide Partitioning-Transmutation Studies* ORNL/TM-2007/24, Oak Ridge National Laboratory, Oak Ridge, TN.

23. Collins, E. D., G. D. Del Cul, and B. A. Moyer. 2010. "Advanced Reprocessing for Fission Product Separation and Extraction. " In *Advanced Separation Techniques for Nuclear Fuel Reprocessing and Radioactive Waste Treatment",* eds. K. L. Nash and G. J. Lummetta. Woodhead Publishing Limited, Cambridge, UK.

24. A Comparison of the Alpha and Gamma Radiolysis of CMPO. FCRD-SWF-2011-000148.

25. Cullen, T. D., S. P. Mezyk, L. R. Martin, and B. J. Mincher. 2012. "Elucidating the Radical Kinetics Involved in the Radiolytic Destruction of Lanthanide-Complexed Dtpa," *J. Radioanal. Nucl. Chem.* DOI 10. 1007/s10967-012-2054-x.

26. Daly, S. R., J. M. Keith, E. R. Batista, K. S. Boland, D. L. Clark, S. A. Kozimor, and R. L. Martin. 2012. "Sulfur K-Edge X-Ray Absorption Spectroscopy and Time-Dependent Density Functional Theory of Dithiophosphinate Extractants: Minor Actinide Selectivity and Electronic Structure Correlations," *Journal of the American Chemical Society*, 134(35):14408-14422.

27. Daly, S. R., J. M. Keith, E. R. Batista, K. S. Boland, S. A. Kozimor, R. L. Martin, and B. L. Scott. 2012. "Probing Ni[S2pr2]2 Electronic Structure to Generate Insight Relevant to Minor Actinide Extraction Chemistry," *Inorganic Chemistry*, 51(14):7551-7560.

28. Daly, S. R., J. R. Klaehn, K. S. Boland, S. A. Kozimor, M. M. Macinnes, D. R. Peterman, and B. L. Scott. 2012. "NMR Spectroscopy and Structural Characterization of Dithiophosphinate Ligands Relevant to Minor Actinide Extraction Processes.," *Dalton Trans.,* 41(7):2163-2175.

29. Delmau, L. H. 2011. *Modeling of Distribution Ratios and Osmotic Coefficients Using Sxfit,* FCRD-SWF-2011-000320, Oak Ridge National Laboratory, Oak Ridge, TN.

30. Delmau, L. H., B. P. Hay, F. V. Sloop, and A. E. V. Gorden. 2009. *Trivalent Actinide-Lanthanide Separation Using Bis-Di-Thiophosphinic Acids,* AFCI-SEPA-PMO-MI-DV-2009-00214, Oak Ridge National Laboratory, Oak Ridge, TN.

31. Delmau, L. H. and P. Marc. 2011. *Trivalent Actinide-Lanthanide Separation Using Bis-Dithiophosphinic Acids,* FCRD-SWF-2011-000274, Oak Ridge National Laboratory, Oak Ridge, TN.

32. Devore, M. A. and A. E. V. Gorden. 2012. "Copper and Uranyl Extraction from Aqueous Solutions Using Bis-Dithiophosphinate Ligands Have Been Characterized," *Polyhedron*, 42(1):271-275.

33. Elias G., G. S. Groenewold, B. J. Mincher, S. P. Mezyk, 2012. Determination of CMPO using HPLC-UV. *J. Chromatography A* 1243:47-52.

34. Elvington, M. C., T. C. Shehee, T. S. Rudisill, and D. T. Hobbs. 2012. "Separation of Americium and Lanthanides Using Titanium-Based Materials," *Solvent Extraction and Ion Exchange*, Submitted.

35. Fondeur, F. F. and T. S. Rudisill. 2012. "Thermal Stability of Formohydroxamic Acid," *Sep. Sci. Tech.,* Accepted.

36. Francois, M. M. and N. N. Carlson. 2010. "The Balanced-Force Volume Tracking Algorithm and Global Embedded Interface Formulation for Droplet Dynamics with Mass Transfer," *FEDSM 10,* ASME Fluids Engineering Division.

37. Francois, M. M., N. N. Carlson, and N. N. Carlson. 2012. "The Global Embedded Interface Formulation for Interfacial Mass Transfer within a Volume Tracking Framework," *Computers and Fluids*, Submitted. LA-UR 12-01273.

38. Gandhir, A. and K. E. Wardle. 2012. "CFD Analysis of Fluid Flow above the Upper Weir of an Annular Centrifugal Contactor 4," *Sep. Sci. Technol.,* 47:1-10. doi:10.1080/01496395. 2011. 617026.

39. Gelis, A. V. 2011. *Combining Truex and Talspeak in One Process.,* FCRD-SWF-2011-000282, Argonne National Laboratory, Argonne, IL.

40. Gelis, A. V. and G. F. Vandegrift. 2009. *Combining TRUEX and TALSPEAK in One Process,* AFCI-SEPA-AQUE-MI-DV-2009-00, Argonne National Laboratory, Argonne, IL.

41. Gelis, A. V., G. F. Vandegrift, A. Bakel, D. L. Bowers, A. S. Hebden, C. Pereira, and M. Regalbuto. 2009. "Extraction Behaviour of Actinides and Lanthanides in TALSPEAK, TRUEX and NPEX Processes of UREX+," *Radiochim. Acta*, 97:231-232.

42. Goff, G. S., G. D. Jarvinen, and W. Runde. *Sigma Team for Minor Actinide Separations: LANL FY2012 Annual Report*; FCRD-SWF-2012-000353, Los Alamos National Laboratory: Los Alamos, NM, September 14, 2012.

43. Goff, G. S., M. R. Cisneros, C. Kluk, K. Williamson, B. Scott, S. Reilly, and W. Runde. 2010. "Synthesis and Structural Characterization of Molecular Dy(III) and Er(III) Tetra-Carbonates," *Inorg. Chem.,* 49:6558-6564.

44. Goff, G. S., G. Jarvinen, and W. Runde. 2010. *Am/Cm Separations in Alkaline Solutions,* FCRD-SEPA-2010-000119, Los Alamos National Laboratory, Los Alamos, NM.

45. Gray, M. F., P. R. Zalupski, and M. Nilsson. 2012. "Determination of Activity Coefficients of Di-(2-Ethylhexyl)Phosphoric Acid Dimer in Select Organic Solvents Using Vapor Phase Osmometry," *Solvent Extr. Ion Exch.,* Submitted.

46. Grimes, T., M. Nilsson, and K. L. Nash. 2008. "The Behavior and Importance of Lactic Acid Complexation in TALSPEAK

Extraction Systems, in Solvent Extraction: Fundamentals to Industrial Applications," *International Solvent Extraction Conference ISEC*.

47. Grimes, T. S. 2011. "Coordination Chemistry of F Elements in the TALSPEAK Process," Ph. D., Washington State University, Pullman, WA, 2011., Pullman, WA.

48. Grimes, T. S., M. P. Jensen, L. Debeer-Schmidt, K. Littrell, and K. L. Nash. 2012. "Small Angle Neutron Scattering (SANS) Study of Organic Phase Aggregation in the TALSPEAK Process," *J. Phys. Chem. B.,* Submitted.

49. Grimes, T. S., M. A. Nilsson, and K. L. Nash. 2010. "Lactic Acid Partitioning in TALSPEAK Extraction Systems," *Separation Science and Technology*, 45(12-13):1725-1732.

50. Grimes, T. S., G. Tian, L. Rao, and K. L. Nash. 2012. "Optical Spectroscopy Study of Lanthanide Organic Phase Complexes in the TALSPEAK Separations Process.," *Inorganic Chemistry* 51(11):6299–6307. dx. doi. org/10. 1021/ic300503p.

51. Groenewold, G. S., D. R Peterman, J. R. . Klaehn, L. H. Delmau, P. Marc, and R. Custelcean. Oxidative Degradation of Bis(2,4,4-trimethylpentyl)dithiophosphinic Acid in Nitric Acid Studied by Electrospray Ionization Mass Spectrometry. *Rapid Commun. Mass Spectrom.* 2012, *26*, 2195–2203.

52. Groenewold, G. S., G. Elias, B. J. Mincher, S. P. Mezyk, and J. A. Laverene. 2012. "Characterization of CMPO and Its Radiolysis Products by Direct Infusion Esi-MS," *Talanta* 99:909-917.

53. Groenewold, G. S., D. R. Peterman, and J. R. Klaehn. 2012. "Electrospray Ionization Analysis of Bis(2,4,4-Trimethylpentyl)Dithiophosphinic Acid: Oxidative Coupling Augmented by HNO3.," *Rapid Comm. Mass Spect.,* Submitted.

54. Guelis, A. V. and G. F. Vandegrift. 2010. *Combining TRUEX and TALSPEAK in One Process,* FCRD-SEPA-2010-000124, Argonne National Laboratory, Argonne, IL.

55. Hay, B. P. 2012. *Sigma Team for Minor Actinide Separations: Design of New Dithiophophinic Acids Status Report,* ORNL/LTR-2012/173, Oak Ridge National Laboratory, Oak Ridge, TN.

56. Hay, B. P. *Sigma Team for Minor Actinide Separations: Molecular Modeling of Americium Extractants,* FCRD-SWF-2012-000300, Oak Ridge National Laboratory: Oak Ridge, TN, September 18, 2012.

57. Hay, B. P., and B. A. Moyer. *Sigma Team for Minor Actinide Separations: Mixed-Donor Extractant Synthesis,* FCRD-SWF-2012-000299, Oak Ridge National Laboratory: Oak Ridge, TN, September 18, 2012.

58. Hay, B. P. 2011. *Sigma Team for Minor Actinide Separations: Reagent Modeling and Design FY11 Status Report,* FCRD-SWF-2011-000275, Oak Ridge National Laboratory, Oak Ridge, TN.

59. Heathman, C. R. and K. L. Nash. 2012. "Characterization of Europium and Americium Dipicolinate Complexes," *Separation Science and Technology*, in press.

60. Herbst, R. S., P. Baron, and M. Nilsson. 2011. " Standard and Advanced Separation: Purex Processes for Nuclear Fuel Reprocessing. " In *Advanced Separation Techniques for Nuclear Fuel Reprocessing and Radioactive Waste Treatment,* eds. K. L. Nash and G. J. Lumetta, pp. 141-175. Woodhead Publishing, Oxford.

61. Herbst, R. S., D. R. Peterman, P. R. Zalupski, K. L. Nash, R. D. Tillotson, and L. H. Delmau. 2010. "Thermodynamics of Cesium Extraction from Acidic Media by HCCD and PEG," *Solvent Extraction and Ion Exchange* 28(5):563-578.

62. Hill, C. 2011. "Development of Highly Selective Compounds for Solvent Extraction

Processes: Partitioning and Transmutations of Long-Lived Radionuclides from Spent Nuclear Fuels. " In *Advanced Separation Techniques for Nuclear Fuel Reprocessing and Radioactive Waste Treatment,* eds. K. L. Nash and G. J. Lumetta, pp. 311-362. Woodhead Publishing, Oxford.

63. Hill, C. 2010. "Overview of Recent Advances in an(III)/Ln(III) Separation by Solvent Extraction. " In *Ion Exchange and Solvent Extraction,* ed. B. A. Moyer, Vol 19. Taylor and Francis, Philadelphia, PA.

64. Hobbs, D. T., T. C. Shehee, and A. Clearfield. *Minor Actinide Separations Using Ion Exchange*, FCRD-SWF-2012-000242, Savannah River National Laboratory: Aiken, SC, September 13, 2012.

65. Hobbs, D. T., A. Clearfield, A. E. Visser, and N. J. Bridges. 2010. *Minor Actinide Separations Using Ion Exchangers or Ionic Liquids,* FCRD-SEPA-2010-000118, Savannah River National Laboratory, Aiken, SC.

66. Hobbs, D. T., A. Clearfield, A. E. Visser, and N. J. Bridges. 2011. *Minor Actinide Separations Using Ion Exchangers or Ionic Liquids,* FCRD-SWF-2011-000276, Savannah River National Laboratory, Aiken, SC.

67. Hobbs, D. T., A. E. Visser, and N. J. Bridges. 2009. *Minor Actinide Separations Using Ion Exchangers or Ionic Liquids,* AFCI-SEPA-PMO-MI-DV-2009-00202, Savannah River National Laboratory, Aiken, SC.

68. J., L. G., D. Neiner, S. I. Sinkov, J. C. Carter, J. C. Braley, S. L. Latesky, A. V. Gelis, P. Tkac, and G. F. Vandegrift. 2011. "Combining Neutral and Acidic Extractants for Recovering Transuranic Elements from Nuclear Fuel," *19th International Solvent Extraction Conference*, Vol.

69. Jensen, M. P., and R. Chiarizia. *Aqueous Complexes for Americium-Curium Separation*, FCRD-SWF-2012-000277, Argonne National Laboratory: Argonne, IL, September 14, 2012.

70. Jensen, M. P. and R. Chiarizia. 2009. *Initial Studies of Ternary Complexes for Am/Cm Separation,* AFCI-SEPA-PMO-MI-DV-2009-000182, Argonne National Laboratory, Argonne, IL.

71. Jensen, M. P. and R. Chiarizia. 2011. *Sterically Constrained Complexes for Americium-Curium Separation,* FCRD-SWF-2011-000277, Argonne National Laboratory, Argonne, IL.

72. Jensen, M. P. and R. Chiarizia. 2010. *Ternary Complexes for Americium-Curium Separation,* FCRD-SEPA-2010-000120, Argonne National Laboratory, Argonne, IL.

73. Johnson, A. K., J. Kaczor, H. Han, M. Kaur, G. Tian, L. Rao, Y. Qiang, and A. J. Paszczynski. 2011. "Highly Hydrated Poly(Allylamine)/Silica Magnetic Resin " *J. Nanopart. Res.,* 13:4881-4895.

74. Jubin, R. T. 2009. "AFCI Fuel Reprocessing R&D: Performance of Coupled End-to-End Integrated Voloxidation and Dissolver Off-Gas Treatment," *Global*.

75. Jubin, R. T., G. D. Delcul, B. D. Patton, R. S. Owens, D. W. Ramey, and B. B. Spencer. 2009. "Advanced Fuel Cycle Initiative Coupled End-to-End Research, Development, and Demonstration Project: Integrated Off-Gas Treatment System Design and Initial Performance," *Waste Management*.

76. Kang, S. O., S. Vukovic, R. Custelcean, and B. P. Hay. 2012. "Cyclic Imide Dixoimes: Formation and Hydrolytic Stability," *Industrial and Engineering Chemistry Research*, 51(19):6619-6624. 10. 1021/ie300492z.

77. Kang, S. O., S. Vukovic, R. Custelcean, and B. P. Hay, "Cyclic Imide Dioximes: Formation and Hydrolytic Stability," *243rd National Meeting of the American Chemical Society*, San Diego, CA, March 25-29, 2012.

78. Kaur, M., A. Johnson, G. Tian, L. Rao, A. Paszczynski, and Y. Qiang. 2012. "Diethylenetriaminepentaacetic Acid Impregnated Magnetic Nanoparticles for

Separation of Spent Nuclear Fuel," *ACS Nano*, Submitted.

79. Keith, J. M. and E. R. Batista. 2012. "Theoretical Examination of the Thermodynamic Factors in the Selective Extraction of Am3+ from Eu3+ by Dithiophosphinic Acids " *Inorganic Chemistry*, 51(1):13-15.

80. Klaehn, J. R., D. R. Peterman, M. K. Harrup, T. A. Luther, and L. M. Daniels. 2011. "Bis(O-Trifluoromethylphenyl) Dithiophosphinic Methyl Ester.," *Inorg. Chim. Acta*, 370:519-522.

81. Leggett, C. J., Ph. D., 2012. "Thermodynamic Investigations of Aqueous Ternary Complexes for Am/Cm Separation," University of California, Berkeley, CA.

82. Leggett, C. J., G. K. Liu, and M. P. Jensen. 2010. "Do Aqueous Ternary Complexes Influence the TALSPEAK Process? ," *Solvent Extr. Ion Exch.,* 28(3):313-333.

83. Levitskaia, T. G., D. Neiner, and T. A. Robinson. 2011. *Non-Ideality in Solvent Extraction Systems* PNNL-20662, Pacific Northwest National Laboratory, Richland, WA.

84. Levitskaia, T. G., T. A. Robinson, S. A. Bryan, and A. J. Casella. 2011. "TALSPEAK Extraction System under Variable Loading Conditions - Part 1: Distribution Studies," *19th International Solvent Extraction Conference,* Society of Chemical Industry.

85. Long, K. L., G. S. Goff, S. D. Ware, G. D. Jarvinen, and W. R. Runde. 2012. "Anion Exchange Resins for the Selective Separation of Technetium from Uranium in Carbonate Solutions " *Ind. Eng. Chem. Res.,* Submitted.

86. Lumetta, G. J., J. C. Braley, S. I. Sinkov, and J. C. Carter. *Separating the Minor Actinides Through Advances in Selective Coordination Chemistry*, FCRD-SWF-2012-000174 (PNNL-21642), Pacific Northwest National Laboratory: Richland, WA, August 2012.

87. Lumetta, G. J., J. C. Braley, S. I. Sinkov, T. G. Levitskaia, J. C. Carter, M. G. Warner, and J. W. Pittman. 2011. *Sigma Team for Minor Actinide Separation: PNNL FY 2011 Status Report,* FCRD-SWF-2011-000261, Pacific Northwest National Laboratory, Richland, WA.

88. Lumetta, G. J., J. C. Carter, A. V. Gelis, and G. F. Vandegrift. 2010. "Combining Octyl(Phenyl)-N,N-Diisobutyl-Carbamoylmethylphosphine Oxide and Bis-(2-Ethylhexyl)Phosphoric Acid Extractants for Recovering Transuranic Elements from Irradiated Nuclear Fuel," *Nuclear Energy and the Environment*, Vol. 1046*,* 107-118 pp. American Chemical Society.

89. Lumetta, G. J., A. V. Gelis, J. C. Braley, J. C. Carter, J. W. Pittman, M. G. Warner, and G. F. Vandegrift. 2012. "The TRUSPEAK Concept: Combining Cmpo and HDEHP for Separating Trivalent Lanthanides from the Transuranic Elements," *Solvent Extraction and Ion Exchange*, in press.

90. Lumetta, G. J., A. V. Gelis, and G. F. Vandegrift. 2010. "Review: Solvent Systems Combining Neutral and Acidic Extractants for Separating Trivalent Lanthanides from the Transuranic Elements," *Solvent Extraction and Ion Exchange*, 28:287-312.

91. Lumetta, G. J., A. V. Gelis, and G. F. Vandegrift. 2010. "Solvent Systems Combining Neutral and Acidic Extractants for Separating Trivalent Lanthanides from the Transuranic Elements," *Solvent Extraction and Ion Exchange*, 28:287-312.

92. Lumetta, G. J., T. G. Levitskaia, S. L. Latesky, R. V. Henderson, E. A. Edwards, J. C. Braley, and S. I. Sinkov. 2012. "Lipophilic Ternary Complexes in Liquid-Liquid Extraction of Trivalent Lanthanides," *Journal of Coordination Chemistry*, 65(5):741-753.

93. Lumetta, G. J., L. I. Sinkov, J. C. Carter, M. G. Warner, and J. W. Pittman. 2009. *Sigma*

Team for Minor Actinide Separation: PNNL FY 2009 Status Report, FCI-SEPA-AQUE-MI-DV-2009-00136, PNNL-18674, Pacific Northwest National Laboratory, Richland, WA.

94. Lumetta, G. J., L. I. Sinkov, D. Neiner, T. G. Levitskaia, J. C. Braley, J. C. Carter, M. G. Warner, J. W. Pittman, and B. M. Rapko. 2010. *Sigma Team for Minor Actinide Separation: PNNL FY 2010 Status Report,* FCRD-SEPA-2010-000121, PNNL-19655, Pacific Northwest National Laboratory, Richland, WA.

95. Marc, P., R. Custelcean, G. S. Groenewold, J. R. Klaehn, D. R. Peterman, and L. H. Delmau. 2012. "Degradation of CYANEX® 301 in Contact with Nitric Acid Media, . " *Ind. Eng. Chem. Res*, in press.

96. Marie, C., B. Hiscox, and K. L. Nash. 2012. "Characterization of HDEHP-Lanthanide Complexes Formed in a Non-Polar Organic Phase Using 31p NMR and ESI-MS.," *Dalton Transactions*, 41 (3):1054.

97. Martin, L. R., B. J. Mincher, and N. C. Schmitt. 2009. "Extraction of Am(VI) with a Neutral Organophosphorous Ligand," *Radioanalytical Nuclear Chemistry*, 282:523-526.

98. Mezyk, S. P., B. J. Mincher, W. J. Cooper, S. K. Cole, R. V. Fox, and P. R. Gardinali. 2012. "Kinetic Model for the Radical Degradation of Trihalonitromethane Disinfection Byproducts in Water," *Radiat. Phys. Chem.,* 81:1646-1652.

99. Mezyk, S. P., B. J. Mincher, C. Ekberg, and G. Skarnemark. 2012. "Alpha and Gamma Radiolysis of Nuclear Solvent Extraction Ligands Used for an(III) and Ln(III) Separations," *J. Radioanal. Nucl. Chem.* :1-5. DOI 10. 1007/s10967-012-2036-z.

100. Minasian, S. G., K. S. Boland, R. K. Feller, A. J. Gaunt, S. A. Kozimor, I. May, S. D. Reilly, B. L. Scott, and D. K. Shuh. 2012. "Synthesis and Structure of (Pph4)2mcl6 (M = Ti, Zr, Hf, Th, U, Np, Pu) " *Inorganic Chemistry*, Submitted. DOI: 10. 1021/ic300179d.

101. Mincher, B. J., *Degradation issues in aqueous reprocessing systems*, Ch. 104 in: Comprehensive Nuclear Materials, Allen, T., ed. Elsevier, ISBN: 978-0-08-056027-4, July 13, 2012.

102. Mincher, B. J., N. UOhnak, and L. Wurth. *Electrochemical preparation of high valent americium*. FCRD-SWF-2012-000126, Idaho National Laboratory: Idaho Falls, ID, 2012.

103. Mincher, B. J., and N. C. Schmitt. *Fission Product Behavior in DAAP AmVI Extraction*, FCRD-SWF-2012-000171, Idaho National Laboratory: Idaho Falls, ID, June 27, 2012.

104. Mincher, B. J. *Americium Separations Based on Higher Oxidation States*: *FY12 Year End Report*, FCRD-SWF-2012-000285, Idaho National Laboratory: Idaho Falls, ID, September 1, 2012.

105. Mincher, B. J. 2010. *Americium Separation from Nuclear Fuel Dissolution Using Higher Oxidation States,* FCRD-SEPA-2010-000122, Idaho National Laboratory, Idaho Falls, ID.

106. Mincher, B. J. 2011. *Americium Separations Based on Higher Oxidation States,* FCRD-SWF-2011-000278, Idaho National Laboratory, Idaho Falls, ID.

107. Mincher, B. J., L. R. Martin, and N. C. Schmitt. 2009. *Americium Separation from Nuclear Fuel Dissolution Using Higher Oxidation States,* AFCI-SEPA-PMO-MI-DV-2009-00197, Idaho National Laboratory, Idaho Falls, ID.

108. Mincher, B. J., L. R. Martin, and N. C. Schmitt. 2012. "Diamylamylphosphonate Solvent Extraction of Am(VI) from Nuclear Fuel Raffinate Simulant Solution," *Solvent Extr. Ion Exch.,* in press.

109. Mincher, B. J., L. R. Martin, and N. C. Schmitt. 2008. "Tributylphosphate Extraction Behavior of Bismuthate-Oxidized Americium," *Inorganic Chemistry*, 47:6984-6989.

110. Mincher, B. J., N. C. Schmitt, and M. E. Case. 2011. "A Truex-Based Americium/Lanthanide Separation," *Solvent Extraction and Ion Exchange*, 29:247-259.

111. Mincher, M. E., D. L. Quach, Y. J. Liao, B. J. Mincher, and C. M. Wai. 2012. "The Partitioning of Americium and the Lanthanides Using Tetrabutyldiglycolamide (TBDGA) in Octanol and in Ionic Liquid Solution," *Solvent Extr. Ion Exch.,* in press.

112. Moyer, B. A. 2009. *Sigma Team for Minor Actinide Separation Annual Report,* AFCI-SEPA-PMO-MI-DV-2009-000180, Oak Ridge National Laboratory, Oak Ridge, TN.

113. Moyer, B. A. 2010. *Sigma Team for Minor Actinide Separation FY2010 Annual Report,* FCRD-SEPA-2010-000125, Oak Ridge National Laboratory, Oak Ridge, TN.

114. Moyer, B. A. 2011. *Sigma Team for Minor Actinide Separation FY 2011 Annual Report,* FCRD-SWF-2011-000273, Oak Ridge National Laboratory, Oak Ridge, TN.

115. Moyer, B. A. 2011. *Sigma Team for Minor Actinide Separation Peer Review,* FCRD-SWF-2011-000107, Oak Ridge National Laboratory, Oak Ridge, TN.

116. Moyer, B. A. *Sigma Team for Minor Actinide Separations FY2012 Accomplishments and Directions*, FCRD-SWF-2012-000302, Oak Ridge National Laboratory: Oak Ridge, TN, September 28, 2012.

117. Nash, K. L. 2010. *Basic Investigations of Current and Future Options for TALSPEAK,* FCRD-SEPA-2010-000123, Washington State University, Pullman, WA.

118. Nash, K. L. 2011. *Fundamental Studies for Improving TALSPEAK-Type Separations,* FCRD-SWF-2011-000279, Washington State University, Pullman, WA.

119. Nash, K. L. 2008. "Key Features of the TALSPEAK and Similar Trivalent Actinide-Lanthanide Partitioning Processes. In Solvent Extraction: Fundamentals to Industrial Applications," *International Solvent Extraction Conference (ISEC 2008)*.

120. Nash, K. L. 2009. *Thermodynamics and Kinetics of the TALSPEAK Process,* AFCI-SEPA-PMO-MI-DV-2009-000218, Washington State University, Pullman, WA.

121. Nash, K. L. and J. C. Braley. 2011. "Advanced Separation Techniques for Nuclear Fuel Reprocessing and Radioactive Waste Treatment. " In *Chemistry of Radioactive Materials in the Nuclear Fuel Cycle*. Woodhead Publishing, Cambridge, U. K.

122. Nash, K. L. and J. C. Braley. 2010. "Challenges for Actinide Separations in Advanced Nuclear Fuel Cycles," *ACS Symposium Series* Vol. 1046*,* 19-38 pp.

123. Nash, K. L., T. S. Grimes, and M. Nilsson. 2009. "Fundamental Studies of Talspeak Chemistry for Trivalent Actinide – Lanthanide Separations in Advanced Nuclear Fuel Cycles. In Nuclear Fuel Cycle: Sustainable Options & Industrial Perspectives," *Global*.

124. Nash, K. L. and G. J. Lumetta, eds. 2011. *Advanced Separation Techniques for Nuclear Fuel Reprocessing and Radioactive Waste Treatment* Woodhead Publishing Company, Cambridge, U. K.

125. Nash, K. L., C. Marie, M. D. Ogden, and D. Brigham. 2011. "Soft-Donor Extractants vs. Aqueous Complexants in Trivalent Lanthanide/Actinide Separations," *19th International Solvent Extraction Conference*.

126. Nash, K. L., M. Nilsson, T. Grimes, J. Braley, K. Uruga, and C. Marie. 2011. "Complex Interactions in Solvent Extraction—Biphasic Speciation in the TALSPEAK Process " *9th International Solvent Extraction Conference*.

127. Nash, K. L., P. R. Zalupski, L. R. Martin, D. R. Peterman, and R. S. Herbst. 2009. "Thermodynamic Features of Cesiumand Strontium Extraction by Mixtures of H+CCD- and PEG-400 in FS-13," *Global*.

128. Nichols, K. P., R. R. Pompano, L. Li, A. V. Gelis, and R. F. Ismagilov. 2012. "Toward

Mechanistic Understanding of Nuclear Reprocessing Chemistries by Quantifying Lanthanide Solvent Extraction Kinetics via Microfluidics with Constant Interfacial Area and Rapid Mixing," *J. Am. Chem. Soc.,* 133(39):15721-15729.

129. Nilsson, M., C. Hoch, G. P. Meier, and K. L. Nash. 2008. "Separation of Lanthanides from Trivalent Actinides, the Role of Aqueous-Phase Soft-Donor Complexing Agents," *International Solvent Extraction Conference (ISEC 2008)*.

130. Nilsson, M. and K. L. Nash. 2007. "A Review of the Development and Operational Characteristics of the TALSPEAK Process," *Solvent Extraction and Ion Exchange*, 25(6):665-701.

131. Nilsson, M. and K. L. Nash. 2009. "Trans-Lanthanide Extraction Studies in the TALSPEAK System: Investigating the Effect of Acidity and Temperature," *Solvent Extraction & Ion Exchange* 27 (3):354-377.

132. Ogden, M. D., C. L. Hoch, S. I. Sinkov, G. P. Meier, G. J. Lumetta, and K. L. Nash. 2011. "Complexation Studies of Bidentate Heterocyclic N-Donor Ligands with Nd(III) and Am(III) " *Journal of Solution Chemistry*, 40(11):1874-1888.

133. Ogden, M. D., G. P. Meier, and K. L. Nash. 2008. "Synthesis and Evaluation of Sterically-Focused Tetradentate Nitrogen Ligands Containing the 2-Methylpyridyl Moiety for the Separation of an(III) from Ln(III)," *ISEC 2008 International Solvent Extraction Conference*.

134. Ogden, M. D., S. I. Sinkov, G. J. Lumetta, and K. L. Nash. 2012. "Affinity of an(VI) for N4-Tetradentate Donor Ligands: Complexation of the Actinyl(VI) Ions with N4-Tetradentate Ligands," *Journal of Solution Chemistry*, Submitted.

135. Peterman, D., J. Law, C. Riddle, and D. Meikrantz. 2008. *Preliminary Testing of Alternative Calixarenes for the Fission Product Extraction Process,* INL/EXT-06-11542, Idaho National Laboratory, Idaho Falls, ID.

136. Peterman, D. and J. Law. 2008. *Evaluation of Alternative Calixarenes for the Fission Product Extraction Process* INL/EXT-08-13981, Idaho National Laboratory, Idaho Falls, ID.

137. Peterman, D. R., G. S. Groenewold, J. R. Klaehn, and R. G. McDowell. *Evaluation of the Hydrolytic Stability of Dithiophosphinic Acid*. FCRD-SWF-2012-000076, Idaho National Laboratory: Idaho Falls, ID, March 30, 2012.

138. Peterman, D. R., G. S. Groenewold, J. R. Klaehn, and R. G. McDowell. *Stability of Dithiophosphinic Acid Extractants: INL 2012 Status Report*. FCRD-SWF-2012-000267, Idaho National Laboratory: Idaho Falls, ID, September 1, 2012.

139. Peterman, D. R., J. R. Klaehn, R. G. Mcdowell, and M. S. Snow. 2011. *Stability of Dithipphosphinic Acid Extractants: INL 2011 Status Report,* FCRD-SWF-2011-000280, Idaho National Laboratory, Idaho Falls, ID.

140. Peterson, J. M., S. A. Bryan, and T. G. Levitskaia. 2011. "Monitoring and Modeling of Radiolytic Degradation Products of Tbp/N-Dodecane," *19th International Solvent Extraction Conference*, Vol. 98*,* Society of Chemical Industry, London, U. K.

141. Radiation Chemistry in Solvent Extraction, FY 2012 Research. FCRD-SWF-2012-000375.

142. Rao, L. and G. Tian. 2012. "Effect of Temperature on the Complexation of Cm(III) with Nitrate in Aqueous Solutions," *Dalton Trans.,* Submitted.

143. Reed, W. A., A. Oliver, and L. Rao. 2011. "Tetrakis(Tetramethylammonium) Tris(Carbonato-O,O'-)-Dioxauranium(VI) Octahydrate," *Acta. Cryst. C.,* 67:M301-M303. 10. 1107/S0108270111032641.

144. Reed, W. A., A. G. Oliver, and L. Rao. 2011. "Tetra(Tetramethylammonium) Uranyltricarbonate Octahydrate," *Acta Cryst.,* 67:301-303.

145. Regalbuto, M. 2011. "Alternative Separation and Extraction: UREX+ Processes for Actinide and Targeted Fission Product Recovery. " In *Advanced Separation Techniques for Nuclear Fuel Reprocessing and Radioactive Waste Treatment,* eds. K. L. Nash and G. J. Lumetta, pp. 176-200. Woodhead Publishing, Oxford.

146. Robinson, T. A., S. A. Bryan, and T. G. Levitskaia. 2011. "TALSPEAK Extraction System under Variable Loading Conditions - Part 2: Speciation Studies," *19th International Solvent Extraction Conference,* Society of Chemical Industry.

147. Rodriguez, M. A., D. F. Sava, and T. M. Nenoff. 2012. "Catena-Poly[Zinc-Tris(M-Dimethyl- Carbamato-K2O:O')-Zinc-M-(2-Phenyl- Benzimidazolido- K2n:N']," *Acta. Cryst.,* 68:M59-.

148. Roy, L. E., N. J. Bridges, and L. R. Martin. 2012. "Theoretical Insights into Covalency Driven F Element Separations," *Dalton Transactions*. DOI: 10. 1039/c2dt31485a.

149. Rudisill, T. S., M. L. Crowder, and M. C. Thompson. 2010. *Demonstration of the UREX Process Using Formohydroxamic Acid to Prevent the Extraction of Transuranic Elements,* SRNL-STI-2009-000795, AFCI-SYSA-PMO-MI-DV-2009-000209, Savannah River National Laboratory, Aiken, SC.

150. Rudisill, T. S. and T. D. Crute. 2009. *Characterization of Formohydroxamic Acid Synthesized at Augusta State University* SRNL-STI-20009-00750, AFCI-SEPA-AQUE-MI-DV-2009-000125, Savannah River National Laboratory, Aiken, SC.

151. Rudisill, T. S. and E. A. Kyser. 2010. *Distribution of Actinides between the Aqueous and Organic Phases in the TALSPEAK Process* SRNL-STI-2010-000502, FCRD-SEPA-2010-000136, Savannah River National Laboratory, Aiken, SC.

152. Rudisill, T. S. and E. A. Kyser. 2011. *Thermodynamic and Kinetic Studies of the TALSPEAK Solvent Extraction Process,* SRNL-STI-2011-00463, FCRD-SWF-2011-000309, Savannah River National Laboratory, Aiken, SC.

153. Rudisill, T. S. and M. C. Thompson. 2010. *Distribution of Pu and Np between Tbp and Nitric Acid Solutions Containing Fha,* SRNL-STI-2009-00794, AFCI-SYSA-PMO-MI-DV-2009-000209, Savannah River National Laboratory, Aiken, SC.

154. Runde, W. H. and B. J. Mincher. 2011. "The Higher Oxidation States of Americium: Preparation, Characterization and Use for Separations," *Chemical Reviews*, 111(9):5723-2741. dx. doi. org/10. 1021/cr100181f.

155. Schroll, C. A., S. Chatterjee, W. R. Heineman, and S. A. Bryan. 2011. "Spectroelectrochemistry on an Aqueous Micro-Drop in a Semi-Infinite Linear Diffusion Setup," *Anal Chem.,* 83:4214-4219.

156. Schroll, C. A., S. Chatterjee, W. R. Heineman, and S. A. Bryan. 2012. "Thin-Layer Spectroelectrochemistry on an Aqueous Microdrop," *Electroanalysis*, 24(5):1065-1070. DOI: 10. 1002/elan. 201100711.

157. Schwantes, J. M., S. A. Bryan, C. R. Orton, T. G. Levitskaia, and C. G. Fraga. "Monitoring, Controlling and Safeguarding Radiochemical Streams at Spent Fuel Reprocessing Facilities, Part 2: Gamma-Ray Spectroscopic Methods", *International Journal on Nuclear Energy Management and Safety*, 2012. DOI: 10. 5848/IJNEMS. 2012. 00003.

158. Shehee, T. C., L. R. Martin, and K. L. Nash. 2010. "Redox-Based Separation of Americium from Lanthanides in Sulfate Media," *Separation Science and Technology*, 45(12-13):1743-1752.

159. Shehee, T. C., K. M. L. Taylor-Pashow, and D. T. Hobbs. 2012. "Advances in Inorganic and Hybrid Ion-Exchangers.," *Solvent Extr. Ion Exch.,* Submitted.

160. Shkrob, I. A., T. W. Marin, D. C. Stepinski, G. F. Vandegrift, J. V. Muntean, and M. L. Dietz. 2011. "Extration and Reductive Stripping of Pertechnetate from Spent Fuel Waste Streams," *Separation Science and Technology*, 46:357-368. 10. 1080/01496395. 2010. 527893

161. Shkrob, I. A., G. F. Vandegrift, D. C. Stepinski, T. Marin, and M. Dietz. 2009. *Tc(VII) Separations and Electrochemical Deposition in Ionic Liquids,* AFCI-SEPA-PMO-MI-DV-2009-000269, Argonne National Laboratory, Argonne, IL.

162. Sinkov, S. I., G. J. Lumetta, M. G. Warner, and J. W. Pittman. 2012. "Binding of Stereognostically Designed Ligands to Trivalent, Pentavalent, and Hexavalent F-Block Elements," *Radiochimica Acta*, 100:349-357.

163. Sulakova, J., R. T. Paine, M. Chakravarty, and K. L. Nash. 2012. "Extraction of Lanthanide and Actinide Nitrate and Thiocyanate Salts by 2,6-Bis[(Bis(2-N-Octyl)Phosphino)Methyl]Pyridine N,P,P`-Trioxide N Toluene," *Separation Science and Technology*, Submitted.

164. Tian, G., N. M. Edelstein, and L. Rao. 2011. "Spectroscopic Properties and Hydration of the Cm(III) Aqua Ion from 10 to 85oc," *J. Phys. Chem. Letters*, 115(10):1933-1938.

165. Tian, G., L. R. Martin, and L. Rao. 2010. "Complexation of Lactate with Nd(III) and Eu(III) at Variable Temperatures: Studies by Potentiometry, Microcalorimetry, Optical Absorption and Luminescence Spectroscopy " *Inorg Chem.,* 49:10598-10605.

166. Tian, G., L. R. Martin, Z. Zhang, and L. Rao. 2011. "Thermodynamic, Spectroscopic and Computational Studies of Lanthanide Complexation with Diethylenetriaminepentaacetic Acid: Temperature Effect and Coordination Modes," *Inorg. Chem.,* 7:3087-3096.

167. Tian, G. and L. Rao. 2010. "Effect of Temperature on the Protonation of the TALSPEAK Ligands: Lactic and Diethylenetrinitropentaacetic Acids " *Separation Science and Technology*, 45:1718-1724.

168. Tian, G., Y. Shen, J. Wang, and L. Rao. 2012. "Pilot Test for Separation of Sr2+ and Nd(III) from Hllw Using Tiboga," *Separation Science and Technology*, Submitted.

169. Tian, G., P. Zhang, Y. Shen, J. Wang, and L. Rao. 2012. "Bench-Scale Test for Separation of Sr2+ and Nd3+ from Hllw Using Tiboga," *Separation Sci. Tech.,* 47(14-15):2160-2165. DOI: 10. 1080/01496395. 2012. 697515.

170. Tkac, P., G. F. Vandegrift, G. J. Lumetta, and A. V. Gelis. 2012. "Study of the Interaction between HDEHP and CMPO and Its Effect on the Extraction of Selected Lanthanides," *Ind. Eng. Chem. Res.,* 51(31):10433-10444.

171. Todd, T. A. 2011. "Solvent Extraction Research and Development in the U. S. Fuel Cycle Program," *International Solvent Extraction Conference (ISEC 2011)*.

172. Todd, T. A. and B. A. Moyer. 2012. "Novel Approaches to the Separation of Trivalent Actinides from Used Nuclear Fuel," *Nuclear Fuel Cycle Conference*.

173. Vedantam, S., K. E. Wardle, T. V. Tamhane, V. V. Ranade, and J. B. Joshi. 2012. "CFD Simulation of Annular Centrifugal Extractors," *International Journal of Chemical Engineering*:759397. doi:10. 1155/2012/759397.

174. Wardle, K. E., 2012. "Hybrid Multiphase CFD Solver for Coupled Dispersed/Segregated Flows in Liquid-Liquid Extraction," Mixing XXIII, Mayan Riviera, Mexico, June 17-23.

175. Wardle, K. E., 2012. "Hybrid Multiphase CFD Simulations for Flows in Liquid-Liquid Extraction Equipment" (invited), OpenFOAM Seminar, ESI Group, Detroit, MI, October 16.

176. Wardle, K. E. 2011. "Open-Source CFD Simulations of Liquid–Liquid Flow in the Annular Centrifugal Contactor " *Sep. Sci.*

Technol., 46:2409-2417. doi:10. 1080/01496395. 2011. 600748.

177. Wardle, K. E., 2012. "Overview of Multiphase CFD Simulations of Liquid-Liquid Extraction in Annular Centrifugal Contactors" (invited), Lawrence Livermore National Laboratory, June 1.

178. Wardle, K. E., 2012. "Overview of Multiphase CFD Simulations of Liquid-Liquid Extraction in Annular Centrifugal Contactors" (invited), Sandia National Laboratory, August 22.

179. Wardle, K. E., 2012. "Liquid-Liquid Contactor ERT" (invited), ITS 2012 North American Workshop, May 9.

180. Wardle, K. E., 2012. "Investigation of Multiphase Flow in the Mixing Zone of an Annular Centrifugal Contactor" (poster), Mixing XXIII, Mayan Riviera, Mexico, June 17-23.

181. Wardle, K. E. and T. Lee. 2012. "Finite Element Lattice Boltzmann Simulations of Free Surface Flow in a Concentric Cylinder" *Comput. Math. Appl.,* Submitted. doi:10. 1016/j. camwa. 2011. 09. 020.

182. Wardle, K. E. and C. Pereira. 2011. "Advanced Multi-Fluid Simulations and Experiments of Flow in Liquid-Liquid Contactors," *Trans. Am. Nucl. Soc.* , 104:168.

183. Wardle, K. E., 2011. "Advanced Multi-Fluid Simulations of Flow in Centrifugal Contactors" (invited), ANS Winter Meeting, Washington, DC, October 30-November 3.

184. Zalupski, P. 2012. *Complete Recovery of Actinides from UREX-Like Raffinates Using a Combination of Hard and Soft Donor Ligands,* FCRD-SWF-2012-000085, Idaho National Laboratory, Idaho Falls, ID.

185. Zalupski, P. and K. L. Nash. 2008. "Calorimetric Investigations of Metal Extraction for Two Phase Systems in Solvent Extraction: Fundamentals to Industrial Applications " *International Solvent Extraction Conference (ISEC 2008),* The Canadian Institute of Mining, Metallurgy and Petroleum.

186. Zalupski, P. R., R. S. Herbst, D. R. Peterman, L. H. Delmau, L. R. Martin, and K. L. Nash. 2010. "Two-Phase Calorimetry. II. Studies on the Thermodynamics of Cesium and Strontium Extraction by Mixtures of H+CCD- and PEG-400 in Fs-13," *Solvent Extraction & Ion Exchange*, 28(2):161-183.

187. Zalupski, P. R. and K. L. Nash. 2008. "Two-Phase Calorimetry. I. Studies on the Thermodynamics of Lanthanide Extraction by Bis(2-Ethylhexyl) Phosphoric Acid," *Solvent Extraction and Ion Exchange*, 26(5):514-533.

188. Zalupski, P. R., K. L. Nash, and L. R. Martin. 2010. "Thermodynamic Features of the Complexation of Neodymium(III) and Americium(III) by Lactate in Trifluoromethanesulfonate Media," *Journal of Solution Chemistry*, 39:1213-1229.

189. Zalupski, P. R. and D. R. Peterman. 2012. *Complete Recovery of Actinides from UREX-Like Raffinates Using a Combination of Hard and Soft Donor Ligands, Fuel Cycle Research and Development Report,* FCRD-SWF-2012-000350, Idaho National Laboratory, Idaho Falls, ID.

190. Zhao, H., K. Beyer, T. M. Nenoff, P. J. Chupas, and K. W. Chapman. 2012. "Combining Simultaneous Pair Distribution Function with Diffuse Reflectance Infrared Spectroscopy to Study Silver Particle Growth on Porous Template," Submitted.

191. Zhao, H., T. M. Nenoff, G. Jennings, P. J. Chupas, and K. W. Chapman. 2011. "Determining Quantitative Kinetics and the Structural Mechanism for Particle Growth in Porous Templates," *J. Phys. Chem. Letters*, 2(21):2742-2746.

Electrochemical Reprocessing

1. Bryan, S. A., S. D. Chatterjee, W. R. Heineman, and C. Schroll. 2011. "Method and Apparatus for Simultaneous Spectroelectrochemical Analysis," United

States Patent Application Number: 13,246,090; Filing Date: September 27, 2011.

2. Frank, S. M. 2011. *Radiogenic Iodine Partitioning the Electrochemical/Pyrometallurgical Treatment of Na-Bonded Metallic Fuel,* FCRD-WAST-2011-000091, Idaho National Laboratory, Idaho Falls, ID.

3. Fredrickson, G. 2011. *Final Report for the FY 2010 Series of U/TRU Codeposition Tests,* FCRD-SWF-2011-000102, Idaho National Laboratory, Idaho Falls, ID.

4. Fredrickson, G. 2012. *Final Report for the FY 2011 Series of U/TRU Codeposition Tests,* FCRD-SWF-2012-000093, Idaho National Laboratory, Idaho Falls, ID.

5. Fredrickson, G. 2011. *Thermal Characterization of Molten Salt Systems,* FCRD-SWF-2011-000364, Idaho National Laboratory, Idaho Falls, ID.

6. Fredrickson, G. 2010. *Treating FFTF"U-Zr" and EBR-II "U-Fs" Fuels in the Mk-IV and Mk-V Electrorefiners,* INL/TEV-976, Idaho National Laboratory, Idaho Falls, ID.

7. Fukada, S., M. F. Simpson, and R. A. Ander. 2007. "Reaction Rate of Beryllium with Fluorine Ion for Flibe Redox Control," *Journal Of Nuclear Materials*, 367:1190-1196. 10. 1016/j. jnucmat. 2007. 03. 218.

8. Garrett, P. E., K. L. Green, H. Lehmann, J. Jolie, C. A. Mcgrath, M. Yeh, and S. W. Yates. 2007. "Properties of Cd-112 from the (N,N 'Gamma) Reaction: Lifetimes and Transition Rates," *Physical Review C* 75(5). 10. 1103/PhysRevC. 75. 054310.

9. Gese, N. 2010. "The Electrochemistry of Li-LiCl-Li2o Molten Salt Systems and the Role of Moisture," Masters Thesis University of Idaho, Moscow, ID.

10. Goff, K. M., J. C. Wass, and K. C. Marsden. 2010. "Electrochemical Processing of Used Nuclear Fuel," *Nuclear Engineering And Technology*, 43(4):335-342. DOl: 1 0. 5516/NET. 2011. 43. 4. 335 Published: AUG 2011.

11. Gutknecht, T. 2011. "Thermal Analysis of Surrogate Simulated Molten Salts with Metal Chloride Impurities for Electrorefining Used Nuclear Fuel," Masters, University of Idaho, Moscow, ID.

12. Herrmann, S., and M. Simpson. 2007. "Electrolytic Reduction of Spent Light Water Reactor Fuel Beach Scale Experiment Results," *ournal of Nuclear Science and Technology*, Vol. 44(No. 3).

13. Herrmann, S. D. 2010. *Results of Dross Treatment Efforts,* FCRD-SEPA-2010-000159, Idaho National Labortory, Idaho Falls, ID.

14. Herrmann, S. D. 2009. *Sample Analysis Results from the Electrorefining Reduced MOX Fuel,* AFCI-SEPA-PMO-MI-DV-2009-000227, Idaho National Laboratory, Idaho Falls, ID.

15. Hoover, R. O., S. Phongikaroon, S. Li, M. Simpson, and T. S. Yoo. 2011. "A Computational Model of the Mark-V Electrorefiner: Phase I-Fuel Basketjsalt Interface," *Journal of Engineering for Gas Turbines and Power*, 131(5).

16. Hoover, R. O., S. Phongikaroon, M. F. Simpson, S. X. Li, and T. S. Yoo. 2011. "Development of Computational Models for the Mark-IV Electrorefiner-Effect of Uranium, Plutonium, and Zirconium Dissolution at the Fuel Basket/Salt Interface," *Nuclear Technology*, 171(3):276-284.

17. Laplace, A. F., J. Lacquement, J. L. Willit, R. A. Finch, G. A. Fletcher, and M. A. Williamson. 2008. "Electrodeposition of Uranium and Transuranics Metals on Solid Cathode," *Nuclear Technology*, 163(3):366-372.

18. Li, S. X., S. D. Herrmann, and K. M. Goff. 2009. "Actinide Recovery Experiments with Bench-Scale Liquid Cadmium Cathode in Real Fission Product-Laden Molten Salt," *Nuclear Technology*, 165(2):190-199.

19. Li, S. X., S. D. Herrmann, and M. F. Simpson. 2011. "Electrochemical Analysis of Actinides and Rare Earth Constituents in

Liquid Cadmium Cathode Product from Spent Fuel Electrorefining " *Nuclear Technology*, 171(3):292-299.

20. Li, S. X., D. Vaden, and B. R. Westphal. 2009. "Integrated Efficiency Test for Pyrochemical Fuel Cycles," *Nuclear Technology*, 166(2):180-186.
21. Li, S. X., D. Vaden, B. R. Westphal, G. L. Fredrickson, R. W. Benedict, and T. A. Johnson. 2007. "Integrated Efficiency Test for Pyrochemical Fuel Cycles," *Global 2007: Advanced Nuclear Fuel Cycles and Systems,* American Nuclear Society.
22. Mariani, R. D. and D. Vaden. 2010. "Modeled Salt Density for Nuclear Material Estimation in the Treatment of Spent Nuclear Fuel," *Journal Of Nuclear Materials*, 404(1):25-32.
23. Marsden, K. C. and B. Pesic. 2011. "Evaluation of the Electrochemical Behavior of $CeCl_3$ in Molten Lici-KCl Eutectic Utilizing Metallic Ce as an Anode," *Journal Of The Electrochemical Society*, 158(6).
24. Sachdev, P., M. F. Simpson, and S. M. Frank. 2008. "Selective Separation of Cs and Sr from LiCl-Based Salt for Electrochemical Processing of Oxide Spent Nuclear Fuel," *Separation Science And Technology*, 43 (9-10):2709-2721.
25. Serrano, B. E. 2009. *Results Report on "Platinum Anode Degradation Testing in Molten Salt Furnace II,* AFCI-SEPA-PMO-MI-DV-2009-000223, Idaho National Laboratory, Idaho Falls, ID.
26. Simpson, M. F. 2009. *Complete Literature Review for U/TRU Drawdown,* AFCI-SEPA-PMO-MI-DV-2009-000229, Idaho National Laboratory, Idaho Falls, ID.
27. Simpson, M. F. 2011. *Labscale Testing of Drawdown Using Lithium and Actinide Bearing Salt,* FCRD-SEPA-2011-000325, Idaho National Laboratory, Idaho Falls, ID.
28. Simpson, M. F. 2010. *Process Report on TRU/Fp Drawdown from Molten LiCl-Kci Used for Electrorefining,* FCRD-SEPA-2010-000200, Idaho National Laboratory, Idaho Falls, ID.
29. Simpson, M. F. and S. D. Herrmann. 2008. "Modeling the Pyrochemical Reduction of Spent UO2 Fuel in a Pilot-Scale Reactor," *Nuclear Technology*, 162(2):179-183.
30. Vaden, D. 2009. *Electrorefine 400 Kg Blanket Fuel in Mark V Er,* AFCI-SEPA-PMO-MI-DV-2009-000225, Idaho National Labortory, Idaho Falls, ID.
31. Vaden, D. and G. L. Fredrickson. 2007. "Material Control and Accountabilty Experience at the Fuel Conditioning Facility," *Global*.
32. Vaden, D., S. X. Li, and B. R. Westphal. 2008. "Engineering-Scale Liquid Cadmium Cathode Experiments," *Nuclear Technology*, 162(2):124-128.
33. Westphal, B. R., K. J. Bateman, C. D. Morgan, J. F. Berg, P. J. Crane, D. O. Cummings, J. J. Giglio, M. W. Huntley, R. P. Lind, and D. A. Sell. 2008. "Effect of Process Variables During the Head-End Treatment of Spent Oxide Fuel," *Nuclear Technology*, 162(2):153-157.
34. Westphal, B. R., R. P. Lind, J. J. Giglio, D. G. Cummings, M. W. Huntley, C. D. Morgan, K. J. Bateman, D. L. Wahlquist, and D. A. Sell. 2007. "Direct Assay of Filter Media Following Deox Testing," *Global,* American Nuclear Society.
35. Westphal, B. R., K. C. Marsden, and J. C. Price. 2009. "Development of a Ceramic-Lined Crucible for the Separation of Salt from Uranium," *Metallurgical And Materials Transactions A* 40A(12):2861-2866.
36. Westphal, B. R., K. C. Marsden, and J. C. Price. 2008. "On the Development of a Distillation Process for the Electrometallurgical Treatment of Irradiated Spent Nuclear Fuel," *Nuclear Engineering And Technology*, 40(3):163-174.
37. Westphal, B. R., J. J. Park, J. M. Shin, G. I. Park, K. J. Bateman, and D. L. Wahlquist. 2008. "Selective Trapping of Volatile

Fission Products with an Off-Gas Treatment System," *Journal of Separation Science and Technology*, 43(9-10):2695-2708.

38. Westphal, B. R., J. C. Price, and D. Vaden. 2007. "Engineering-Scale Distillation of Cadmium for Actinide Recovery," *Journal Of Alloys And Compounds* 444(561-564).

39. Yoo, T. S., S. M. Frank, M. F. Simpson, P. A. Hahn, T. J. Battisti, and S. Phongikaroon. 2011. "Salt-Zeolite Ion Exchange Equilibrium Studies for Complete Set of Fission Products in Molten Lici-Kci," *Nuclear Technology*, 171(3):306-315.

40. Yoo, T. S. and H. E. Garcia. 2008. "Diagnosis of Behaviors of Interest in Partially-Observed Discrete-Event Systems," *Systems & Control Letters* 57(12):1023-1029.

Uranium from Seawater

1. "Extracting Uranium from Seawater," *Chemical and Engineering News*, Volume 90 (36), pp 60-63, September 3, 2012.

2. Hay, B. P., S. Vukovic, and S. O. Kang, "Improving the Chemistry of Amidoxime-based Uranium Adsorbents," *244th National Meeting of the American Chemical Society*, Philadelphia, PA, August 19-23, 2012

3. Rao, L. 2012. "Application of Radiation Grafting: Progress and Status of the Extraction of Uranium from Seawater in Japan," *Journal of Isotopes*, Submitted.

4. Rao, L. 2010. *Recent International R&D Activities in the Extraction of Uranium from Seawater,* LBNL-4034E, Lawrence Berkeley National Laboratory report, Berkeley, CA.

5. Tian, G. and L. Rao. 2011. "Bonding Modes and Strength of Uranyl Ion with Imidedioxme Ligand for Extraction of Uranium from Seawater " *Global,* American Nuclear Society.

6. Tian, G., S. J. Teat, and L. Rao, "Thermodynamic studies of U(VI) complexation with glutardiamidoxime for sequestration of uranium from seawater. "

7. Tian, G., S. J. Teat, Z. Zhang, and L. Rao. 2012. "Sequestering Uranium from Seawater: Binding Strength and Modes of Uranyl Complexes with Glutarimidedioxime," *Dalton Trans.,* Submitted.

8. Vukovic, S., L. A. Watson, R. Custelcean, S. O. Kang, and B. P. Hay, "Binding Motif of Amidoxime to the Uranyl Ion," *243rd National Meeting of the American Chemical Society*, San Diego, CA, March 25-29, 2012.

9. Vukovic, S., L. A. Watson, R. Custelcean, S. O. Kang, and B. P. Hay. 2012. "How Amidoxime Binds Uranyl Cation," *Inorganic Chemistry 2012*, 51:5502-5512.

10. Vukovic, S., and B. P. Hay, "Interaction of Uranium with Poly(acrylamidoxime) Adsorbents," *36th Actinide Separation Conference*, Chattanooga, TN, May 19-23, 2012

11. Vukovic, S., L. A. Watson, R. Custelcean, S. O. Kang, and B. P. Hay, "Interaction of Uranium with Poly(acrylamidoxime) Adsorbents," *244th National Meeting of the American Chemical Society*, Philadelphia, PA, August 19-23, 2012.

12. Watson, L. A. and B. P. Hay. 2011. "Role of the Uranyl Oxo Group as a Hydrogen Bond Acceptor," *Inorganic Chemistry*, 50:2599-2605.

Waste Forms and Off-Gas

1. Alaniz, A. J., L. Delgado, B. Werbick, and T. Hartmann. 2012. *Remote operated hot uniaxial press to fabricate Tc-99 bearing waste forms,* Atalante 2012: Nuclear Fuel Cycle for a Sustainable Fuel Cycles, Montpellier, France, 2-7 September, Proceedings, A168 (2012); to be published in Procedia Chemistry.

2. Bateman, K. J. and C. W. Solbrig. 2008. "Stabilizing Glass Bonded Waste Forms Containing Fission Products Separated from Spent Nuclear Fuel," *Separation Science And Technology*, 43(9-10).

3. Bateman, K. J. and C. W. Solbrig. 2008. "Stabilizing Glass Bonded Waste Forms

Containing Fission Products Separated from Spent Nuclear Fuel," *Journal of Separation Science and Technology*, 43(9-10):2722-2746.

4. Bateman, K. J. and C. W. Solbrig. 2008. "Use of Similarity Analysis on Experiments of Different Size to Predict Critical Cooling Rates for Large Ceramic Waste Forms," *ICONE16 International Conference on Nuclear Engineering*

5. Billings, A., K. Brinkman, K. Fox, and J. C. Marra. 2010. *Preliminary Study of Crystalline Ceramics for Immobilization of Advanced Fuel Cycle Reprocessing Wastes-FY10 Annual Report,* SRNL-STI-2010-00560, Savannah River National Laboratory, Aiken, SC.

6. Billings, A. L., K. S. Brinkman, K. M. Fox, J. C. Marra, M. Tang, and K. E. Sickafus. 2010. "Development of Ceramic Waste Forms for an Advanced Nuclear Fuel Cycle," *Ceramic Transactions*, Vol. 227*,* American Ceramic Society.

7. Bourg, I. C. and C. I. Steefel. 2012. "Molecular Dynamics Simulations of Water Structure and Diffusion in Silica Nanopores," *J. Phys. Chem. C*, 116:11556-11564.

8. Brinkman, K., K. Fox, J. C. Marra, and M. Tang. 2012. *Crystalline Ceramic Waste Forms: Reference Formulation Report,* FCRD-SWF-2012-000116, SRNL-STI-2012-00281, Savannah River National Laboratory, Aiken, SC, May 15.

9. Brinkman, K., K. Fox, J. C. Marra, and M. Tang. 2012. *Crystalline Ceramic Waste Forms: Report Detailing Data Collection in Support of Potential FY13 Pilot Scale Melter Test,* SRNL-STI-2012-00587, FCRD-SWF-2012-000329, Savannah River National Laboratory, Aiken, SC, September 21.

10. Brinkman, K., K. Fox, and M. Tang. 2011. *Development of Crystalline Ceramics for Immobilization of Advanced Fuel Cycle Reprocessing Wastes-FY11 Annual Report,* SRNL-STI-2011-00516, Savannah River National Laboratory, Aiken, SC.

11. Brinkman, K. S., K. M. Fox, J. C. Marra, J. Reppert, J. Crum, and M. Tang. 2012. "Single Phase Melt Processed Powellite (Ba,Ca)Moo_4 for the Immobilization of Mo-Rich Nuclear Waste," *Journal of Alloys and Compounds*, 551:136–142.

12. Bruffey, S. H., K. K. Anderson, R. T. Jubin, and J. F. Walker. 2012. *Aging and Iodine Loading of Silver-Functionalized Aerogels,* FCRD-SWF-2012-000256, Oak Ridge National Laboratory, Oak Ridge, TN.

13. Chapman, K. W., P. Chupas, and T. M. Nenoff. 2010. "Radioactive Iodine Capture in Silver-Containing Mordenites through Nanoscale Silver Iodide Formation," *J. Amer. Chem. Soc*, 132 (26):8897.

14. Chapman, K. W., D. F. Sava, G. J. Halder, P. J. Chupas, and T. M. Nenoff. 2011. "Trapping Guests within a Nanoporous Metal-Organic Framework through Pressure-Induced Amorphization," *J. Amer. Chem. Soc.,* 133(46):18583-18585.

15. Chen, J., D. Zagidulin, and D. W. Shoesmith. 2011. *Electrochemical and Corrosion Behaviour of Metal Alloy Waste Forms,* FCRD-WAST-2011-000012, Argonne National Laboratory, Argonne, IL.

16. Collins, E. D., G. D. Delcul, J. E. Rushton, and K. A. Williams. 2010. *A Practical Solution to Used Nuclear Fuel Treatment to Enable Sustained Nuclear Energy and Recovery of Vital Materials* ORNL/TM-2010/81, Oak Ridge National Laboratory, Oak Ridge, TN.

17. Collins, E. D., G. D. Delcul, B. B. Spencer, R. R. Brunson, J. A. Johnson, D. S. Terekhov, and N. V. Emmanuel. 2012. "Process Development Studies for Zirconium Recovery/Recycle from Used Nuclear Fuel Cladding - Nuclear Chemistry for Sustainable Fuel Cycles," *ATALANTE*.

18. Collins, E. D., G. D. Delcul, D. S. Terekov, and N. V. Emmanuel. 2011. "Recycle of Zirconium from Used Nuclear Fuel

Cladding A Major Element of Waste Reduction " *Waste Management*.

19. Collins, E. D., G. D. Delcul, K. A. Williams, and J. E. Rushton. 2012. "A Practical Approach to a Closed Nuclear Fuel Cycle and Sustained Nuclear Energy," *Waste Management*.

20. Collins, E. D., B. B. Spencer, and G. D. Delcul. 2011. "Importance of Decay Time on HLW Disposal " *2011 International High-Level Radioactive Waste Management Conference,* American Nuclear Society.

21. Crawford, C. L. and J. C. Marra. 2012. *Characterization of Glass Solids from Long-Term Corrosion Testing,* FCRD-SWF-2012-000250, Savannah River National Laboratory, Aiken, SC.

22. Criscenti, L. J., P. A. Schultz, C. I. Steefel, P. Zapol, and I. Bourg. 2011. *Progress toward Bridging from Atomistic to Continuum Modeling to Predict Nuclear Waste Glass Dissolution,* SAND2011-8250, Sandia National Laboratories Albuquerque, NM.

23. Crum, J. V., A. L. Billings, J. Lang, J. C. Marra, C. P. Rodriguez, J. V. Ryan, and J. D. Vienna. 2009. *Baseline Glass Development for Combined Fission Products Waste Streams,* AFCI-WAST-WAST-MI-DV-2009-000075, Pacific Northwest National Laboratory, Richland, WA.

24. Crum, J. V., B. J. Riley, S. K. Sundaram, S. A. Arreguin, J. Matyas, M. J. Schweiger, B. T. Rieck, and J. D. Vienna. 2009. *Alternative Waste Forms for Electro-Chemical Salt Waste,* AFCI-WAST-PMO-MI-DV-2009-000293, Pacific Northwest National Laboratory, Richland, WA.

25. Crum, J. V., B. J. Riley, L. R. Turo, M. Tang, and A. Kossoy. 2011. *Summary Report: Glass-Ceramic Waste Forms for Combined Fission Products,* FCRD-WAST-2011-000358, Pacific Northwest National Laboratory, Richland, WA.

26. Crum, J. V., C. Rodriguez, J. Mccloy, J. D. Vienna, and C. Chung. 2012. *Glass Ceramic Formulation Data Package,* FCRD-SWF-2012-000139, Pacific Northwest National Laboratory, Richland, WA.

27. Crum, J. V., D. M. Strachan, and M. R. Zumhoff. 2012. *Epsilon Metal Commercial Processing Study,* PNNL-21350, Pacific Northwest National Laboratory, Richland, WA.

28. Crum, J. V., D. M. Strachan, and M. R. Zumhoff. 2012. *Initial Evaluation of Processing Methods for an Epsilon Metal Waste Form*. Report No. FCRD-SWF-2012-000108, Pacific Northwest National Laboratory, Richland, WA.

29. Crum, J. V., S. K. Sundaram, B. J. Riley, J. Matyas, S. A. Arreguin, and J. D. Vienna. 2009. *Alternate Waste Forms of Electro-Chemical Processing,* PNNL-18930, Pacific Northwest National Laboratory, Richland, WA.

30. Crum, J. V., L. A. Turo, B. J. Riley, M. Tang, and A. Kossoy. 2012. "Multi-Phase Glass-Ceramics as a Waste Form for Comined Fission Products: Alkalis, Alkaline Earths, Lanthanides, and Transisition Metals," *Journal of the American Ceramics Society*, 95(4):1297-1303. 10. 1111/j. 1551-2916. 2012. 05089. x.

31. Crum, J. V., L. R. Turo, B. J. Riley, M. Tang, A. Kossoy, and K. E. Sickafus. 2010. *Glass Ceramic Waste Forms for Combined Cs+Ln+TM Fission Products Waste Streams,* FCRD-WAST-2010-000181, Pacific Northwest National Laboratory, Richland, WA.

32. Cunnane, J. C. 2010. *Alternative Waste Forms for Separated Fractions from Advanced Aqueous Processing of Used Nuclear Fuels,* FCRD-WAST-2010-000014, Argonne National Laboratory, Argonne, IL.

33. Cunnane, J. C. 2010. *Conceptual Model and Results of Corrosion Experiments,* FCRD-WAST-2010-000162, Argonne National Laboratory, Argonne, IL.

34. Cunnane, J. C. 2010. *Initial Conceptual Corrosion Model and Planned Testing Approach-Metal Waste Form,* FCRD-

WAST-2010-000014, Argonne National Laboratory, Argonne, IL.

35. Cunnane, J. C. 2010. *Preliminary Electrochemical Reaction Mechanism and Kinetic Data for Reactive Transport Code,* FCRD-WAST-2010-000113, Argonne National Laboratory, Argonne, IL.

36. Ebert, W., E. Buck, and J. Fortner. 2011. *Heat Treatments of RAW-1(Re),* FCRD-WAST-2011-000289, Argonne National Laboratory, Argonne, IL.

37. Ebert, W., T. Cruse, J. Cunnane, J. Chen, D. Zagidulin, J. Noël, and E. Mausolf. 2011. *Electrochemical Testing to Support Development of an Alloy Waste Form Degradation Model,* FCRD-WAST-2011-000394, Argonne National Laboratory, Argonne, IL.

38. Ebert, W., J. Cunnane, M. Williamson, S. Frank, E. Buck, D. Kolman, E. Mausolf, and D. Shoesmith. 2010. *FY2010 Status Report: Developing and Iron-Based Alloy Waste Form,* FCRD-WAST-2010-000161, Argonne National Laboratory, Argonne, IL.

39. Ebert, W., J. Fortner, I. Shkrob, and G. Jarvinen. 2009. *Options for Recovering and Immobilizing the Tc Dissolved During Oxide Fuel Dissolution,* AFCI-SEPA-PMO-MI-DV-2009-000161, Argonne National Laboratory, Argonne, IL.

40. Ebert, W., M. Williamson, and S. M. Frank. 2009. *Immobilizing Tc-Bearing Waste Streams in an Iron-Based Alloy Waste Form,* AFCI-WAST-PMO-MI-DV-2009-000160, Argonne National Laboratory, Argonne, IL.

41. Ebert, W. L. 2012. *Development of a Corrosion Model for Metal Waste Forms: Fy2012 Status Report,* FCRD-SWF-2012-000158, Argonne National Laboratory, Argonne, IL.

42. Ebert, W. L. 2010. *Formulating a Glass-Bonded Mineral Waste Form for Waste Salts with High Cs and Sr Contents,* FCRD-WAST-2010-000173, Argonnne National Laboratory, Argonne, IL.

43. Ebert, W. L. 2011. *Formulation of Reference Alloy Waste Form RAW-1,* FCRD-WAST-2011-000004, Argonne National Laboratory, Argonne, IL.

44. Ebert, W. L. 2008. *Immobilizing GNEP Wastes in Pyrochemical Process Waste Forms,* GNEP-WAST-PMO-MI-DV-2008-000150, Argonne National Laboratory, Argonne, IL.

45. Ebert, W. L. 2012. *Solution Replacement Tests with SON-68 Glass,* FCRD-SWF-2012-000122, Argonne National Laboratory, Argonne, IL.

46. Ebert, W. L. 2010. *Test Plan for FY2010 Glass Testing Activities at ANL,* FCRD-WAST-2010-000026, Argonne National Laboratory, Argonne, IL.

47. Ebert, W. L. 2008. *Testing Protocols to Support Waste Form Developmnet, Production, and Acceptance,* AFCI-WAST-WAST-AI-RT-2008-000302, Argonne National Laboratory, Argonne, IL.

48. Ebert, W. L., T. A. Cruse, and J. A. Fortner. 2012. *Electrochemical Measurements with RAW-1(Tc),* FCRD-SWF-2012-000200, Argonne National Laboratory, Argonne, IL.

49. Ebert, W. L., J. C. Cunnane, and J. L. Jerden. 2009. *A Strategy for Conditioning Truex Raffinate Waste for Immobilization,* AFCI-SUI-WAST-WAST-MI-DV-2009-000001, Argonne National Laboratory, Argonne, IL.

50. Ebert, W. L., J. A. Fortner, A. L. Billings, and C. Crawford. 2011. *Glass Testing Activities at ANL and SRNL: FY11 Progress Report,* FCRD-WAST-2011-000404, Argonne National Laboratory, Argonne, IL.

51. Ebert, W. L., J. A. Fortner, C. L. Crawford, and J. C. Marra. 2012. *Stage 3 Dissolution Tests with AFCI Glass,* FCRD-SWF-2012-000204, Argonne National Laboratory, Argonne, IL.

52. Ebert, W. L., S. M. Frank, L. Olson, E. Buck, and D. Zagidulin. 2011. *Reference Alloy Waste Form RAW-1,* FCRD-WAST-

2011-000185, Argonne National Laboratory Argonne, IL.

53. Ebert, W. L., J. C. Marra, and E. M. Pierce. 2010. *FY2010 Glass Testing Activities at ANL, SRNL, and PNNL,* FCRD-WAST-2010-000015, Argonne National Laboratory, Argonne, IL.

54. Felicione, F. S., S. M. Frank, and D. D. Keiser. 2007. *WIPP Gas-Generation Experiments: Final Program Report,* INL/EXT-07-12631, Idaho National Laboratory, Idaho Falls, ID.

55. Fernandez, C. A., J. Liu, P. K. Thallapally, and D. M. Strachan. 2012. "Switching Kr/Xe Selectivity with Temperature in a Metal–Organic Framework," *J. Am. Chem. Soc.,* 134(22):9046-9049.

56. Fortner, J. A. 2012. *Analysis of Component Phases in RAW-2(Utc),* FCRD-SWF-2012-000366, Argonne National Laboratory, Argonne, IL.

57. Fortner, J. A. 2012. *Effects of Alteration Phase Precipitation on Glass Dissolution,* FCRD-SWF-2012-000266, Argonne National Laboratory, Argonne, IL.

58. Fortner, J. A. and W. L. Ebert. 2012. *Status of Static Corrosion Tests with RAW-1(Tc),* FCRD-SWF-2012-000202, Argonne National Laboratory, Argonne, IL.

59. Frank, S. M., K. Bateman, T. P. O'holleran, and M. F. Simpson. 2008. *Production and Sampling Plan for Ceramic Waste Form Process Qualification,* INL/INT-08-14586, Idaho National Laboratory, Idaho Falls, ID.

60. Frank, S. M., J. D. D. Keiser, and K. Marsden. 2007. "Immobilization of Teclmetium in a Metallic Waste Form," *Global,* American Nuclear Society.

61. Frank, S. M., P. A. Hahn, W. L. Ebert, and L. Olson. 2012. *Test Alloy Fabrication and Oxide Addition Studies,* FCRD-SWF-2012-000234, Idaho National Laboratory, Idaho Falls, ID.

62. Frank, S. M., T. P. O'holleran, and P. A. Hahn. 2010. *Composition of Tc-Fe Alloy Produced for Testing,* FCRD-WAST-2010-000011, Idaho National Laboratory, Idaho Falls.

63. Frank, S. M., T. P. O'holleran, and P. A. Hahn. 2011. *Reference Alloy Waste Form Fabrication and Initiation of Reducing Atmosphere and Reductive Additives Study on Alloy Waste Form Fabrication,* FCRD-WAST-2011-000089, Idaho National Laboratory, Idaho Falls, ID.

64. Garino, T. G., T. M. Nenoff, T. J. Park, and A. Navrotsky. 2009. "The Crystallization of Ba-Substituted CsTiSi2O6. 5 Pollucite Using CsTiSi2O6. 5 Seed Crystals," *J. Amer. Cer. Soc.,* 92(9):2144-2146.

65. Garino, T. J., T. M. Nenoff, J. L. Krumhansl, and D. Rademacher. 2011. "Low-Temperature Sintering Bi-Si-Zn Oxide Glasses for Use in Either Glass Composite Materials or Core/Shell 129I Waste Forms," *J. Amer. Ceram. Soc.,* 94(8):2412-2419.

66. Garino, T. J., T. M. Nenoff, J. L. Krumhansl, and D. X. Rademacher. 2011. "Development of Iodine Waste Forms Using Low-Temperature Sintering Glass in Materials Challenges in Alternative and Renewable Energy," *Ceramic Transactions*, Vol. 224*,* 305-312 pp. American Ceramic Society.

67. Garino, T. J., T. M. Nenoff, J. L. Krumhansl, and D. X. Rademacher. 2010. "Development of Waste Forms for Radioactive Iodine," *Ceramic Transactions*, Vol. 217*,* 35-42 pp. American Ceramic Society.

68. Garino, T. J., D. X. Rademacher, M. Rodriguez, and T. M. Nenoff. 2012. "The Synthesis and Characterization of Ba and Fe Substituted $CsAlSi_2O_6$ Pollucites," *J. Am. Ceram. Soc.,* Submitted.

69. Garn, T. G., M. R. Greenhalgh, and J. D. Law, “Results of Physisorption Testing for Ni-DOBDC MOF at the INL”, BEA Material Transfer/Non-Disclosure Agreement (MTA) 12-MT-NDA-001, June 2012.

70. Garn, T. G., J. D. Law, M. R. Greenhalgh, and T. A. Tranter, "A Composite Media For Fluid Stream Processing, A Method Of Forming The Composite Media, And A Related Method Of Processing A Fluid Stream" 2939-10703 BA-590 Patent Application.

71. Garn, T. G., M. R. Greenhalgh, and J. D. Law. 2012. *FY-12 INL Kr Capture Activities Supporting the Off-Gas Sigma Team,* FCRD-SWF-2012-000252, Idaho National Laboratory, Idaho Falls, ID.

72. Garn, T. G., M. R. Greenhalgh, and J. D. Law. 2012. *Strategy for Analyses of Legacy Kr-85 Samples,* FCRD-SEPA-2011-000027, Idaho National Laboratory, Idaho Falls, ID.

73. Garn, T. G. and T. J. Tranter. 2010. *Kr Capture FY-10 Testing* INL/MIS-10-19736, Idaho National Laboratory, Idaho Falls, ID.

74. Garn, T. G. and T. J. Tranter. 2010. *Kr Capture Studies at the INL FY-10,* INL-MIS-19757, Idaho National Laboratory, Idaho Falls, ID.

75. Gombert, D., J. Carter, W. L. Ebert, S. Piet, T. Trickel, and J. D. Vienna. 2009. "A Trade Study for Waste Concepts to Minimize HLW Volume," *Scientific Basis for Nuclear Waste Management XXXII*, Vol. 1124*,* 53-64 pp. Materials Research Society.

76. Gombert, D., R. Counce, A. Cozzi, J. V. Crum, W. L. Ebert, C. M. Jantzen, J. Jerden, R. Jubin, M. D. Kaminski, V. Maio, J. C. Marra, T. M. Nenoff, R. D. Scheele, H. D. Smith, B. Spencer, D. M. Strachan, and J. D. Vienna. 2007. *Global Nuclear Energy Partnership Integrated Waste Management Strategy Waste Treatment Baseline Study,* GNEP-WAST-AI-RT-2007-000324, Idaho National Laboratory, Idaho Falls, ID.

77. Gombert, D., W. L. Ebert, J. C. Marra, R. T. Jubin, and J. D. Vienna. 2008. "Global Nuclear Energy Partnership Waste Treatment Baseline," *Atalante*.

78. Greenhalgh, M., T. Garn, and J. Law. 2011. *Kr-85 Legacy Sample Strategy* INL/MIS-11-22362, Idaho National Laboratory, Idaho Falls, ID.

79. Greenhalgh, M., T. Garn, and J. Law. 2011. *Kr Capture Studies at the INL,* INL/MIS/11-21406, Idaho National Laboratory, Idaho Falls, ID.

80. Greenhalgh, M., T. G. Garn, and J. Law. 2011. *Summary of FY-11 Krypton Capture Activities at the INL* INL/EXT-11-23139, Idaho National Laboratory, Idaho Falls, ID.

81. Haefner, D. and N. Soelberg. 2009. *Experimental Sorption Testing of Elemental Iodine on Silver Mordenite* INL/EXT-09-16837, Idaho National Laboratory, Idaho Falls, ID.

82. Haefner, D., N. Soelberg, and L. Lauerhass. 2007. *Off-Gas System Design for Aqueous Separations Solidification Processes,* INL/EXT-07-12851, Idaho National Laboratory, Idaho Falls, ID.

83. Hartmann, T., A. Alaniz, F. Poineau, P. F. Weck, J. A. Valdez, M. Tang, G. D. Jarvinen, K. R. Czerwinski, and K. E. Sickafus. 2011. "Structural Studies on Lanthanide Technetium Pyrochlores as Prospective Host Phases to Immobilize 99technetium and Fission Lanthanides from Effluents of Reprocessed Used Nuclear Fuels," *J. Nucl. Matl.,* 411((1-3)):60-71.

84. Hartmann, T., A. J. Alaniz, and D. J. Antonio. 2012. "Fabrication and Properties of Technetium-Bearing Pyrochlores and Perovskites as Potential Waste Forms," *Atalante 2012: Nuclear Fuel Cycle for a Sustainable Fuel Cycles*. 2-7 September, Proceedings, A210 (2012); to be published in Procedia Chemistry.

85. Hartmann, T., A. J. Alaniz, and D. J. Antonio. 2012. "Fabrication and properties of Tc-bearing pyrochlores, perovskites and spinel derivates." *243rd ACS National Meeting: Chemistry for Life, session: Waste Forms for Environmental Remediation*, San Diego, 25-29 March, Pub 253.

86. Icenhower, J. P. and C. Steefel. 2012. "Experimentally Determined Dissolution

Kinetics of SON68 Glass at 90°C over a Silica Saturation Interval: Evidence against a Linear Rate Law," *Journal of Nuclear Materials*, Submitted.

87. Jaffe, J. E., R. M. V. Ginhoven, and W. Jiang. 2012. "Interstitial and Substitutional Zirconium in SrTiO3," *Computational Materials Science* 53(1):153-157. 10. 1016/j. commatsci. 2011. 08. 023.

88. Jiang, W., and R. Van Ginhoven. *Progress Report on the Pollucite Work*, FCRD-UFD-2012-000377, Pacific Northwest National Laboratory, Richland, WA, September 2012.

89. Jiang, W., M. E. Bowden, Z. Zhu, P. A. Jozwik, J. Jagielski, and A. Stonert. 2012. "Defects and Minor Phases in O+ and Zr+ Ion Co-Implanted SrTiO3.," *Industrial and Engineering Chemistry Research* 51(2):621-628. 10. 1021/ie200267n

90. Jiang, W., R. M. V. Ginhoven, L. Kovarik, J. E. Jaffe, and B. W. Arey. 2012. "Superlattice Structure and Precipitates in O+ and Zr+ Ion Co-Implanted SrTiO3: A Model Waste Form for 90Sr," *Journal of Physical Chemistry C*, Submitted.

91. Jiang, W., R. M. Van Ginhoven, and D. M. Strachan. 2011. *Chemical and Chargem Imbalance Induced by Radionuclide Decay: Effects on Waste Form Structure,* FCRD WAST-2011-000070, Pacific Northwest National Laboratory, Richland, WA.

92. Jubin, R. T. 2011. "Effects of Aging on Iodine Capture by Silver-Exchanged Mordenite," *GLOBAL,* American Nuclear Society.

93. Jubin, R. T. 2012. "Impact of Pretreatment and Aging on the Iodine Capture Performance of Silver Exchanged Mordenite," *Waste Management*.

94. Jubin, R. T. 2011. *Report of the FY11 Activities of the Off-Gas Sigma Team,* FCRD-SWF-2011-00306, Oak Ridge National Laboratory, Oak Ridge, TN.

95. Jubin, R. T. 2012. *Summary of FY 2012 Off-Gas Sigma Team Activities,* FCRD-SWF-2012-000331, Oak Ridge National Laboratory, Oak Ridge, TN.

96. Jubin, R. T., W. S. Aaron, C. Ausmus, E. D. Collins, V. F. D. Almeida, G. D. Delcul, L. K. Felker, B. D. Patton, R. J. Vedder, and S. L. Voit. 2011. "Development of a Cermet High-Level Waste Form" *Waste Management*.

97. Jubin, R. T., E. D. Collins, L. K. Felker, B. B. Spencer, and J. L. Binder. 2009. "Cete R&D at Oak Ridge National Laboratory Supporting Management of Nuclear Waste," *Waste Management*.

98. Jubin, R. T., D. W. Ramey, R. S. Owens, E. S. Meyers, B. B. Spencer, P. D. Bailey, and J. M. Giaquinto. 2010. "Control of Volatile Radionuclides from the Dissolution of Used Nuclear Fuel," *Waste Management*.

99. Jubin, R. T., N. R. Soelberg, D. M. Strachan, and G. Ilas. 2012. *Fuel Age Impacts on Gaseous Fission Product Capture During Separations,* FCRD-SWF-2012-000089, Oak Ridge National Laboratory, Oak Ridge, TN.

100. Jubin, R. T., N. R. Soelberg, D. M. Strachan, and G. Ilas. 2012. *Position Paper on Practicable Performance Criteria for the Removal Efficiency of Volatile Radionuclides,* FCRD-SWF-2012-000091, Oak Ridge National Laboratory, Oak Ridge, TN.

101. Jubin, R. T., B. B. Spencer, G. D. Delcul, B. D. Patton, and D. W. Ramey. 2011. "Control of Radioactive Gas Releases from the Processing of Used Nuclear Fuel: Possible Waste Forms and Volume Considerations," *International High-Level Radioactive Waste Management Conference,* American Nuclear Society.

102. Kane, M. and R. Sindelar. 2008. *Initial Characterization and Performance Evaluation of a Zirconium-Based Metallic Waste Form* GNEP-WAST-TD-RT-2008-000299, SRNS-STI-2008-00013, Savannah River National Laboratory, Aiken, SC.

103. Kim, S., Y. Oyola, T. Saito, R. T. Mayes, C. J. Janke, S. Dai, and C. Tsouris. 2012.

"Recovery of Uranium from Seawater: A Review of Current Status and Future Research Needs " *Separation Science & Technology*, Submitted.

104. Kleykamp H., J. O. Paschoal, R. Peisa, and F. Thommler. 1985. "Composition and Structgure of Fission Product Precipatates in Irradiated Oxide Fuels: Correlation with Phase Studies in the Mo-Ru-Rh-Pd and Bao-UO_2-ZrO_2-MoO_2 Systems," *Journal of Nuclear Materials*, 130:426-433.

105. Kossoy, A., R. Schulze, D. J. Safarik, R. Mccabe, and M. Tang. 2012. "Nd-Mo-Borosilicate Glass-Ceramic: Synthesis, Characterization and Response to Ionizing Radiation," *Journal of Nuclear Materials*, Submitted.

106. Krumhansl, J. L. and T. M. Nenoff. 2011. "Hydrotalcite-Like Layered Bismuth-Iodine-Oxides as Waste Forms," *Applied Geochemistry*, 26(1):57-64.

107. Krumhansl, J. L., T. M. Nenoff, D. Haefner, and R. T. Jubin. 2009. "Novel Bismuth–Based Inorganic Oxide Waste Forms for Iodine Storage " *Global*.

108. Liu, H., N. Bell, B. B. Cipiti, T. G. Lewis, D. F. Sava, and T. M. Nenoff. 2012. *Functionalized Ultra Porous Titania Nanofiber Membranes,* SAND2012-8025, FCRD-SWF-2012-000359, Sandia National Laboratories, Albuquerque, NM.

109. Liu, J., P. K. Thallapally, and D. M. Strachan. 2012. "Metal-Organic Frameworks for Removal of Xe and Kr from Nuclear Fuel Reprocessing Plant," Submitted.

110. Marra, J. C., C. L. Crawford, A. L. Billings, and W. L. Ebert. 2010. *Glass/Ceramic Waste Form Behavior over Geologic Time Scales-FY10 Glass Testing Activities at ANL and SRNL,* FCRD-WAST-2010-000141, Savannah River National Laboratory, Aiken, SC.

111. Marra, J. C., J. V. Crum, and K. E. Sickafus. 2010. *FY10 Advanced Waste Form Development Testing Activities at SRNL, PNNL, and LANL,* FCRD-WAST-2010-000022, Savannah River National Laboratory, Aiken, SC.

112. Matyáš, J., G. E. Fryxell, B. J. Busche, K. Wallace, and L. S. Fifield. 2011. "Functionalized Silica Aerogels: Advanced Materials to Capture and Immobilize Radioactive Iodine, in Ceramic Materials for Energy Applications," *Ceramic Engineering and Science*, Vol. 32, 23-33.

113. Matyáš, J., G. E. Fryxell, and M. J. Robinson. 2012. *Characterization of Dry-Air Aged Granules of Silver-Functionalized Silica Aerogel,* FCRD-SWF-2012-000214, Pacific Northwest National Laboratory, Richland, WA.

114. Matyáš, J., G. E. Fryxell, and M. J. Robinson. 2012. *Silver-Functionalized Silica Aerogel for Capture and Immobilization of Gaseous Radioiodine from Reprocessing Off-Gas,* PNNL-21792, Pacific Northwest National Laboratory, Richland, WA.

115. Matyáš, J., M. J. Robinson, and G. E. Fryxell. 2012. "The Effect of Temperature and Uniaxial Pressure on the Densification Behavior of Silica Aerogel Granules," *Ceramic Engineering and Science*, Vol. 33 (9), 121-125.

116. Mausolf, E., F. Poineau, and K. Czerwinski. 2011. *Production, Characterization, and Polarization Curves of Fe-Tc and Ss-Tc Alloys,* FCRD-WAST-2011-000099, University of Nevada at Las Vegas, Las Vegas, NV.

117. Mendez-Torres, A., M. J. Williamson, D. L. Fisher, R. L. Sindelar, and G. T. Chandler. 2010. *FY2010 Status Report: Investigating of the Incorporation of ZrO2 in an Fe-Based Alloy Waste Form.* FCRD-WAST-2010-000195, SRNL-STI-2010-00597, Savannah River National Laboratory, Aiken, SC.

118. Nenoff, T. M. "Alternative Energy Systems: Nuclear Energy, Introduction to the Special Section on Nuclear Energy", *Ind. Eng. Chem. Res*, 2012, 51 (2), 605–606.

119. Nenoff, T. M. 2012. *Complete Analysis of I2-Loaded Aged/Reduced Ag-Mor from ORNL,* FCRD-SWF-2012-000258, Sandia National Laboratories, Albuquerque, NM, June 2012.

120. Nenoff, T. M., P. V. Brady, T. J. Garino, and C. D. Mowry. 2012. *Determination of Baseline Iodine Waste Form Performance Characteristics,* FCRD-SWF-2012-000172, Sandia National Laboratories.

121. Nenoff, T. M., P. V. Brady, C. D. Mowry, D. F. Sava, D. X. Rademacher, P. S. Crozier, J. A. Greathouse, M. A. Rodriguez, and J. L. Krumhansl. 2012. *Summary Report, Iodine Capture and Storage Studies,* FCRD-SWF-2012-000337, Sandia National Laboratories, Albuquerque, NM.

122. Nenoff, T. M., T. J. Garino, D. X. Rademacher, and M. A. Rodriguez. 2012. *The Synthesis of Ba and Fe Substituted $CaAlSi_2O_6$ Pollucites,* FCRD-SWF-2012-000365, Sandia National Laboratories, Albuquerque, NM.

123. Nenoff, T. M., *Synthesis of Cs,Ba,Fe,Al-Si_2O_6 Pollucites*, M4FT-12SN0304143, August 2012.

124. Nenoff, T. M., *Characterization of Cation Substitution Pollucites*, M4FT-12SN0304141, June 2012

125. Nenoff, T. M. and J. L. Krumhansl. 2012. "Cs+ Removal from Seawater by Commercially Available Molecular Sieves," *Solvent Extraction & Ion Exchange*, 30:33-40.

126. Nutt, W. M. 2012. *Proposed Waste Management Metrics for the 2013 Evaluation and Screening of Fuel Cycle Options,* FCRD-UFD-2012-000061, Argonne National Laboratory, Argonne, IL.

127. Olson, L. 2012. *Formulation of Reference Alloy Waste Form RAW-3,* FCRD-SWF-2012-000348, Savannah River National Laboratory, Aiken, SC.

128. Olson, L. 2011. *FY2011 Status Report: Chromium Content in Iron Based Alloy Waste Forms* FCRD-SWF-2011-000366, SRNL-STI-2011-00579, Savannah River National Laboratory, Aiken, SC.

129. Olson, L. 2011. *FY2011 Status Report: Oxide Incorporation in Iron Based Alloy Waste Forms,* FCRD-SWF-2011-000222, SRNL-STI-2011-00429, Savannah River National Laboratory, Aiken, SC.

130. Olson, L. 2011. *Task Technical and Quality Assurance Plan: Alloy Waste Form Development for the Fuel Cycle Research and Development Program - FY11,* SRNS-TR-2011-00014, Savannah River National Laboratory, Aiken, SC.

131. Olson, L. 2012. *Task Technical and Quality Assurance Plan: Alloy Waste Form Development for the Fuel Cycle Research and Development Program – FY12* FCRD-SWF-2012-000043, SRNL-TR-2011-00349, Savannah River National Laboratory, Aiken, SC.

132. Olson, L. and S. Frank. 2012. *Effect of Cr Content in Metallic Waste Forms: Oxidation Layer Formation, Electrochemistry, and Morphology,* FCRD-SWF-2012-000161, Savannah River National Laboratory, Aiken, SC.

133. Park, T. J., M. A. Davis, T. G. Garino, T. M. Nenoff, J. L. Krumhansl, and A. Navrotsky. 2009. "Thermochemistry and Aqueous Durability of Ternary Glass Forming Ba-Titanosilicates: Fresnoites (Ba2TiSi2O8) and Ba-Titanate (BaTiSiO5)," *J. Amer. Cer. Soc.,* 92(9):2053-2058.

134. Park, T. J., T. J. Garino, T. M. Nenoff, D. Rademacher, and A. Navrotsky. 2011. "The Effect of Vacancy and Ba-Substitution on the Stability of the CsTiSi2O6. 5 Pollucite " *J. Amer. Ceram. Soc.*

135. Poineau, F., T. Hartmann, G. W. C. Silva, G. Jarvinen, and K. Czerwinski. 2009. "Preparation of Technetium Metal by Thermal Treatment under Argon/H_2O," *J. Radioanal. Nucl. Chem*, 279:43-28.

136. Poineau, F., J. D. Mazaubrun, D. Ford, J. Fortner, J. Kropf, G. W. C. Silva, N. Smith, K. Long, G. Jarvinen, and K. Czerwinski. 2008. "Uranium/Technetium Separation for

the UREX Process – Synthesis and Characterization of Solid Reprocessing Forms," *Radiochim. Acta*, 96:527-533.

137. Poineau, F., P. F. Weck, T. Hartmann, E. Kim, G. W. C. Silva, G. D. Jarvinen, and K. R. Czerwinski. 2010. "Structural Studies of Technetium-Zirconium Alloys by X-Ray Diffraction, High-Resolution Electron Microscopy, and First-Principles Calculations " *Inorganic Chemistry*, 49(4):1433-1438.

138. Riley, B. J., J. Chun, J. V. Ryan, J. Matyas, X. S. Li, D. W. Matson, S. K. Sundaram, D. M. Strachan, and J. D. Vienna. 2011. "Chalcogen-Based Aerogels as a Multifunctional Platform for Remediation of Radioactive Iodine," *RSC Advances*, 1(9):1704-1715.

139. Riley, B. J., J. V. Crum, W. C. Buchmiller, B. T. Rieck, M. J. Schweiger, and J. D. Vienna. 2009. *FY09 AFCI Quartz Crucible Scale Melter Tests,* PNNL-18781, Pacific Northwest National Laboratory, Richland, WA.

140. Riley, B. J., J. V. Crum, W. C. Buchmiller, B. T. Rieck, M. J. Schweiger, and J. D. Vienna. 2009. *Initial Laboratory-Scale Melter Test Results for Combined Fission Product Waste,* AFCI-WAST-PMO-MI-DV-2009-000184, Pacific Northwest National Laboratory, Richland, Washington.

141. Riley, B. J., J. V. Crum, J. Matyas, J. S. Mccloy, and W. C. Lepry. 2012. "Solution-Derived, Chloride-Containing Minerals as a Waste Form for Alkali Chlorides," *Journal of the American Ceramic Society*, Accepted.

142. Riley, B. J., B. T. Rieck, J. V. Crum, J. Matyas, J. Mccloy, S. K. Sundaram, and J. D. Vienna. 2010. *Alternative Electrochemical Salt Waste Forms, Summary of FY2010 Results,* FCRD-WAST-2010-000129, Pacific Northwest National Laboratory, Richland, WA.

143. Riley, B. J., B. T. Rieck, J. S. Mccloy, J. V. Crum, S. K. Sundaram, and J. D. Vienna. 2012. "Tellurite Glass as a Waste Form for Mixed Alkali-Chloride Waste Streams: Candidate Materials Selection and Initial Testing," *Journal of Nuclear Materials*, 424(1-3):29-37.

144. Rohatgi, A. and D. M. Strachan. 2011. *Potential Production Technologies for E-Metal, Tc, and Noble Metals – an Initial Assessment,* PNNL-20313, Pacific Northwest National Laboratory, Richland, WA.

145. Roy, L. E. N. J. Bridges, and L. R. Martin, Dalton Transactions, 2012, DOI: 10. 1039/c2dt31485a

146. Rudisill, T. S. 2008. *Decontamination of Spent Fuel Cladding Hulls,* GNEP-AFCI-IMPT-MS-2007-000192, Savannah River National Laboratory, Aiken, SC.

147. Rudisill, T. S. 2009. "Decontamination of Zircaloy Cladding Hulls from Spent Nuclear Fuel," *J. Nuc. Mat.,* 385:193-195.

148. Ryan, J. V., E. C. Buck, J. Chun, J. V. Crum, B. J. Riley, D. M. Strachan, S. K. Sundaram, L. A. Turo, and J. V. Vienna. 2009. *Alternate Waste Forms: Aqueous Processing,* AFCI-WAST-PMO-MI-DV-2009-000360, Pacific Northwest National Laboratory, Richland, WA.

149. Ryan, J. V., W. L. Ebert, J. P. Icenhower, D. K. Schreiber, D. M. Strachan, and J. D. Vienna. 2012 Joint EM-NE-International Study of Glass Behavior over Geologic Time Scales. In *Proceedings of Waste Management,* Waste Management, Tucson, AZ.

150. Ryan, J. V., W. L. Ebert, J. P. Icenhower, D. M. Strachan, C. I. Steefel, L. J. Criscenti, I. C. Bourg, R. E. Williford, K. A. Murphy, C. G. Pantano, E. M. Pierce, D. K. Shuh, G. A. Waychunas, J. C. Marra, J. D. Vienna, P. Zapol, and C. M. Jantzen. 2011. *Technical Program Plan for the International Technical Evaluation of Alteration Mechanisms (I-Team),* PNNL-21031, Pacific Northwest National Laboratory, Richland, WA.

151. Ryan, J. V., C. P. Rodriguez, D. M. Strachan, G. F. Piepel, and J. D. Vienna.

2008. *A Matrixed Study on Vitreous Waste Forms for a Mixed Cs/Sr/Ba/Rb Waste Stream,* PNNL-18646, Pacific Northwest National Laboratory, Richland, WA.

152. Ryan, J. V., D. K. Schreiber, and D. M. Strachan. 2011. *Initial Assessment of Ancient Roman Glass Analyses for Use in Glass Alteration Modeling,* PNNL-20790, Pacific Northwest National Laboratory, Richland, WA.

153. Ryan, J. V., D. M. Strachan, J. Mccloy, J. V. Crum, D. Jansik, D. Dixon, D. K. Schreiber, and C. Chamberlain. 2012. *Ancient Roman Glass Characterization for Use in Glass Corrosion Modeling,* PNNL-21847, Pacific Northwest National Laboratory, Richland, WA.

154. Ryan, J. V., J. D. Vienna, W. L. Ebert, J. P. Icenhower, D. M. Strachan, C. I. Steefel, P. Zapol, L. J. Criscenti, I. C. Bourg, and E. M. Pierce. 2011. *Peer Review and Response for the International Technical Evaluation of Alteration Mechanisms (I-Team),* FCRD-SWF-2011-000342, Pacific Northwest National Laboratory, Richland, WA.

155. Sava, D. F., T. J. Garino, and T. M. Nenoff. 2012. "Iodine Confinement into Metal-Organic Frameworks (MOFs): Low Temperature Sintering Glasses to Form Novel Glass Composite Material (GCM) Alternative Waste Forms," *Ind. Eng. Chem. Res.,* 51(2):612-618.

156. Sava, D. F., M. A. Rodriguez, K. W. Chapman, P. J. Chupas, J. A. Greathouse, P. S. Crozier, and T. M. Nenoff. 2011. "Capture of Volatile Iodine, a Gaseous Fission Product, by Zeolitic Imidazolate Framework-8," *J. Amer. Chem. Soc.,* 133(32):12398-12401.

157. Schreiber, D. K., J. V. Ryan, and S. Gin. 2012. "Examinations of the Corrosion of Simulated Nuclear Waste Glass Using Atom-Probe Tomography," *Ultramicroscopy*, Submitted.

158. Shkrob, I. 2011. *Alternative Waste Forms for Fission Products: Collabsible Nanoporous Glass for Sequestration and Disposal of Lanthanide Ions,* FCRD-WAST-2011-000013, Argonne National Laboratory, Argonne, IL.

159. Simpson, M. F. and S. Prateek. 2008. "Development of Electrorefiner Waste Salt Disposal Process for the EBR-II Spent Fuel Treatment Project," *Nuclear Engineering And Technology*, 40(3):175-182.

160. Simpson, M. F. and P. Sachdev. 2008. "Development of Electrorefiner Waste Salt Disposal Process for the EBR-II Spent Fuel Treatment Project," *Nuclear Engineering and Technology*, 40(3):175-182.

161. Simpson, M. F., T. S. Yoo, R. W. Benedict, S. Phongikaroon, S. Frank, P. Sachdev, and K. Hartman. 2007. "Strategic Minimization of High Level Waste from Pyroprocessing of Spent Nuclear Fuel," *Global*.

162. Skorski, D. C., J. V. Ryan, D. M. Strachan, and W. C. Lepry. 2011. *Engineering Glass Passivation Layers -Model Results,* PNNL-20615, Pacific Northwest National Laboratory, Richland, WA.

163. Soelberg, N., D. Gombert, and D. Haefner. 2007. "Waste Management Planned for the Advanced Fuel Cycle Facility," *Global*.

164. Soelberg, N. and T. Watson. 2012. *Deep Bed Adsorption Testing Using Silver-Functionalized Aerogel,* FCRD-SWF-2012-000173, INL/EXT-12-26522, Idaho National Laboratory, Idaho Falls, ID.

165. Soelberg, N. and T. Watson. 2011. *Deep Bed Iodine Sorbent Testing FY 2011 Report,* FCRD-SWF-2011-000316, INL/EXT-11-23191, Idaho National Laboratory, Idaho Falls, ID.

166. Soelberg, N. and T. Watson. 2012. *Iodine Sorbent Performance in FY 2012 Deep Bed Tests,* FCRD-SWF-2012-000278, INL/EXT-12-27075, Idaho National Laboratory, Idaho Falls, ID.

167. Solbrig, C. W. and K. J. Bateman. 2010. "Modeling Solidification-Induced Stress in Ceramic Waste Forms Containing Nuclear Wastes," *Nuclear Technology*, 172(2):189-203.

168. Spencer, B. B., R. T. Jubin, S. H. Bruffey, K. K. Anderson, and J. F. Walker. 2012. *Assessment of Tritium (Water)/Iodine Co-Adsorption on Agz,* FCRD-SWF-2012-000210, Oak Ridge National Laboratory, Oak Ridge, TN.

169. Strachan, D. M. 2012. "Glass Dissolution as a Function of pH and Its Implications on Mechanism and Experiments," *Geochimica et Cosmochimica Acta*, Submitted

170. Strachan, D. M., S. A. Bryan, J. C. H. Henager, T. G. Levitskaia, J. Matyas, P. K. Thallapally, R. D. Scheele, W. J. Weber, and F. Zheng. 2009. *Processes for Removal and Immobilization of 14C, 129I, and 85Kr.,* PNNL-18852, Pacific Northwest National Laboratory, Richland, WA.

171. Strachan, D. M., E. C. Buck, K. T. Mueller, J. M. Schwantes, M. J. Olszta, S. Thevuthasan, and R. M. Heeren. 2011. *Analytical Plan for Roman Glasses,* PNNL-20204, Pacific Northwest National Laboratory, Richland, WA.

172. Strachan, D. M., J. Chun, C. H. Henager, Jr., J. Matyas, B. J. Riley, J. V. Ryan, and P. K. Thallapally. 2010. *Summary Report for the Development of Materials for Volatile Radionuclides,* PNNL-20007, Pacific Northwest National Laboratory, Richland, WA.

173. Strachan, D. M., J. Chun, J. Matyas, W. C. Lepry, B. J. Riley, J. V. Ryan, and P. K. Thallapally. 2011. *Summary Report on the Volatile Radionuclide and Immobilization Research for FY2011 at PNNL,* PNNL-20807, FCRD-SWF-2011-000378, Pacific Northwest National Laboratory, Richland, WA.

174. Strachan, D. M., J. V. Crum, E. C. Buck, B. J. Riley, and M. R. Zumhoff. 2010. *Fiscal Year 2010 Summary Report on the Epsilon-Metal Phase as a Waste Form for ^{99}Tc,* Report No. FCRD-WAST-2010-000188 (PNNL-19828), Pacific Northwest National Laboratory, Richland, WA.

175. Strachan, D. M., J. V. Crum, M. R. Zumhoff, C. C. Bovaird, C. F. Windisch, and B. J. Riley. 2011. *Epsilon Metal Summary Report FY 2011,* Report No. FCRD-WAST-2011-000389 (PNNL-20975), Pacific Northwest National Laboratory, Richland, WA.

176. Tang, M., P. Fuierer, P. Dickens, and E. Fu. 2012. "Irradiation Study on $Sr_{n+1}ti_no_{3n+1}$ Ruddlesden-Popper Phases Synthesized by Hot-Forging," *Physica Status Solidi*, Submitted.

177. Taylor, C. 2011. "Surface Segregation and Adsorption Effects of Iron–Technetium Alloys from First-Principles," *Journal of Nuclear Materials*, 408:183-187.

178. Thallapally, P. K., J. W. Grate, and R. K. Motkuri. 2012. "Facile Xenon Capture and Release at Room Temperature Using a Metal–Organic Framework: A Comparison with Activated Charcoal," *Chemical Communication*, 48:347-349.

179. Thallapally, P. K. and D. M. Strachan. 2012. *Initial Proof of Principle for near Room Temperature Xe and Kr Separation from Air with Mofs* PNNL-21452, Pacific Northwest National Laboratory, Richland, WA.

180. Tranter, T. 2009. *Krypton-85 Capture Studies for the Treatment of Off-Gas Streams from Light Water Reactor Fuel Reprocessing* AFCI-SEPA-PMO-MI-DV-000186, Idaho National Laboratory, Idaho Falls, ID.

181. Trivelpiece, C. L., J. J. Petrunis, R. G. Downing, and C. G. Pantano. 2012. "Glass Surface Gel-Layer Density by Neutron Depth Profiling," *International Journal of Applied Glass Science*, 3(2):137-143.

182. Van Ginhoven, R. M., J. E. Jaffe, W. Jiang, and D. M. Strachan. 2010. *Chemical and Charge Imbalance Induced by Radionuclide Decay: Effects on Waste Form Structure,* PNNL-20049, Pacific Northwest National Laboratory, Richland, WA.

183. Van Ginhoven, R. M., J. E. Jaffe, W. Jiang, and D. M. Strachan. 2011. *Chemical and Charge Imbalance Induced by Radionuclide Decay: Effects on Waste Form Structure,*

PNNL-20312, Pacific Northwest National Laboratory, Richland, WA.

184. Van Ginhoven, R., J. Jaffe, and W. Jiang, "Combined Theoretical/Experimental Study of Zr-implanted SrTiO3 as a Model Wasteform for the Decay of Sr to Zr", *Spring MRS*, San Francisco, CA, April 2012.

185. Vienna, J. D. 2010. "Nuclear Waste Vitrification in the United States: Recent Developments and Future Options," *International Journal of Applied Glass Science* 1(3):309-321.

186. Vienna, J. D. 2010. *Waste Form Campaign Implementation Plan,* PNNL-19282, Pacific Northwest National Laboratory, Richland, WA.

187. Vienna, J. D., J. V. Crum, G. J. Sevigny, and G. L. Smith. 2012. *Preliminary Technology Maturation Plan for Immobilization of High-Level Waste in Glass-Ceramics,* FCRD-SWF-2012-000152, Pacific Northwest National Laboratory, Richland, WA.

188. Vienna, J. D., T. A. Todd, and M. E. Peterson. 2012. *Separations and Waste Forms Campaign Implementation Plan,* FCRD-SWF-2012-00123, U. S. Department of Energy, Office of Nuclear Energy, Idaho Falls, ID.

189. Wass, J. C. 2011. *Development and Characterization of New High-Level Waste Forms for Achieving Waste Minimization from Pyroprocessing* FCRD-WAST-2011-000090, Idaho National Laboratory, Idaho Falls, ID.

190. Wass, J. C. 2009. *Prepare Report Describing Initial Waste Form Development and Characterization* AFCI-SEPA-PMO-MI-DV-2009-000234, Idaho National Laboratory, Idaho Falls, ID.

191. Wass, J. C. 2010. *Report on Metal Waste Development Runs Using Surrogate Material* FCRD-SEPA-2010-000135, Idaho National Laboratory, Idaho Falls, ID.

192. Williamson, M., J. Mickalonis, D. Fisher, and R. Sindelar. 2010. *Passivation Layer Stability of a Metallic Alloy Waste Form,* FCRD-WAST-2010-000127, SRNL-STI-2010-00477, Savannah River National Laboratory, Aiken, SC.

193. Williamson, M. and R. Sindelar. 2009. *Development of an Fe-Based Alloy Waste Form for Spent Nuclear Fuel,* AFCI-SEPA-WAST-TD-RT-2009-000143, SRNL-STI-2009-00522, Savannah River National Laboratory Aiken, SC.

194. Zhao, H., K. Beyer, T. M. Nenoff, P. J. Chupas, and K. W. Chapman. "Combining Simultaneous Pair Distribution Function with Diffuse Reflectance Infrared Spectroscopy to Study Silver Particle Growth on Porous Template" 2012, (submitted).

195. Zhao, H., T. M. Nenoff, G. Jennings, P. J. Chupas, and K. W. Chapman. "Determining Quantitative Kinetics and the Structural Mechanism for Particle Growth in Porous Templates", *J. Phys. Chem. Letters*, 2011, 2, 2742–2746.

General Separations and Waste Forms and Other

1. Baker, J. D., C. A. Mcgrath, and T. S. Hill. 2010. "Actinide Targets for Neutron Cross Section Measurements," *Journal Of Radioanalytical And Nuclear Chemistry*, 276(2):555-560. DOI: 10. 1007/s10967-008-0541-x Published: MAY 2008

2. Bathke, C. G., B. B. Ebbinghaus, B. W. Sleaford, R. K. Wallace, B. A. Collins, K. R. Hase, G. D. Jarvinen, K. S. Bradley, J. R. Ireland, M. W. Johnson, A. W. Prichard, and B. W. Smith. 2009. "The Attractiveness of Materials in Advanced Nuclear Fuel Cycles for Various Proliferation Scenarios," *Global*.

3. Borland, M. and S. M. Frank. 2009. "An Evaluation of Alternative Production Methods for Pu-238 General Purpose Heat Source Pellets," *Nuclear and Emerging*

Technologies for Space (NETS-2009), American Nuclear Society.

4. Borland, M., S. M. Frank, P. Lessing, D. F. Bickford, R. Cannon, K. Chidester, T. Wheeler, L. Seward, and W. West. 2008. *Evaluation of Aqueous and Powder Processing Techniques for Pu-238 Fueled General Purpose Heat Sources,* INL/EXT-08-14017, Idaho National Laboratory, Idaho Falls, ID.

5. Bredt, P., A. R. Felmy, P. A. Gauglitz, D. Hobbs, S. Krahn, N. Machara, M. Mcilwain, B. A. Moyer, A. P. Poloski, K. Subramanian, J. D. Vienna, and B. Wilmarth. 2008. *Scientific Opportunities to Reduce Risk in Nuclear Process Science,* PNNL-17699, Pacific Northwest National Laboratory, Richland

6. Bresee, J. C., A. R. Griffith, E. D. Collins, R. T. Jubin, and G. D. Delcul. 2012. "Chemical Pre-Treatment of Used Fuel for Long-Term Storage," *Atalante 2012*, International Conference, Montpellier, France.

7. Bruhn, D. F., F. F. Roberto, P. J. Pinhero, S. M. Frank, and S. G. Johnson. 2009. "Microbial Biofilm Growth on Irradiated, Spent Nuclear Fuel Cladding," *Journal of Nuclear Materials*, 384(2):140-145.

8. Cipiti, B. 2010. "Optimizing near Real Time Accountability for Reprocessing," *Nuclear Materials Management Annual Meeting*, Vol. Proceedings of the 51st Institute of Nuclear Materials Management Annual Meeting.

9. Collins, E. D. 2009. "Advanced Fuel Cycle Treatment, Recycling, and Disposal of Nuclear Waste," *Global,* American Nuclear Society.

10. Collins, E. D., Del Cul, G. D., Rushton, J. E., Williams, K. A. 2010. "A Practical Solution to Used Nuclear Fuel Treatment to Enable Sustained Nuclear Energy and Recovery of Vital Materials," *Proceedings of 51st Annual Meeting of the Institute of Nuclear Materials Management*.

11. Collins, E. D., G. D. Delcul, R. D. Hunt, J. A. Johnson, and B. B. Spencer, *Advanced Dry Head-End Reprocessing of Light Water Reactor Spent Nuclear Fuel*, U. S. 2011/0250108 A

12. Collins, E. D. and J. P. Renier. 2007. "Practical Combinations of Light-Water Reactors and Fast Reactors for Future Actinide Transmutation," *Global*.

13. Delcul, G. D., R. T. Jubin, and B. B. Spencer. 2012. *1-Kg Scale Nitration Test Equipment – Initial Test,* ORNL/LTR-2012/251, Oak Ridge National Laboratory, Oak Ridge, TN.

14. Delcul, G. D., B. B. Spencer, and E. D. Collins. 2007. "A New Paradigm: Near Complete Recycling of Spent Fuel, A Path to Sustainable Nuclear Energy," *Global,* American Nuclear Society.

15. Delcul, G. D., B. B. Spencer, and R. T. Jubin. 2011. *Design Criteria for 1-Kg Scale Nitration Test Equipment,* ORNL/LTR-2011/482, Oak Ridge National Laboratory, Oak Ridge, TN.

16. Del Cul, G. D., E. D. Collins, B. B. Spencer, and R. T. Jubin, "Conceptual Design of a Simplified Head-End Process for the Recycling of Used Nuclear Fuel," American Nuclear Society 2012 Annual Meeting, Chicago, Illinois, June 24–28, 2012. (presented June 25, 2012).

17. DelCul, G. D., B. B. Spencer, R. D. Hunt, R. T. Jubin, and E. D. Collins, "Advanced Head End for the Treatment of Used LWR Fuel," OECD/NEA 11th Information Exchange Meeting on Actinide and Fission Product Partitioning and Transmutation, November 1-5 2010, San Francisco.

18. Delcul, G. D., L. D. Trowbridge, J. P. Renier, R. J. Ellis, K. A. Williams, B. B. Spencer, and E. D. Collins. 2007. *Analysis of the Reuse of Uranium Recovered from the Processing of Commercial LWR Spent Fuel,* ORNL/TM-2007/098, Oak Ridge National Laboratory Oak Ridge, TN.

19. Farawila, A. F., M. J. O'Hara, H. Z. Taylor, C. M. Wai, and Y. -J. Liao. 2012. *Selective Extraction of Uranium from Liquid or Supercritical Carbon Dioxide,* PNNL-21590, Pacific Northwest National Laboratory, Richland, WA.

20. Felker, L. K., R. J. Vedder, E. A. Walker, and E. D. Collins. 2008. "Product Conversion: The Link between Separations and Fuel Fabrication," *Atalante*.

21. Gray, J., R. Torres, M. Martinez-Rodriguez, S. Sherman, B. Garcia-Diaz, J. Becnel, A. Visser, P. Korinko, and T. Adams. 2012. "Reactive Gas Recycle Technologies for Used Nuclear Fuel," *J. Nuclear Materials*, Submitted.

22. Hyland, B., E. D. Collins, R. J. Ellis, G. D. Delcul, and M. Magill. 2011. "Transmutation of Americium in a Lanthanide Matrix," *Global,* American Nuclear Society.

23. Inabinett, D., G. Cerefice, T. Knight, M. Martinez-Rodriguez, J. Becnel, B. Garcia-Diaz, T. Adams, and J. Gray. 2012. "Alternate Fluorination Approaches for Reactive Gas Recycle of Used Nuclear Fuel," *Journal of Nuclear Materials*, Submitted.

24. Johnson, J. A., G. D. Delcul, B. B. Spencer, E. D. Collins, and R. D. Hunt. 2012. *Advanced Voloxidation with NO_2 and Tests with Used Nuclear Fuel,* FCRD-SWF-2012-000105, Oak Ridge National Laboratory, Oak Ridge, TN.

25. Laidler, J. J. 2008. "An Overview of Spent-Fuel Processing in the Global Nuclear-Energy Partnership," *ISEC 2008 International Solvent Extraction Conference,* 695-701 pp.

26. Lewis, T. G. and E. Al. 2012. *Modified Open Cycle Modeling,* FCRD-SWF-2012-000259, SAND2012-5456, Sandia National Laboratories, Albuquerque, NM.

27. Mcnamara, B. K., A. M. Casella, R. D. Scheele, and A. E. Kozelisky. 2011. *Nitrogen Trifluoride-Based Fluoride-Volatility Separations Process: Initial Studies* FCRD-SWF-2011-000390, Pacific Northwest National Laboratory, Richland, WA.

28. Nenoff, T. M. 2012. "Alternative Energy Systems: Nuclear Energy, Introduction to the Special Section on Nuclear Energy," *Ind. Eng. Chem. Res.,* 51(2):605-606.

29. Scheele, R. D., B. K. Mcnamara, A. M. Casella, and A. Kozelisky. 2012. "On the Use of Thermal NF3 as the Fluorination and Oxidation Agent in Treatment of Used Nuclear Fuels " *Journal of Nuclear Materials*, 424:224-236.

30. Schwantes, J. M., S. A. Bryan, C. R. Orton, T. G. Levitskaia, and C. G. Fraga. 2012. "Monitoring, Controlling and Safeguarding Radiochemical Streams at Spent Fuel Reprocessing Facilities, Part 2: Gamma-Ray Spectroscopic Methods," *International Journal on Nuclear Energy Management and Safety*, Published.

31. Soelberg, N. 2008. *Evaluation of Existing Department of Energy (DOE) Facilities to Support the Advanced Fuel Cycle Facility (AFCF) Mission,* GNEP-AFCF-PMO-AI-EA-2008-000271, Rev. 1, Idaho National Laboratory, Idaho Falls, ID.

32. Svoboda, J., V. Rutledge, and L. Macaluso. 2011. *Enhanced Sampling and Analysis: Demonstration System Design* FCRD-SWF-2011-000391, Idaho National Laboratory, Idaho Falls, ID.

33. Todd, T. A. 2010. "Separations Research for Advanced Nuclear Fuel Cycles. " In *Nuclear Energy and the Environment*. American Chemical Society.

34. Todd, T. A., L. K. Felker, J. D. Vienna, J. Bresee, and S. Lesica. 2009. "The Advanced Fuel Cycle Initiative Separations and Waste Campaign: Accomplishments and Strategy," *Global*.

35. Torres, R., J. Gray, P. Korinko, M. Martinez-Rodriguez, J. Becnel, B. Garcia-Diaz, and T. Adams. 2012. "Sulfur Hexafluoride Treatment of Used Nuclear Fuel to Enhance Separations. " FCRD Annual Report, FCRD-SWF-2012-000332.

36. Torres, R., M. Martinez-Rodriguez, J. Gray, P. Korinko, and T. Adams. 2012. "Kinetics of Fluorination of Fission Products with Sulfur Hexafluoride," *J. Nuclear Materials*, Submitted.

37. Torres, R., M. Martinez-Rodrigues, J. Gray, P. Korinko, and T. Adams. 2012. "Kinetics of Fission Product Fluorination with Sulfur Hexafluoride. " Accepted for Presentation at *Winter ANS Meeting*.

38. Tranter, T. J. 2011. "Solid Phase Extraction Technology for Actinide and Lanthanide Separations. " In *Advanced Separation Techniques for Nuclear Fuel Reprocessing and Radioactive Waste Treatment,* eds. K. L. Nash and G. J. Lumetta. Woodhead Publishing, Cambridge, U. K.

39. Tripathy, P. K., M. Gauthier, and D. J. Fray. 2007. "Electrochemical Deoxidation of Titanium Foam in Molten Calcium Chloride," *Metallurgical And Materials Transactions B*, 38(6):893-900.

40. Tripp, J., N. Soelberg, and R. Wigeland. 2011. *Innovative Separations Technologies,* FCRD-SYSA-2011-000097, INL/EXT-11-22297, Idaho National Laboratory, Idaho Falls, ID.

41. Wang, Y., T. S. Yoo, and S. Lafortune. 2007. "Diagnosis of Discrete Event Systems Using Decentralized Architectures," *Discrete Event Dynamic Systems-Theory And ApplicationS*, 17(2):233-263.

42. Wanigasekara, E., X. G. Sun, L. H. Delmau, H. Luo, S. Dai, and B. A. Moyer. 2011. *Transformational Approach Using Ionic Liquids,* FCRD-SWF-2011-000383, Oak Ridge National Laboratory, Oak Ridge, TN.

43. Wanigasekara, E., X. G. Sun, R. A. Meisner, H. M. Meyer, H. Luo, L. H. Delmau, S. Dai, and B. A. Moyer. 2012. "Direct Electrodeposition of UO2 from Uranyl Bis(Trifluoromethanesulfonyl)Imide Dissolved in 1-Ethyl-3-Methylimidazolium Bis(Trifluoromethanesulfonyl)Imide Room Temperature Ionic Liquid (Rtil) System.," *Electrochim. Acta*, Submitted.